SCUOLA DI DOTTORATO
UNIVERSITÀ DEGLI STUDI DI MILANO-BICOCCA

Department of Earth and Environmental Sciences

Ph.D. program: Chemical, Geological and Environmental Sciences **Cycle:** XXXIII

Curriculum: Chemical Sciences

Thermally Regenerable Redox-Flow Batteries

Surname: Facchinetti **Name:** Irene

Registration number: 750483

Tutor: Prof. Mustarelli Piercarlo

Supervisor: Prof. Ruffo Riccardo

Coordinator: Prof. Frezzotti Maria Luce

ACADEMIC YEAR: 2019/2020

Declaration

I, Facchinetti Irene, declare that this thesis is an original work which was conducted by the undersigned using the laboratory facilities of the Department of Material Sciences, University of Milano Bicocca, in Milan, Italy, and the Faculty of Production Engineering, University of Bremen, in Bremen, Germany.

CONTENTS

Abstract

Low-Temperature Heat (LTH), heat below 100°C, has recently elicited great interest among the scientific community, as a source of energy since it actually does not see any form of utilization as it is currently simply released into the environment. The conversion of such form of energy from various sources thus becomes of utmost importance as its efficient recycling would allow decreasing the environmental footprint caused by humankind during energy production, and it would open the doors to the exploitation of a huge amount of heat as well, such as geothermal, solar, and industrial waste heat.

Even though the conversion of High-Temperature Heat (HTH) is well-established thanks to its high energy level and the widespread availability of methodologies able to convert it in a quite efficient way, the conversion of LTH is still a challenge due to its complexity. As a matter of fact, the conversion efficiencies of low-temperature heat are really low because of the limitations imposed by Carnot law, as well as the existence of technological limits which further reduce the efficiency of the conversion of LTH into a form of energy that can be stored for appropriate timeframes, facts that negatively affect the overall performance and thus development, production and commercialization of devices based upon the process.

For these reasons, even though LTH is a ubiquitous energy source, it is potential as a viable energy source still remains unexploited due to the lack of an optimized methodology capable of simultaneously integrating heat-exchange and energy conversion, and capable of converting this otherwise wasted heat source into electrical energy with an efficiency close to the theoretical maximum value in a cost-effective way.

In order to be suitable for extensive industrial production, technologies capable of converting Low-Temperature Heat into electrical energy should show high power densities, scalable and efficient whilst being cost-effective; to this point, the techniques proposed for this afore mentioned application all failed to achieve suitable efficiencies and practical values of power density, thus making the LTH conversion unfeasible.

To fill this technological gap in contemporary energy production and storage, this research project focused on the development of a suitable system that is able not only to convert LTH into electricity but also to store it in form of chemical energy.

The efforts put in the studies for this Ph.D. project lead to the design of a device called Thermally Regenerable Redox-Flow Battery (TRB) consisting of a redox-flow battery that can be recharged by a thermal process in light of the objective of efficiently exploit the energy of LTH, which otherwise would simply be lost to the environment.

The device is based upon a two-stages technology composed of a “power production” stage and a “thermal” stage: power production happens in an electrochemical cell which releases electricity at the expenses of the mixing free energy of two water solutions of the same salt at different concentrations, referred to as a concentration cell.

When the two solutions reach the same concentration, the exhausted fluid is sent to the second stage, the thermal process, which regenerates the initial mixing free energy, by exploiting LTH sources, through vacuum distillation. The efficiency of the technology is the product between the efficiencies of the units in the device where both stages happen: the electrochemical cell, engineered for power production, and a distillation unit, designed to be responsible for the thermal conversion.

To achieve all these objectives, thermodynamic studies have shown the importance related to the solvent and salt choice to ensure high energy conversion efficiencies in the device.

To increase said conversion efficiency, it is important to optimize the efficiency of the second stage, the one dedicated to thermal conversion: in fact, as already mentioned above, if theoretically the efficiency of the "power production" stage could reach the maximum value possible, the conversion efficiency related to the thermal stage would still be limited by Carnot law, thus limiting the applicability of the technology for widespread use.

Thermodynamic concepts were studied for the optimization of the engineering of the distillation unit in charge of thermal conversion and the subject highlights the importance of a high boiling point of the solution that undergoes to distillation and, additionally, to increase the amount of stored energy in the device, thermodynamics points out the importance to choose not only the highest concentration difference between the solutions, but also to use a solvent with a large latent heat of vaporization.

Given the requirements just described for the optimization of LTH conversion devices, aqueous solutions appear to be the rational choice for TRBs, due to the large latent heat of water vaporization and the large solubility of a great array of salts: the most suitable salt may be chosen among those with the highest solubility, such as halides and hydroxides, which are capable of increase the boiling point of water by 20-50°C as well once the saturation point is reached.

Among these salts, NaI/I_2 and $LiBr/Br_2$ will be the most discussed redox couple in this thesis, as result of thermodynamic analysis.

The achieved results, as well as the main research activities, are briefly reported in this abstract:

starting from the determination of the activity coefficients, mixing free energy of the initial solutions, and the open-circuit voltage of the electrochemical are calculated, furthermore, thermodynamic evaluations of the formation of the poly-halide ions are considered to determine energy losses in the process upon which the proposed device is based.

Electrochemical cells are specifically designed for both systems: electrochemical cells are based on the technology of sodium ion-conducting ceramic membrane, for the Thermally Regenerable Redox-Flow Battery based on NaI, as well as membranes based on the technology of lithium ion-conducting ceramic materials, for the TRB based on LiBr solutions. Such cells are then coupled with a liquid-liquid extraction process, performed by a novel, unconventional device, called "Through Liquid Exchanger" (TLE).

To evaluate the electrochemical performances of the systems, in terms of power density and maximum current density, cyclic voltammetry is performed while discharge profiles are recorded by galvanostatic cycling with potential limitation (GCPL), which is an electrochemical technique that

allows measuring the extracted energy as well as the electrochemical efficiency of the device, specifically of the power production stage.

Modeling of the operational conditions of the thermal stage allows determining the parameters that would allow an efficient way to run the distiller as well as determines the distillation efficiency of both lithium and sodium-based systems.

Improvements of the electrochemical cells and working conditions are made for both the developed TRBs.

Specifically, for the TRB based on NaI solutions, the optimization of the electrochemical cell consists in the improvement of the morphology, permeability, conductivity, and perm-selectivity of NASICON membrane, obtained through different synthetic procedures; further improvements of the system are centered around the choice of the organic solvent used to fill Through Liquid Exchanger, as well as the general setup of the redox-flow cell, in terms of fluxes, pumps, cell, and TLE positions along the circuit.

On the other hand, the optimization of the Thermally Regenerable Redox-flow Battery based on LiBr water solutions, consists in the implementation of a new shape of Through Liquid Exchanger, coupled with the choice of thinner commercial membranes.

The initial experiments prove an unprecedented heat-to-electricity efficiency for both the systems: 3% for TRB-NaI and 4-5% for TRB based on LiBr water solutions, depending on the thickness of the membrane with a power density output of almost 10 W m^{-2} for both technologies, which opens various possibilities to implement further improvements into this new class of energy storage/converter devices.

Particularly, new materials may be studied as electrodes for the system based on LiBr, as they actually involve platinum electrodes, which may increase the power output as well as dramatically reduce the cost of these devices to make them an attractive candidate for large scale production.

Whereas for TRB systems based on NaI technology, the main improvements would be related to the NASICON membranes, as their properties may be enhanced by changing synthetic procedures.

List of Figures

List of Tables

CHAPTER 1

Introduction

Climate change, due to its increasing impact on eco-systems and their biodiversity, represents an urgent and potentially irreversible threat to the planet and human societies: the Earth's average temperature is about 15°C and even though there are natural climatic fluctuations, temperatures are now rising at a higher rate than other time (Figure 1.1).

In 2018, the Intergovernmental Panel on Climate Change (IPCC) confirmed that the effects of climate change start acting rapidly with increasing global mean temperature and suggested that with a mere increase of 2°C in average temperature, the world would see dramatic impacts due to climate change[1]. With the term "warming" is indicated the increase in multi-decade global mean surface temperature above pre-industrial levels. Specifically, warming at a given point in time is defined as the global average of combined land surface air and sea surface temperatures for a 30-year period centred on that time, expressed relative to the reference period 1850–1900 as an approximation of pre-industrial levels, excluding the impact of natural climate fluctuations within that 30-year period and assuming any secular trend continues throughout that period, extrapolating into the future if necessary.

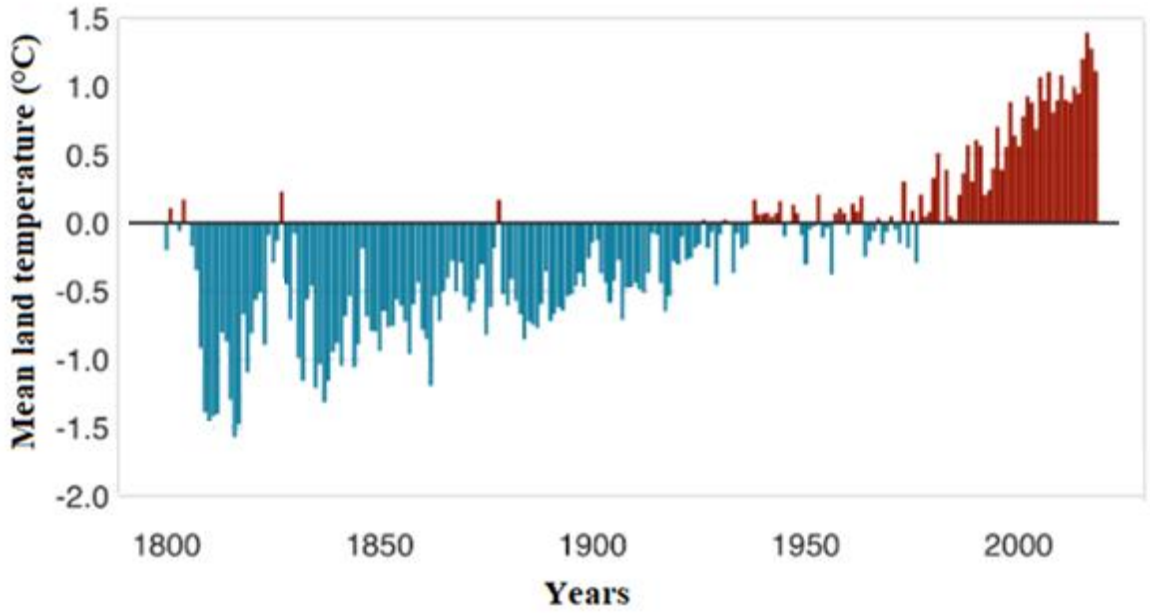

Figure 1.1. Average mean land temperature above or below average (°C). Average is calculated from 1951 to 1980 land surface temperature data. Sources: University of California Berkeley.

According to the above-mentioned report, Arctic land regions will see cold extremes be as warm as 5.5°C with an average increase of 1.5°C warming, while if such increase would lay in a range of 1.5°C to 2°C, cold extremes will be up to 8°C warmer. The report also finds that with a warming of 2°C, some places will see an increase in heavy rainfall, especially in the Northern Hemisphere, and more land areas will also be affected by flooding and increased runoff. Another estimation shows that nearly 250 million people could be potentially exposed to water scarcity by 2050 if the global warming will surpass the threshold of 1.5°C. If this raise in average temperature of 1.5°C is reached,

about 14% of Earth's population is predicted to be exposed to severe heatwaves, while if the increase goes beyond 2°C, that number would rises to 37%. Limiting warming to 1.5°C would reduce the number of people frequently exposed to extreme heatwaves from 420 million to nearly 65 million fewer people.

With an average warming of 1.5°C, this report also shows as 6% of the insects, 8% of the plants and 4% of the vertebrates will see their climatically determined geographic habitat reduced by more than half, whereas with a 2°C average warming, these values would increase to 18%, 16%, and 8% respectively.

With these changes coming into play, entire ecosystems would be radically transformed from what we are currently used to know: above 1.5°C warming, for instance, in the Mediterranean biome desertification is expected to become more relevant and oceans will become more acidic due to higher concentration of CO_2, which will become even higher if the average increase in temperature reaches 2°C; this last climatic effect would negatively impact several marine species, spanning from algae to fish and, furthermore, ocean oxygen levels would decrease, causing a decrease in aquatic life. Another effect of oceans acidification and warming would cause coral reefs to decline by 70 to 90% if the average water temperature is raised by 1.5°C, becoming virtually non-existent if this increase reaches 2°C.

On another note, human life would also be impacted with temperatures warmer by 1.5°C: specifically, risks in human health, livelihoods, food security, water supply and economic growth would become more common and some of the already economically unstable populations would see an increase in poverty rates.

IPCC estimates that in order to limit temperature increase to 1.5°C, net-zero CO_2 emissions at global level needs to be achieved around 2050. For this reason, in March 2020, the European Commission proposed to enshrine in legislation the political commitment to be climate neutral by 2050[2]. With the European Climate Law, the European Commission proposes a legally binding target of net zero CO_2 emission and all the greenhouse gas emission.

One important contribution towards meeting this target is to exploit conventional energy sources more efficiently as well as to incentivize the use of renewable or wasted energy; in this regard, the conversion of low-temperature heat into electrical current can contribute to the overall reduction of consumption of fossil fuels if employed for waste heat recovery or for co-generation.

Low-Temperature Heat (LTH) is defined as heat below of 100°C; it is a widely available thermal energy source but still unexploited because of the lack of suitable devices able to convert this type of energy in efficient and cheap way[3]. A few examples of such Low-Temperature Heat sources available in the world are solar heat, geothermal sources, biomass, co-generation and wasted heat.

Considering wasted heat, more than 60% of this resource gets wasted as Low-Temperature Heat (Figure 1.2): specifically, it is lost to the environment (released in atmosphere or in fluids) without any re-utilization, thus wasting an opportunity for resource optimization. With all this in mind, the conversion of Low-Temperature Heat from various sources, described below, becomes therefore of

utmost importance since it would allow to decrease the environmental footprint of energy production caused by humankind.

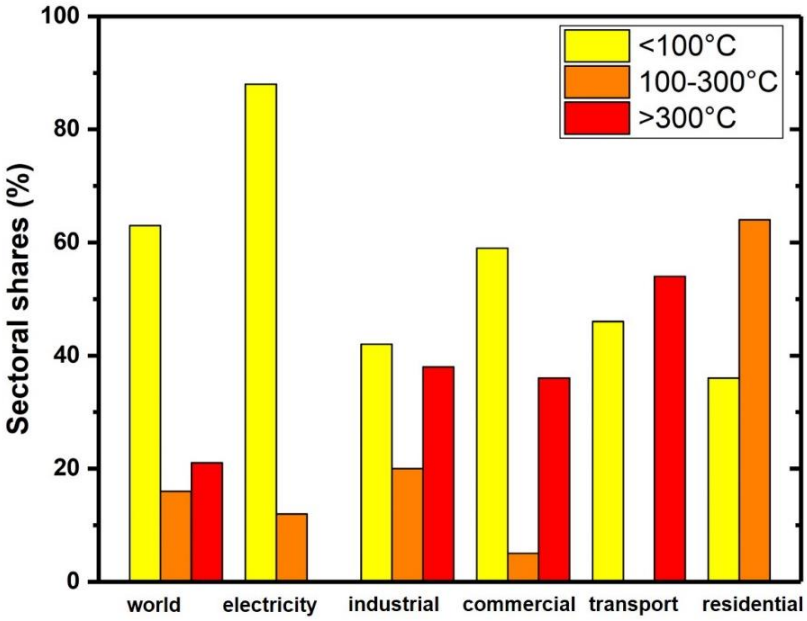

Figure 1.2. Sectoral shares of waste heat distribution.

1.1. Sources of Low-Temperature Heat

1.1.1. Industrial Waste Heat

Industrial waste heat is the energy released during industrial processes without being put to practical use. More than 60% of the industrial energy consumption is released as Low-Temperature Heat.
In 2009, "ENOVA international" reported a study of the waste heat deriving from industries in Norway. The study temperature distribution of the waste heat is showed in Figure 1.3: 47% of the waste heat has less than 60°C, 16% has a temperature between 60°C and 140°C and 37% of the total waste heat has a temperature higher than 140°C. In 2011, the same study was carried out by Pehnt et al[4] about the situation in Germany: results showed that 88% of the total waste heat has a temperature lower than 140°C and, in particular, 80% of the heat has a temperature lower than 60°C (Figure 1.3).

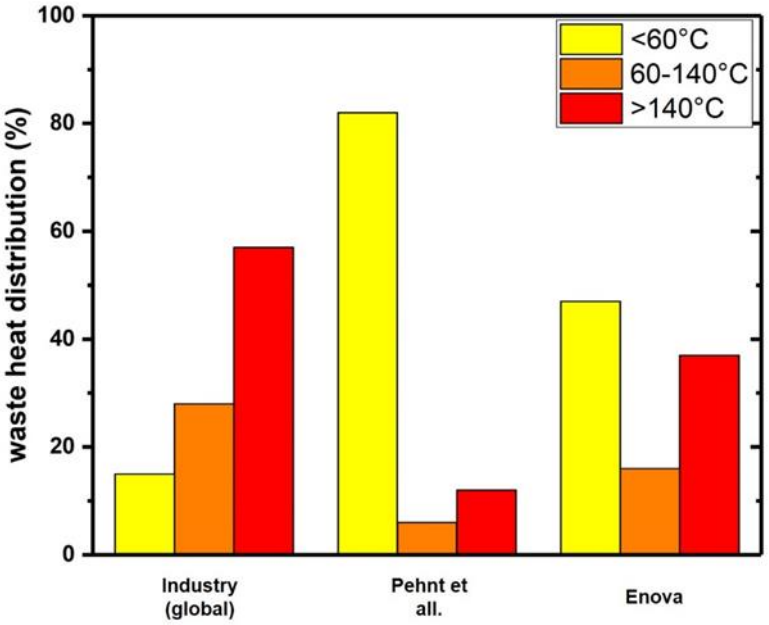

Figure 1.3. Comparison of waste heat distribution in the industrial sector: ENOVA (Potensialstudie for utnyttelse av spillvarme fra norsk industri. Rapport.Enova SF; 2009.) Pehnt et al[4].

Even if some waste heat losses are inevitable, it is possible to reduce the losses by installing waste heat recovery technologies that capture heat and use it directly for heating or the generation of electrical/mechanical work. The estimation of the work potential of waste heat at different temperatures is reported in Figure 1.4. The analysis is based on the amount of heat estimated using a reference temperature of 25°C which represents the maximum heat recoverable if, for example, exhausted gases are cooled down to room temperature. The graph in Figure 1.4 shows not only that Low-Temperature Heat is abundant, as already known, but also its corresponding work potential exceeds that of Medium and High-Temperature Heat. Thus, even if LTH has lower value, the large amount of available Low-Temperature Heat makes it worthy of further investigation.

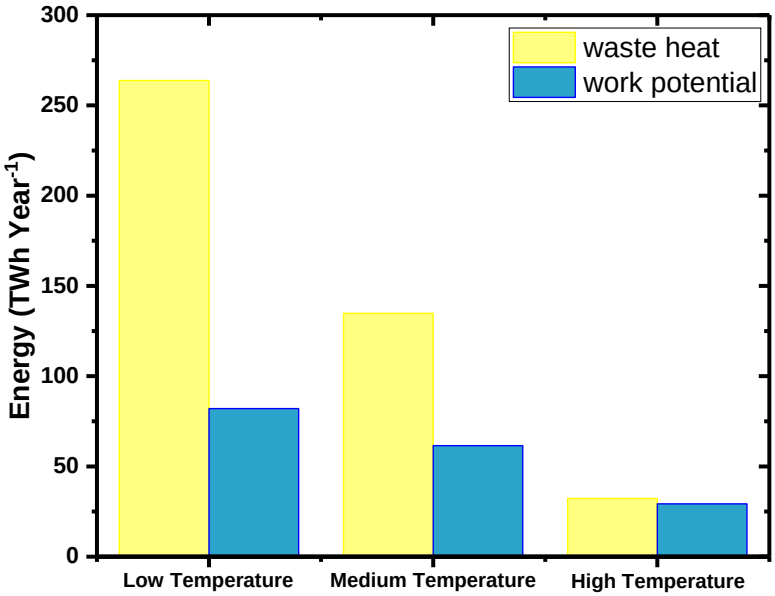

Figure 1.4. Amount of waste heat and relative work potential in different temperature groups. The estimation of the amount of heat is based on a reference temperature of 25°C.

1.1.2. Low-Temperature Geothermal Heat

Geothermal heat is a renewable, clean energy resource which can be sustainably exploited. This type of thermal energy is stored in the Earth's subsurface, located in geologically favorable places. In general, the temperature of the Earth's interior increases from the surface at increasing depth reaching a maximum estimated temperature of 5500°C at the Earth's core. Nevertheless, in some locations, high temperatures are available at low depth. In these places, the heat can be exploited by means of geothermal power plants which consist of heat engines. Currently, there are more than 500 geothermal power plants in operation in 30 different countries, with a total installed capacity of about 13 GW (Figure 1.5).

Usually, high geothermal energy (temperature above 100°C) is used for power generation while low geothermal energy, (temperature lower than 100°C) is mainly used for district heating or it is unexploited.

Geothermal sources at lower temperature are more widespread than the sources at higher temperature, both in Europe and in the USA, as it can be observed in Figure 1.6 and 1.7. Nevertheless, this kind of energy source is still untapped due to the lack of suitable devices able to exploit it.

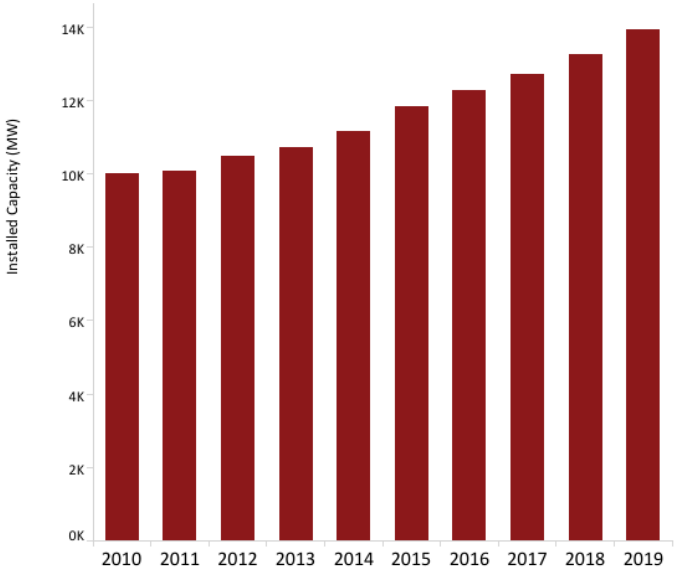

Figure 1.5. Installed capacity trends of geothermal plants in all the world from 2010 to 2019. Available data from IRENA,International Renewable Energy Agency.

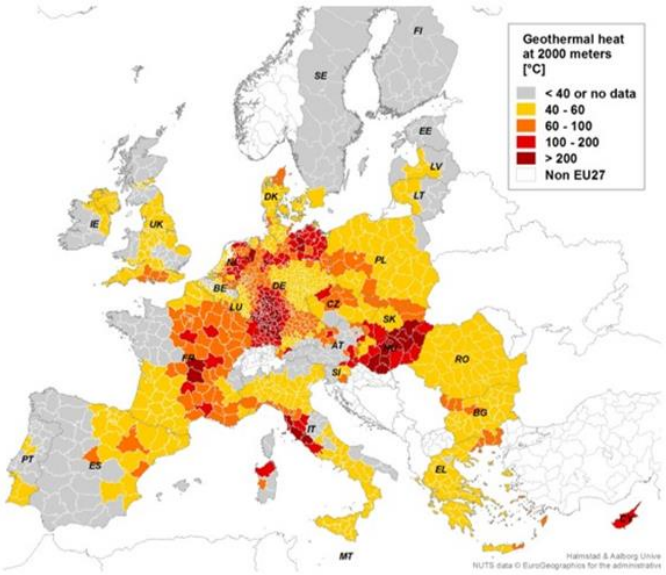

Figure 1.6. Geothermal heat sources at 2 km depth in the EU. (2016). (Halmastad & Aalborg Universities, NUTS data)

Figure 1.7. Extent of low-temperature heat < 100°C, (orange color) geothermal sources in United States. (DATA: OIT-GHC, 1996).

1.1.3. Low-Temperature Solar Heat

Solar thermal energy is a form of renewable energy that can be exploited in several areas in order to reduce dependence on non-renewable energy sources, such as coal combustion or natural gas.

The solar heating system is designed to produce heat, unlike the solar photovoltaic cell array, which is designed to produce electricity.

Generally, 55% of the annual domestic hot water requirement could be provided by solar heating system.

Collecting heat from the sun and using it to produce electrical current could be also a viable alternative to photovoltaic plants: thermal solar energy has already been used to produce electrical energy in industrial-scale solar thermo-electric plants. These power plants concentrate the rays of the sun using mirrors to release high-temperature heat in order to drive a steam turbine. Usually, the heat is transferred to a fluid, which in turn is passed through heat exchangers to run a traditional electricity steam cycle.

Nowadays, solar thermo-electric plants work only at high temperatures and thus require high optical concentration of solar energy involving the use of suitably shaped mirrors and tracking of the sun[5,6]. Unfortunately, solar optical concentration is a valid and economic option only in regions where the sky is extremely clear for a substantial fraction of days per year, like in the southern countries of Europe. Globally, at the end of 2016, an estimated 4 GW of thermal-solar power plants were under construction or under development. The high cost of investments causes a raising of electricity costs and this is one of the down sides of this technology.

Low-Temperature solar thermal energy is exploited in several areas for domestic use (production of hot water and heating), heating swimming pools, or for industrial uses that requires hot water, lower than 100°C, but it is currently not exploited to produce electricity even if its production from low-temperature solar heat is cheaper: in fact, low levels of solar concentration can be easily achieved with concentrators working with the so-called non-imaging optics. These concentrators do not require the tracking of the sun and therefore are cheaper. Hence, the harvesting of LTH from the sun is less expensive than the harvesting of High-Temperature solar heat. For example, in 2009, low-temperature collectors totaled nearly 1 km^2: 94% of these low-temperature collectors were used in the residential sector (Figure 1.8).

1.1.4. Household Cogeneration

As shown in Figure 1.9, Low-Temperature Heat is widely required in space heating, more than in other sectors like industries or transportation. The most efficient way to deliver heating, cooling, and electricity could be Cogeneration or Combined Heat and Power (CHP).

For example, producing electrical current from fossil fuels also produces unused heat, on the other hand, room heating consumes fossil fuels that could be also fruitfully used for producing electrical current. Cogeneration is based on the simultaneous production of electricity and thermal energy.

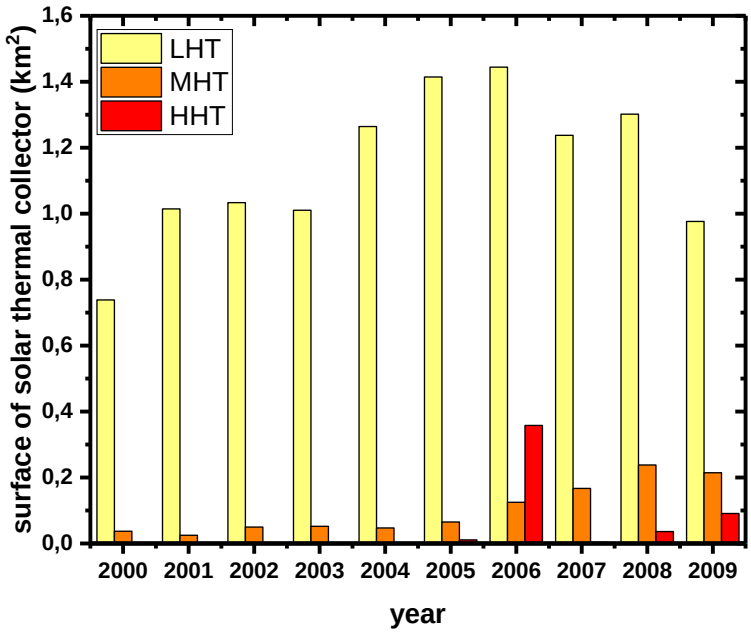

Figure 1.8. Surface of solar thermal collector implemented in USA from 2000 to 2008 divided by type (yellow: low-temperature heat collector; orange: medium-temperature heat collector and red: high-temperature heat collector).

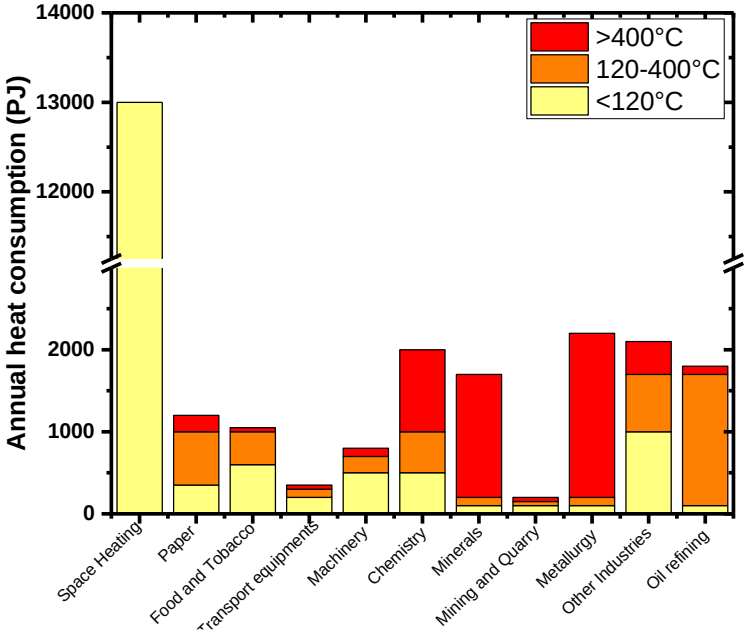

Figure 1.9. Heat consumption in Europe. (Data from Euroheatcool, 2006).

Combining the two processes would allow increasing the overall efficiency: indeed, CHP is up to 40% more efficient than the separate generation of heat and power. Currently, in Europe, cogeneration supplies 11% of electricity and 15% of heat, saving 200 million tons of CO_2 every year. Right now, 27% of fuels used in cogeneration in Europe are renewable, such as biomass and biogas. Nowadays, cogeneration is mainly applied in medium-large plants, for district heating.

Household cogeneration is efficiently performed by condensing boilers, working at low temperatures, so that the latent heat of vaporization of water is recovered by condensation. This system does not find a wide application due to the high costs required for the available technologies, whose costs can be amortized only in several years or, better, in medium-large scale plants.

1.2. Conversion Technologies

Low-Temperature Heat is an energy source that can be directly used or can be converted into another form of energy. The direct use of LTH includes hot water production systems[7], district heating[8], biomass processing[9], radiation-convection recuperator[10] and etc.

LTH conversion systems convert Low-Temperature Heat into heat with different temperatures or in electrical energy, named "power production". Options for the so-called "heat to heat" conversion include the absorption heat pump[11], absorption heat transformer[12], and vapor compression heat pump[13], while the conversion of LTH in electricity can be performed by several technologies that will be discussed in the next section.

Before treating all the possible systems that can convert LTH into electricity, it is fundamental to understand the complexity behind this process.

Actually, the conversion of LTH is harder compared to the conversion of HTH (High-Temperature Heat) due to its low energy level and the lack of technologies able to convert this heat efficiently.

Moreover, distributed waste heat recovery increases the installation space requirement, requiring higher investments, and operation costs[3].

Technologies to convert LTH into electricity must show high power densities, be cost-effective, scalable, and efficient. Up to now, the most extensive system studied to convert LTH sources are Thermoelectric Generators (TEG), Organic Rankine Cycle (ORC), and Kalina Cycle (KC) which are considered the "traditional" heat-to electricity converters because they already found application in the conversion of HTH.

Recently, other technologies were proposed to convert Low-Temperature Heat into electricity based on osmosis or electrochemical processes. These methodologies can be classified on the heat source utilization: devices that directly convert LTH into electricity and devices that involve a power stage and a second thermal treatment where heat is consumed.

Here it is proposed a review of the principal type of technologies proposed to convert LTH and produce electricity. All the technologies here reported are evaluated in terms of power output and thermal-electrical efficiency.

The thermal-electrical efficiency, also called heat-to electricity efficiency or energy conversion efficiency, or again power conversion efficiency, is usually expressed in its generic form as the ratio between the produced electrical work (W) and the required heat (Q):

$$\eta = \frac{W}{Q} \quad (1.1)$$

It is widely known that the maximum thermal conversion efficiency of a power generation system is the Carnot efficiency which represents the ideal efficiency when the heat input is realized in constant heat source temperature:

$$\eta_C = \frac{|W|}{q_{in}} = \frac{q_{in} - |q_{out}|}{q_{in}} = \frac{T_H - T_L}{T_H} = 1 - \frac{T_L}{T_H} \quad (1.2)$$

Where W is the produced work, q_{in} is the heat introduced in the system, q_{out} is the heat released to the heat sink, T_H is the temperature of the heat source and T_L is the temperature of the sink that generally corresponds to the room temperature.

Another important parameter, useful to compare different technologies, is the efficiency relative to Carnot engine ($\eta_{T/C}$):

$$\eta_{T/C} = \frac{\eta}{\eta_C} \quad (1.3)$$

where η_C is the efficiency of a Carnot engine operating at ΔT, η is the power conversion efficiency of the thermal converter operating at ΔT. This parameter, $\eta_{T/C}$ is also known as exergy efficiency or second law efficiency.

Furthermore, it will be discussed the electrochemical efficiency for the technologies that involve electrochemical cells and other important parameters like costs, materials and system complexity.

1.2.1. Traditional Heat-to-Electricity Converters

The most studied heat converters are Thermo-Electric Generator (TEG), Organic Rankine Cycle (ORC), and Kalina Cycle (KC) systems. Despite much progress over the past decades, all these systems have not been used for large-scale conversion of LTH to electricity due to the low heat-to-electricity conversion efficiencies, low power densities, high material and high operational costs, lack of capacities for energy storage, and system complexity[14–16].

The Organic Rankine Cycle is a power production system based on the steam Rankine cycle, which converts heat into mechanical work that is then used to produce electrical power.

Rankine cycle consists in four different steps: in the first one, the working fluid, which is in liquid state, is pumped from low to high pressure, this means that the pump requires energy to work. In the second stage, the high-pressure liquid is heated at constant pressure to saturated vapor. The third process consists in the expansion of the vapor through a turbine producing mechanical work: in this part of the cycle, some condensation may occur because of the decrease of the temperature. The complete condensation, at constant pressure, takes place in the last process where the vapor enters in a condenser (Figure 1.10).

In the case of an ORC, water is substituted with an organic solvent as working fluid. Several are the advantages of ORC systems such as the lower temperature and pressure required for the evaporation process[14]. This means that ORC power plant is more suitable for low-temperature applications compared to Rankine cycle power generator based on water fluid[14].

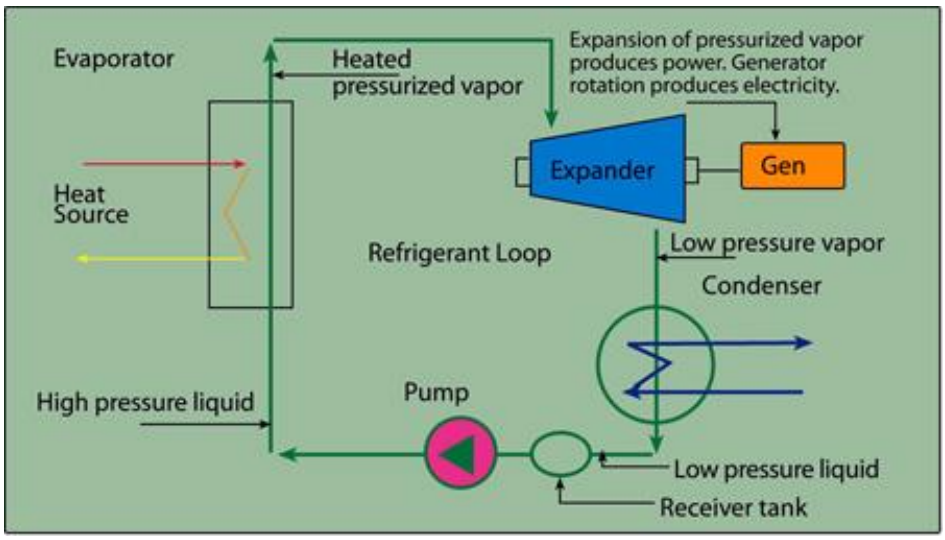

Figure 1.10. Organic Rankine Cycle Heat recovery System. (Alaska Energy Wiki).

ORCs can assume different configurations such as basic ORC[17–20], single[21,22] stage regenerative ORC, dual-loop ORC[22,23], or ORC with a recuperator[24,25].

The working fluids in ORC are responsible for the performance of the plant: for this reason, the research focalized its attention on the fluid selection for several different heat recovery applications[26–29]. In general, organic working fluids must have relatively low boiling points and high vapor pressures in order to evaporate exploiting LTH; at the same time, they must be no toxic, safe, and cheaper.

In a work of 2008, Tchanche et al[27] studied several organic fluids concluding that R134a followed by R152a, R290, R600, and R600a (1,1,1,2-tetrafluoroethane, 1,1-difluoroethane, propane, butane, i-butane respectively) are the most suitable fluids for application at low temperature, with heat sources below 90°C.

In 2011, another study showed the optimal operation condition of several working fluids which were determined by a procedure employing MATLAB and REFROP taking into account a double-organic Rankine cycle systems[30]. The authors concluded that for waste heat recovery from a fixed Low-Temperature Heat source, the working fluids have limited influence on the optimal operation conditions: in fact, the research pointed out as, at the optimal operation condition, the thermal efficiency difference between each working fluid was less than 0.255% while the power difference was around 0.2 MW (Figure 1.11).

Even if ORC is a mature technology, its application at lower temperatures requires further optimizations because of its high material and operational costs[31,32] (Figure 1.12), system complexity, and low efficiency[33]. In particular, the low efficiency and the high maintenance costs hindered the widespread application of ORCs.

ORCs show better results when are applied to recover Medium-Temperature Heat: an example is the work of Peris[35], where ORC reaches energy efficiency closer to 11% exploiting heat sources temperature about 155°C. Starting from thermal power input ranged from 95.14 kWt to 146.41 kWt, the maximum gross and net electrical powers achieved were 18.03 kWe and 15.93 kWe, respectively.

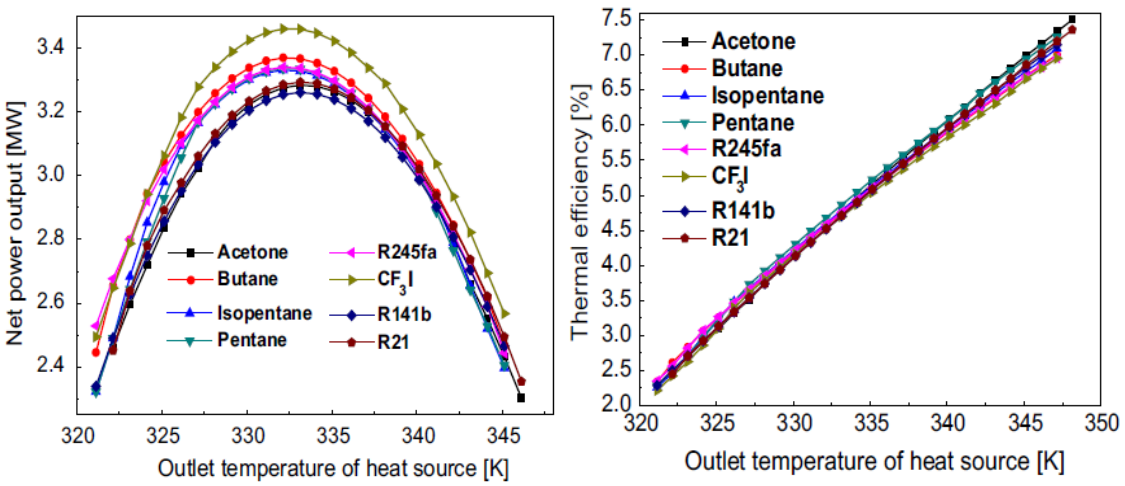

Figure 1.11. a) Net power output and b) thermal efficiency with respect to the outlet temperature of heat source. The inlet temperature of heat source = 358.18°K.[30]

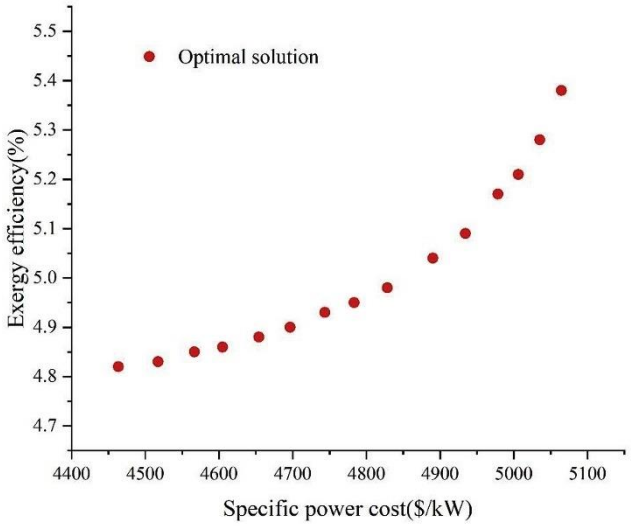

Figure 1.12. Optimal solution for the net exergy efficiency vs. the specific power cost[34]

In a more recent work[36], researchers tried to integrate a heat pump with an ORC to improve the net power output of the device. Starting from several assumptions, someone also disputable, they showed, using R236fa (1,1,1,3,3,3-exafluoropropane) as working fluid, that the amount of heat recovered, and the net power output was increased by ≈ 12% and ≈ 9.5% respectively. Also, in this studied case, the heat sources temperature was about 150°C.

The most significant improvement in the steam power cycle since the development of the Rankine cycle in the mid-1800s was the Kalina Cycle. It consists in a working mixture fluid composed of two liquids with different boiling points. In this way, the solution boils and condenses over a range of temperatures, which means more extracted heat from the thermal energy sources than with a pure working fluid. Adjusting the ratio between the components of the solution, the range of boiling points of the working fluids is thus tailored on the heat input temperature. Generally, Kalina Cycle generates from 10% to 50% more power than conventional steam power generation systems.

The first and simplest Kalina Cycle system proposed was based on a superheated mixture of ammonia-water vapor which was expanded in a turbine to generate work[15]. The exhausted fluid was cooled, diluted with ammonia-poor liquid, and condensed in the absorber by cooling water. The saturated liquid was then compressed to an intermediate pressure and heated. The mixture was separated into an ammonia-poor liquid, which was cooled and depressurized and an ammonia-rich vapor which was cooled and mixed with some of the original condensates in order to obtain an ammonia concentration of about 70%. The mixture was then cooled, condensed, compressed, and sent to the boiler via regenerative feed water heater (Figure 1.13).

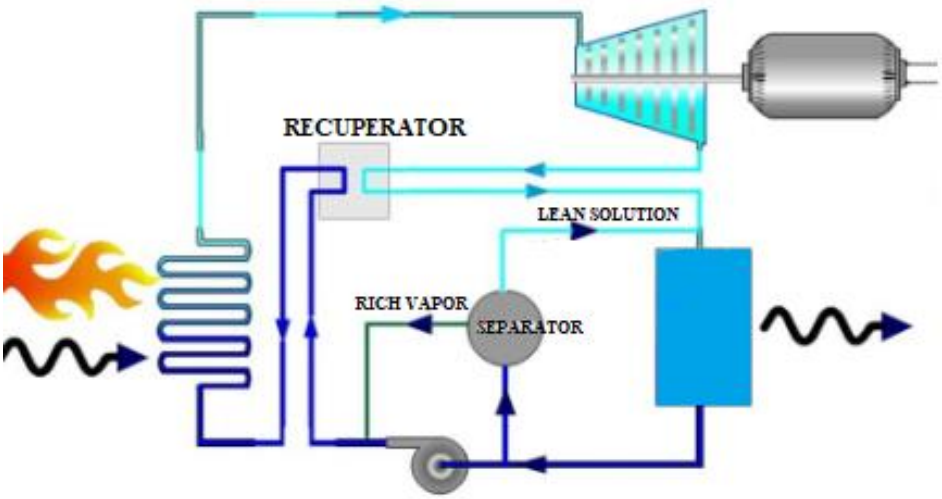

Figure 1.13. Configuration of a Kalina Cycle[39].

In a work of 2007[37], the performances of a KC are compared to the performances of an ORC exploiting low-temperature geothermal heat sources. They concluded that, under a moderate turbine inlet pressures (15 to 40 bar) and a turbine inlet temperature of 90°C, KC performs better than ORC. In 2013[38], Rodriguez et al. carried out comparative exergoeconomic analyses for the KC and ORC implemented for a geothermal plant in Brazil. They tested a mixture of 84% ammonia and 16% water as working fluid for the KC and R-290 (propane) as working fluid for ORC, showing the superiority of the KC from the economic and thermodynamic points of view. The heat source worked at 100°C and the turbine inlet pressure was in the range between 15 bar to 50 bar. In several studies, KC results competitive with ORC systems in terms of the specific investment cost and the specific electricity generation cost. For example, for energy generation from geothermal source, the specific investment costs of the KC were approximately 1200\$ kW^{-1} while the ORC were approximately 1500\$ kW^{-1} [19]. In 2014, a study demonstrated as KC has better efficiency than other evaluated cycles when applied to recover medium temperature heat sources[40]. Under these operational conditions, KC technology reaches energy efficiency of 10.6% and exergetic efficiency of 59.3%.

Recently, another thermodynamical study demonstrated how the gross power and the conversion efficiency of a KC are in general higher compared to ORC, when applied to exploit geothermal heat at low temperature, < 86°C (Figure 1.14)[41].

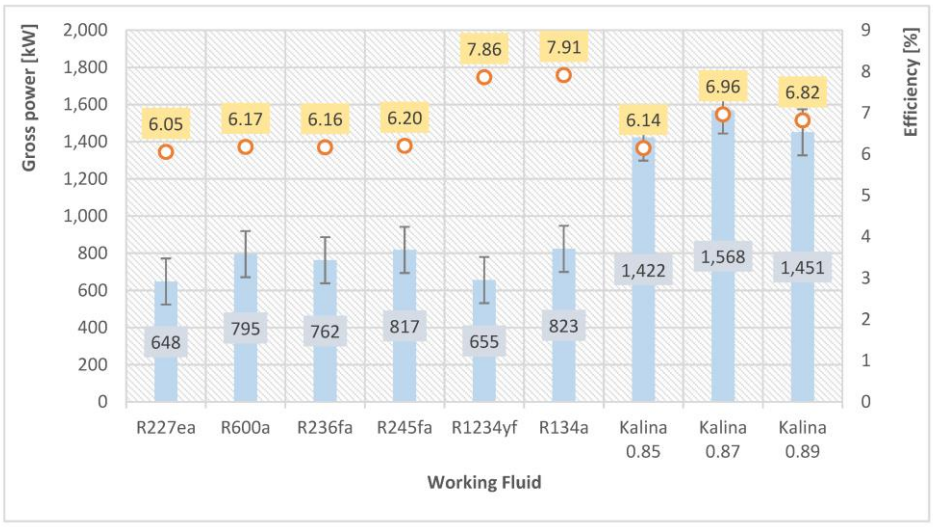

Figure 1.14. Comparison of results obtained for power and efficiency depending on working fluid[41].

Despite its performances, KC is a technology that remains too expensive and complex, and therefore its application at low temperatures is still not diffuse.

The third and last type of "traditional converter" is the Thermoelectric Generator, a solid-state device that directly converts heat in electricity. TEG can work an extended period of time, exploiting limited temperature differences. This ability added to the fact that TEGs do not contain any moving parts, and thus associated with the limited need of maintenance and probability of failure over long periods, and they can withstand extremely harsh environments, make these devices able to operate in situations where traditional engines are not implementable[16,42].

The main element of a TEG is the thermoelectric module[43] (Figure 1.15) which transforms heat into electricity by taking advantage of the Seebeck effect[44]. The Seebeck effect describes the generation of electrical potential in an open circuit formed by two dissimilar conductors or semiconductors when their junctions are maintained at different temperatures. When there is not a temperature gradient, the charge carriers are uniformly distributed in the two materials. However, when a temperature difference is maintained between the junctions, the kinetic energy of charge carriers at the hot end will be greater than the kinetic energy at the cold end. Therefore, the charge carriers will diffuse from the hot side to the cold one. The gradient in the number of charges is then balanced by the resulting internal electric field.

Thanks to the Seebeck effect, a temperature gradient can be exploited to generate an electrical potential which can be convert into electricity when a load is connected across the thermoelectric material/s, resulting in an electrical current: both the thermoelectric module and the temperature gradient determine the resulting power.

To increase the temperature gradient, heat exchangers are used at both hot and cold sides of the modules, which dramatically affected the power output of a TEG, as demonstrated in a study of 2015[45].

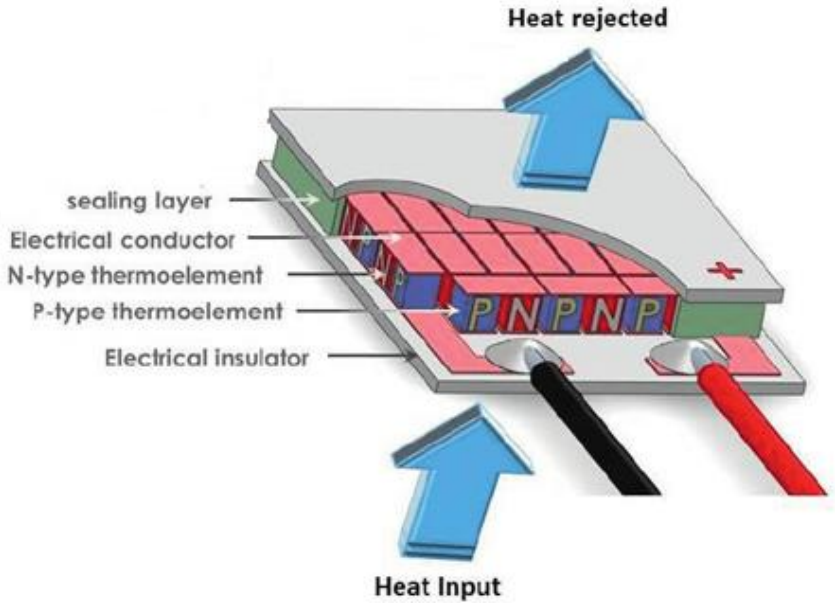

Figure 1.15. Scheme of a commercial thermoelectric generator module[46].

To compare the performances of different thermoelectric materials, the thermoelectric figure of merit *ZT* becomes a relevant parameter. It takes into account the electrical conductivity (σ), the thermal conductivity (κ), and the Seebeck coefficient (α) which is related to the density of states[47] at a certain temperature *T*.

$$ZT = \frac{\alpha^2 \sigma}{\kappa} T \quad (1.4)$$

Good thermoelectric materials should have large Seebeck coefficient to increase the electrical potential; high electrical conductivity to minimize the so-called Joule heating related to the Ohmic losses; low thermal conductivity to retain heat at the junction.

The main drawback of this technology is related to the low heat-to-electricity conversion efficiency when applied at low temperatures. In a study of 2009[16], a TEG unit was designed and tested for Low-Temperature waste Heat power recovery (Figure 1.16 c). The power output and the energy conversion efficiency were affected by the hot fluid inlet temperature and flow rate: when the hot fluid was injected at 150°C, the efficiency was 4.44%; but when the temperature of the hot fluid decreased to 90°C the efficiency decreased too, reaching 2.45% (Figure 1.16 a-b).

Integrating theoretical analysis and experiment, Gou et al[48], studied the influence of heat transfer irreversibility on TEG performances and proposed several improvements for the system. The model confirmed the experimental data: when the hot fluid inlet temperature was 80°C, the thermal efficiency was only 2% and did not change significantly with temperature.

To increase the energy recovery efficiency, thermoelectric modules are normally coupled with heat pipes and finned heat sinks because that can provide larger heat transfer rates across the TEG cell[49].

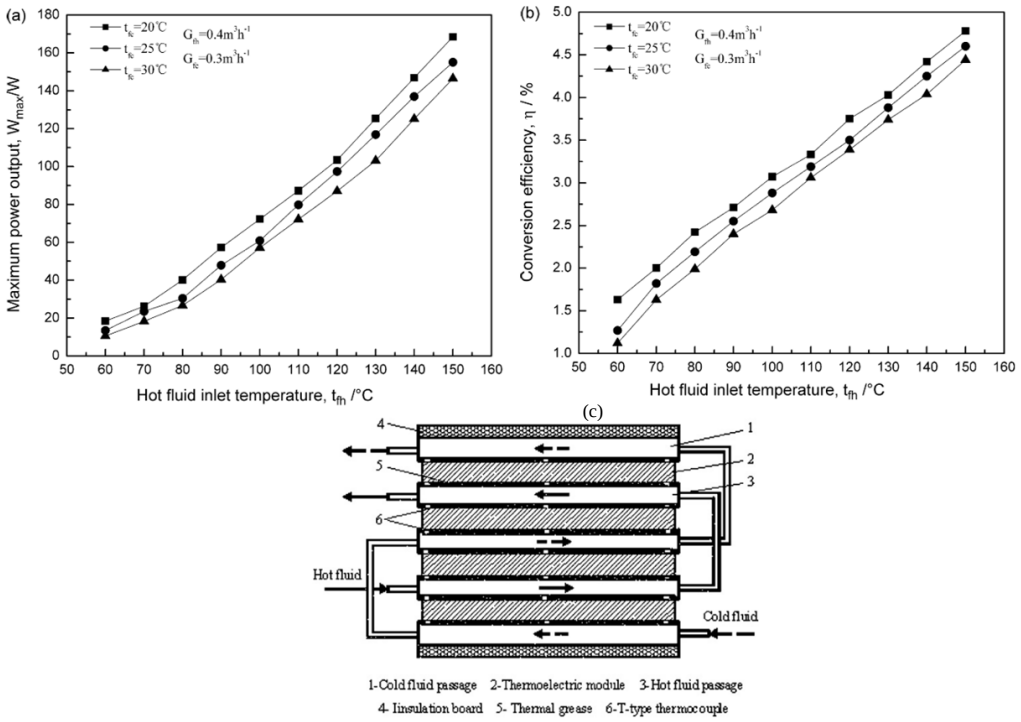

Figure 1.16. a) Maximum power output and b) conversion efficiency as a function of the fluid inlet temperatures; c) schematic diagram of TEG[16].

In fact, a heat pipe works as passive heat exchanger which is used to improve the heat dissipation from the cold side of a thermoelectric module or to transfer heat effectively from a heated space to a cooler space. The integration of heat pipes and heat sinks into the TEG devices, increases the overall conversion efficiency of approximately 0.8-1%[50,51].

In 2020, Fathabadi proposed a novel system composed of a photovoltaic module paired with a TEG module in order to convert both solar radiation and solar heat into electric power[52]. In the same work, the researcher solved the problem of the low output power of TGE module due to the small temperature difference increasing it by the utilization of a two-phase closed thermosiphon heat pipe, a concentrator, and a radiator.

An innovative application of TEG was made in 2019 by Sulaiman et al[53]. They studied a system composed by a PEM fuel cell on-board a mini vehicle, coupled with a single TEG (with finned heat pipe) which produces electrical energy in order to produce hydrogen through electrolysis. If the PEM fuel cell produces 1 kW of electrical power at 50% conversion efficiency, then the thermal power would also be 1 kW requiring nearly 45 TEG units.

Some of these systems represent only a proof-of-concept and are not use for real and commercial applications because of the complexity of installing prototypes, dealing with system dimension, assembly pressure, efficient cooling system, contact resistances and so on[54].

These are the reasons why this type of converter is still not widespread for LTH applications.

1.2.2. New Heat-to-Electricity Converters: direct conversion of Low-Temperature Heat into electricity

In the last decade, researchers have proposed new kind of devices to convert LTH into electricity. These new systems can be classified in two different groups: devices that directly convert heat into electricity and devices that perform this conversion in an "indirect way". The first category it will be discuss here, while the second type of devices will be discussed in the next section.

When the heat source is directly applied to the device which produces electrical energy, a directly conversion of heat into electricity is observed. Three different systems belong to this category of heat-converters: Thermo-Electrochemical Cells (TEC), Thermal Regenerative Electrochemical Cycles (TREC) and Thermo-Osmotic Energy Conversion systems (TOEC).

TEC and TREC devices are electrochemical systems while TOEC convert heat into mechanical work to move a turbine. Another distinction is related to the use of the heat: in TREC devices, the cell is charged and discharged at different temperatures while in TOEC and TEC systems, two different temperatures are applied at the same time to different sides of the cell.

Thermo-Osmotic Energy Conversion approach consists in a membrane-based device which has the potential to harvest Low-Temperature Heat by using a temperature difference to create a pressurized fluid flux, which, in turn, can be converted to mechanical work via a turbine, driving an electrical generator[55] (Figure 1.17).

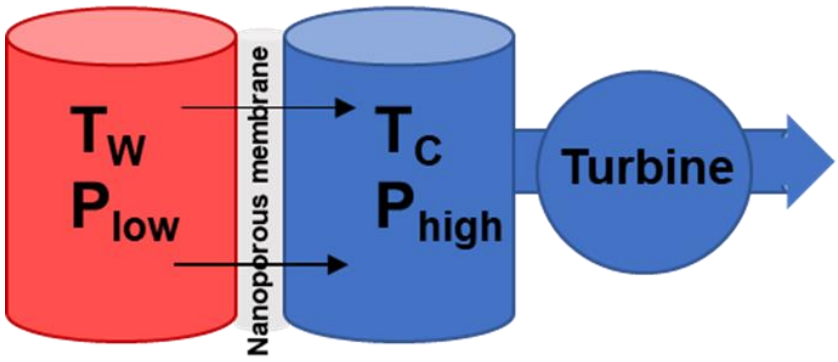

Figure 1.17. Schematic TOEC process.

In the TOEC system, the temperature gradient is maintained across a membrane resulting in the transportation of fluid from the warm, low-pressure reservoir to the cool, high-pressure sink. This flux gives rise to an osmotic pressure difference.

Different working fluids and membranes can be used in this system even if researchers focalized their attention on water and nanoporous, hydrophobic membranes, respectively.

Membranes trap air within their pores when submerged in water. The temperature difference, applied across the membrane, causes a partial vapor pressure difference which results in a net vapor flux

from the hot to the cold side of the membrane: the fluid moves from a sink at ambient pressure to a reservoir at higher hydrostatic pressure by thermo-osmosis.

The first TOEC was proposed by Straub et al[56]. in 2016. This experiment was conducted using a hydrophobic polytetrafluoroethylene membrane and water as working fluid. Applying a hydraulic pressure difference of 13 bar to the membrane, in a system composed by a hot sink at 60°C and the cold one at 20°C, the technology achieved a power density close to 3.5 W m^{-2}.

To evaluate the heat conversion, several parameters have to be taken into account, like the thermal efficiency of the membrane, which quantifies the effectiveness of heat transfer for a given membrane, the temperature difference in the heat exchanger and in the membrane and, finally, the hydraulic pressure. Straub, in a second work, developed a TOEC able to reach a heat-to-electricity energy conversion efficiency up to 4.1% (Figure 1.18), operating in the same condition of the first work, in terms of temperature difference, but increasing the hydraulic pressure from 13 bar to 50 bar[57]. This result was obtained at the expense of the power density, which was relatively low: just 1 W m^{-2}. Vice versa, in order to obtain higher power density values, the energy efficiency must be sacrificed[58,59].

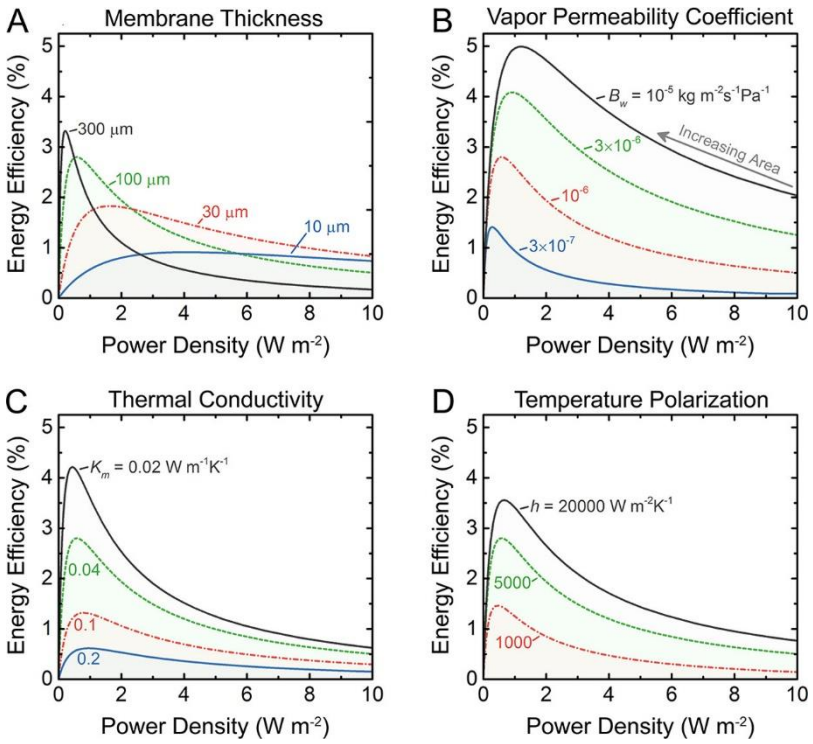

Figure 1.18. Energy conversion efficiency and power density curves for TOEC systems with varied membrane and hydrodynamic properties. Curves are generated by increasing the membrane area of a given system with higher membrane area from right to left. Results are shown for variations in (A) membrane thickness, (B) vapor permeability coefficient, B_w, (C) thermal conductivity of the membrane, K_m, and (D) heat transfer coefficient, h. Unless otherwise stated, the vapor permeability of the membrane, B_w, is 1 × 10^{-6} kg m^{-2} s^{-1} Pa^{-1}; the thermal conductivity of the membrane, K_m, is 0.04 W m^{-1} K^{-1}; the thickness is 100 μm; and the heat transfer coefficient, h, on both sides of the membrane is 5000 W m^{-2} K^{-1}. The heat source temperature is 60 °C, and the heat sink temperature is 20 °C. The hydraulic pressure difference between the two streams is 5 MPa (50 bar), equal flow rates are used at any point in the membrane module, and a perfect heat exchanger efficiency is assumed[57].

A hybrid device was proposed by Chen et al. in 2019[60]. This work reports the storage and conversion of energy from combined salinity and temperature gradient. The membrane consists of ultrasmall silica nanochannels positioned on the poly (ethylene terephthalate) (PET). Thanks to the high perm-

selectivity of silica nanochannels, the power output of osmotic energy conversion from a salinity gradient (0.5M/0.01M of NaCl) reaches 1.0 W m^{-2}. Moreover, applying an additional temperature gradient of 10°K increases the output power by 40.4%.

Researchers are focalizing their attention on the development of new membranes[61,62] in order to reduce the material costs and at the same time, improving the hydrodynamic of the cell[63]. However, this type of systems is still unfeasible due to the impractical conversion efficiencies and lower power density.

Another proposed device is the Thermo-Electrochemical Cell, also called thermo-galvanic cell, which is an electrochemical device able to directly convert heat energy into electricity. As for Thermoelectrics, TECs generate electrical energy in continuous under an applied temperature gradient, without consuming any materials or producing emissions.

TEC is composed by two electrodes kept at different temperatures: generally, the one at higher temperature is the anode while the cold electrode is the cathode. The cell is then filled with a temperature-dependent redox couple in an aqueous[64,65], non-aqueous[66,67], mixed solution[68] or a solid-state membrane[69,70]. When connected to a load, electric current flows from the anode, where the reduced species are consumed, to the cathode, where the reduced species are generated. The oxidized species are transported through the electrolyte by convection, migration, and diffusion to the cathode, where they are reduced, while the reduced species move to the anode where are oxidized. In this way, the redox reaction can theoretically continue infinitely, and TEC sustains a steady-state current until the difference temperature between the electrodes exists (Figure 1.19).

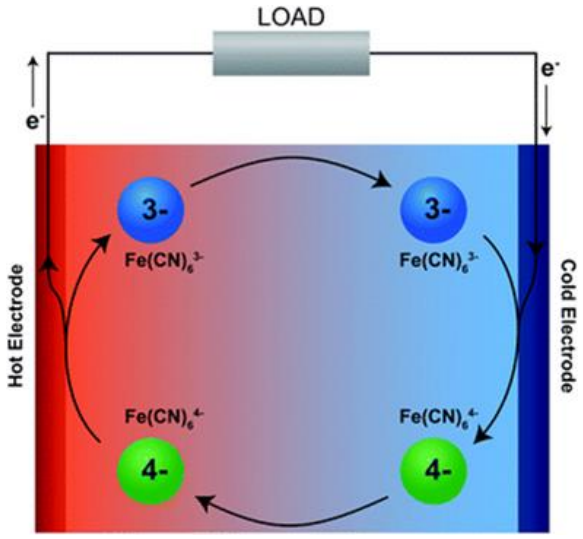

Figure 1.19. Schematic of a thermo-cell containing the aqueous ferri/ferrocyanide redox couple ($Fe(CN)_6^{3-}/Fe(CN)_6^{4-}$). This system has a negative Seebeck coefficient ($-1.4\ mV\ K^{-1}$) meaning that oxidation occurs at the hot electrode and reduction at the cold electrode. For a redox couple with a positive Seebeck coefficient, this would be reversed, with oxidation occurring at the cold electrode and reduction at the hot electrode.[72]

The performance of a Thermo-Electrochemical Cell is often evaluated by the figure of merit ZT (Equation 1.4), as for the Thermoelectric Generators.

To obtain the maximum power conversion of a TEC, it is necessary to find an electrolyte characterized by a high Seebeck coefficient which means a large potential difference at a given temperature. It is also necessary to increase the ratio between the electrical conductivity to the thermal conductivity which is translated in choosing a solvent with low thermal conductivity. In the end, like in any electrochemical devices, the overpotentials related to activation, ohmic, and mass transport have to be minimized in order to reduce the voltage losses[71].

The most significant factors limiting the implementations of TECs are their low conversion efficiency and power density output: most reported TECs show value of efficiencies relative to Carnot minor of 1%[72].

One of the first examples in literature, proposed in 1996 by Mua and Quickenden[73], was a TEC based on aqueous electrolyte and ferri/ferrocyanide redox couple. This device showed a thermal-electric conversion efficiency relative to Carnot of 0.6% and produced only 3.6 x 10^{-3} W m^{-2}. The low efficiencies were attributed to the low kinetic reversibility of the process due to the use of platinum as electrodes. A promising alternative to platinum is the nano-structured carbon-based electrodes, particularly appealing for their lower cost, high surface area (which increases the reaction sites), and fast electron transfer kinetics for the ferri/ferrocyanide redox couple.

Their behavior was confirmed by Hu et al[74]. which showed a TEC based on the same redox couple aqueous solution proposed by Mua et al. The converter reached higher efficiency and power density (P = 1.8 W m^{-2}; $\eta_{t/C}$ = 1.4% with respect to Mua's value of 3.6 x 10^{-3} W m^{-2} and 0.6%, respectively) only because the Pt electrodes were exchanged with multiwall carbon nanotube (MWCNT).

Further improvement was obtained in 2016, where a carbon nanotube aerogel-based Thermo-Electrochemical Cell was developed[65]. The TEC exploited an aqueous solution of ferri/ferrocyanide electrolyte obtaining a record Carnot-relative efficiency of 3.95% and a maximum power output of 6.6 W m^{-2}. This work also demonstrated the importance of electrode purity and engineered porosity on thermo-galvanic performance.

In a recent study, non-noble metal-based electrode made of cupper was implemented in the TEC, combined with a fine control of the electrolyte pH in order to work in a voltage window where cupper is immune to corrosion. The cell was filled with the aqueous solution of ferri/ferrocyanide based electrolyte. The device showed a power density slightly lower than that of platinum TEC (less than 5%) and the conversion efficiency was only around 0.85%[75].

Several other improvements were realized but in general, these devices still suffer of low power densities and low heat-to-electricity conversion efficiencies (from 0.02 to 0.2%[76,77]). The higher power output obtained for a TEC was reported in a work of Zhang et al. which reached a value of 12 W m^{-2} using activated carbon cloth as electrodes and a concentrated ferri/ferrocyanide based-electrolyte[77]. Unfortunately, to maximize the power, the efficiency relative to Carnot was reduced to a 0.4% and the heat-to-electricity efficiency was only around 0.007%.

In 2017, Yang at al. presented a solid state thermo-electrochemical cell to harvest low grade thermal energy[78]. The device was realized by feeding hydrogen gas to both cathode and anode chambers

which were separated by a polymer electrolyte (proton exchange membrane). The device produced a maximum power density of 0.2 W m^{-2} and an efficiency around 0.042% applying a temperature difference of 15.3°C.

The efficiency can be improved to a 2% as reported in a study in 2018[69]: Marquardt et al. modelized the same solid-state TEC calculating the optimum operating condition which corresponded to a maximum power density of 1.46 W m^{-2}.

To improve the power output, researchers focalized their attention on the electrode materials: a study of Burmistrov et al.[79] showed that nickel electrode ensures double power output than copper electrode (Figure 1.20), opening the door for a possible commercialization in the next future.

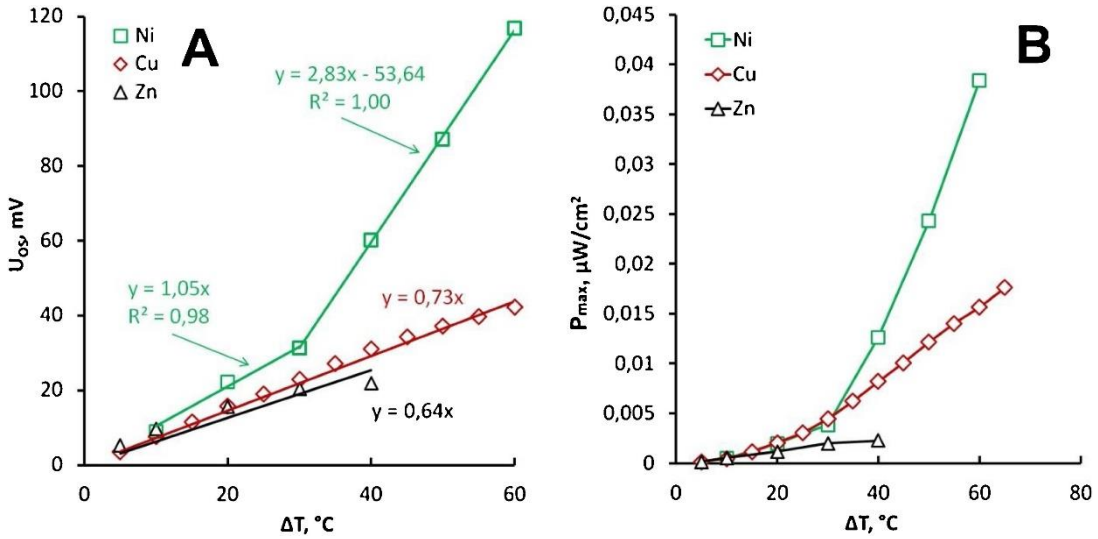

Figure 1.20. Temperature dependences of open circuit voltage (A) and output power (B) of cells based on $Cu^{2+}/Cu_{(s)}$; $Zn^{2+}/Zn_{(s)}$; $Ni^{2+}/Ni_{(s)}$ systems[79].

The limited heat-to-electricity efficiency and the lower power density make TEC systems not suitable for the harvesting of LTH. Furthermore study are required in order to make this technology comparable to the other techniques.

The last device that belongs to the category of direct heat converters is the Thermal Regenerative Electrochemical Cycle. TREC is an electrochemical cell which explores a thermodynamic cycle based on the thermo-galvanic effect.

Typically, the cycle consists of four steps (Figure 1.21):

- $A \rightarrow B$ = TREC is heated from the lower temperature (T_L) to the higher one (T_H) under open circuit condition.
- $B \rightarrow C$ = the cell is charged at lower voltage. The entropy of the system increases through heat absorption during the electrochemical reaction at T_H temperature.
- $C \rightarrow D$ = TREC is cooled down from T_H to T_L in open circuit condition: the open circuit voltage increases in this process.
- $D \rightarrow A$ = the last process, which closes the cycle, corresponds to the cell discharge at T_L temperature. The entropy of the cell increases through the heat released into the cold reservoir.

After the cycle, the cell returns to its initial state. If the charging voltage at T_L is lower than the discharging voltage at T_H, net energy is produced by the voltage difference.

TRECs have thermal-electrical efficiency relative to the Carnot efficiency significantly higher than TECs because they are not limited by the transport properties, as the TEC devices, but the limiting factor is the heat capacity of the materials and effectiveness of the heat exchanger. The cell material characteristics, like isothermal coefficient, internal resistance and specific charge/discharge capacity, also affect the maximum power production of the device[80].

The efficiency of the system is calculated as the net work divided by the thermal energy input which consists in two different parts: the heat absorbed at T_H and the external heat required to increase the temperature of the cell. Part of released heat during the cooling process can be collected and used for the following heating process.

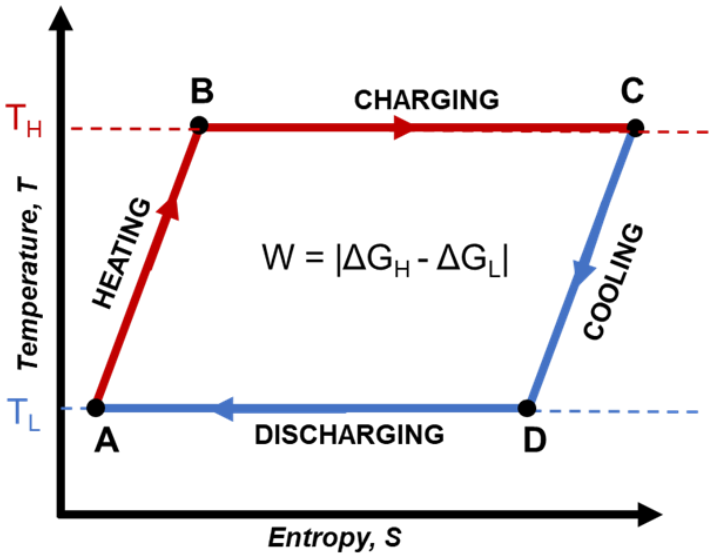

Figure 1.21. Temperature–entropy (T–S) diagram of thermal cycling assuming a temperature range between TL and TH. The theoretical energy gained over one cycle is the area of the loop determined by the temperature difference and entropy change[81].

A Thermally Regenerative Electrochemical Cycle based on a copper hexacyanoferrate (CuHCF) cathode and a Cu/Cu^{2+} anode was proposed to convert heat into electricity in 2014[81]. The device showed, between 10°C and 60°C, an efficiency relative to Carnot of 24% when no heat recuperation was assumed and increased to 37% when heat recuperation was around 50% (heat to electricity efficiency around 3.7%). Even if the efficiencies were higher than TECs (values higher than 2%[81–84]), the system suffered of low power density: the maximum value showed by this TREC was 0.144 W m^{-2}.

A charging-free TREC was proposed by Yang et al. in the same year[85]. The cell, based on Prussian Blue electrodes and an aqueous solution of $Fe(CN)_6^{3-}/Fe(CN)_6^{4-}$, had a power density of 0.05 W m^{-2} and efficiency between $\eta_{t/C}$ = 5.8% - 17% (heat-to-electricity efficiency around 2%) depending on the heat recuperation (0%, 70% respectively). Another example reported a TREC[82] based on nickel hexacyanoferrate (NiHCF) cathode and a silver/silver chloride anode. Second law efficiency of

21.5% was achieved with assumed heat recuperation of 50% in a range temperature between 15°C and 55°C.

In 2019, Liu et al. proposed a TREC based on spinel lithium manganese oxide ($LiMn_2O_4$) as the cathode and CuHCF as the anode, in a hybrid aqueous electrolyte of lithium and potassium ions[86]. The cell reached an efficiency relative to Carnot of $\eta_{t/C}$ = 19% in a temperature range of 10°C - 40°C, when no heat recuperation was assumed. If 50% heat recuperation efficiency was considered, the efficiency in the same temperature range was raised to $\eta_{t/C}$ = 39%.

In 2020, Zhang et al[87]. coupled TREC cycle with a flow cell, converting heat with an unprecedented thermoelectric efficiency of 3.61% in the temperature range of 22-55°C (Figure 1.22).

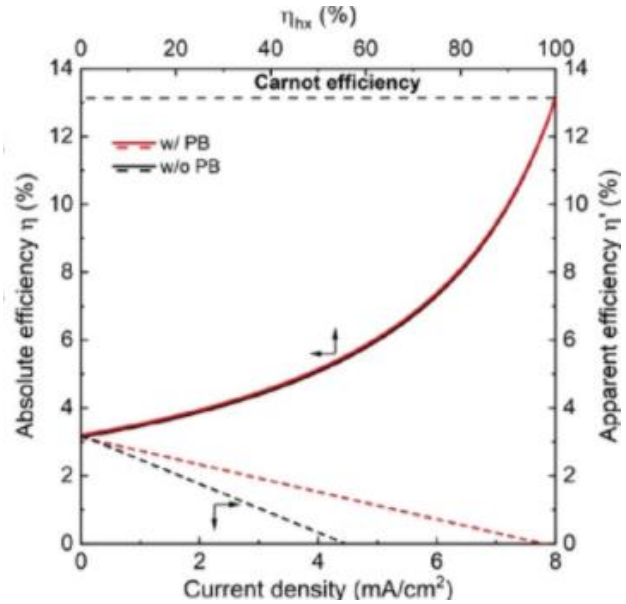

Figure 1.22. Dependence of the absolute thermoelectric efficiency (η) on the heat recuperation efficiency, and the dependence of the apparent conversion efficiency (η') on the current density with and without 4 g Prussian Blue in the catholyte[87].

Up to now, TRECs are the devices with the highest heat-to-electricity conversion efficiencies; however, their low power densities make the systems unfeasible for real applications. Therefore, it is necessaire improve the power output before to consider their use in a real plant.

1.2.3. New Heat-to-Electricity Converters: indirect conversion of Low-Temperature Heat into electricity

A different approach to convert heat into electrical power is applied by the systems that belong to the second class of new converters. These technologies are generally based on two stages: one for the "power production", at the expenses of some chemicals, and one for the "thermal regeneration", where actually heat is consumed, and the chemicals are regenerated.

This means that these devices are not only able to convert thermal energy but also to store it in form of chemical energy. The indirect exploitation of LTH consists of using available heat for a thermal separation, to regenerate the chemicals that feed the "power stage" unit, instead of the direct utilization during the power production.

In this section there are the so called Thermally Regenerative Complex Batteries (TRCB) and the devices based on salinity gradients (SGE): Pressure Retarded Osmosis (PRO), Reverse Electrodialysis (RED) and Capacitive Mixing cells (CapMix). This last category of devices, devices based on SGE exploits the mixing Gibbs free energy of two solutions of the same salt but at different concentrations: high concentrated solution (H) and the low concentrated solution (L).

1.2.3.1. Salinity Gradient Energy Systems (SEG)

Salinity Gradient Energy systems (SEG) are two stages devices where, in the power production stage, the mixing free energy of two solutions is converted into electricity.

The mixing free energy corresponds to the theoretical amount of energy that can be extracted from the mixing of two solutions of the same salt at different concentrations, hence corresponds to the variation of the Gibbs free energy after the mixing process. Of course, only a fraction of this energy can be effectively recovered due to the process efficiencies.

After the power production from the Salinity Gradient technologies, the exhausted solution is circulated into the regeneration stage where a Low-Temperature thermal source restores the initial gradient: for example, aqueous solutions based on NaCl can be parted into high and low concentrated solutions by distillation or membrane distillation[88–90].

The overall efficiency of this device is the product of the efficiencies of the power production stage and the thermal stage. Generally, the thermal stage is the one which mainly affects the overall efficiency of the system, due to the thermodynamic constrained of the boiling point elevation[89]. For example, for NaCl solutions, the distillation energy efficiency is less than 1% while for $ZnCl_2$ or NaOH can be nearly 10%[89,91], taking into account a single-effect distiller. Higher energy efficiencies can be achieved by using multiple effects in case of distillation or more membrane modules for the membrane distillation.

Another approach consists in the use of aqueous solutions of thermolytic salts which have the property of decomposed into gaseous compounds at low temperatures. Ammonium bicarbonate, NH_4HCO_3, is the most common salt used as thermolytic compound as in these applications, it is decomposed into CO_2 and NH_3 above 50-60°C.

Based on the system used to regenerate the solutions, the devices are named as MED-(multi effect distillation), MD- (membrane distillation), MSF- (multi-stage flash distillation), T- (thermolytic salts): MED-RED[92], MD-RED[93], T-RED[94], as example. More in general, all the distillation systems can be easily named with D-.

Originally, Salinity Gradient Energy systems were developed to exploit the natural salinity gradient between river waters and seawater, commonly called "blue energy". Other potential resources of

salinity gradient involve brine solutions from industrial streams, or natural sources (e.g. the Dead Sea), and saline wastewater from industrial processes or domestic source.

Pressure Retarded Osmosis (PRO) is one of the devices proposed to tap the natural Salinity Gradient Energy. In the PRO method, two solutions with the same chemical composition, but different concentrations, are brought into contact by a semi-permeable membrane. PRO exploits the osmotic pressure difference developed by the semipermeable membrane to drive the permeation of the solvent from the diluted solution (L) to the concentrated one (H). The transport of the solvent (generally water), from the low-pressure diluted solution to the high-pressure concentrated solution, results in pressurization of the volume of the solvent which can be used to generate electrical power through a turbine (Figure 1.23).

If one osmotic agent is recycled by using Low-Temperature Heat, the device is called "closed cycle PRO" or Osmotic Heat Engine (OHE). In this technology, heat is applied to re-concentrate the solution by evaporation of a portion of the water into steam, which would be condensed to form the deionized working fluid. Other approaches consist in removing the volatile organic solute or in precipitating the solute and in its following dissolution[95]. Different working fluids are studied[96], starting from water solution of sodium chloride to thermolytic solution of ammonia and carbon dioxide.

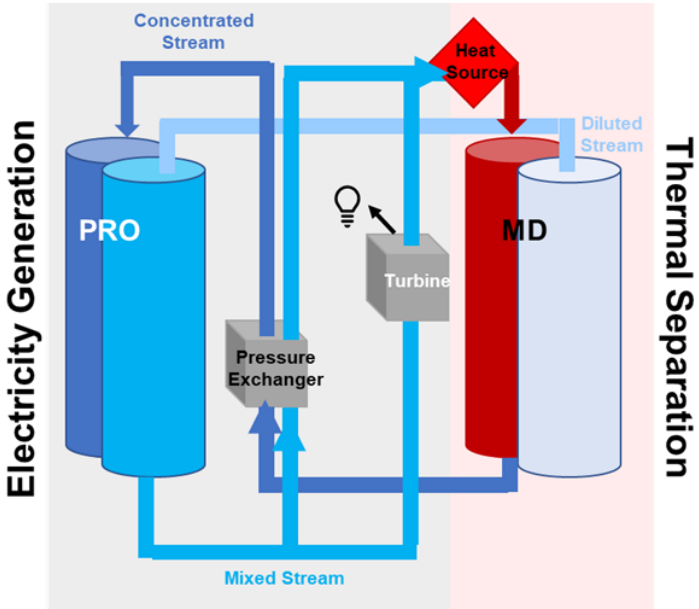

Figure 1.23. Schematic illustration of a closed cycle PRO, or a membrane-based osmotic heat engine for low-temperature heat harvesting.

One of the first and remarkable report of a PRO device based on sodium chloride solutions showed that, working with cold and hot temperatures respectively of 20°C and 60°C and a working solution 4 molal of NaCl, the system can achieve an energy efficiency of around 5%[88]. In this condition, the maximum energy efficiency, the Carnot efficiency, is 12%.

The thermodynamic analysis demonstrated also that this system is theoretically capable of achieving 9.8% efficiency. Furthermore, progress have been obtained by improving the membrane, the flux, and the engineering of the system. For example, a recent work published in 2019, showed a new membrane composed by MXene and Kevler nanofibers, studied in a PRO system with two solutions at different concentrations of NaCl (0.5M and 0.01M)[97]. The main result was the improvement of the power density which was 4 W m^{-2}, approximately twice of the value of the state-of-art. They also tested other salts, like KCl and LiCl obtaining promising results.

Other interesting results were obtained with PRO systems based on a concentrated ammonia-carbon dioxide solution. This type of solution has several advantages: high solubility of the ammonium salts in water, low molecular weights, high diffusivities which leads to high osmotic pressure and the thermal energy required for the removal and recycling of these solutes is significantly lower than that required to vaporize water[98].

In the work of McGinnis et al[99], the power production of their PRO system reached high values, around 250 W m^{-2} of membrane area, although the overall energy efficiency was low, around 5-10% of the Carnot efficiency, in the temperature range of 25-50°C.

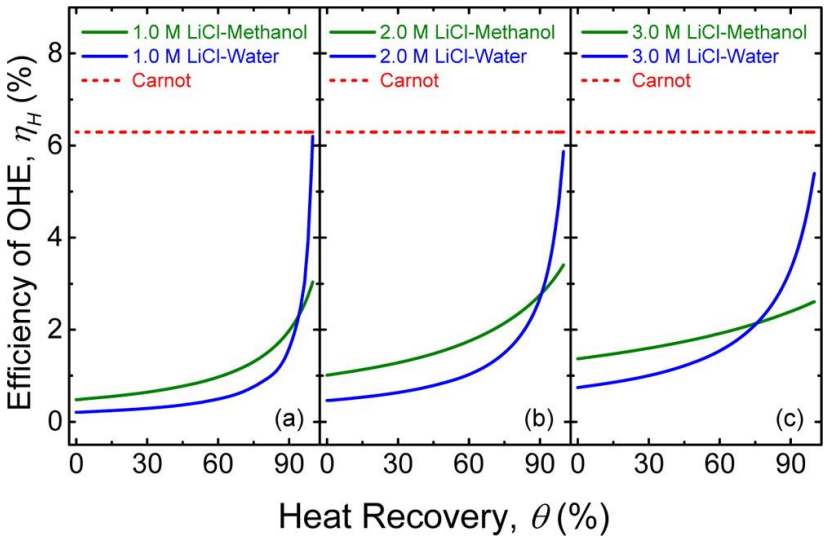

Figure 1.24. Energy efficiencies of the PRO-MD hybrid OHE system with LiCl–methanol and LiCl–water draw solutions as a function of the extent of heat recovery at draw solution concentrations of (a) 1.0, (b) 2.0, and (c) 3.0 M. The temperature of the heat source, T_H, and heat sink, T_C, are assumed to be 318.15 and 298.15 K, respectively[90].

Recently, thermally responsive ionic liquids (TRIL) with an upper critical solution temperature, were also proposed as working fluids[100]. The output power density was up to 2.3 W m^{-2} and the overall energy efficiency reached values around 2.6% (18% of the Carnot efficiency) at no heat recovery, and up to 10.5% (71% of the Carnot efficiency) at 70% of the heat recovery.

In the last few years, the research has focused in finding new thermolytic salts, organic solvents, and membranes able to improve the power output, maximize the Carnot efficiency and the relative overall efficiency of the device. Solutions of trimethylamine-carbon dioxide[101], magnesium chloride or magnesium sulfate[102], LiCl-methanol working fluid[90] (Figure 1.24), polyacrylonitrile nanofibers

supported thin-film composite membrane[103], freestanding graphene oxide membrane[104] were tested in PRO devices giving promising results.

Another technology proposed to convert LTH in electricity by exploiting the salinity gradient energy is the Reverse Electrodialysis (RED) which produces power by the ion migrations across selective ion-exchange membranes. It consists of an alternating series of cation and anion exchange membranes between a cathode and an anode, at fix distances, separated by spacers which originate thin compartments. These compartments are alternately filled with a concentrated (H) and diluted (L) salt solutions. The salinity gradient results in a potential difference over each membrane (membrane potential) which is the driving force of the anions and cations migration from H solution to the L one, across the anion and cation exchange membranes, respectively. In the extreme compartments of the cell, two redox reactions take place at the electrodes producing electricity. The two exhausted solutions are then regenerated in concentration by heat separation. In this type of device, the concentration of the solutions and intermembrane distances are two necessary parameters to evaluate and compare the RED performances[105] (Figure 1.25).

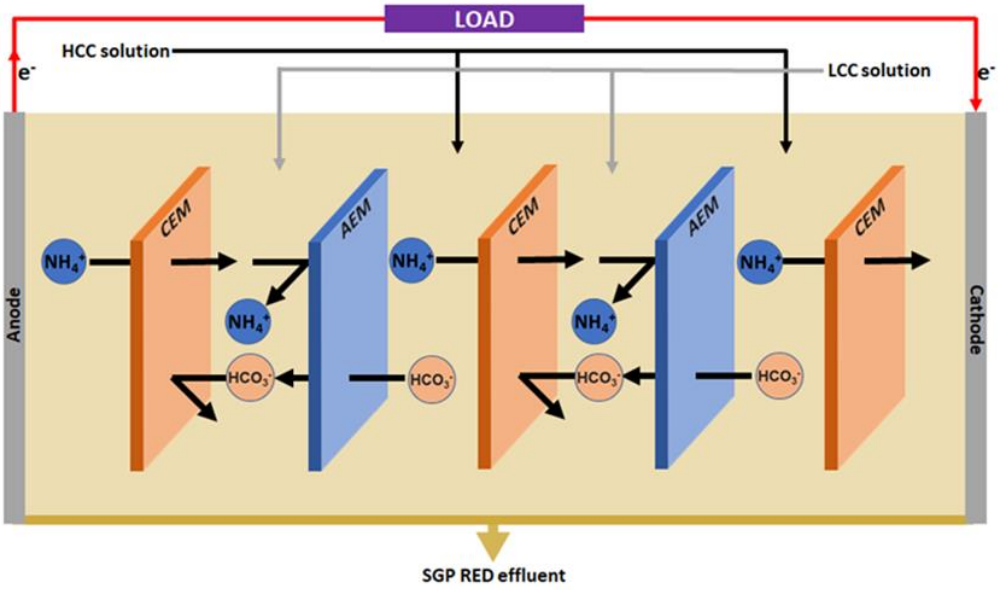

Figure 1.25. Schematic of a RED device.

As for all the technologies based on salinity gradient, changing the concentration of the H and L solutions change the response of the electrochemical cell: the higher is the difference in concentration between H and L solution, the higher is the Nernst voltage of the cell, which in turns means higher energy that can be stored and extracted. At the same time, low L solution concentration leads to a high Ohmic resistance in the cell related to the low ionic conductivity of the solution itself, and it is translated in low power density. Therefore, there is an optimal value for the L solution concentration, which also depends on temperature, flux, length, and thickness of the cell chamber.

Another parameter which affects the performances of a RED is the spacer thickness: basically, the power density decreases with the increase of the spacer thickness because of the higher internal resistance of the cell, especially in the low-concentration compartments[106,107].

Finally, also the intermembrane distance plays a critical role in determining the final power output of the RED technology: generally, the lower the intermembrane distances, the lower are the resistances in the cell and, therefore, the higher is the resulting power output[108].

RED based on NH_4HCO_3, thermolytic solutions, as working fluid coupled with a distillation column, was proposed for the first time in 2012 by Luo et al[109] because a device based on this salt can reach higher Carnot efficiency compared to NaCl[89,110,111]. The device reached power density of 0.33 W m^{-2} using two solutions at 0.02 M and 1.5 M and an intermembrane distance of 0.5 mm.

Decreasing L solution concentration and the intermembrane distance, Kwon[112] in the 2015 and Kim[113] in the 2017, developed RED systems with an increased power density: 0.77 W m^{-2} and 0.84 W m^{-2}, respectively. Similarly, Bevaqua et al.[114] maximized the performance of a laboratory RED unit based on the thermolytic salt ammonium bicarbonate: the system achieved the highest power density of 2.42 W m^{-2}.

In 2019, Giacalone et al.[115] validated a model to analyze the performance of a RED heat engine based again on NH_4HCO_3. The highest exergy efficiency achieved in a current scenario, where commercial membranes are used, is equal to 1.25% while in the future scenario, where enhanced membrane properties will be adopted, it will be equal to 2% (heat-to-electricity efficiency of 0.2% and 0.12%, respectively). These values can increase only if multi-stage regeneration units are adopted with consequent increase of the thermal efficiency of the regeneration process: the exergy efficiency, for example, increases from 1.25% to 5.2% when using 5 columns. In 2020, the same research team proposed the first prototype of a thermolytic RED heat engine[94]. The RED unit, fed with ammonium bicarbonate solutions (1.9M; 0.05M), was coupled with a vapor-stripping column operated at temperatures below 90°C. The system achieved exergy efficiency equal to 1.1%.

In a work of Tamburini et al[116]., RED units were modeled to identify the maximum power output, considering different solutes in aqueous solutions. The results showed that the highest power density is reached with lithium salts like LiBr or LiCl. These salts also induce a high boiling point elevation, thus possibly increasing the thermal efficiency if the thermal stage is performed by distillation. The authors also developed a model of a MED-RED technology which showed theoretical heat-to-electricity efficiency closer to 15%, thus suggesting that this technology could be a promising solution in the LTH conversion.

The first thermolytic reverse electrodialysis heat engine was proposed by Giacalone et al.[94] in the 2020. In the study, the first prototype unit was composed by a RED unit based on the SGE of two solutions of thermolytic salts, while the regenerative unit was based on a stripping process. The device was characterized by long-run tests considering several concentrations of ammonium bicarbonate (Figure 1.26).

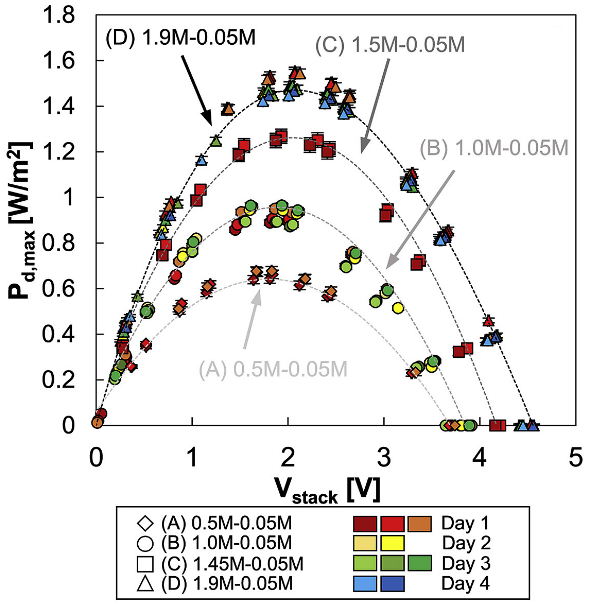

Figure 1.26. Electrical power density vs stack voltage generated by the RED unit. Different series report measurements performed at different number of cycles in the RED unit[94].

The highest exergy efficiency measured was equal to 1.1% for the case of 1.9 M /0.05 M ammonium bicarbonate solutions. In general the system showed good stability during the days, suggesting that this technology could be a promising solution in the LTH conversion.

Recently, a new method was proposed to convert Salinity Gradient Energy in electricity by the so-called Capacitive Mixing (Cap Mix) devices, where "accumulators" are charged in a concentrated solution and discharged in a dilute solution. The capacitive method is able to extract part of the mixing free energy of the H, and L solutions because the energy released during the discharge process is higher than the given energy to charge the accumulators.

The concept of Cap Mix includes three different approaches which are distinguished by accumulator materials and reactor configuration: Capacitive Double-Layer Expansion (CDLE), Capacitive Donnan Potential (CDP) and Battery Mixing (Batt Mix).

The "Capacitive Double-Layer Expansion" (CDLE) are devices which contain capacitive electrodes. These systems capture/release energy through the work done by contraction and expansion of the electrochemical double layer related to the change in salt concentration. Porous "supercapacitor" electrodes, made of activated carbon, are the first proposed solution[117–119] .

A second type of Cap Mix is called "Capacitive Donnan Potential" (CDP), which uses ion-selective membrane to develop the Donnan potential (equilibrium potential of the membrane), the driving force for ion migration. In this technique, electrodes are an assembly composed of activated carbon film and ion-exchange membrane which separates the carbon from the solution in the cell[120,121].

The third and last type of Cap Mix does not store electrical energy in a capacitive way but exploiting a faradic process. For this reason, these types of devices are called Battery Mixing (Batt Mix), also called "Mixing Entropy Battery". These technologies are composed by two different electrodes which specifically react with only one species of ion.

Because batteries and capacitors are collectively called “accumulator”, the whole family of these techniques is in general called “Accumulator Mixing” (Acc Mix).

The Acc Mix family is based on an electrochemical cell which undergoes on a four-step cycle, sketched in Figure 1.27.

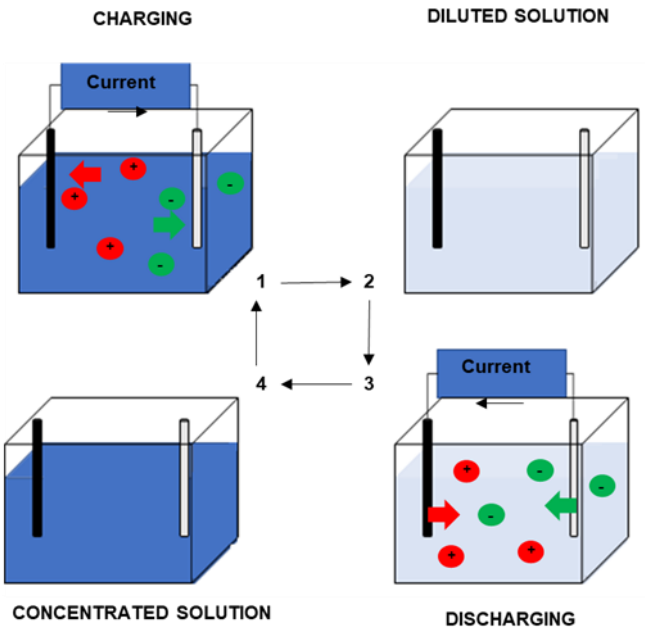

Figure 1.27. Scheme of a general Acc Mix.

At the first step, the electrochemical cell is filled with the concentrated solution: current flows in one direction, charging the cell and storing energy.

After the charging step, the solution is changed with the lower concentrated solution at open circuit: at this moment, the voltage rises, and it is described by Nernst equation.

During the third step, the circuit is closed and current flows in the opposite direction with respect to the first step, discharging the electrodes. In this way, the captured ions in the first step are here released.

The last step takes place at open circuit: as in the second stage, the solution is changed with the high-salinity feed solution in order to charge again the electrochemical cell in the following process: the voltage of the charge process is lower than that at which the cell is discharged.

The first Cap Mix device was proposed by Brogioli et al[117,118]. and it was a membrane-less Cap Mix based on pristine activated carbon electrodes and the expansion of the electric double-layer. The system exploited the Salinity Gradient Energy of two NaCl solutions of 1 mM and 500 mM respectively, with an energy efficiency of 0.99%. The power production of the system was of the order of 10 mW m^{-2}.

Optimization of the power and energy production of this kind of device was obtained in 2014 by a study of electrode materials in terms of porosity and hydrophilisation[122].

Other studied showed that the modification of electrodes may improve the voltage rise of the device. In particular, it was investigated the possibility to modify the electrode by coating on it a charged

polymer[123], or by absorption of small molecules on the surface of the electrode[124] or again, by implemented few-layer or graphene[125].

Recently, another study showed how the temperature can improve the performances of a Cap Mix based on the CDEL: when operating isothermally, the increase of the operating temperature aids in the maximation of the net-work output from the device by up to 50%[126].

One of the first membrane-based Cap Mix was reported by Liu et al[120]. The Cap Mix works with two sodium chloride solutions of 500 mM and nearly 20 mM. Thanks to a high perm-selectivity membrane, the increase of voltage was close to the thermodynamic limit and the maximum power density was in the order of 200 mW m^{-2}.

Several improvements have been made in the years in terms of electrode geometry and membrane composition: the electrode geometry has a relevant impact on the overall performance of the device. Indeed, in two works of 2012, researchers improved the system by using wire-shaped electrodes obtaining more power per material invested compared to traditional flat plate designs[127,128].

In a recent study of this year, 2020, an interpolymer ion exchange is proposed as membrane of a CDP device[129]. The membrane is based on styrene which polymerizes and penetrates a matrix of polyethylene, forming the interpenetrating polymer network. Using this type of membrane, the power output increases up to 160 mW m^{-2}.

The first Batt Mix, was proposed by La Mantia et al.[130] in the 2011. In their work, they demonstrated an energy extraction efficiency of up 74% with a device which contained a nanorod electrode made by $Na_2Mn_5O_{10}$, used to capture sodium ions, and a silver electrode, used to capture chloride ions.

Three years later, Ye et al[131] improved the reactor design stressing the need to keep on looking for new electrode materials to increase the capacity and decrease the cost. In fact, sodium manganese oxide has a low discharge capacity which means that a large mass of active material is required per unit of extracted energy.

Other sodium-captured electrodes were proposed, like the Prussian Blue analogue family. For example, an electrode made by manganese hexacyanomanganate open-framework anode, was combined with a copper hexacyanoferrate cathode and the resulting devices showed high efficiency ranging between 84% to 97% without measurable capacity loss[132].

These technologies are still at the beginning of their development, and they have never been tested or modeled for the coupling with a thermal stage; hence, data related to the overall heat-to-electricity efficiency are not available.

1.2.3.2. Thermally Regenerative Complex Battery (TRCB)

Thermally Regenerative Complex Battery (TRCB) is a redox-flow cell which, operating at a fix temperature, exploits Low-Temperature Heat to regenerate the electrolyte[133] or only the anolyte/catholyte[134].

Redox-flow cell uses two soluble redox couple as electroactive species which undergo to a reduction or oxidization in order to release or store energy. An ion exchange membrane divides the two half

cells composed by anolyte and catholyte, respectively, and the electrodes, where the redox process takes place. The reactants solutions are stored in separates tanks and are recirculated through the redox-flow cell, through a pump, in a close circuit loop[135].

A pioneering work of Peljo et al[133]. consisted in the combination of the redox-flow cell device with a distiller introducing one of the first TRCB. The system was based on the complexation of copper with acetonitrile; the battery could be recharged by distillation of acetonitrile. This process, which took place at a temperature lower than 100°C, destabilized the copper complex, leading to the recovery of the starting materials (Figure 1.28).

The redox-flow system was composed by Nafion as cation exchange membrane, copper wire as anode and platinum or tungsten wire as cathode. The electrochemical stage showed reasonable battery performances, in terms of stability and energy efficiency but the heat recovery part was not considering in this work. Therefore, the overall efficiency of the device was not calculated.

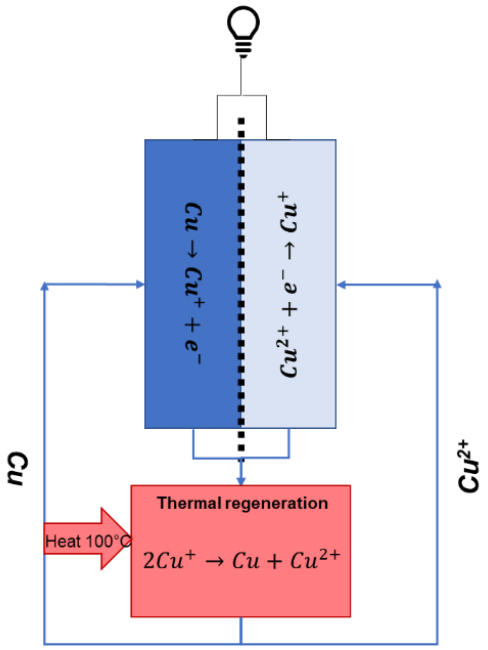

Figure 1.28. All copper Thermally Regenerable Complex Battery.

In 2015, Zhang et al[136], inspired by the Peljo's work, developed a TRB based on ammonia (named TRAB), evaluating not only the electrochemical performances of the device, but also the thermal stage of the system (Figure 1.29). In the TRAB, both the electrodes made of copper and were immersed in cupper nitrate solutions and separated by an anion exchange membrane. Only in the anolyte, ammonia was added to produce a potential difference between the two half cells, thanks to the formation of ammine complex with Cu^{2+} ions. The redox reaction of the entire cell is reported here:

$$\text{Catholyte: } Cu^{2+} + 2e^- \rightarrow Cu \quad (E^0 = +0.340V)$$

$$\text{Anolyte: } Cu + 4NH_3 \rightarrow Cu(NH_3)_4^{2+} + 2e^- \quad (E^0 = -0.040V)$$

The heat recovery involves only the anolyte which was directed to the distillation column in order to separate ammonia and regenerate the electrolyte. This system showed an energy density around 450 Wh m^{-3}, a thermal efficiency of 0.5%, an efficiency relative to Carnot efficiency of 3.8% and an average power density of 60 W m^{-2}.

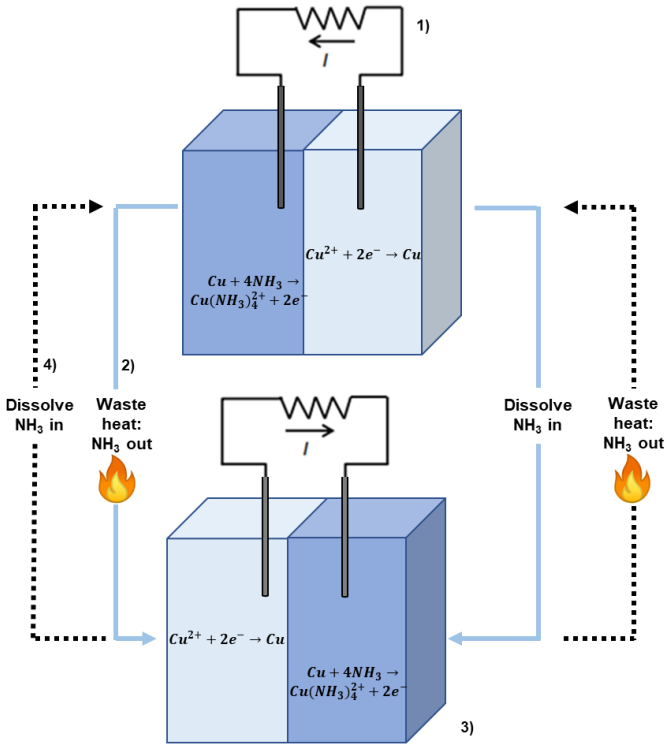

Figure 1.29. Schematic of the TRAB. 1) power production with the initial Cu^{2+} solution and Cu-ammonia complex solution. 2) Regeneration of the electrolyte exploiting LTH. 3) Power production with regenerated solutions, which also regenerates the electrode. 4) Regeneration of the solutions by LTH.

The optimization of this TRCB was obtained operating at higher temperature[134]: at 72°C the maximum power density increases to ≈ 236 W m^{-2}. However, operating at higher temperatures also decreased the selectivity of the membrane which allowed the transport of ammonia. This resulted in a global worsening of the energy density and energy efficiency. A further optimization was obtained by Zhu et al[137], in 2016: changing the configuration of the cell, increasing the electrode surface area, the membrane area, and implementing a single copper plate which was used as both the cathode and the anode, they were able to increase the energy density up to 1260 Wh m^{-3} and the thermal efficiency related to the Carnot efficiency to 5%.

The TRAB was further optimized in the years, in terms of power production, energy density, thermal efficiency relative to the Carnot efficiency, and stability during cycle processes changing the electrodes[138,139] and the anion exchange membrane[140].

A bimetallic TRAB based on copper and zinc was proposed by Wang et al.[141] in 2020. This device showed a maximum power density of 723 W m^{-2} in a temperature range of 10-40°C. the thermoelectric conversion was only 0.37% but, with a simulation, this value could be improved to 1.28% reducing the condenser temperature (Figure 1.30).

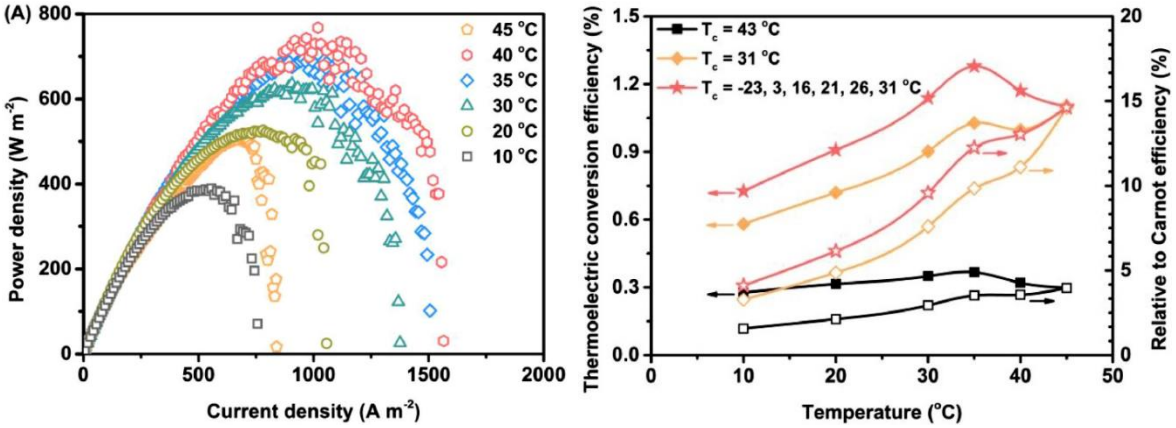

Figure 1.30. a) Power generations of a Cu/Zn-TRAB operated at different temperatures; b) Thermoelectric conversion efficiency and relative to Carnot efficiency of a Cu/Zn-TRAB operated at a constant current density of 100 A m^{-2} with different operating temperatures and condenser temperatures T_c.[141]

A TRCB based on copper complexation with acetonitrile was recently proposed. The system worked with an average power density of 70 W m^{-2} and a theoretical heat-to-electricity efficiency of 2.2%. This is one of the best results in terms of efficiency for this kind of devices[142], along with the TRAB proposed by Palakkal et al.[143], which reaches an efficiency of 2.99%.

Up to now, TRCB are the technologies with the highest power density reached in this field but, unfortunately, the heat-to-electricity efficiency is so low to make them still unsuitable for real applications.

1.2.4. System to regenerate the exhausted solution: desalination processes

In these years, several processes were proposed to desalinate water in order to solve one of the biggest problems of the 21st century: the lack of freshwater resources. If a process is able to recover fresh water from a salt solution, therefore the same process is able to recover the salt from the water. This means that the desalination methods are also processes able to regenerate the exhausted solutions derived from salinity gradient devices. In fact, as the recovery of freshwater is increased, the remaining solution becomes more concentrated.

Desalination process can be achieved in several different ways, summarized in Figure 1.31.

There are two general approaches: the one that exploit thermal energy and the one that does not use it. This second approach for desalination consists in physical or chemical separation of the components.

The physical separation requires membranes and can be distinguished in two major processes: reverse osmosis[144] and electrodialysis[145]. In the reverse osmosis, water passes through a membrane due to a chemical potential gradient achieved through pressurization[146,147].

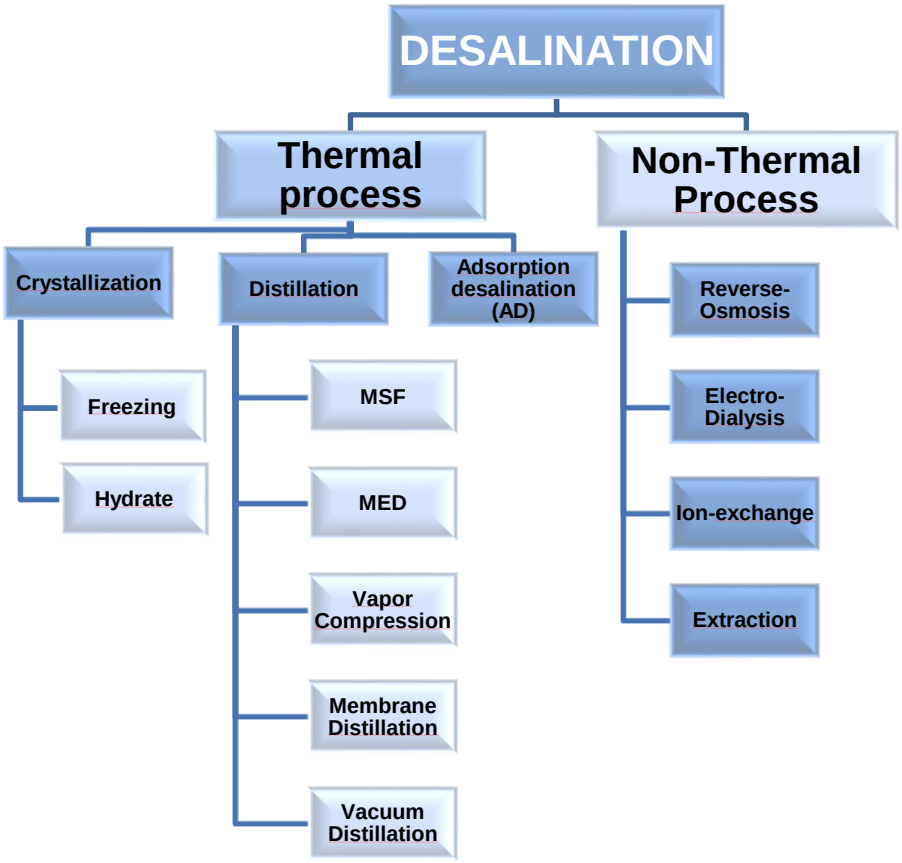

Figure 1.31. Categories of desalination processes.

In the case of electrodialysis, the species passes through the membranes are the ions. Ions migrate through anion/cation selective membranes in response to an electric field[148].

The chemical approaches for the solution desalination, consist in ion exchange processes, gas hydration, extraction, and other different methods. In general, these processes are too expensive to be applied for the water desalination and for this reason these strategies are not widely diffuse.

Finally, the thermal methods consist in regenerating a solution via an endergonic phase transition (e.g. evaporation, crystallization), to separate the solvent and concentrate the solution for future uses in the power stage. This last category of processes can exploit Low-Temperature Heat to desalinate water. LTH can be converted in electricity if one of this thermal process is then coupled with a SGE system: the thermal separation converts heat into chemical energy, while SGE device converts chemical energy into electricity. For this reason, a brief overview of the thermal separation processes is reported here.

1.2.4.1. Distillation

Distillation is a thermal separation process used to separate components from a liquid mixture.

It occurs when a liquid sample is heated to produce a vapor that is subsequently condensed to a liquid richer in the more volatile components of the original one. The volatilization process is achieved by

heating the liquid, but it may also be obtained by reducing the pressure or by a combination of both the mechanisms[149].

The theoretical principles are generally illustrated by reference to a vapor-liquid equilibrium diagram related to a binary mixture as reported for example in Figure 1.32 (vapor-liquid equilibrium graph of a mixture of *"P"* and *"Q"*). Generally, the upper curve gives the composition of the vapor in equilibrium with the boiling liquid while the lower curve gives the composition of the liquid phase; points *x* and *y* represent the boiling temperature of pure *P* and *Q* components.

In the point *A*, the temperature is *X* and the composition, that is read on the X-axis, is approximately 90% of *P* and 10% of *Q*. In a continuous distillation process, liquid of composition *C* vaporizes to vapor of composition *D* and condensed to liquid of composition *E*.

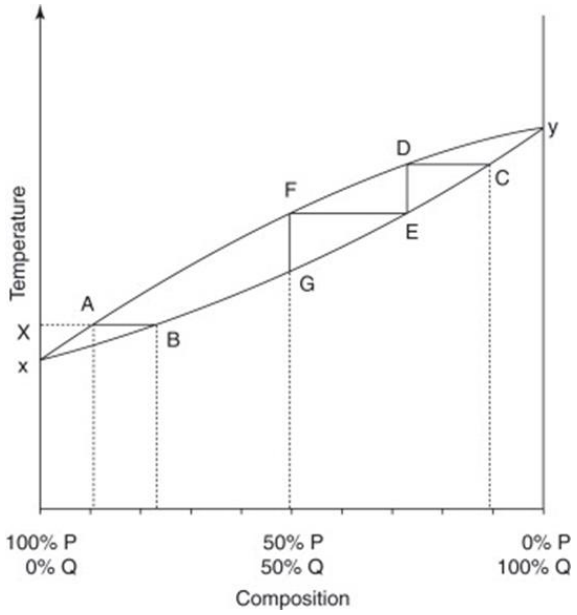

Figure 1.32. Vapor-liquid diagram of a mixture of components "P" and "Q"[149].

Different kind of distillation plants can be implemented with SGE systems, such as Multi-Effect Distillation, Multi Flash Distillation, Vacuum Distillation and Membrane Distillation that are here discussed.

To determine the better distillation plant for any technology, several parameters must be evaluated such as costs, efficiency, and the Gained Output Ratio (GOR).

GOR is a measure of how much thermal energy is consumed in a desalination process. It is defined as the number of kilograms of distilled water produced per kilogram of steam consumed, hence it is a dimensionless parameter. Generally, the higher its value, the better the performances of the system[150]. This parameter is used to compare the capital and operating costs of units and it has to be considered at the design stage of the plant[150].

Multi-Effect Distillation (MED)

Multi-effect distillation (MED) is one of the thermal process proposed for the desalination of seawater (Figure 1.33).

It finds applications in several industries for economical concentration of fluid, such as pulp and paper industry.

MED is a distillation process which consists of multiple stages called "effects"; any effect is composed by an evaporator and a condenser. In the first effect the solution is heated by the heat source until the boiling point. The steam produced inside the one effect is consumed as the energy source of the subsequent effect: whereas on one side the entering steam is condensing, on the other side, the feedwater is boiling, generating extra steam. The number of effects used is dependent on the performance ratio required.

Unlike a Multi-Stage Flash (MSF) distillation plant, MED usually operates as a once through system without a large amount of brine recirculating around the plant; in this way, the dimensions of the entire plant are reduced[151]. MED requires less specific energy, is cheaper and require only a simple water treatment. Nevertheless, MED is still not widely used, but it has gained attention thanks to the better thermal performance compared to MSF.

There are different configurations for MED plants depending on the combinations of heat exchanger configurations: the MED plant can be divided into a rising film vertical tube evaporator plant, a vertical climbing film tube plant, and the horizontal tube falling film spray tube plants[152].

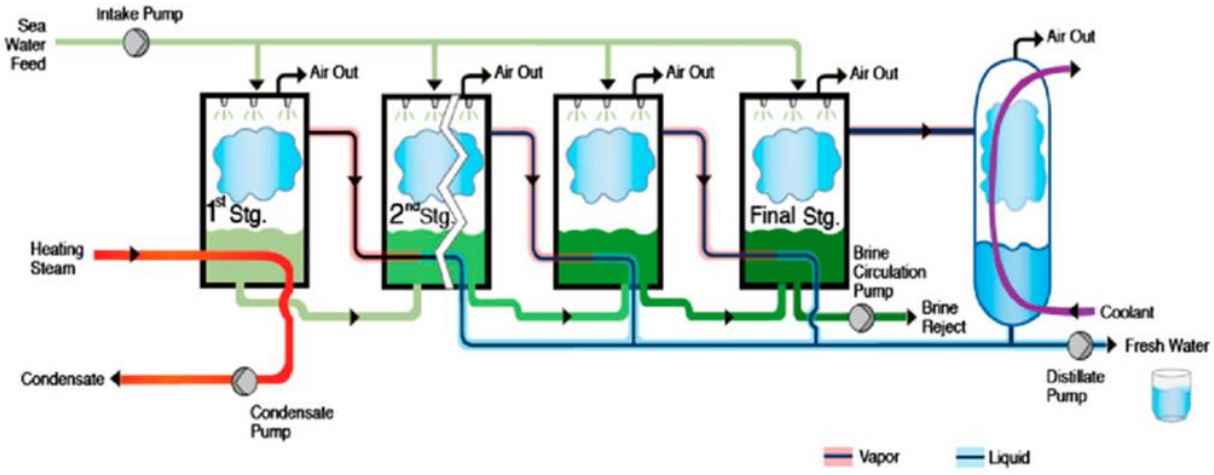

Figure 1.33. Scheme of a MED plant for desalination[153].

Other configurations depend on the flowsheet arrangements used, such as forward-feed, backward-feed, and parallel-feed[154]. In the forward-feed design, the most common arrangement for the water desalination, feed from one effect is pumped to the next effect in parallel to the vapor flow.

In 2019, Brogioli et al[155]. thermodynamically analyzed a MED system coupled with heat exchangers, in order to evaluate the achievable efficiencies when the system is coupled with a SEG device, exploiting Low-Temperature Heat sources. The main result of this study is that the highest efficiency

is obtained with the high boiling point elevation because it is compatible with the available temperature difference between the heat source and the reservoir. In general, the higher is the boiling point elevation, the lower is the number of stages required, having a higher efficiency per effect.

MED-TVC

A MED system can be coupled with a Thermal Vapor-Compression (TVC) process which is based on raising the pressure of the steam from a stage by means a compressor, thus increasing the condensation temperature. The plant works as a conventional MED system, in which the vapor produced from the first effect is used as heat input to the second one, at lower pressure. In the last effect, the vapor is compressed, and its saturation temperature is raised before it is returned to the first effect.

In terms of costs and design process, the TVC system is not particularly convenient used by itself, but it can be coupled with a MED system, as reported in Figure 1.34[156].

The vapor generated in the first effect, D_1, at a pressure P_1, is directed to the second effect where it condenses, acting as a heat source for the feed stream, F_2, of the second effect. F_2 is, thus, heated from the feed temperature, T_f, to its boiling point and generates vapor, D_2. Similarly, the vapor generated in the second effect condensed in the third one acting, again, as a heat source, and so on to the last effect. The vapor generated in the last effect is divided in two different streams: the stream D_r, is directed to the steam ejector, where it is recompressed and returned to the first effect; the stream D_f, is condensed and heats the feed stream from its temperature to the feed temperature T_f.

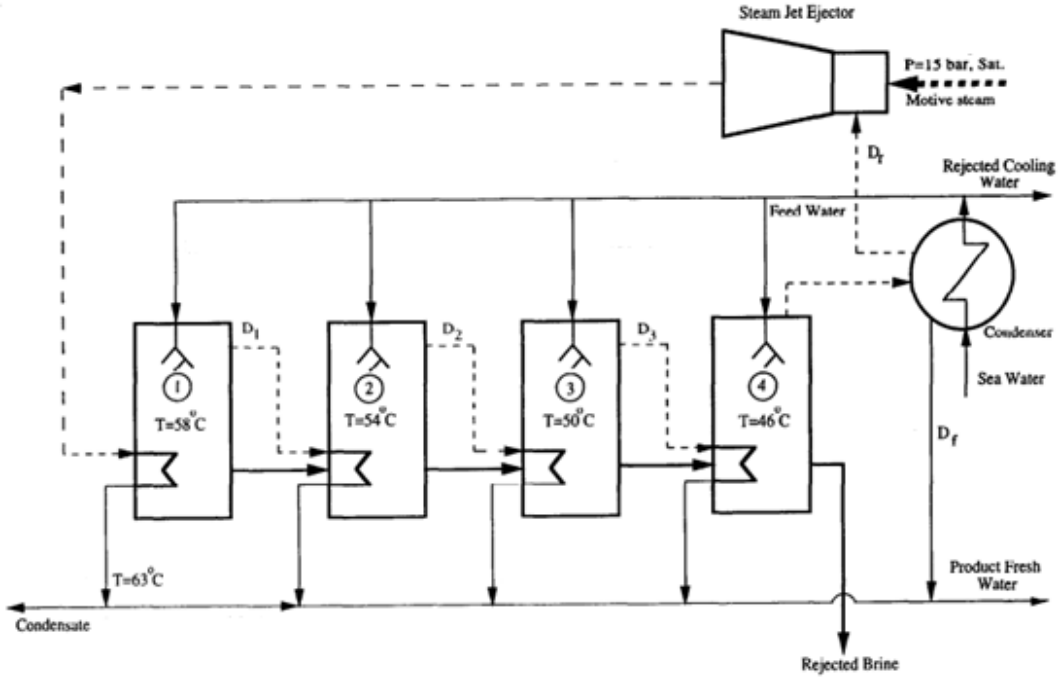

Figure 1.34. Four effect MED-TVC desalination plant[156].

Coupled a MED system with a TVC process increases the GOR number. In general, coupling a MED with three effects, that has a GOR of 3, while coupling a MED with the TVC process raises the GOR to the double.

MED-MVC

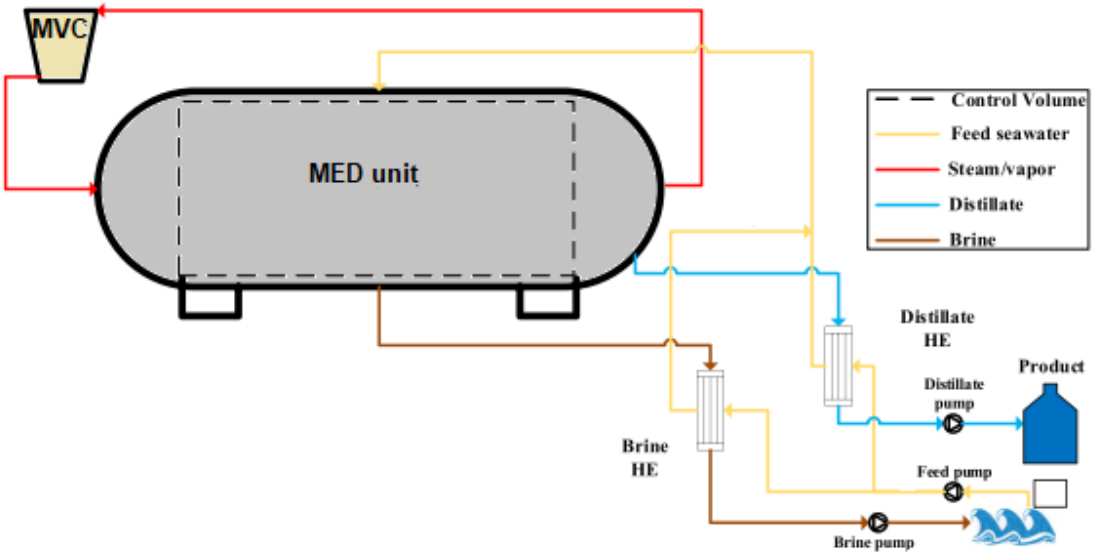

Figure 1.35. MED-MVC desalination system.

Multi-Effect Distillation with Mechanical Vapor Compressor (MVC) system is widely used for medium-scale plants. The vapor generated in the last effect is recycled by means a centrifugal compressor driven by an electrical engine. In this desalination system, the end condenser in a conventional MED is absent because all the vapor produced in the last effect is sucked out by the mechanical compressor in order to use it as a heating vapor for supplied feed (Figure 1.35).[157]

A MED-MVC system has several advantages such as compact equipment, low-temperature design, long-term stable operation, high-quality water recovered, and minimal corrosion formation.[157] The main limitation of this system is the low capacity of the available mechanical compressors which limits the production capacity to 5000 m^3/day.[158]

Multi-Stage Flash Distillation (MSF)

MSF process consists in a series of "stages" in which condensed steam is used to pre-heat the solution feed, as in MED (Figure 1.36).

The system is able to approach ideal total latent heat recovery by fractionating the overall temperature difference between the warm source and the solution, into a large number of stages.[154]

A normal MSF plant comprises 4-40 stages, and each stage operates at a successively lower pressure in order to maximize water recovery.[159] In this way, the boiling point is always achievable without providing extra heat to the leaving brine.[159]

Compared to MED process, MSF plant requires higher energy, demanding 13.5-25.5 kWh m^{-3}, that is the reason why MSF plants are recommended where large amount of renewable or waste energies are available.[160]

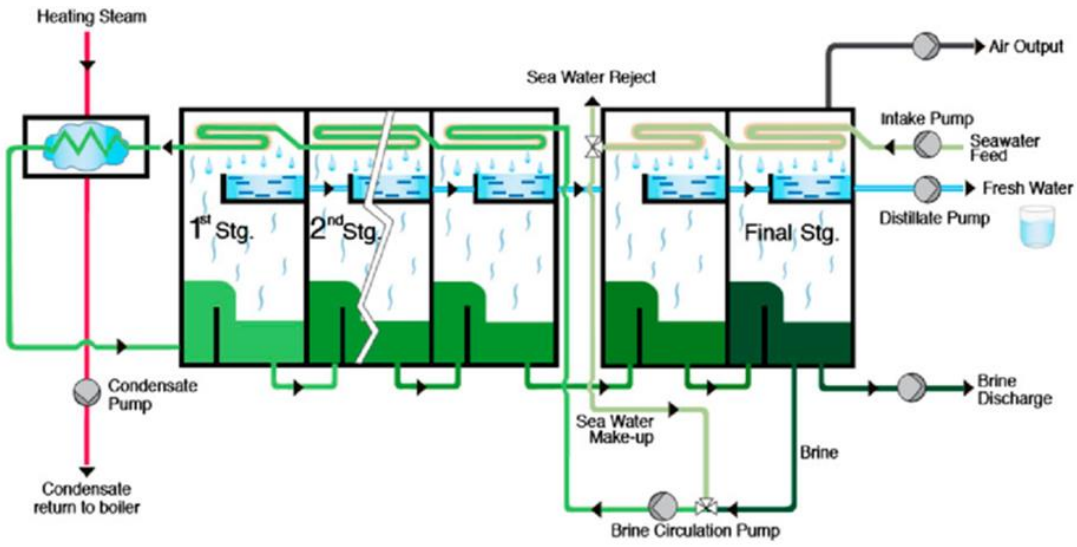

Figure 1.36. Scheme of MSF plant for desalination[153].

Vacuum Distillation

Vacuum distillation is a physical separation method used to separate higher boiling fractions.

The process is analogous to the general atmospheric distillation, used to separate the lighter fractions. The only difference between the two processes is that vacuum distillation occurs at a significantly reduced pressure (hence the name "vacuum"), in order to decrease the boiling point of the substances. In this way, high boiling components can be boiled, and therefore separates, at lower temperatures.

As in MED technology, the vaporization and condensation compartments are usually called "effect".

Generally, the pressure used in vacuum distillation is in the range of 50 to 100 mmHg, but this pressure can be also lower for particular substances like lubricating oil.

When this method is applied to restore the salinity gradient of the fed solution in SGE systems, the pressure in the distiller is lowered by removing air, in order to reduce the boiling point of the water solution below 100°C.

Membrane Distillation (MD)

Membrane distillation (MD) consists in a hot feed stream which is passed over a microporous hydrophobic membrane. On the two sides of the membrane, a temperature difference is kept which leads to a vapor pressure difference. The pressure difference causes the water evaporation from the hot side: the evaporated water pass through the pores of the membrane toward the cold side where can be condensed.

MD process is used to treat the high salinity brines; it is easily scalable and does not require high pressure feed.

MD process ca be used in direct contact (DCMD), where the vapor is condensed on a pure water stream contacting the other side of the membrane[161]. Its design is very simple as the required operations. It has high permeated flux but suffers of low thermal efficiency (Figure 1.37a).

Another configuration is called Air Gap Membrane Distillation (AGMD) in which an air gap separates the membrane from a cold condensing plate in which the vapor is collected[162]. It has higher thermal efficiency compared to DCMD but in turns, it has lower permeated flux due to higher resistances because the air gap (Figure 1.37b).

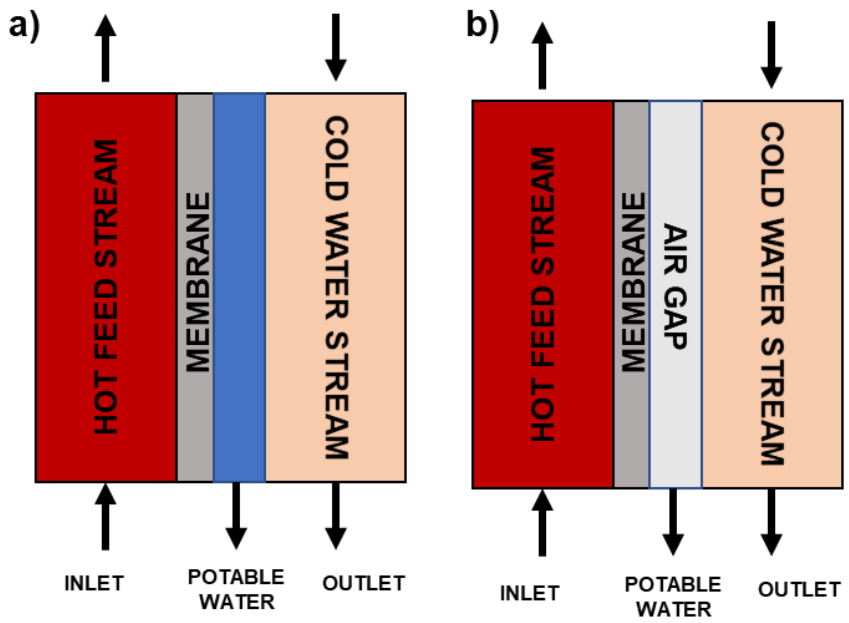

Figure 1.37. Schemes of a) DCMD and b) AGMD

There is also the possibility to perform MD separation in a vacuum (VDM)[163]. In VDM, the permeate side is kept at lower pressure to increase the pressure difference across the membrane. The vapor condensation takes place in an external condenser or in a module (Figure 1.38b). VDM is characterized by lower operating temperature, lower hydrostatic pressure, and higher permeated flux compared to the other possible MD configurations.

A less common MD separation uses a carrier gas to remove the vapor, which is condensed in a separate apparatus. This type of separation is called Sweeping Gas Membrane Distillation (SGMD)[164] and its main disadvantages are the requirement of a larger condenser, the difficulty of heat recovery and to deal with sweeping gas (Figure 1.38a).

One of the main drawbacks of this kind of technique is related to the flux of heat across the membrane due to the thermal conduction of the membrane itself; this process leads to heat loss and, therefore, should be minimized.

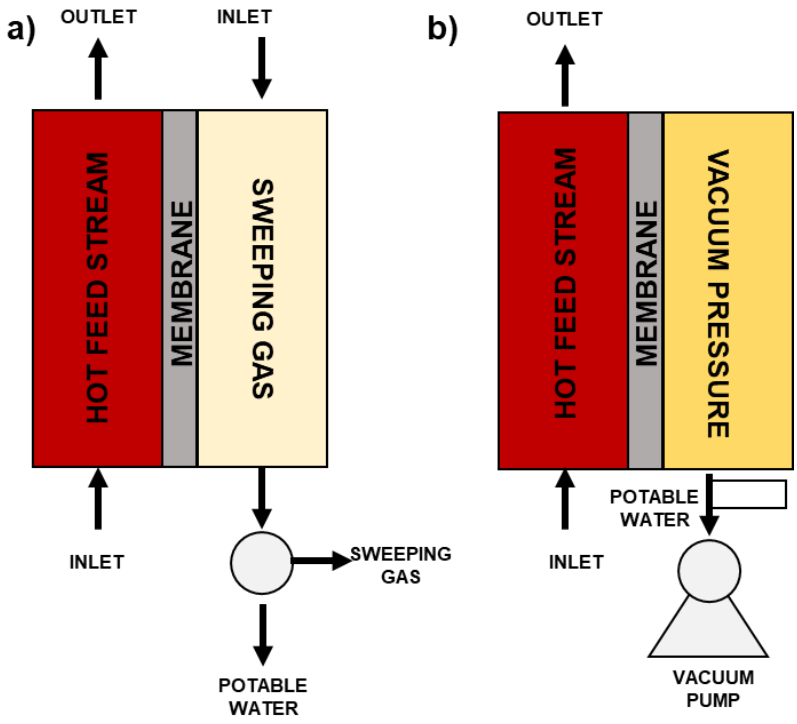

Figure 1.38. Schemed of a) SGMD and b) VMD.

For this reason, the research on MD systems is focused on the development of new membranes, maximizing membrane flux and energy efficiency[165–167].

1.2.4.2. Crystallization

Crystallization is another thermal desalination process, based on a liquid to solid phase transformation in order to separate the solid phase from the remaining liquid phase. Crystallization can be performed in two different processes: a freeze desalination, in which the phase change is obtained by thermal means, or a gas hydrates desalination, which is not a thermal approach because it exploits the elevated pressures to precipitate the water as a gas hydrates or clathrates.

Freeze Desalination (FD)

Freeze desalination is a traditional thermal crystallization that was developed in the 1950s[168,169].
In FD process, through the application of a cold source, ice crystals are formed while dissolved salts diffuse in the liquid phase. Ice is then washed and melted. This method consumes low energy since the latent heat of water fusion is approximately 333.5 kJ kg^{-1}: it is almost one-seventh of its latent heat of evaporation, 2256.7 kJ kg^{-1}. Furthermore, due to the low working temperatures, FD systems require inexpensive materials and consequently demand lower investments and operational costs.
A direct and indirect freezing desalination process can be identified: in the first case, the direct freezing process, the refrigerant is mixed directly with the brine while, in the second approach, the refrigerant is separated from the brine by a heat transfer surface. Direct contact FD processes may use water itself as a refrigerant, but they must operate under vacuum. On the contrary, the indirect process consists in a conventional compressor driven refrigeration with the evaporator serving as the

ice freezer, and the condenser as the ice melter (Figure 1.39).[170] Ice is separated from the brine by different methods such as centrifugation. Ice is than washed and send to the melter where freshwater is recovered. In this part of the process, a heat exchanger is used to recover energy from the melting.[171]

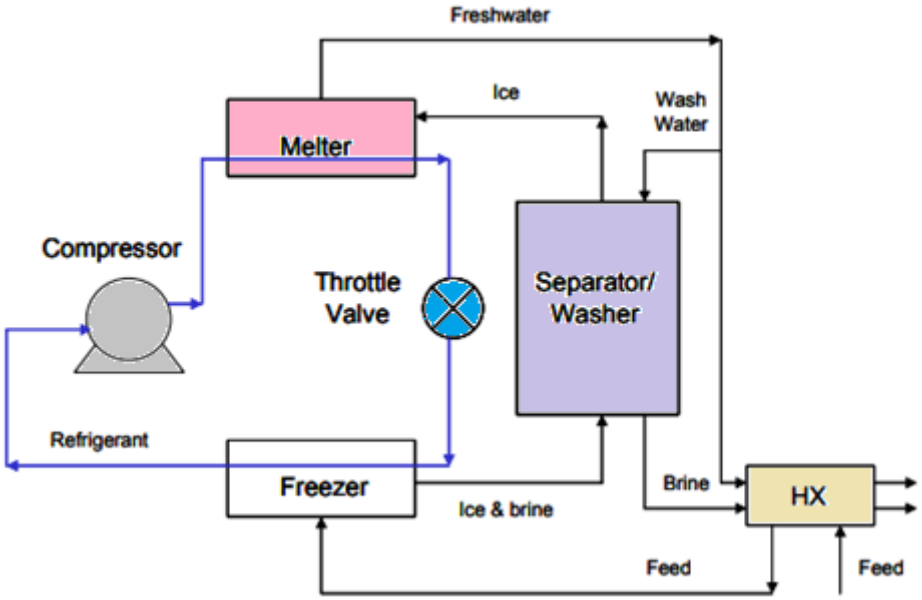

Figure 1.39. Scheme of indirect freeze desalination plant[170].

Gas Hydrate

Gas hydrates or clathrates are crystalline aggregation of water molecule around a central gas molecule driven by hydrogen bonds. These compounds have a freezing point at least as high as 12°C, but they are formed under elevated pressure.

In this separation method, like a direct FD, gas and solution are mixed in order to precipitate hydrates compounds. The crystals are then separated from the liquid phase, washed, and melted, while the gas is recovered for reuse.

One of the advantages of this approach is the higher operating temperature which decreases the energy requirements. However, the process requires higher pressure than indirect FD process and the separation of crystals could become difficult.

1.2.4.3. Adsorption Desalination (AD)

Adsorption Desalination (AD) is an emerging separation method driven by thermal energy. It exploits LTH sources, below 90°C, and environmentally friendly adsorbent/adsorbate pairs. It has no major moving parts, which means low maintenance costs.

The AD system consists in an evaporator, a condenser and the so-called adsorbent beds (silica adsorber gel), which are composed by microporous adsorbent particles[172].

In AD, the exhausted solution from SGE or the saline water replace the fresh water of chiller-only systems and, at the end of each cycle, the fresh water produced by the condenser is drained off while the more concentrated brine is recovered (Figure 1.40).

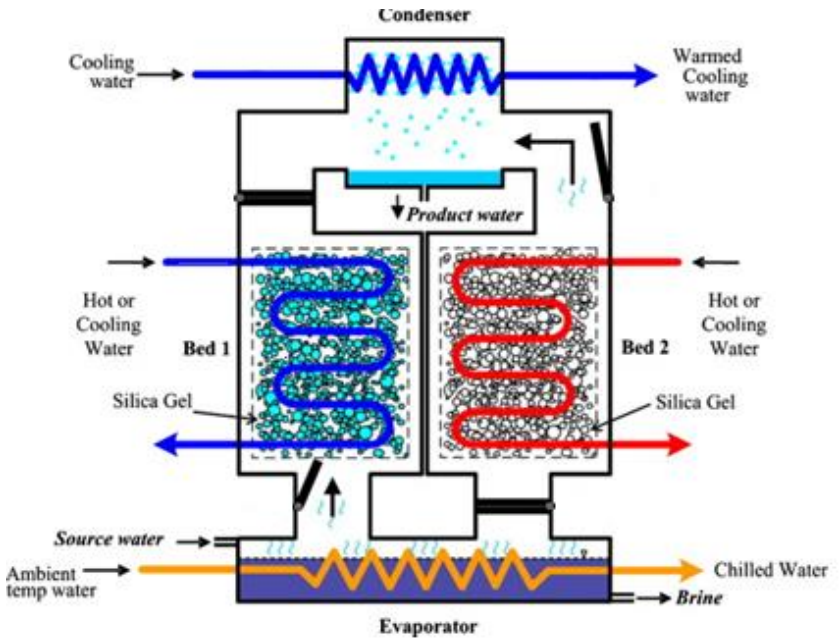

Figure 1.40. Schematic of a two-bed adsorption desalination system[173].

The AD process starts with the injection of the solution in the evaporator, which is the only unit built of anti-corrosive material. The evaporator is vacuumed to a pressure commensurate with the desired temperature of the chiller water, which also flows in an external circuit, providing the heating load to maintain the evaporator process. At the same time, the adsorption bed and condenser are kept at the saturation pressure corresponding to the temperature of the cooling water.

The evaporator is connected to the adsorbent beds where the water vapor is adsorbed by the silica gel, while the adsorption heat is removed by coolant from the cooling tower. Once the adsorbent bed is saturated with vapor, the adsorbed water is driven off the silica gel and the pressure in the bed raised by circulating hot water in the bed. The desorbed vapor is condensed, and the condensation heat is driven to the cooling water from the cooling tower[174]. Beds 1 and 2 (but they could be also four) operate alternatively in order to produce fresh water and concentrated solution in a continuous manner.

Even if it is a less expensive desalination method, this approach is still under studied in order to evaluate the water yield respect to key parameters such as heat source temperatures, coolant temperatures and half-cycle operational times[175].

1.2.4.4. Thermolytic salt: Stripping

Among the possible "salt extraction-desalination" processes, the use of thermolytic salts with aqueous solutions seems to be the most promising and, therefore, requires a specific discussion.

At ambient conditions of temperature and pressure, thermolytic salts are soluble in water, while at a higher temperature, these salts become gases which can be easily separated from the solution through a stripping process. After the separation process, a further absorption step is necessary to let the concentrated solution to absorb the salt.

Stripping process is a physical separation method in which components are removed from a liquid stream by a vapor stream.

When a water stream is stripped, the process acts essentially like a distillation, where the heavy product is water and the light one is volatile organic compounds. The volatility of the organic chemicals depends on the temperature, therefore, the stripping column design changes with the type of organic compound, the degree of organic removal, and the operating pressure and temperature.

One of the most common thermolytic salt for LTH harvesting is ammonium bicarbonate. It is decomposed into NH_3 and CO_2 at very low temperatures, around 50°- 60°C[112].

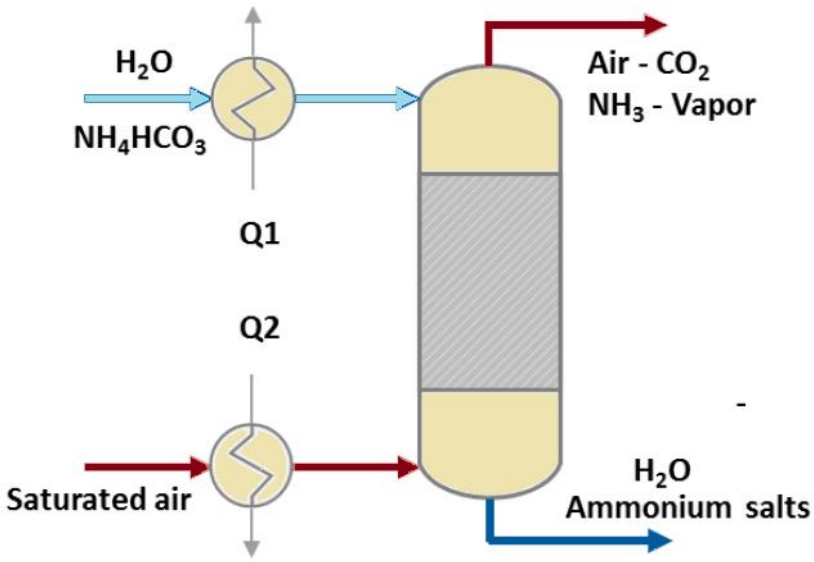

Figure 1.41. Schematic representation of a stripping column operating with hot saturated air for ammonium bicarbonate salt degradation and removal NH_3 and CO_2 gases[176].

The stripping column (Figure 1.41) is generally filled from the top with ammonium bicarbonate solution while hot air, saturated with water in order to avoid sudden water evaporation, is fed from the bottom. The counter-current contact between the two phases and the high temperature of the air fosters the salt degradation and the passage of ammonia and carbon dioxide from the liquid phase to the gaseous one.

The gaseous stream, rich of NH_3 and CO_2, leaves the column from the top and it is directed to an absorption column to regenerate the concentrated solution, while the liquid stream is removed from the bottom of the column resulting in the diluted solution ready to be sent in the power stage.

1.3. Aim of the research

LTH has recently elicited great interest as a source of energy among the scientific community since it is actually wasted in the environment. Its conversion in other forms of energy becomes of utmost importance as it would allow to open the doors to the exploitation of a huge amount of heat, such as solar, geothermal, and industrial waste heat.

The conversion of LTH is still a challenge due to the low heat-to-electricity efficiency because of the limitations imposed by Carnot law. Moreover, the overall efficiency is further reduced by technological limitations.

For these reasons, even though LTH is a widely available energy source, its potential remains unexploited due to the lack of an optimized technology able to convert it in an efficient way, reaching high power density with reasonable costs.

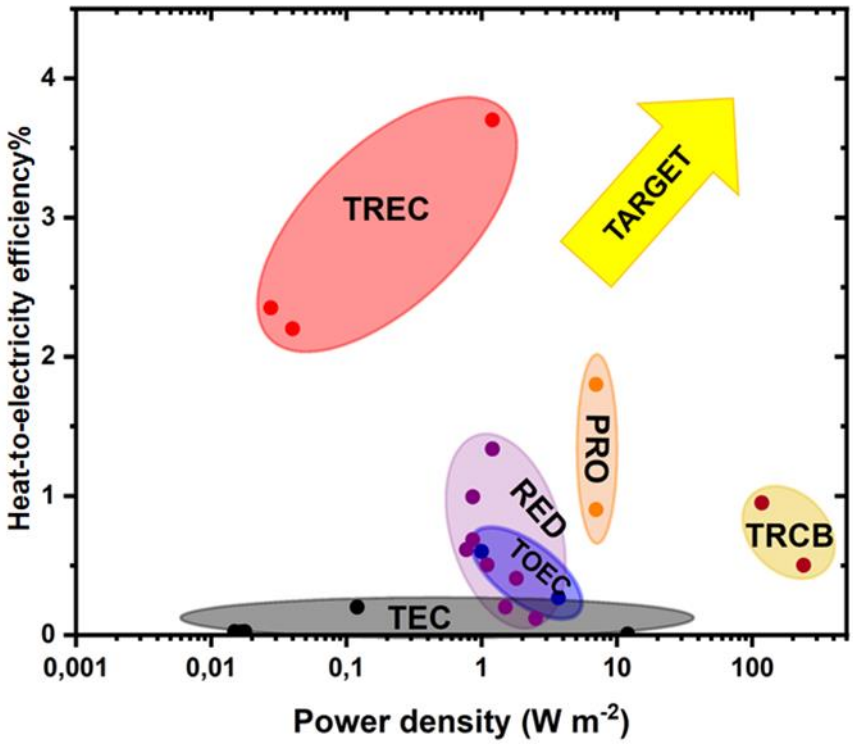

Figure 1.42. Energy efficiency vs power density of state-of-the-art technologies to harvest LTH reported in literature. Red points: Thermal Regenerative Electrochemical Cycle systems (TREC)[81,82,85]*; Black points: Thermal Electrochemical Cell devices (TEC)*[76,177,178]*; Blue points: Thermo-Osmotic Energy Conversion technologies (TOEC)*[57,97]*; Orange points: Pressure Retarded Osmosis systems (PRO)*[99,179,180]*; Purple points: Reverse Electrodialysis Devices (RED)*[115,116,181,182]*, Brown points: Thermally Regenerative Complex Batteries (TRCBs)*[139,183]*.*

In Figure 1.42. are reported all the "new" technologies proposed to exploit LTH in terms of power output (X-axis) and heat-to-electricity conversion efficiency (Y-axis).

Up to now, the best compromise is represented by TREC systems, devices that directly convert LTH into electricity with high efficiencies but with limited power densities (Figure 1.42, red points). Higher values of power output are typical for TRCBs, devices that can also store heat in form of

chemical energy. However, they usually have smaller efficiencies (Figure 1.42, brown points), making them unfeasible.

This research is focused on the development of a new device for the LTH conversion to fill this technological gap. This new device will be a mix between a technology that converts the Salinity Gradient Energy and a TRCB. Therefore, it will be a two-stages device able not only to convert LTH, but also to store it in form of chemical energy.

The target of this project is reported in Figure 1.42: the device would be able to convert LTH with higher efficiency than TREC technologies and, at the same time, higher power density, making it comparable to TRCBs systems.

CHAPTER 2

Thermodynamic

In this chapter it will be discuss general thermodynamic principles related to the mixing solutions, the electrochemistry, the heat conversion, and the distillation in order to better understand the discussion of the results of this work.

2.1. General principles of mixtures[184]

To explain the thermodynamic of solutions it is necessary to start from the definition of partial molar quantities that can be easily described as the effect that a change in a single component of a mixture has on the particular thermodynamic properties and can be applied to any extensive state function.
The partial molar Gibbs energy (*G*) of a pure substance *i* is named chemical potential, μ, and is defined as

$$\mu_i = \left(\frac{\partial G}{\partial n_i}\right)_{p,T,n_{i\,(i\neq j)}} \quad (2.1)$$

For pure substances, the chemical potential is equal to the change in the Gibbs energy of the system as the amount of material changes, and it is identified with the apex *. It is a measure of how much a species wants to undergo a physical or chemical change.
Considering a possible change in the amount of substance *i*, the general expression of the infinitesimal change in *G*, *dG*, now becomes:

$$dG = \left(\frac{\partial G}{\partial T}\right)_{p,n} dT + \left(\frac{\partial G}{\partial p}\right)_{T,n} dp + \sum_i \left(\frac{\partial G}{\partial n_i}\right)_{p,T,n_j(i\neq j)} dn_i \quad (2.2)$$

$$dG = -SdT + Vdp + \sum_i \mu_i dn_i \quad (2.3)$$

This equation is referred to as the "Fundamental equation of chemical thermodynamics" because it embodies all state variables of conditions and amount.
At constant pressure and temperature, the equation 2.3 becomes

$$dG = \sum_i \mu_i dn_i \quad (2.4)$$

Given a binary mixture, when the compositions are changed infinitesimally, *G* of the system is

$$dG = \mu_i dn_i + \mu_j dn_j + n_i d\mu_i + n_j d\mu_j \quad (2.5)$$

Because *G* is a state function, equation 2.4 and 2.5 must be equal: this means that, at constant temperature and pressure

$$n_i d\mu_i + n_j d\mu_j = 0 \quad (2.6)$$

Equation 2.6 is named *Gibbs-Duhem* equation and it is in general expressed

$$\sum_i n_i d\mu_i = 0 \quad (2.7)$$

When temperature and pressure are kept constant or

$$\sum_i n_i d\mu_i = SdT - VdP \quad (2.8)$$

When temperature and pressure can change.

This equation demonstrates that the chemical potential of one component of a mixture cannot change independently of the chemical potentials of the other components.

In order to discuss the properties of liquid mixture, it's important to know how the Gibbs energy of a liquid varies with composition.

When a vapor *A* is in equilibrium with its liquid phase, their chemical potential must be equal. The chemical potential for the vapor is expressed at

$$\mu_A^* = \mu_A^0 + RTln\left(\frac{p_A^*}{p_0}\right) \quad (2.9)$$

Where μ_i^0 is the standard chemical potential of the substance, which is the molar Gibbs free energy of the pure gas at 1 bar (p^0).

When another substance is also present in the liquid, for example a solute, the chemical potential of *A* in the liquid is not the potential of a pure substance but it changes to μ_A while its vapor pressure changes to p_A. Vapor and solvent are still in equilibrium so we can write

$$\mu_A = \mu_A^0 + RTln\left(\frac{p_A}{p_0}\right) \quad (2.10)$$

Rewriting equation 2.9 in order to define the standard chemical potential and substitute this expression in the equation 2.10, we obtain

$$\mu_A = \mu_A^* + RTln\left(\frac{p_A}{p_A^*}\right) \quad (2.11)$$

In the 1880s, François Raoult discovered that the ratio p_A / p_A^* is approximately equal to the molar fraction (x) of the substance *A* in the liquid mixture:

$$p_A = x_A p_A^* \quad (2.12)$$

The equation 2.12 is the so called Raoult's law and it is valid only for ideal solutions. An ideal solution is a solution in which a solvent molecule required an amount of energy to break away from

the surface of the solution that is the same that it requires to break away from the surface in the pure solvent.

Therefore, for an ideal solution, the chemical potential of a substance *A* can be written as

$$\mu_A = \mu_A^* + RTln(x_A) \quad (2.13)$$

As already said, Raoult's law is valid only in ideal solutions. However, William Henry experimentally found that, for solutions at low concentrations, the vapor pressure of the solute is proportional to its molar fraction, but the constant is an empirical value, with the dimension of a pressure.

$$p_B = x_B K_B \quad (2.14)$$

Where *B* indicates the solute.

The chemical potential of the solute *B*, which satisfied the Henry's law, is

$$\mu_B = \mu_B^* + RTln\left(\frac{K_B}{p_B^*}\right) + RTln(x_B) \quad (2.15)$$

The constant K_B and p_B are characteristic of the solute. Therefore, the second term of the equation (2.15) can be combined with the first one, defining a new standard chemical potential:

$$\mu_B = \mu_B^\circ + RTln(x_B) \quad (2.16)$$

When the solution is ideal, $K_B = p_B$ and $\mu_B^\circ = \mu_B^*$.

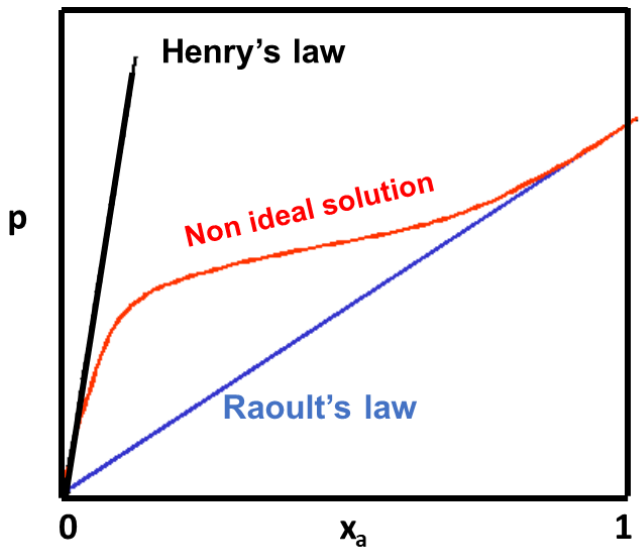

Figure 2.1. Relationship between vapor pressure of a solution and its molar fraction. The black curve represents the profile of the Henry's law followed by the solute in an ideal-diluted solution. Profile of the Raoult's law, followed by the solvent in an ideal-diluted solution is showed in blue while the red curve represents the profile of a non-ideal solution[185].

The mixture in which the solute obeys Henry's law while the solvent obeys Raoult's law are called ideal-dilute solutions. This different behaviors between solvent and solute at low concentrations is

due to the different environment in which they are. In fact, in a dilute solution, the solvent molecules are in an environment similar to the environment of a pure liquid, while the solute molecules in a dilute solution are surrounded by solvent molecule, which means a completely different environment compared to its pure liquid.

Considering two pure liquids, *A* and *B*, placed in two separated sinks, the initial Gibbs free energy is

$$G_i = n_A \mu_A^* + n_B \mu_B^* \quad (2.17)$$

When they are mixed in the same sink, forming an ideal solution, the final Gibbs free energy is

$$G_f = n_A[\mu_A^* RTln(x_A)] + n_B[\mu_B^* RTln(x_b)] \quad (2.18)$$

The difference between G_f and G_i is defined as the mixing free energy (ΔG_{mix}):

$$\Delta G_{mix} = G_f - G_i = nRT\ [x_A \ln(x_A) + x_B \ln(x_B)] \quad (2.19)$$

Where *n* is the sum of the molecules of both the substances *A* and *B*.

In general, processes in which the Gibbs free energy decreases will take place spontaneously without specific external action.

For this mixture, the entropy of mixing, ΔS_{mix} is:

$$\Delta S_{mix} = \left(\frac{\partial \Delta G_{mix}}{\partial T}\right)_{p,n_A,n_B} = -nR\left[[x_A \ln(x_A) + x_B \ln(x_B)]\right] \quad (2.20)$$

Because *ln x* is negative, $\Delta G_{mix} < 0$ and $\Delta S_{mix} > 0$.

For two pure liquids that are mixed forming an ideal solution, the enthalpy of mixing is

$$\Delta H_{mix} = \Delta G_{mix} + T\Delta S_{mix} = 0 \quad (2.21)$$

The driving force of the mixing comes from the increment of the system entropy because the entropy of the surroundings is unchanged. As discussed before, the mixing of the two liquids forms an ideal solution that means that the average energy of the interactions between the two liquids, *A*-*B*, is equal to the average energy of the interactions in the pure liquids, *A*-*A* and *B*-*B*.

In the case of real solutions, the *A*-*A*, *A*-*B* and *B*-*B* interactions are different. Furthermore, enthalpy and volume changes after the mixing. It can happen a rearrangement of the molecules that results in an orderly mixture affecting the entropy; therefore, sometimes the mixing Gibbs free energy might be positive. In this case the two liquids are immiscible, and the separation is spontaneous. Alternatively, the liquids might be partially miscible: the two liquids are able to mix only over a certain range of composition.

When you are dealing with a real solution, it becomes necessary introduce thermodynamic excess functions which are defined as the difference between the observed thermodynamic function of the real solution and the respective function of ideal solution.

For example, the excess mixing free energy is defined as:

$$G^E = \Delta G_{mix} - \Delta G_{mix}^{ideal} \quad (2.22)$$

The excess volume and enthalpy are always the observing volume and enthalpy because their values for ideal solutions are zero.
Another important concept that as to be introduced in the case of real solution, is the "activity" which assumes a different meaning and standard states according to the specific case.

2.1.1. Solvent

For the solvent of a real solution, that does not follow the Raoult's law, the chemical potential can be written in a similar way of the solvent in an ideal solution (equation 2.13), replacing the molar fraction with the activity of the solvent:

$$\mu_A = \mu_A^* + RTln(a_A) \quad (2.23)$$

The activity of the solvent is expressed as

$$a_A = \frac{p_A}{p_A^*} \quad (2.24)$$

And it represents the "effective" molar fraction.
When the concentration of the solute is close to zero, the activity of the solvent approaches the molar fraction. To express this convergence, it is introduced the activity coefficient, γ:

$$a_A = \gamma_A x_A \quad : \quad \gamma_A \to 1 \; as \; x_A \to 1 \quad (2.25)$$

The chemical potential of the solvent becomes then

$$\mu_A = \mu_A^* + RTln(\gamma_A) + RTln(x_A) \quad (2.26)$$

The standard state of the solvent consists in the pure liquid solvent at 1 bar of pressure.
In this condition $x_A = 1$.

2.1.2. Solute

Define the standard states and the activity for the solute becomes more difficult because it is close to ideality when its molar fraction tends to a zero and not to a 1 as pure solute.
Considering a solute that deviates from the Henry's law, the chemical potential of the solute in real solutions is defined as

$$\mu_B = \mu_B^\circ + RTln(a_B) \quad (2.27)$$

The deviations from ideality are considering in the activity, while the standard state remains unchanged compared the solute that follows the Henry's law. The activity of the solute is defined as:

$$a_B = \frac{p_B}{K_B} = \gamma_B x_B \quad (2.28)$$

Introducing the activity coefficient, all the deviations from ideality are content in it.
The solute follows the Henry's law when its concentration goes to zero, therefore:

$$a_B \to x_B \quad ; \quad \gamma_B \to 1 \ as \ x_B \to 0 \quad (2.29)$$

This is true at all pressures and temperatures.
Instead of molar fraction, compositions are often expressed in molalities, *b*; therefore, we can rewrite the equation 2.29 as:

$$a_B \to b_B \quad ; \quad \gamma_B \to 1 \ as \ b_B \to 0 \quad (2.30)$$

2.1.3. Ion in solution

Special attention is required for the activities of ions in solution due to the strong interactions that arise between them. In fact, the approximation of the activities to molalities is valid only for very diluted solutions, in which the total amount of ions has to be less than 10^{-3} mol kg^{-1}.
Indicating μ_+ the chemical potential of a cation M^+ and μ_- the chemical potential of an anion Y^-, in an electrically neutral solution, where ν^+ is the stoichiometric coefficient of the cation and ν^- is the stoichiometric coefficient of the anion, the molar Gibbs energy of the ions, is

$$\begin{aligned} G_m = \nu^+\mu_+ + \nu^-\mu_- &= \nu^+\mu_+^{ideal} + \nu^-\mu_-^{ideal} + \nu^+ RTln(\gamma_+\chi_+) + \nu^- RTln(\gamma_-\chi_-) \\ &= \nu^+\mu_+^{ideal} + \nu^-\mu_-^{ideal} + RTln\left({\gamma_+}^{\nu^+}{\gamma_-}^{\nu^-}{\chi_+}^{\nu^+}{\chi_-}^{\nu^-}\right) \quad (2.31) \end{aligned}$$

Once again, all the deviations from ideality are contained in the last term. Since there is no experiment able to separate the parameter $\gamma_+\gamma_-$ into contributions from the cations and the anions, scientists have decided to assign it equally to both kinds of ions. Hence, the mean activity coefficient can be introduced, defined as the geometric mean of the activity coefficients

$$\gamma_\pm = \left({\gamma_+}^{\nu^+}{\gamma_-}^{\nu^+}\right)^{1/\nu} \quad (2.32)$$

Where ν is the sum of the stoichiometric coefficients.
Therefore, for each ion, the chemical potential becomes

$$\mu_i = \mu_i^{ideal} + RTln(\gamma_\pm\chi_i) \quad (2.33)$$

In the 1923, Peter Debye and Erich Hückel elaborated a theory which still provides theoretical expression for the mean ionic activity coefficients in electrolyte solutions.

The theory assumes that electrolytes in solution were fully dissociated and that nonideal behavior arise because of electrostatic interactions between ions. It also assumes that ions are spherically symmetrical, unpolarizable charges, which means that the ion is a simple charge with no possibility for displacement of the charge in presence of an electric field.

At the same time, the solvent is considered as a structureless, continuous medium. Hence, solvent-solvent interactions, ion-solvent interactions and polarizability of the solvent are not considered.

Debye-Hückel model also introduces the concept of ionic atmosphere associated to every ion. This region is a spherical area around a central ion which is filled by the opposite ions. The charge of the central ion is therefore balanced by the charge on the ionic atmosphere. Although the ions which composed the ionic atmosphere are discrete charges, the ionic atmosphere is treated as a cloud of charge whose charge density changes throughout the solution.

The Coulombic potential at a distance r from an ion of charge $z_i e$ is:

$$\phi_i = \left(\frac{z_i e}{4\pi\varepsilon_0}\right)\left(\frac{1}{r}\right) \quad (2.34)$$

This is the potential due to an isolated ion in a vacuum, where ε_0 is the electric permittivity in vacuum. In solution, two modifications are needed. First, the solvent decreases the strength of the potential:

$$\phi_i = \left(\frac{z_i e}{4\pi\varepsilon}\right)\left(\frac{1}{r}\right) \quad (2.35)$$

Where ε is the electric permittivity which is usually expressed as

$$\varepsilon = \varepsilon_0 \varepsilon_r \quad (2.36)$$

ε_r is the relative permittivity or dielectric constant. Since $\varepsilon_r > 1$, the potential is reduced from its vacuum value. This reduction is very important in several solvents, such as water: the Coulombic interactions are so strongly reduced by the solvent that ions interact only weakly with each other and do not aggregate into a crystal.

The second modification of the potential is due to the ionic atmosphere: if we consider an imaginary probe which is measuring the potential near an ion, it will enter the weak, oppositely charged ionic atmosphere as it moves away from the central ion. Therefore, the potential decreases more rapidly than is predicted by equation 2.35. The central ion is "shielded" by the atmosphere. Hence, the appropriate potential is the "shielded Coulombic potential", defined as

$$\phi_i = \left(\frac{z_i e}{4\pi\varepsilon}\right)\left(\frac{1}{r}\right) e^{-r/r_D} \quad (2.37)$$

Where r_D is called the "shielding length" or the "Debye length"

$$r_D = \frac{\varepsilon RT}{2\rho F^2 Ib} \quad (2.38)$$

Where ρ is the charge density around the central ion, F is the Faraday constant, I is the ionic strength and b the molality of the solution.

The ionic strength is defined as

$$I = \frac{1}{2}\frac{(b_+ z_+^2 + b_- z_-^2)}{b} \quad (2.39)$$

Where b_+ and b_- are the molality of cation and anion, respectively, while z_+ and z_- their charges.

The chemical potential of any central ion is lowered due to its electrostatic interaction with its ionic atmosphere. This lowering of energy can be identified as the difference between the ideal free energy and the observed free energy, and therefore is expressed by the activity coefficient.

$$\ln(\gamma_\pm) = -|\nu^+ z_+ \nu^- z_-| \frac{F^2}{8\pi\varepsilon r_D N_A RT} \quad (2.40)$$

$$\log(\gamma_\pm) = -1.825 \times 10^6 \, |\nu^+ z_+ \nu^- z_-| \left\{ I \left(\frac{\rho}{\varepsilon^3 T^3} \right) \right\}^{\frac{1}{2}} = -A|\nu^+ z_+ \nu^- z_-| \, I^{\frac{1}{2}} \quad (2.41)$$

Where $\nu^+\nu^-$are the stoichiometric coefficients of anion and cations as said before, and N_A is the Avogadro constant.

Equations 2.41 and 2.40 are the expressions of the limiting law of the Debye Hückel theory.

If the approximation of negligible ion size is removed and considering an ionic radius r_i, the shielded Coulombic potential takes the form:

$$\phi_i = \left(\frac{z_i e}{4\pi\varepsilon}\right)\left(\frac{1}{r}\right)\left(\frac{1}{1+\frac{r_i}{r_D}}\right) e^{-\frac{(r-r_i)}{r_D}} = \left(\frac{A'}{r}\right) e^{-\frac{(r-r_i)}{r_D}} \quad (2.42)$$

Where *A'* is independent of *r* and it is:

$$A' = \left(\frac{z_i e}{4\pi\varepsilon}\right)\left(\frac{1}{1+\frac{r_i}{r_D}}\right) \quad (2.43)$$

Therefore, equation 2.41 can be manipulated and led to equation 2.44:

$$\log(\gamma_\pm) = -|\nu^+ z_+ \nu^- z_-| \left\{ \frac{A}{1+\frac{r_I}{r_D}} \right\} \sqrt{I} \quad (2.44)$$

When the solution is very dilute, the denominator in equation 2.44 is almost unity, obtaining the limiting law. The criterion is $r_i/r_D \ll 1$, which is equivalent to assuming that the ions have negligible size.

When the concentration rises to the point where r_i is small but no longer negligible in comparison with r_D the approximation $(1+x)^{-1} \approx 1-x$ leads to the "extended Debye-Hückel law:

$$\log(\gamma_{\pm}) = -|\nu^{+}z_{+}\nu^{-}z_{-}|A\sqrt{I} + AA^{*}|\nu^{+}z_{+}\nu^{-}z_{-}|I \quad (2.45)$$

Where A^{*} is another constant.

The extended law predicts the deviations from the limiting law which correspond to an increase in the activity coefficient. This equation accounts for some activity coefficients over a moderate range of dilute solutions[184]; nevertheless it remains very poor for molalities closer to 1 mol kg^{-1}.

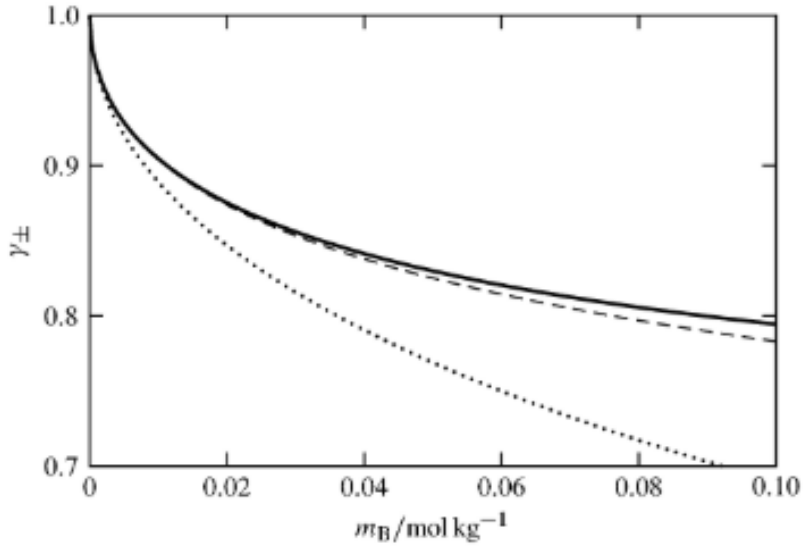

Figure 2.2. Mean ionic activity coefficient of aqueous HCl at 25∘C25∘C. Solid curve: experiment (Herbert S. Harned and Benton B. Owen, The Physical Chemistry of Electrolytic Solutions*, 3rd edition, Reinhold, New York, 1958, Table 11-5-1); dashed curve: Debye–Hückel theory; dotted curve: Debye–Hückel limiting law.*

2.1.4. Colligative properties

Colligative properties depend on the number of molecules of solute dissolved in the solvent. These properties are the elevation of boiling point, the lowering of vapor pressure, the depression of freezing point and the increasing of the osmotic pressure.

Assuming that the solute is not volatile, the heterogeneous equilibrium between the solvent and the solution at 1 atm has to be considered in order to discuss the boiling point elevation.

At a certain temperature

$$\mu_A^{*}(g) = \mu_A^{*}(l) + RTln\,(x_A) \quad (2.46)$$

This equation can be rearranged in

$$ln(x_A) = \frac{\mu_A^{*}(g) - \mu_A^{*}(l)}{RT} = \frac{\Delta G_{vap}}{RT} \quad (2.47)$$

Where ΔG_{vap} is the Gibbs free energy of vaporization of the pure solvent.

Differentiating both sides of the equation 2.47 respect to temperature, it can be written:

$$\frac{d\ln(x_A)}{dT} = \frac{1}{R}\frac{d(\frac{\Delta G_{vap}}{T})}{dT} = -\frac{\Delta H_{vap}}{RT^2} \quad (2.48)$$

Integrating:

$$\int_0^{\ln x_A} d\,ln(x_A) = -\frac{1}{R}\int_{T^*}^{T}\frac{\Delta H_{vap}}{T^2}dT \quad (2.49)$$

Where T^* is the boiling point of pure solvent *A*. The integration limit of the first integral are $x_A = 1$, ($ln(x_A) = 0$) to x_A, when the boiling point is *T*. Assuming that the enthalpy of vaporization is a constant over the small range of temperatures involved, equation 2.49 becomes:

$$\ln(1 - x_B) = \frac{\Delta H_{vap}}{R}\left(\frac{1}{T} - \frac{1}{T^*}\right) \quad (2.50)$$

Considering a diluted solution, where $x_B << 1$, and $T \approx T^*$:

$$x_B = \frac{\Delta H_{vap}}{R}\left(\frac{1}{T} - \frac{1}{T^*}\right) = \frac{\Delta H_{vap}}{R}\frac{\Delta T}{T^{*2}} \quad (2.51)$$

ΔT is the boiling point elevation and it is equal to the difference between the boiling point of the solution and the boiling point of the pure solvent. It can also be expressed as

$$\Delta T = K x_B \quad (2.52)$$

Where *K* is

$$K = \frac{RT^{*2}}{\Delta H_{vap}} \quad (2.53)$$

2.2. Electrochemistry: thermodynamic and some kinetic concepts[186]

2.2.1. Electrochemical potential, Nernst potential

The energy of an ion depends not only on chemical forces, but also on the electrostatic field. Therefore, a new physical quantity, which takes into account both the contributes, must be introduced:

$$\mu_i^{el} = \mu_i + z_i F\varphi \quad (2.54)$$

Where μ_i^{el} is the electrochemical potential of the specie *i*, *F* is the Faraday's constant, φ is the electrostatic potential of the phase containing the ion and *z* is the charge of the ion which can be positive or negative for cations and anions, respectively. The term $z_i F\varphi$ is the electrostatic potential energy of the ion.

Equation 2.54 assumes that a concentration change will affect only the chemical potential while a potential change will affect only the electrostatic potential. Actually, a potential change involves a change in the amount of charge in the electric double layer implying changes in the concentration of ions in the bulk. However, in diluted solutions, the concentration variation associated to the potential change is very limited that could be consider constant.

Before to continue with the thermodynamic discussion, the concept of electrochemical cell should be introduced.

An electrochemical cell is a system in which a redox process takes place. It is composed by an ionic conductor (named electrolyte) which could be liquid, solid or a gel, that separates two electron conductors (electrode), which in general are metals or semiconductors.

When the redox process takes place spontaneously, the electrochemical cell is also called galvanic cell, and the spontaneous redox process released electrical energy.

When the electrolyte is in contact with the electrode, a potential difference, $\Delta\varphi^{M,E}$, at the interface arises

$$\Delta\varphi^{M,E} = \varphi^M - \varphi^E \quad (2.55)$$

where φ^M and φ^E are the inner potential of the two phases.

The inner potential characterizes the electrical state of any phase and it is defined as the sum of the external, outer potential induced by free electrostatic charges of the phase, ψ, and the surface potential, χ:

$$\varphi^M = \chi^M + \psi^M \quad (2.56)$$

In equilibrium conditions of the charged species at the interface between electrode and electrolyte, their electrochemical potentials are the same

$$\sum_i \tilde{\mu}_i = 0 \quad (2.57)$$

Therefore, the potential difference at the equilibrium is

$$\Delta\varphi^{M,E} = \Delta\Psi = -\frac{\Delta\mu}{zF} \quad (2.58)$$

Equation 2.58 means that the potential difference depends only on the nature of the two phases; specifically, by the difference of the chemical potential of all the species involved at the interface metal/electrolyte.

The transition of electrons or ions across the interface is possible only in connection with an electrode reaction in which other species may also be involved.

The current produced by a galvanic cell is the result of a spontaneous redox reaction and can be utilized to do electrical work. At constant temperature and pressure, the maximum non-expansion work that the cell can do is given by the Gibbs free energy of the spontaneous reaction in the cell. When the reaction advances by an infinitesimal amount $d\xi$ (ξ is the extent of reaction: it has the dimension of amount of substances.

When the extent of reaction changes by a finite amount $\Delta\xi$, the amount of a reagent *A* changes from n_A to n_A-$\Delta\xi$ while the product *B* changes from n_B to $n_B + \Delta\xi$):

$$dG = \sum_i \mu_i dn_i = \sum_i \mu_i \nu_i d\xi = \Delta_r G \, d\xi \quad (2.59)$$

Where $\Delta_r G$ is the Gibbs free energy of the reaction and υ is the stoichiometric coefficient.

The maximum non-expansion work, the electrical work, which the reaction can do as it advances by $d\xi$ is therefore

$$dw_e = \Delta_r G \, d\xi \quad (2.60)$$

at constant pressure, temperature, and composition.

When the reaction advances by $d\xi$, $\upsilon d\xi$ electrons move from the anode to the cathode. The total charge per mole of electrons is -$\upsilon e N_A d\xi$ (where *e* is the elementary charge, N_A is the Avogadro number and ν is the stoichiometric coefficient of the electrons).

Knowing that the Faradaic constant is expressed

$$eN_A = F \quad (2.61)$$

The work done by the electrons is

$$dw_e = EMF = -\vartheta F E d\xi \quad (2.62)$$

Where *EMF* is the Electromotive force.

Equation 2.62 and equation 2.60 must be equal, therefore:

$$\Delta_r G = -\vartheta F E \quad (2.63)$$

This equation shows the connection between electrical measurements and thermodynamic properties. For a generic redox reaction

$$Ox + \nu e^- \rightleftarrows Red \quad (2.64)$$

The potential of the electrode on which this reaction happens is

$$E_{eq} = -\frac{\Delta_r G}{\nu F} = -\frac{\Delta_r G^0}{\nu F} - \frac{RT}{\nu F}\ln\left(\frac{{a_{red}}^{\nu_{red}}}{{a_{ox}}^{\nu_{ox}}}\right) = E^0 - \frac{RT}{\vartheta F}\ln\left(\frac{{a_{red}}^{\nu_{red}}}{{a_{ox}}^{\nu_{ox}}}\right) \quad (2.65)$$

Where E^0 is the so-called standard potential and the equation is named *Nernst equation*.
Considering an electrochemical cell, as the one reported in Figure 2.3, composed by two electrodes, one of copper and one of platinum, dipped in a solution of copper sulfate, $CuSO_4$, and oxygen, which is bubbled on the surface of platinum electrode, the spontaneous electrochemical reactions which take place on the two electrodes are (written in the sense of the reduction, as the convention requires):

$$(-)\ Cu^{2+} + 2e^- \rightleftarrows Cu \quad (2.66)$$

$$(+)\ O_2 + 2H_2O + 4e^- \rightleftarrows 4OH^- \quad (2.67)$$

While the total reaction of the electrochemical cell is:

$$O_2 + 2H_2O + 2Cu \rightleftarrows 2Cu^{2+} + 4OH^- \quad (2.68)$$

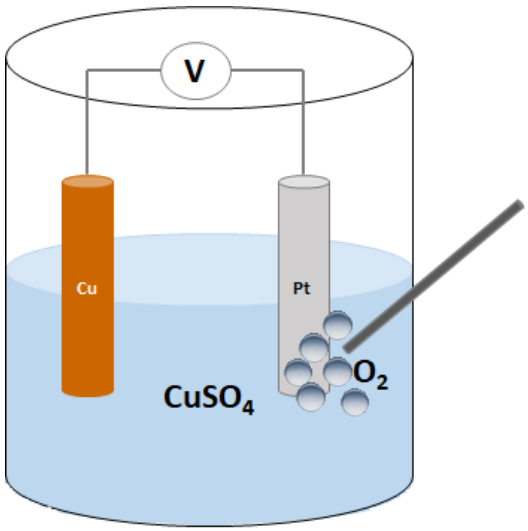

Figure 2.3. Electrochemical cell based on copper and platinum electrodes dipped in a water solution of copper sulfate. Oxygen is bubbled on the surface of platinum electrode.

Where (-) indicates the negative pole and (+) indicates the positive pole. In a galvanic cell, the negative pole is also called anode, and on its surface, the oxidation reaction takes place. Vice versa,

on the positive pole, named cathode, the reduction process happens. Since the two reactions are independent, it is possible to think to separate the cell, and also the potential, in two separated part, called "half-cell".

The electrochemical cell can be schematized by means the Galvani representation: a scheme of the cell, where the phases are reported separated by slashes. It starts from the electrode attached to the negative pole.

$$Cu|Cu|CuSO_4\ (H_2O)\big|O_{2\ (g)}Pt\big|Cu \quad (2.69)$$

In this representation, the circuit is always starting and ending with the same metal which represents the contact of the cell to the voltmeter.

The Nernst potential of this electrochemical cell is the difference between the potential of the cathode minus the anode potential:

$$E_{eq} = E_+ - E_- = E_+^0 - E_-^0 + \frac{RT}{4F} ln\left(\frac{a_{O_2} a_{H_2O}^2}{a_{OH^-}^4}\right) - \frac{RT}{4F} ln\left(\frac{a_{Cu^{2+}}^2}{a_{Cu}^2}\right)$$

$$= E_+^0 - E_-^0 + \frac{RT}{4F} ln\left(\frac{1}{a_{OH^-}^4\ a_{Cu^{2+}}^2}\right) \quad (2.70)$$

The activity of water, which is the solvent and therefore in high amount, oxygen, which is pure gas, and copper, which is in the solid state, are equal to one, hence they can be neglected. Therefore, the potential of this cell depends only on the activity of copper ions and hydroxyl ions.

It is physically impossible to measure the potential of a single electrode: only the difference between the potentials of two different half-cells can be measured.

In order to determinate the half-cell voltage, the scientific community have chosen as standard the so-called Standard Hydrogen Electrode (SHE) and defined its potential exactly to 0V. It consists in a platinum wire placed in a 1.0 M strong acid solution, like HCl, and hydrogen is bubbled on its surface at a pressure of 1 atm, at 25°C. Thus, the half reaction at this electrode is:

$$2H^+ + 2e^- \rightleftarrows H_2 \quad (2.71)$$

In this way, all the standard potentials of the half-cells (in the sense of the reduction reaction) are measured and reported in literature versus SHE electrode, connecting SHE at the negative pole of the circuit, as indicted by IUPAC.

2.2.2. Liquid junction potential, Donnan potential, Membrane potential

A potential develops at any interface or junction, where there is a separation of charge. The potential difference between two electrolytes separated by a boundary, such as a membrane or salt bridge, is called liquid junction potential. This potential difference is related to the different mobility of the ions in the electrolyte.

For example, considering two solutions of the same electrolyte, HCl, but with different concentrations, separated by an interface, at the junction there is a steep concentration gradient in H^+ and Cl^- hence both ions tend to move from the concentrated compartment to the diluted one. Hydrogen ions move faster than chloride ions, therefore they penetrate the dilute phase at a higher rate. This process leads to a positive charge in the diluted phase and a negative one in the concentrated phase, resulting in a potential difference. The corresponding electric field then retards the movement of other hydrogen ions and speeds up the diffusion of chlorides until the two cross the boundary at equal rates. This means that there is a steady-state potential, which is not related to an equilibrium process and it is called diffusion potential.

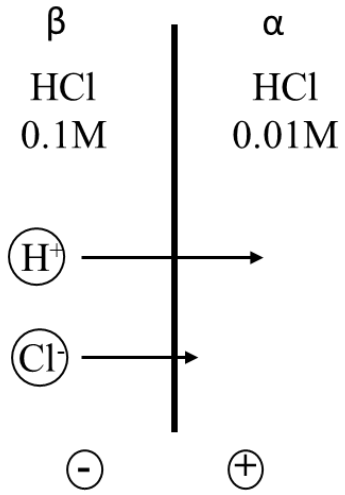

Figure 2.4. Interface between two water solutions of HCl at different concentration.

To determine the junction potential, it is essential introduced the transport number, *t*, which is related to the kinetic transport:

$$t_i = \frac{|z_i|\mu_i C_i}{\sum_j |z_j|\mu_j C_j} \quad (2.72)$$

Where *z* is the charge of the ion, μ, its mobility, *C* the concentration.
The electrical mobility of an ion in an electric field, which is measured in $cm^2\ s^{-1}\ V^{-1}$, is determined by equation 2.73:

$$\mu_i = \frac{|z_i|e}{6\pi r_i \eta} \quad (2.73)$$

Where r_i is the hydrated radius of ion and η is the viscosity of the medium.
Therefore, the liquid junction potential is determined as

$$E_J = \left(\Phi^\beta - \Phi^\alpha\right) = (t_+ - t_-)\frac{RT}{F} ln \frac{a_\alpha}{a_\beta} \quad (2.74)$$

If the interface is a selective membrane, the junction potential is more complex.

The membrane has to be considered as composed by three different regions (Figure 2.5): the bulk of the membrane, *m*, where the selective ion is the only specie that can diffuse; two interfacial zones, *m'* and *m''*, in which selective ions are adsorbed on the membrane surface.

Ion	Mobility ($cm^2\ s^{-1}\ V^{-1}$)
H^+	3.625×10^{-3}
Li^+	4.010×10^{-4}
Na^+	5.193×10^{-4}
Cl^-	7.912×10^{-4}
Br^-	8.13×10^{-4}
I^-	7.96×10^{-4}

Table 2.1. Electrical mobility of several ions.

These adsorptions are in equilibrium; hence, the whole system comprises five phases and the overall potential difference across the membrane is the sum of the different contribution of the junctions.

$$E_m = \left(\Phi^{\alpha} - \Phi^{m'}\right) + \left(\Phi^{m\prime} - \Phi^{m}\right) + \left(\Phi^{m} - \Phi^{m''}\right) + \left(\Phi^{m''} - \Phi^{\beta}\right) \quad (2.75)$$

The first and last terms represents the potential difference related to the equilibrium balance of selective charge exchange across the interfaces and this condition is named "Donnan equilibrium", while the second and third terms refers to the junction potential within the membrane and the specific literature named it "diffusion potential".

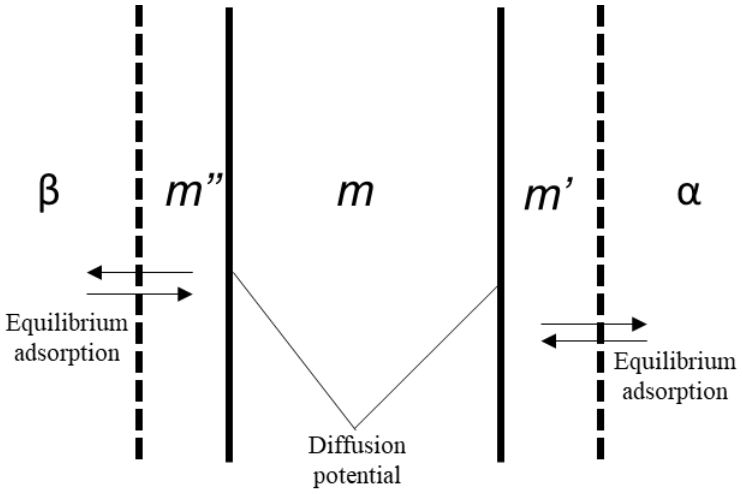

Figure 2.5. Interfaces and equilibriums formed between a membrane which separates two different solutions of the same salt but at different concentration.

The Donnan equilibrium is due to the different distribution of ions on the membrane surface: the presence of impermeant ion species on one side of the boundary leads to a difference in concentration of permeant ions on both sides of the boundary. These concentration differences lead to a potential difference across the membrane which can be compensated by an additional electric potential difference between the two solutions. At equilibrium, the electrochemical potentials of permeant ions in both the solutions are identical. Therefore, assuming equal standard chemical potentials, the electric potential difference is the Donnan potential.

2.3. Thermodynamic of distillation and heat conversion efficiency

2.3.1. Heat-to-electricity efficiency

The efficiency of a two stages device, which exploits a Salinity Gradient to convert Low Temperature Heat into electricity, can be divided in two different contributions: the efficiency of the "power stage" (which generally is an electrochemical cell, η_{el}) and the efficiency of the thermal separation (η_{dis}):

$$\eta = \eta_{dis}\eta_{el} \quad (2.76)$$

In the next sections these two parameters will be defined.

2.3.2. Thermodynamic of distillation

Here it is reported a synthetic derivation of the efficiencies for the specific scope of the present thesis; a more detailed discussion can be found in literature[187–189].

Considering a distillation process which is driven by a heat sources at temperature T_H, while the water solution that has to be distilled is at a temperature T_L, the temperature of the reservoir. The efficiency of the distillation is defined as:

$$\eta_{dis} = \frac{\Delta G}{Q_H} \quad (2.77)$$

Where ΔG is the increase free energy from the feed solution to the concentrated solution and pure solvent, determined at T_L, and Q_H is the heat adsorbed from the heat source.
From the first principle of thermodynamic:

$$Q_H - Q_L = \Delta H \quad (2.78)$$

Q_L is the heat released to the heat sink and ΔH is the enthalpy variation of the solutions induced by the distillation.
The second principle enounces that:

$$\Delta S + \Delta S_e \geq 0 \quad (2.79)$$

ΔS is the entropy variation of the solutions induced by distillation while ΔS_e is the entropy variation of the environment. This leads to:

$$-\frac{Q_H}{T_H} + \frac{Q_L}{T_L} > -\Delta S \quad (2.80)$$

Combining equation 2.78 and 2.80:

$$\left(1 - \frac{T_L}{T_H}\right) Q_H > \Delta H - T_L\, \Delta S \quad (2.81)$$

From the definition of ΔG ($\Delta G = \Delta H - T\Delta S$), at $T = T_L$:

$$\left(1 - \frac{T_L}{T_H}\right) Q_H = \Delta G \quad (2.82)$$

Combining equation 2.77 with equation 2.82, it can be written:

$$\eta_C = 1 - \frac{T_L}{T_H} \quad (2.83)$$

Equation 2.83 is known as Carnot law which says that all the heat engines have an efficiency lower than the Carnot heat engine, which efficiency could never be 100% because its value depends by the ratio of the temperature difference between the reservoirs and the heat source.
The second law efficiency, also called exergy efficiency or efficiency related to Carnot, is defined as:

$$\eta_{2nd-law} = \frac{\eta}{1 - \frac{T_L}{T_H}} \quad (2.84)$$

It represents the ratio between the efficiency and the efficiency of an ideal Carnot cycle.

Efficiency of a single-effect distiller

As reported at page 35, in a vacuum distiller, each effect is composed by the evaporation and condensation compartments. In the evaporation side, the solution is heated by the heat source until the solvent boils while in the condenser side, the steam is cooled down by dissipating heat to the heat sink. The pressure inside the effect is determined by the gas-liquid equilibria of the solution and the pure solvent at the temperature of the two chambers because all the air and other gases are removed from the vessels. In particular, the pressure in the vacuum distillation is lower than 1 atm in order to condense the pure solvent around the room temperature.
Considering that no mechanical work is performed by the vapor, assumptions almost met in real distillation unit, the limiting temperatures for T_H and T_L are:

$$T_H \geq T_{BP}(X_{max}) \quad (2.85)$$

$$T_L \leq T_{BP,w} \quad (2.86)$$

Where T_{BP} is the boiling point of the solution at a molar fraction X; X_{max} represents the maximum of the molar fraction that is reached during the distillation, usually also corresponding to the maximum boiling point elevation, and $T_{BP,W}$ is the boiling point of the pure solvent (tin this study it is water).
Therefore, the efficiency of the single effect can be written as follow:

$$\eta_{single\ effect} \leq 1 - \frac{T_{BP,W}}{T_{BP}(X_{max})} \quad (2.87)$$

Equation 2.87 does not depend on the temperature of the available heat source, nor on the realization of the distillation unit. Hence, the efficiency of the whole process cannot be increased by suppling heat at a larger temperature, unless it is possible to increase the boiling point temperature of the solution.

Efficiency of a multi-effect distiller

In a multi-effect distiller, the heat released in an effect, is used in the subsequent one, so that the same amount of heat is used more than one time. The pressure P^n inside the effect decreases with n: in this way, the boiling temperature of the fluid matches the temperature of the heat exchanger.
Calling T_H^n and T_L^n the temperature in the n-effect of the heat-exchange fluid in the evaporation and condensation respectively, $T_L^n = T_H^{n+1}$, the temperatures of the effect are defined as:

$$T_H^n = T_{BP}(X_{max}, P^n) + \Delta T_{HE} \quad (2.88)$$

$$T_L^n = T_{BP,W}(P^n) - \Delta T_{HE} \quad (2.89)$$

ΔT_{HE} is a temperature difference between the heat exchange fluid and the boiling/condensation temperature. This temperature difference must be a non-vanishing temperature difference in practical devices, in order to have a substantial heat flow without the need of huge heat exchangers.
Considering N effects:

$$T_H - T_L = 2N\Delta T + N\Delta T_{BP} \quad (2.90)$$

Where ΔT_{BP} is the boiling point elevation, which is kept constant, not changing with the pressure of the effect. In order to increase the boiling point elevation, the solute concentration (X_{max}) has to be increased; however, defined solute and solvent, there is a maximum value of concentration of salt that can be dissolved, which is defined by its solubility. Therefore, there is also a maximum boiling point elevation, ΔT_{BP}^{max}.
The maximum efficiency of the multi-effect distiller can be calculated from equation 2.87 and 2.90:

$$\eta_{multi-effec} < \eta_{multi-effect}^{max} = \frac{N\Delta T_{BP}}{T} \quad (2.91)$$

Where T is the approximation of the values T_L^n.
In general, a larger number of effects is helpful only with a smaller boiling point elevation. However, it always leads to a smaller efficiency compared to a single-effect distiller.

Evaluation of the voltage of the electrochemical cell which exploits salinity gradient energy

The cell voltage of an electrochemical cell which produces electricity at the expenses of the mixing free energy of two water solutions can also be evaluated by using only thermo-physical parameters.
Assuming that n_w molecules of solvent require an amount Q_H of heat to be evaporated:

$$Q_H = n_w \Lambda \quad (2.92)$$

Where Λ is the latent heat of evaporation of the solvent. Therefore, the free energy of the process is:

$$\Delta G = n_w \Lambda \left(1 - \frac{T_{BP,W}}{T_{BP}(X_{max})}\right) \quad (2.93)$$

During the discharge of the electrochemical cell, n_s moles of solute pass from the more concentrated solution to the diluted one, until their concentrations become equal to X_f:

$$n_s = \frac{X_f}{1 - X_f} n \quad (2.94)$$

Assuming also that the passage of n moles of electrons through the cell leads to the transfer of 1 mole of salt, the produced electrical work, W, is thus:

$$W = nF\Delta V n_s \quad (2.95)$$

Where ΔV is the voltage of the cell averaged on the charge.
Ideally, the work produced by the cell is ΔG, hence, from equation 2.95 and 2.93, it results:

$$\Delta V = \frac{1}{nF} \frac{1 - X_f}{X_f} \Lambda \left(1 - \frac{T_{BP,W}}{T_{BP}(X_{max})}\right) \quad (2.96)$$

Equation 2.96 means that a high boiling point elevation does not only increase the efficiency of the distillation process, but it also leads to a higher cell voltage which is an important parameter in order to have good electrical performances.
Further, a large latent heat of vaporization is also useful, because increases the available free energy.

CHAPTER 3

Materials and Methods

3.1. Thermally Regenerable Redox-Flow Battery based on NaI

3.1.1. Experimental setup

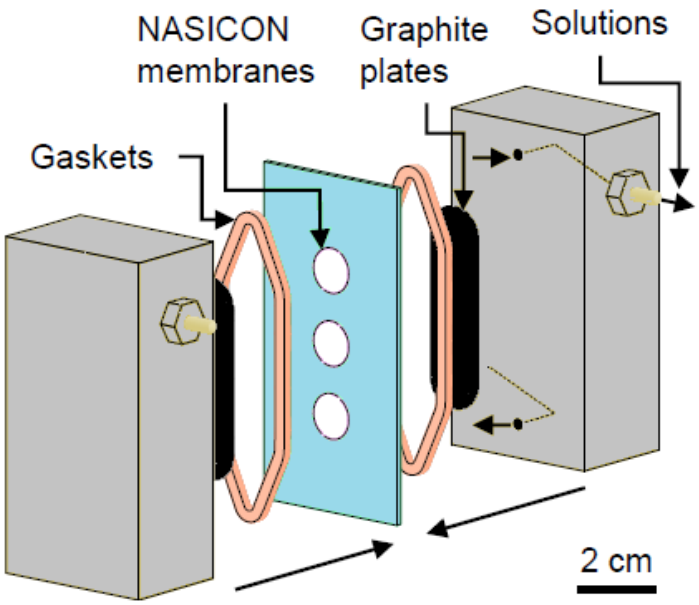

Figure 3.1. Scheme of the electrochemical part of the TRB-NaI device.

The electrochemical cell of the Thermally Regenerable Redox-Flow Battery (TRB) based on NaI is composed by two graphite plates as electrodes separated by three NASICON membranes which are sealed with silicone glue (*Silicoset 158, ACC*) in a rectangular frame, made of 1 mm-thick polycarbonate. The holder has three holes, with diameter of 10 mm, in which the NASICON membranes are placed. The exposed parts of the diaphragms have a diameter of 8 mm resulting in a total surface of 1.5 cm^2.

An eye-shaped gasket, made of silicone rubber (*Viton*®, thickness = 0.1 mm), is located on each side of the frame to form a channel for the passage of solution.

All these parts have kept together by two final plates made of PTFE (polytetrafluoroethylene).

A platinum wire, (diameter = 0.35 mm), is used as electrical contact, passing through the PTFE plate itself. There are hole on this plates to pump the solutions through the cell.

The solutions are heated at approximately at 90°C before entering in the electrochemical cell in order to heat the NASICON membranes and reduce their electrical resistance.

The heat process is released by means a tube-and-shell heat exchanger. For each solution flow, the "tube" of the heat exchanger is composed by a sequence of four 10 cm-long glass capillaries with outer diameter of 1 mm and wall thickness of 100 µm. The capillaries are connected in series by

means of tubes, 1.52 mm-diameter, made of fluoropolymereleastomer (*Fluran HCA, Ismatec*). The capillaries are placed into the shell made by a stainless tube where the heat exchanger fluid flows. This fluid consists in a mixture of glycerol and water 1:1 in volume. The heat exchanger fluid is kept at 100°C in a thermostatic bath (*ECO RE 415, Lauda*) and continuously re-circulated through the shell of the heat exchanger. The temperature inside the electrochemical cell, measured by a thermistor inserted into the cell, is 90°C.

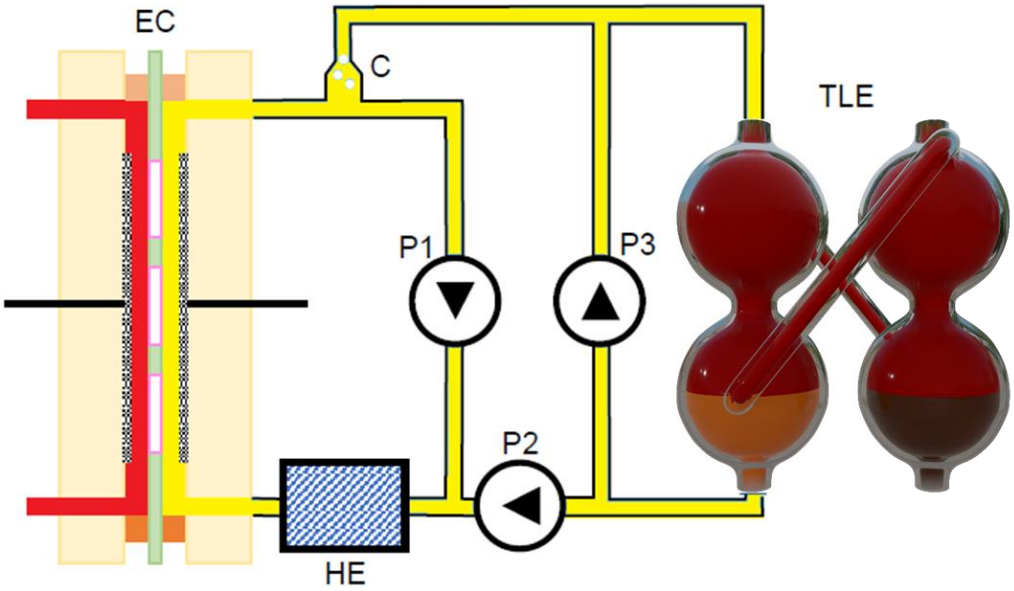

Figure 3.2. Scheme of the hydraulic circuit for one of the solutions. EC is the electrochemical cell, TLE is the through liquid exchanger, C is the connector between EC and TLE, HE is the heat exchanger and P1, P2, P3 are the peristaltic pumps. The hydraulic circuit of the second solution is equivalent.

The whole hydraulic circuit of the experimental setup is composed by two identical sections for the two solutions; one of the two sections is schematically shown in Figure 3.2.

The pump **P1** provides the recirculation of the solution through the electrochemical cell. The solution passes through the tube-and-shell heat exchanger **HE**, which is fed with a mixture of water/glycerol 1:1 in volume at 100°C. **HE** is placed before the inlet of the cell in order to stabilize the temperature inside the electrochemical cell. The pump **P3** allows the recirculation through the **TLE**. A slower exchange of the solution between the circuit of the electrochemical cell and the circuit of **TLE** is provided by the pump **P2**. The exchange circuit is closed by the connection **C**, which also provides a way for removing air from the electrochemical cell at starting time.

All the pumps are channels mounted on the same peristaltic pump head (*Ecoline VC-MS/CA 4-12, Ismatec*), with six rollers rotating at 35 rpm. The tubes are made of thermoplastic polypropylene (*PharMed Ismaprene, Ismatec)* able to work at elevated temperatures. The inner tube diameters are 2.79 mm for pumps P1 and P3 and 0.89 mm for pump P2, in order to provide flows of 13 mL min^{-1} and 2mL min^{-1}, respectively. In this way, it is possible to control separately the recirculation in the electrochemical cell, in the TLE and the exchange between them. All other tubes are made of fluorpolymerelastomer (*Fluran HCA, Ismatec*), with 1.52 mm diameter.

The whole hydraulic circuit is completely filled by using 6 mL of each solution.

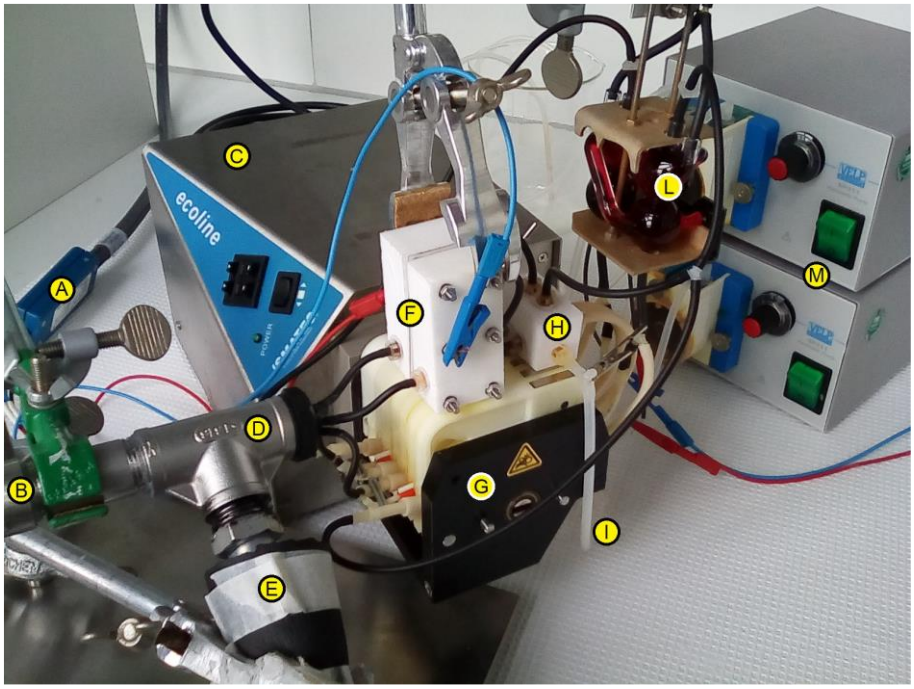

Figure 3.3. Picture of the whole TRB composed by the electrochemical cell, TLE and all the hydraulic circuit.

The complete hydraulic circuit is reported in the Figure 3.3 where the multichannel peristaltic pump is indicated with the letters **G,** which is the head of the pump with six channels and **C** which is the pump driver. With the letter **F** it is indicated the electrochemical cell which is connected to the potentiostat through the cable **A**. Two channels of the pump are used to recirculate the solutions in the electrochemical cell, while other two channels are used for recirculating the solutions in the through-liquid exchanger (TLE) (**L**).

The last two channels exchange the solutions between the electrochemical cell circuit and the TLE exchanger circuit passing through the connection **H.** Two tubes (one is visible in the Figure 3.3 and it is named **I**) are connected to the peristaltic pump **M**, used for the evacuation of the system. **D** is the heater described before: the shell-and-tubes heat exchanger. The shell is connected to an inlet **E** and an outlet **B** for the recirculation of the heat exchange fluid kept at 100°C by a thermostatic bath, not shown in the figure.

3.1.2. Materials

Concentrated (H) and diluted (L) aqueous solutions of NaI (*>99.55, VWR chemicals*) are prepared with a molar fraction of 17.5% and 1.75%, respectively. I_2 (*99%, Alfa Aesar*) is added in order to reach a concentration of 100 mM and 10 mM, respectively. At these concentrations, the chemical potentials of iodine are similar in the two solutions H and L because most of iodine is complexed to form I_3^-.

A solution of I_2 mM in toluene (*99.8%, Sigma Aldrich*) is used to fill the "Through-liquid exchanger".

The preparation of NASICON follows the procedure outlined in the CRC Handbook of Chemistry and Physics[190,191]. The precursors are Na_3PO_4 $10H_2O$ (*>89%, Sigma Aldrich*), ZrO_2 (*5mm powder, >99%, Sigma Aldrich*), SiO_2 (*0.5-10mm powder, >99%, Sigma Aldrich*) and Camphor (*>95%, Sigma Aldrich*).

The other NASICON synthesis requires other precursors which are: Na_2CO_3 (*>99%, Sigma Aldrich*), $NH_4H_2PO_4$ (*>98%, Sigma Aldrich*), $(ZrO_2)_{0.97}(Y_2O_3)_{0.03}$ (*Sigma Aldrich*), La_2O_3 (*>99.9%, Sigma Aldrich*).

3.1.2.1. NASICON preparation

NASICON diaphragm, with composition $Na_3Zr_2Si_2PO_{12}$, is used as "membrane" in the device.

Starting from sodium phosphate $Na_3PO_4 \cdot 10H_2O$, zirconia ZrO_2 and silica SiO_2 batches of approximately 1 g are prepared by mixing the chemicals in stoichiometric amounts[190]. The powder is dried at 120°C overnight. Camphor is added (1.5% in weight) and the powder is manually ground in an agate mortar, in presence of ethanol. The grinding is carried on until all ethanol evaporates. Approximately 330 mg of powder is pressed in a cylindrical steal cast with diameter of 1 cm, with a force of 4.5 metric tons. The resulting pellets are approximately 1.5 mm thick. The pellets are then thermally treated in a furnace, following the temperature program shown in Figure 3.4.

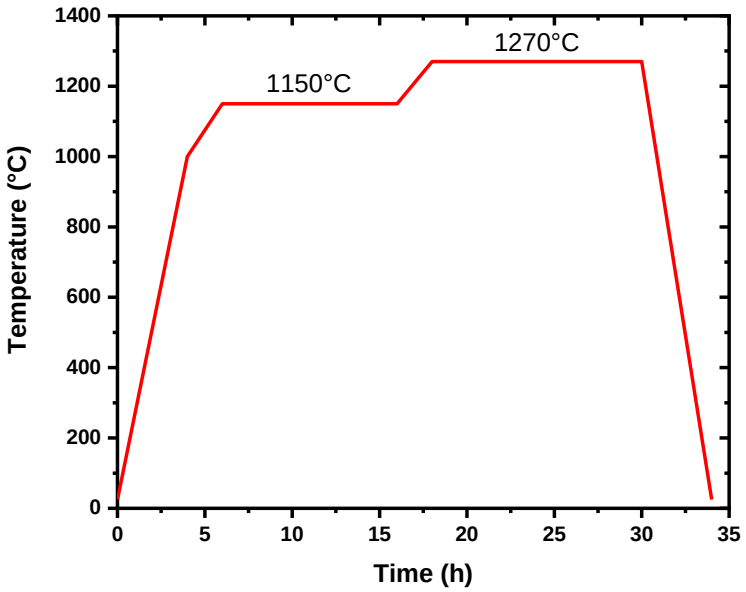

Figure 3.4. Heat treatment to produce NASICON pellets.

The first plateau of the temperature treatment, at 1150°C, leads to the solid-state synthesis, while the second plateau at 1270°C performs the sintering. Above this temperature the material decomposes in zirconia. It is important to notice that the material decomposes also if the temperature is brought to 1270°C without the step at 1150°C.

After the sintering, the diameter of the pellets decreases to nearly 9 mm. The pellets are then grinded to 0.5 mm thick only from one side, preserving the impermeable surface of the opposite side.

Other two NASICON syntheses have been followed starting from two different batches of reactants:

A) $SiO_2, Na_3PO_4 \cdot 12H_2O, ZrO_2$

B) $Na_2CO_3, ZrO_2, NH_4H_2PO_4, SiO_2$

In both the cases, a stoichiometric amount of powders, nearly 1g per synthesis, is used.

The powders have been finely ground and calcinated under different working conditions:

1)1100°C, 8h, 3°C min^{-1};

2) 1150°C, 8h, 3°C min^{-1};

3) 1150 °C, 15h, 3°C min^{-1};

4) 1150°C, 6h, 3°C min^{-1};

5) 1150°C, 6h, 5°C min^{-1}.

From the resulting powder of the batch B, after the thermal treatment number 5, it was produced a pellet (20 mm diameter and 0.5 mm thick) which has been sintered at 900°C for 2 hours.

3.1.2.2. NASICON characterization

Structural characterization: X-ray diffraction

Experimental patterns are collected on a Rigaku Miniflex 600 equipped with a Cu source (1.54 Å). Every spectrum is recorded from 10 to 80° with a step rate of 1° min^{-1} using a quartz sample holder.

Morphological characterization: Scanning Electron Microscope

Scanning electron microscope (SEM) and energy dispersive microanalysis (EDS) are performed using a Zeiss Gemini 500 instrument in a high-vacuum configuration. A field emission source is used as electron source and the electrons are accelerated using an electric potential around 5-10kV.

Perm-selectivity

Perm-selectivity is evaluated in an electrochemical cell with two Ag/AgCl electrodes dipped in two sodium chloride solutions at different concentrations, 1 M and 0.5 M respectively, using the NASICON diaphragm that has to be tested, as electrolyte (Figure 3.5). The cell voltage of this cell would be 111 mV if the membrane is perfectly perm-selective. In the absence of perm-selectivity, the voltage decreases to one and half, 55mV.

Permeability

To evaluate the permeability of sintered NASICON membranes, a device, like the one schematizes in Figure 3.6 is used.

NASICON membrane is clamped between two O-rings becoming a wall of the chamber. Air is compressed in this chamber by means a syringe, while the pressure inside the chamber is monitored by a pressure gauge.

Starting from a syringe with 10 mL of air, by manual compression, it was decreased to 5 mL, resulting in an increasing of the pressure up to 1.7 bar. The syringe volume is kept constant for approximately 30 seconds, then the syringe piston is released.

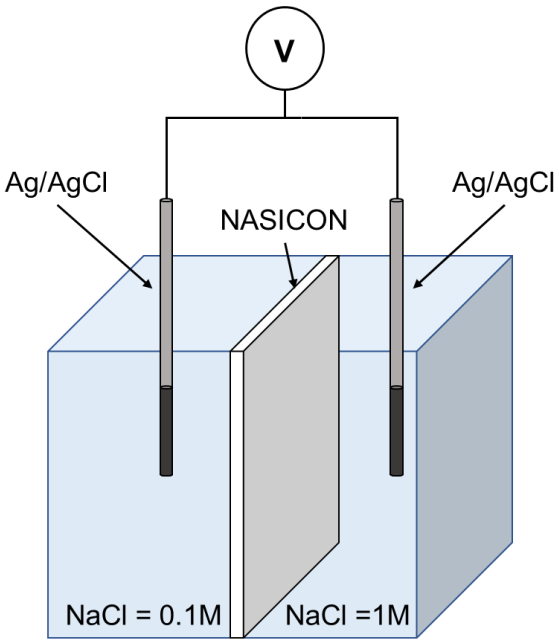

Figure 3.5. Electrochemical cell involved in the perm-selective measurements.

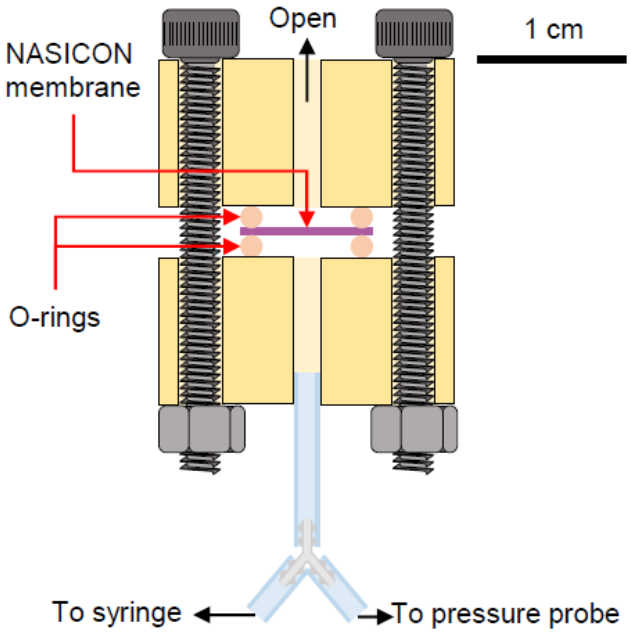

Figure 3.6. Scheme of the cell used to evaluate the permeability of the NASICON diaphragm.

Density

The density measurement of NASICON pellets is performed using the Archimedes balance. The pellet is weight in air to determine the mass, and then weight in pure ethanol, to determine the effective mass. The difference between the real mass and effective mass therefore gives the mass of ethanol displaced and allows the determination of the volume of the NASICON pellet.

Conductivity

The analysis was carried out in an environmental chamber (*Angelantoni ACS*) by Electrochemical Impedance Analysis.

3.1.3. Methods

All the electrochemical characterizations of TRB are performed on a VSP 300 potentiostat/galvanostat.

Cyclic voltammetry measurements are recorded at 1 mV s^{-2}, starting from the open circuit voltage until the 0V for 5 cycles.

Discharge measurements are performed by GCPL (Galvanostatic Cycling with Potential Limitation).

Electrochemical Impedance Spectroscopy under potential control (PEIS) is performed applying frequencies between 1 MHz and 1 Hz.

3.2. Thermally Regenerable Redox-Flow Battery based on LiBr

3.2.1. Experimental setup

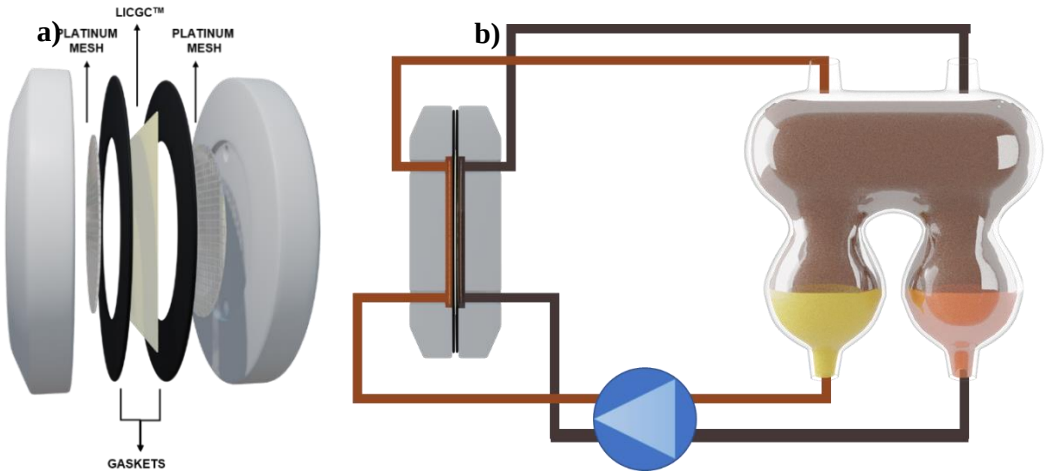

Figure 3.7. a) Scheme of the electrochemical cell; b) Scheme of the hydraulic circuit of the TRB.

A single electrochemical cell contains two platinum meshes as electrodes, with a surface area of 3.92 cm^2, separated by a commercial solid-state electrolyte, LICGC™ membrane. Two Viton® gaskets are placed to avoid the fracture of LICGC™ plate and seal the system. The resulting exposed area of the diaphragm is 3.14 cm^2.

All these parts are kept together by two final plates made of PTFE. A platinum wire, in contact with the electrode, is used as electrical contact, passing through the PTFE plate, through a small hole. The H and L solutions are injected in the electrochemical cell from the bottom, and leave the cell from the top, passing through other two holes on the PTFE plates, as schematically shown in Figure 3.7b. The internal volume for any half cells is 0.628 mL.

The hydraulic circuit is composed by a multichannel pump (*400DM2, 120S, Watson-Marlow*) which recirculates the H and L solutions from the bottom of the Through-liquid exchanger (TLE) to the bottom of the electrochemical cell. The fluxes that coming out from the top of the electrochemical cell, are then dropped in the TLE from the top, closing the cycle. All the tubes are made of marprene (*Watson-Marlow*) with an internal diameter of 0.23 mm and 0.8 mm thick. The flux is 100 rpm and the total volume (TLE, tubes and electrochemical cell) is 8 mL: 4 mL for each solution. To reduce the internal resistance associated to the LICGC™ and improve the power density of the cell, the electrochemical cell is heated at 50°C. The heater consists in a bath of hot oil, in which the cell is placed.

3.2.2. Materials

Platinum meshes (52 mesh woven from 0.1mm diameter wire, *99.9%, Alfa Aesar*) are used as electrodes. Platinum wires (diameter = 0.35 mm) are used as electrical contacts. The gaskets are made by silicone rubber (*Viton*®; thickness = 0.1mm). LiBr (*99%, Alfa Aesar*) and Br_2 liquid (*99.8%,*

Alfa Aesar) are used to prepare the solutions. Diaphragm of LICGC™ (*AG-01 plate*, 25 mm^2, thickness: 0.150 mm or 0.05 mm*; OHARA Corporation*) is used as lithium-ions conductor. Octane (*98+%, Alfa Aesar*) is used as organic solvent in the so-called "Through-liquid exchanger", (TLE). Concentrated (H) and diluted (L) aqueous solutions of LiBr are prepared with a respectively molar fraction of 20% and 1.7%. Br_2 is added in small amount in order to reach a final concentration of 20 mM in both the solutions. A solution of 20 mM of Br_2 in octane fills the TLE: the halogen is added in order to reach the equilibrium in TLE in short time.

3.2.2.1. Electrodes

Before any electrochemical characterization, it is necessary to clean the electrodes because platinum easily adsorbs species when it is passed through by current. The cleaning process consists in different steps where mechanical and electrochemical polishes take place.

The first step consists in cleaning platinum by blowtorch in order to remove all the adsorbed organic species on it, and part of the inorganic species. Then, platinum is dipped in deionized water and sonicate.

After the mechanical treatment, the electrode surface is cleaning electrochemically in 0.5 M solution of H_2SO_4 in deionized water. The electrochemical cell is a 3-electrodes cell composed by platinum that must be cleaned as working electrode, calomel as reference electrode, and another platinum electrode as counter electrode.

At the beginning, the working electrode is hold at 2 V vs SCE for 2/3 minutes (Figure 3.8). During this process, oxygen evolves on the surface of the working electrode and hydrogen evolves on the surface of the counter electrode. This process burns off any organic residue and anodically dissolves trace metals, such as lead and stannous from solder processes.

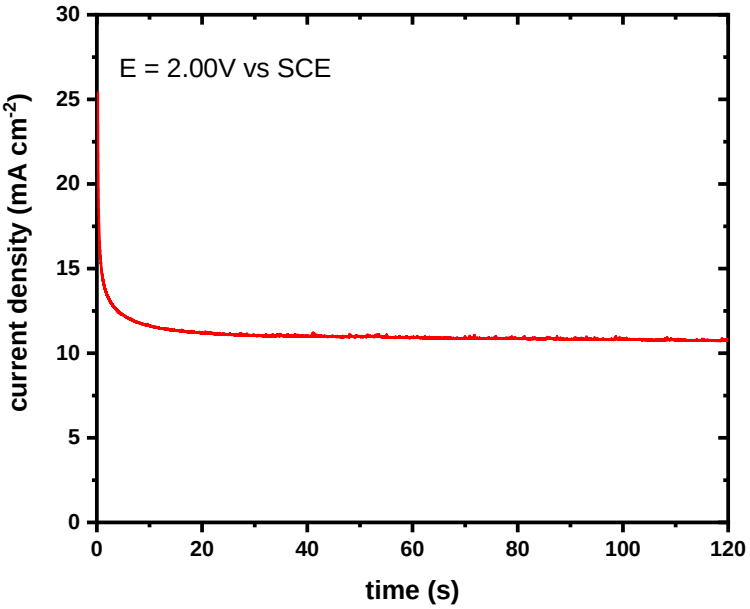

Figure 3.8. Chronoamperometry performed on a platinum electrode in 0.5M H_2SO_4 water solution in order to clean it. The voltage applied is 2.00V vs SCE for 2 minutes.

In the end, cycle-voltammetry is performed between 1.10 V and -0.23 V vs SCE, at a scan rate of 100 mV s^{-1} for 100/200 cycles.

The electrochemical process at negative voltages, closer to the negative limit of the scan window, corresponds to the hydrogen absorption and stripping on the platinum surface, while the anodic process which takes place near the positive limit, is associated to the oxidation of the platinum surface.

At the first cycle (Figure 3.9 a) the cathodic wave related to the oxide stripping to regenerate the platinum surface (E = 0.3V vs SCE), is large due to the thick oxide which is grown during the chronoamperometry measurement. Upon repetitive cycles, this peak decreases and the resulting cyclic voltammetry has a profile like the one reported in Figure 3.9 b[192].

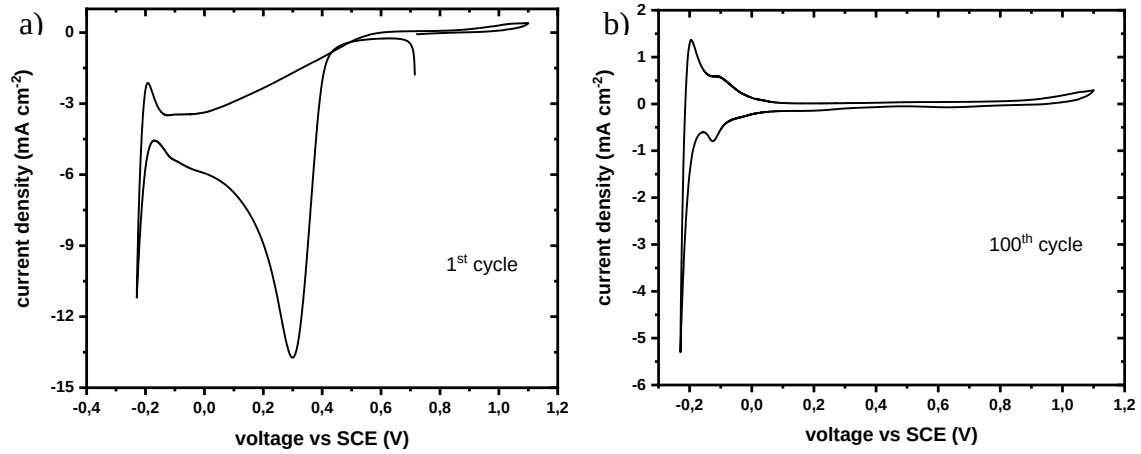

Figure 3.9. Cyclic voltammetry performed on a platinum electrode in 0.5M H_2SO_4 water solution between 1.10V and -0.23V vs SCE applying a scan rate of 100mV/s. a) first cycle (dirty Pt electrode); b) 100th cycle (clean Pt electrode).

3.2.3. Methods

All the electrochemical characterizations of TRB have been performed on a VSP 300 potentiostat/galvanostat.

Cyclic voltammetry measurements have been recorded at 1 mV s^{-2}, starting from the open circuit voltage until the 0V for 5 cycles.

Discharge measurements have been performed by GCPL (Galvanostatic Cycling with Potential Limitation).

Electrochemical Impedance Spectroscopy under potential control (PEIS) have been performed applying frequencies between 1 MHz and 1 Hz.

CHAPTER 4

Thermally Regenerable Redox-Flow Battery

4.1. General Principles

The technology proposed in this project to convert Low-Temperature Heat is called Thermally-Regenerable Redox-Flow Battery, shortly named TRB.

It is a two-stages device (Figure 4.1) where the "power stage" consists in an electrochemical cell which produces electricity at the expenses of the mixing free energy of two water solutions of the same salt but at different concentrations. The second stage, the "thermal separation process" exploits LTH to distill water from the exhausted solution, derived from the power stage, and restore the concentration gradient between the two fed solutions of the electrochemical cell. The thermal stage consists in a distiller; however, other systems could be applied depending on the redox couple that is used in the power stage.

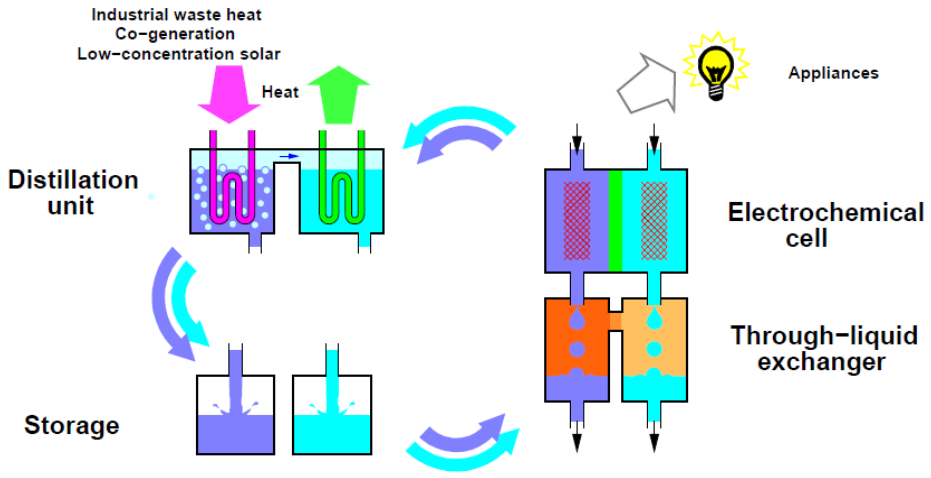

Figure 4.1. General scheme of a TRB. The whole system counts an electrochemical cell, a distillation unit, and the solution reservoirs.

In order to achieve high heat-to-electricity efficiencies, it is important to choose a salt that can give a high boiling point elevation, as it was demonstrated in the section 2.3. Moreover, it is also important to use a solvent with a high latent heat of vaporization because it increases the mixing free energy which is exploited by the electrochemical cell to release electricity (see page 66).

The solvent used in the device is water, due to the high latent heat of vaporization (Table 4.1) but also thanks to the large solubility of several salts in this solvent.

The solute is chosen among the most soluble salts that can give the highest boiling point elevation possible. Good candidates can be some halides (e.g. of Li, Na, Zn) and some hydroxides (e.g. Na, K): at saturation, these salts have boiling point elevation in the order of 20-50°C.

Solvent	Latent Heat of evaporation ($kJ\ kg^{-1}$)
Acetic acid	402
Acetone	518
Ammonia	1369
Benzene	390
Chloroform	247
Decane	263
Dodecane	256
Ethanol	846
Heptane	318
Hexane	365
Octane	298
Toluene	351
Water	2256

Table 4.1. Latent heat of evaporation of primary solvents.

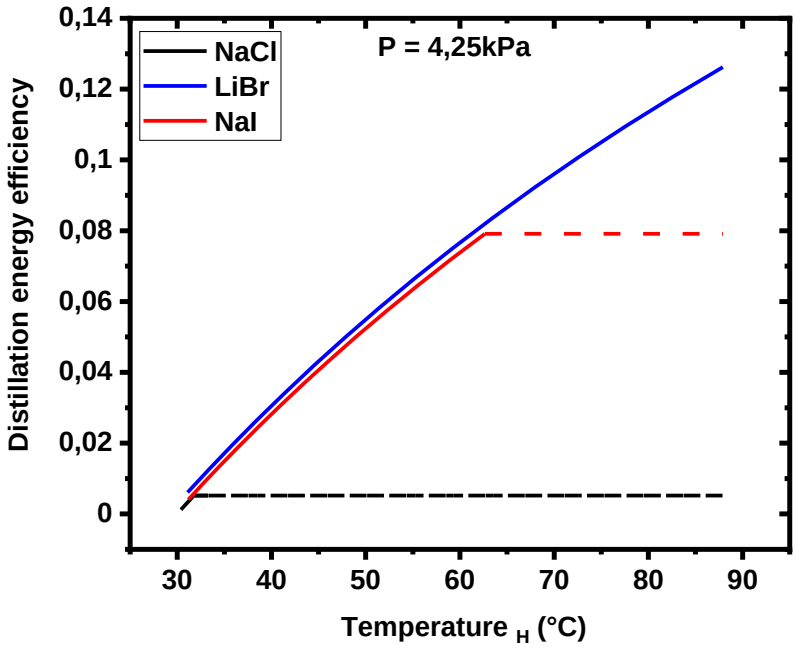

Figure 4.2. Distillation energy efficiency at the increasing of heat temperature for NaCl, LiBr and NaI water solutions. The distillation takes place at 4.25kPa: at this pressure, pure water evaporates at 30°C. The boiling point elevation, at saturation level is nearly 2°C for NaCl, 32°C for NaI and 57°C for LiBr resulting in a distillation efficiency of 0.5%, 8% and 12.6% respectively.

In Figure 4.2 are reported the calculation of the distillation efficiency as a function of the temperature of the heat source[89] for LiBr, NaI and NaCl. In any point of the graph, the molar fraction of the salt

is chosen so that the boiling point of the solution is equal to the temperature of the heat source. The dotted lines represent the maximum boiling point of the solution which reaches the saturation.

The devices which exploit salinity gradient were developed to produce electrical energy from sea/river waters; hence using NaCl solutions. However, sodium chloride has not a high boiling point elevation (less than 5°C, at saturation level), therefore it has not been considering for the device developed in this project.

In this work, two different salts were studied: a TRB based on sodium iodide and a TRB based on lithium bromide. These two salts have high solubility (NaI: 1793 g L^{-1}; LiBr[193]: 1667 g L^{-1} at 20°C), and high conductivity in both diluted and concentrated solutions[194,195].

CHAPTER 5

Thermally Regenerable Redox-Flow Battery based on NaI

5.1. General Principles

The first proposed Thermally Regenerable Redox-Flow Battery is the one based on the iodide/iodine redox couple, choosing sodium iodide as salt. The choice of sodium iodide is related to the high boiling point elevation of this salt, which is very higher than sodium chloride, the salt that generally found application in the SGE devices. The reason why NaI has higher boiling point compared to NaCl is related to the higher solubility in water (1793 g L^{-1} for NaI and 360 g L^{-1} for NaCl), which results in higher mixing energy.

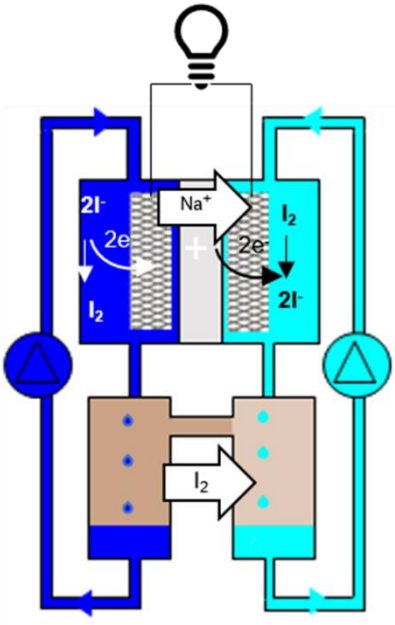

Figure 5.1. Scheme of the electrochemical cell based on NaI solutions.

TRB based on NaI consists in an electrochemical cell, the power stage, filled with two aqueous solutions at different concentration of sodium iodide. In the two solutions, a low concentration of iodine is also dissolved, in order to form the redox couple in both the sides of the cell.

In the concentrated compartment (*H* side) iodide is oxidized to iodine, while, in the diluted compartment (*L* side) the halogen is reduced to halide:

$$H: \quad I^- + e^- \rightarrow \frac{1}{2} I_2 \quad (5.1)$$

$$L: \quad \frac{1}{2} I_2 \rightarrow I^- + e^- \quad (5.2)$$

To maintain the electroneutrality, sodium ions move from the concentrated side to the diluted one through the selective cation-exchange membrane, a NASICON diaphragm, which bars the passage of water, iodide, and iodine.

Due to the slightly solubility of iodine in water, only 0.289 g L^{-1}, a problem may occurs during the discharge of the cell: in fact, it is impossible to reach a concentration of iodine in the L side that is enough to carry on the redox reaction. Therefore, after few minutes, when all the dissolved iodine in the diluted compartment has reacted, the electrochemical cell turns off. To avoid this problem, the electrochemical cell is directly connected with an innovative device named "Through-Liquid Exchanger" (TLE) which allows the equilibrium of iodine between H (where it is produced) and L (where it is consumed) compartments preventing the exchange of water, sodium and iodide ions (Figure 5.1). The working mechanism it will be widely explained in the section 5.3.1. and 5.4.1.

5.2. Thermodynamic/Kinetic discussion

As it has been already discussed in chapter 2, the total efficiency of the TRB depends on the efficiency of the power production stage, the electrochemical cell (η_{el}), and the efficiency of the thermal stage, the distillation unit (η_{dis})

$$\eta = \eta_{el} \cdot \eta_{dis} \quad (5.3)$$

The efficiency of the electrochemical cell is expressed as

$$\eta_{el} = \frac{W}{\Delta Gmix} \quad (5.4)$$

Where *W* is the extracted work from the cell, and ΔG_{mix} is the maximum energy, obtained only if the electrochemical process is ideal and reversible. This value is determined as a difference between the Gibbs free energy of the exhausted solution and the sum of the Gibbs free energy of the H and L solutions at the beginning of the discharge:

$$\Delta G_{mix} = G_2 - G_1 = n_{tot}\mu_2 - (n_H\mu_H + n_L\mu_L) \quad (5.5)$$

Where n_H, n_L, n_{tot} are the sodium iodide moles in the *H* solution, *L* solution and the sum of both solutions, respectively while μ_H, μ_L, μ_2 are the chemical potential of the *H, L* and exhausted solutions.

The efficiency of the distillation unit is:

$$\eta_{dis} = \frac{\Delta Gmix}{Q_H} = \frac{n_W\lambda \cdot (1 - \frac{T_W}{T_s})}{n_W\lambda} \quad (5.6)$$

Where n_w are the moles of solvent that must evaporate, λ is the latent heat of evaporation, *Tw* is the boiling point of the pure water and *Ts* is the boiling point of the NaI solution. This parameter is limited by the Carnot law[110,111,196].

To increase the efficiency of the heat conversion, thermodynamic analysis evidence the importance to increase the boiling point elevation of the implemented solutions compared to the pure solvent[89,110].

In order to extract more electrical energy from the system, is also clear that it is better to choose a solvent with a high latent heat of evaporation[110,197].

Therefore, water solution of sodium iodide is the easier choice because even if sodium iodide has not the highest boiling point elevation (in the working conditions the boiling point elevation reaches 17°K), the engineering of the system is quite simple. In fact, any parts of the setup do not require particular operating conditions compared to a TRB based on LiBr (see chapter 6).

The distillation efficiency of a system based on water solutions of NaI, which has to restore a solution with 17.6% molar fraction, is theoretically

$$\eta_{dis} = 10\% \quad (5.7)$$

To evaluate the achievable mixing free energy, it is necessary to define the concentration difference between the two solutions.

5.2.1. Activity coefficients, Mixing Free Energy and Open Circuit Voltage

A theoretical determination of the available mixing free energy and of the expected open circuit voltage is required, not only to compare the experimental data, but also to understand the initial conditions, their potentialities, and possible improvements.

The Galvani representation of the TRB based on NaI is the following:

α	ϵ	σ	ϵ’	α'
Graphite	$NaI_H\,(H_2O)$	NASICON	$NaI_L\,(H_2O)$	Graphite

Where the phases α and α' represent the electronic conductors, the electrode, ϵ and ϵ' the solutions where the redox couple are dissolved, and σ is the solid-state electrolyte, the NASICON membrane. On the interphase $\alpha|\epsilon$ and $\alpha'|\epsilon'$ the redox equilibrium takes place:

$$I_2 + 2e^- \rightleftarrows 2I^- \quad (5.8)$$

Therefore, the equilibrium equations are:

$$\tilde{\mu}_{\epsilon}^{I_2} + 2\tilde{\mu}_{\alpha}^{e^-} = 2\tilde{\mu}_{\epsilon}^{I^-} \quad (5.9)$$

$$\tilde{\mu}_{\epsilon'}^{I_2} + 2\tilde{\mu}_{\alpha'}^{e^-} = 2\tilde{\mu}_{\epsilon'}^{I^-} \quad (5.10)$$

Two other equilibriums take place between the NASICON and the solutions, related to the diffusion of Na^+ ions through the NASICON electrolyte, the so-called Donnan equilibrium:

$$\tilde{\mu}_{\epsilon}^{Na^+} = \tilde{\mu}_{\sigma}^{Na^+} = \tilde{\mu}_{\epsilon'}^{Na^+} \quad (5.11)$$

Combining the three equations:

$$2\tilde{\mu}_{\alpha}^{e^-} - 2\tilde{\mu}_{\alpha'}^{e^-} = 2\tilde{\mu}_{\epsilon}^{I^-} - 2\tilde{\mu}_{\epsilon'}^{I^-} + \tilde{\mu}_{\epsilon'}^{I_2} - \tilde{\mu}_{\epsilon}^{I_2} + \tilde{\mu}_{\epsilon}^{Na^+} - \tilde{\mu}_{\epsilon'}^{Na^+} \quad (5.12)$$

It is easy to note that $\tilde{\mu}^{Na^+}$ and $\tilde{\mu}^{I^-}$ is the electrochemical potential of the salt in the ϵ and ϵ’ phases. Using the definition of the electrochemical potential, equation 5.12 can be rewritten explicating the open circuit voltage (OCV):

$$OCV = \frac{\tilde{\mu}_{\epsilon'}^{I_2} - \tilde{\mu}_{\epsilon}^{I_2}}{2F} + \frac{\tilde{\mu}_{\epsilon}^{NaI} - \tilde{\mu}_{\epsilon'}^{NaI}}{F} \quad (5.13)$$

Thanks to the TLE device, connected to the electrochemical cell, the chemical potential of iodine is kept in equilibrium in both the *H* and *L* solutions, respectively. For this reason, the first part of equation 5.13 can be deleted and the OCV can be calculated using a simplified Nernst equation:

$$OCV = \frac{RT}{F} ln \left[\frac{a_H^{Na^+} a_H^{I^-}}{a_L^{Na^+} a_L^{I^-}} \right] = \frac{RT}{F} ln \left[\frac{X_H^{NaI^2} \gamma_H^{NaI^2}}{X_L^{NaI^2} \gamma_L^{NaI^2}} \right] \quad (5.14)$$

Where X^{NaI} is the molar fraction of sodium iodide in the *H* or *L* solution while γ is the mean activity coefficient of the ions (Na^+ and I^-).

It must be noticed that the cell voltage depends on the presence of dissolved iodine not only because it takes a part in the redox process, but also because it is involved in the formation of the complex I_3^- :

$$I^- + I_2 \rightleftarrows I_3^- \quad (5.15)$$

The discussion made previously is rigorously valid also in the presence of the complexation: in fact, even if the formation of I_3^- decreases the concentration of NaI (and for this reason, decreases its chemical potential) affecting the cell voltage, the amount of dissolved iodine in the solution is small compared to the concentration of sodium iodide, thus this effect can be neglected. Anyway, a further discussion of the iodine complexation will be reported in detail in the TLE section and in the paragraph 5.2.2.

Therefore, it is necessary to choose the concentration of the feed solutions in order to define the mixing free energy and hence, the OCV of the electrochemical cell.

Higher is the salinity gradient, higher is the mixing free energy that can be converted in electricity; thus, it is important to use two solutions with a high concentration difference. At the same time, it is also important to choose concentrations that do not affect too much the conductivity, otherwise the overvoltage increases resulting in worst electrochemical performances.

To determine the mixing free energy, the chemical potentials and hence the activity coefficients must be calculated for both the *H* and *L* solutions.

In the last years, several models have been developed to identify mathematical and physical relationships between thermodynamic properties of electrolyte solutions. However, reliable prediction of activity coefficients, even in low concentrated univalent electrolyte solutions, is still challenging.

Shilov et al[198]., have tried to model thermodynamic activities in aqueous solutions of NaI, at room temperature, applying the extended Debye-Hückel theory. Calculations without parameter fitting have shown a good agreement with experimental data in the concentration range up to 7 molal.

Even if these results are promising, this model cannot be applied in this research; in fact, the concentrated solution involved in the TRB has a concentration higher than 7 molal.

In this research, the activity coefficients have been determined by the fitting of experimental values of activity coefficients reported in literature[199] at different molalities.

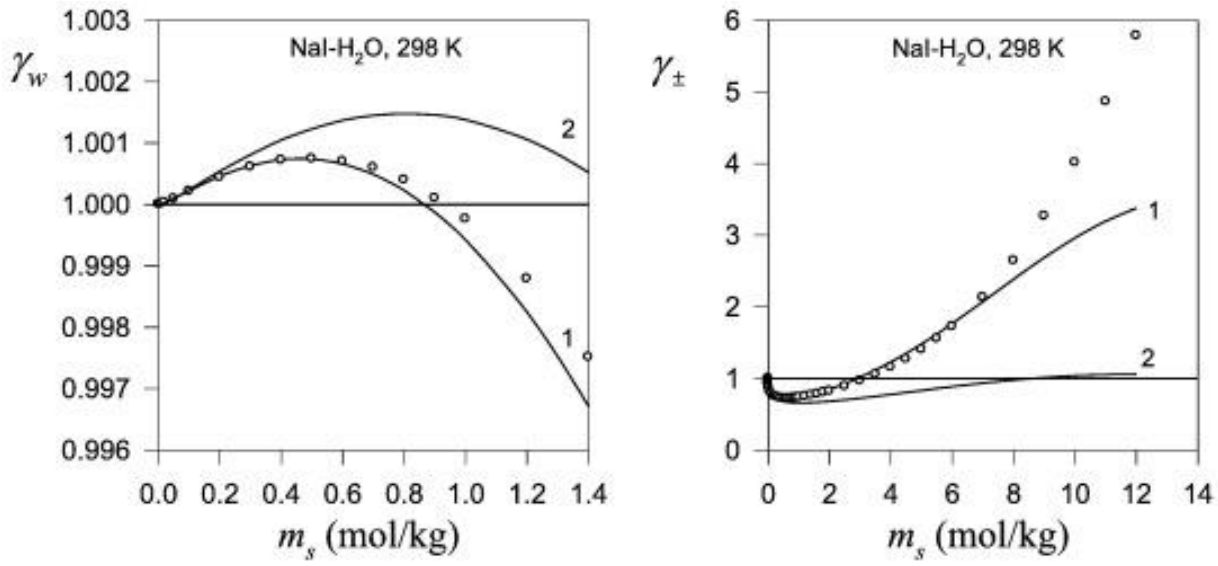

Figure 5.2. Water activity (left) and mean ionic activity coefficient (right) in aqueous solution of NaI at 298°K. solid lines 1 and 2 are calculated using the extended Debye-Hückel theory with two different methods[198] *while open circles are experimental data*[199].

Actually, the experimental data cover all the concentration range of interest for this research and then, the fitting curve and related equation can be considered enough accurate for the aim of this project.

The best fitting is obtained with a polynomial fitting of the third order, as shown in Figure 5.3.

Knowing the activity coefficients, the open circuit voltage of the cell may be calculated from equation 5.14.

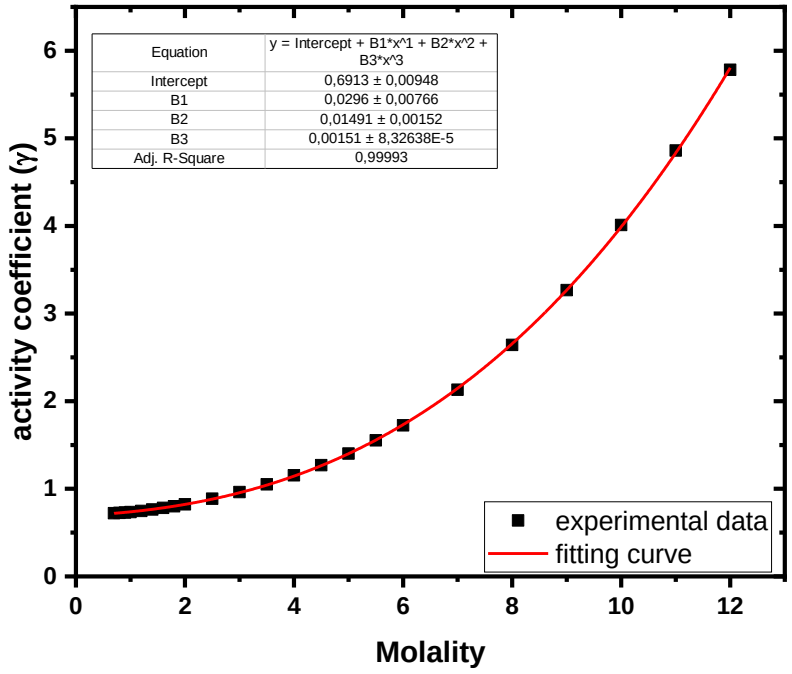

Figure 5.3. Fitting curve of the activity coefficient vs molality for NaI. The activity coefficients are reported in literature[199]*. The fitting function is a polynomial curve.*

Considering a fixed concentration of NaI in the *H* solution (17.5% molar fraction; 11.8 molal), the OCV is determined taking into account different concentrations of *L*, by calculations.

The results are reported in Figure 5.4 (red profile).

Experimental values are also reported (black dots) considering a diluted solution with a concentration of 1.75% molar fraction: the experimental values agree with the thermodynamic results demonstrating that the calculated activity coefficients can be considered valid.

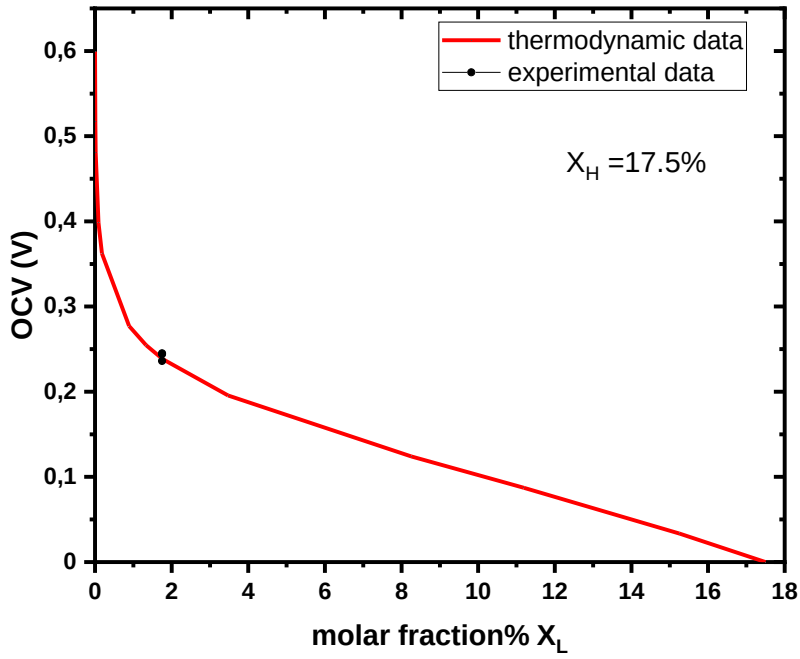

Figure 5.4. OCV of a TRB based on a concentrated solution with a molar fraction of 17.5% vs increasing molar fraction of the diluted solution. Black points represent the experimental OCV using a diluted solution with a molar fraction of 1.75%.

In the electrochemical cell reported in this work, using NaI with molar fraction of X_H = 17.5%, X_L = 1.75% for *H* and *L* solutions respectively, the maximum energy that may be exploit is ΔG_{mix} = 22.7 kJ L^{-1} (6.3 Wh L^{-1}).

This value is calculated subtracting the chemical potential of the initial solutions, *H* and *L*, from the chemical potential of the exhausted solution, which is the result of the electrochemical discharge. In fact, the exhausted solution is composed by the diluted *L* solution and the concentrated *H* solution, when they have equal activities.

5.2.2. Electrochemical reaction

The half-cell reaction of iodine molecules is:

$$I_{2\,(aq)} + 2e^- \rightleftarrows 2I^-_{(aq)} \quad (E^0 = 0.54V\ vs\ SHE) \quad (5.16)$$

Impedance analysis[200] shown the mechanism of this reaction follows a Volmer-Heyrovsksy mechanism on platinum or graphite electrode:

$$I^- \rightarrow I_{ads} + e^- \ (Volmer)$$

$$I_{ads} + \ I^- \rightarrow I_2 + e^- \ (Heyrovsksy)$$

The second step, the Heyrovsksy reaction, is the rate determining step.

However, polyhalides can be formed and undergo to electrochemical processes with somewhat different standard potentials and mechanisms[201].

Iodine reacts with iodide forming triiodide, with an equilibrium constant of

$$K = \frac{[I_3^-]}{[I_2][I^-]} \frac{\gamma_{I_3^-}}{\gamma_{I_2}\gamma_{I^-}} \cong 723 \ (5.17)$$

Triiodide complex is the predominant one, even if I_6^- can be formed too[202]. This dimerization is possible at high concentration of iodide. Experiments show also the presence of poly-iodine species[203], such as ions in the form I_{2x} that could be stabilized by protons from the solvent[204].

To identify the exact nature and structure of these polyiodide molecules, more research is required. Therefore, up to know, it is necessaire consider the fact that the experimental open circuit voltage will not be exactly as the theoretical one, determined by calculations.

5.3. Experimental setup

5.3.1. Through-Liquid Exchanger

To equilibrate the activity of iodine between the *H* and *L* solutions, an unconventional device, named Through-Liquid Exchanger (TLE), has been developed (Figure 5.5). Here, the two solutions are in contact with an organic solvent phase which dissolves iodine, but it does not dissolve water nor NaI. The equilibration process works as a liquid-liquid extraction: iodine diffuses from the concentrated solution, where it is produced, in the organic phase, then it diffuses from the organic phase in the dilute solution, where it is consumed.

Figure 5.5. Scheme of the TLE device and its picture.

Liquid-liquid extraction is efficiently performed on industrial scale, by means of mixer-settlers or supported liquid membranes. Same techniques may be applied to implement TLE but, scaling such techniques down to laboratory size is complicated, mainly due to the increase of dead volume. This is the reason why a new glassware is specifically designed to solve this task, avoiding a direct mixing between the two solutions and, at the same time, keeping the dead volume small.

The tailored glassware is schematically reported in Figure 5.6 b and its function is represented in Figure 5.6 a.

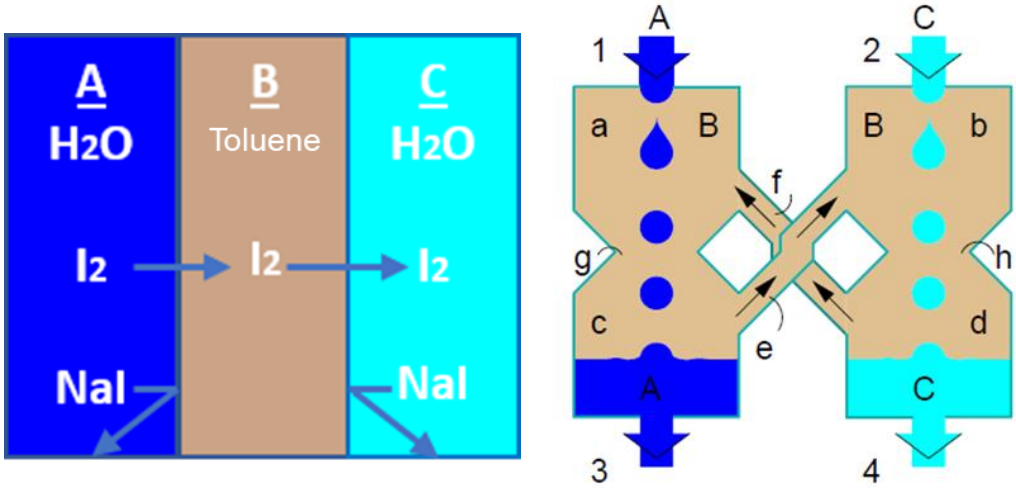

Figure 5.6. a) Scheme of the liquid-liquid extraction of iodine from the A water solution to the C water solution passing through the organic phase. b) simplified scheme of the TLE.

In Figure 5.6 b, the two water solutions of NaI and I_2 are reported as *A* and *C*, while *B* is the insoluble organic solvent; in the specific case it is toluene. As already said, sodium iodide is not soluble in toluene and thus it is not exchanged between the two solutions. Contrary, iodine is soluble in toluene and thus it diffuses from solution *A*, where it is produced, to solution *C*, where it is consumed and therefore in less amount, through the intermediate liquid toluene *B*.

TLE is composed by four chambers: *a, b, c,* and *d*. The chambers are connected in couples through the bottlenecks *g* and *h*. Moreover, two tubes, *e* and *f*, connect the chamber *c* with the chamber *b* and chamber *a* with the *d* one.

The chambers are filled with the organic solvent, while the two solutions (*A* and *B*) are injected drop-by-drop through the tubes *1* and *2* and are drawn from the tubes *3* and *4*. The drops generate an increase of the pressure in the bottom chambers *c* and *d* respect to the chambers *a* and *b*, because the passage through the bottlenecks *g* and *h*. This pressure difference drives the solvent from chamber *c* to *b* and from chamber *d* to *a*, respectively through the tubes *e* and *f*. This motion enables a quite fast mixing of toluene in the TLE and equilibrate the activity of iodine, which is the extracted species.

During the experiments, TLE is filled with a solution of iodine 10 mM in toluene.

5.3.2. NASICON membrane

NASICONs, sodium superionic conductor, are a class of materials of structurally isomorphous 3D framework compounds possessing high conductivity, with the general formula $Na_{1-x}Zr_2Si_xP_{3-x}O_{12}$ ($0 < x < 3$). It has been proposed as a solid electrolyte for applications such as gas sensors[205–207], ion selective electrodes[208,209], and sodium-sulfur batteries[210].

The ionic conductivity of $Na_{1+x}Zr_2Si_xP_{3-x}O_{12}$ ($0 < x < 3$) varies according to the stoichiometry of the NASICON composition: the highest conductivity is obtained in the range of $1.8 < x < 2.2$: the maximum value found in literature is $6.7 \cdot 10^{-4}$ S cm^{-1} at room temperature[211]. In particular, the conductivity obtained for the composition $Na_3Zr_2Si_2PO_{12}$[212–214] is comparable to that obtained for the Na β″ alumina.

In general, the NASICON structure consists in a rhombohedral symmetry except in the interval $1.8 < x < 2.2$ where a small distortion to monoclinic symmetry occurs[212].

The NASICON structure is a three-dimensional framework created by alternatively arranged ZrO_6 octahedra and SiO_4 or PO_4 tetrahedra. Each PO_4 or SiO_4 fragments are connected to four ZrO_6 octahedra, which, in turns, shares its corner with six SiO_4 or PO_4 tetrahedra (Figure 5.7).

In this way, “hexagonal bottlenecks” are created with large space enables sodium ions to move through.

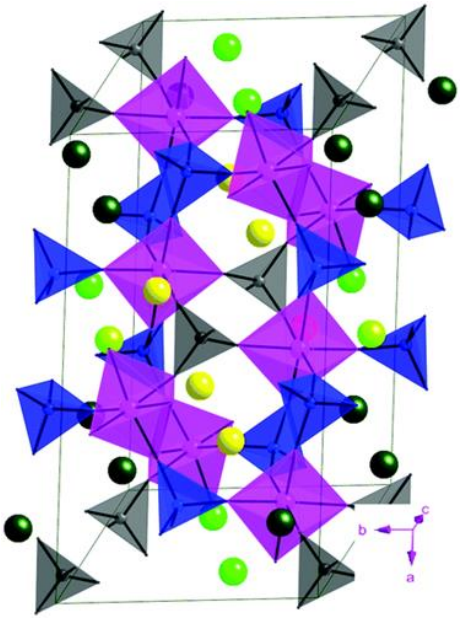

Figure 5.7. Orthorhombic crystal structure of the most common NASICON[215]. Yellow balls represent Na(1), light green ballr represent Na(2) and dark green balls are Na(3). Zr octahedra are reported in purple, Si tetrahedra are blue, P tetrahedra are reported in black.

In particular, three different positions where sodium ions may be located, are identifiable. The first position, indicated as Na(1) (shows as yellow ball in Figure 5.7), is linked three-dimensionally to two Na(2) (light green balls) sites and four Na(3) sites, while each Na(2) or Na(3) (dark green balls) sites are connected to two Na(1) positions.

A tremendous problem is connected to the synthesis of NASICON: during the sintering, a second phase of zirconia, which is an electrical insulator, is always formed. A good NASICON synthesis results in a small amount of ZrO_2.

In Figure 5.8 is reported a model, which suggests the optimal conditions to synthesize a pure NASICON phase.

Starting from a high content of zirconia (>50%w) as precursor, leads to a final composition made of two-phase regions: zirconia is naturally expulsed because of the increased temperature.

If, instead, it is used an amount of zirconia between 35-45%w results in a single-phase NASICON up to the temperature where the phase boundary is crossed (1275°C). If this temperature is exceeded, zirconia is expulsed creating a mixture of two-phases. If the temperature does not reach the melting point of NASICON, the result is the complete dissolution of the NASICON phase.

5.3.2.1. NASICON Characterization: Structural and Morphological Characterization

NASICON diaphragm, with composition $Na_3Zr_2Si_2PO_{12}$, is used as "membrane" in the device. Several procedures have been followed to synthesized NASICON with good properties in terms of conductivity, perm-selectivity, and permeability.

The results of the NASICON pellets synthesized following the procedure reported at page 72 are here discussed.

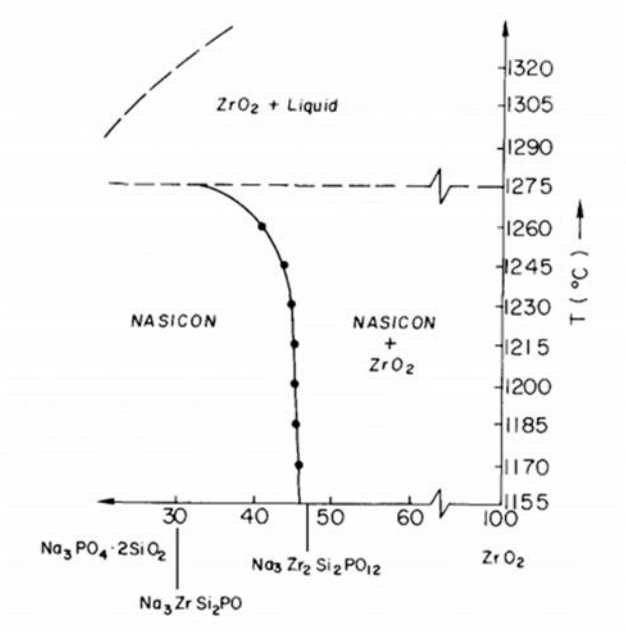

Figure 5.8. Tentative phase relations in the Nasicon ZrO_2 phase field[216].

Structural and morphological characterization of sintered NASICON is performed by X-Ray power diffraction and Scanning Electron Microscopy.

The X-Ray diffraction measurement on the produced NASICON (Figure 5.9) confirms the formation of the desired crystal structure. A small amount of zirconia is also detectable: as already said, it is impossible avoid its formation.

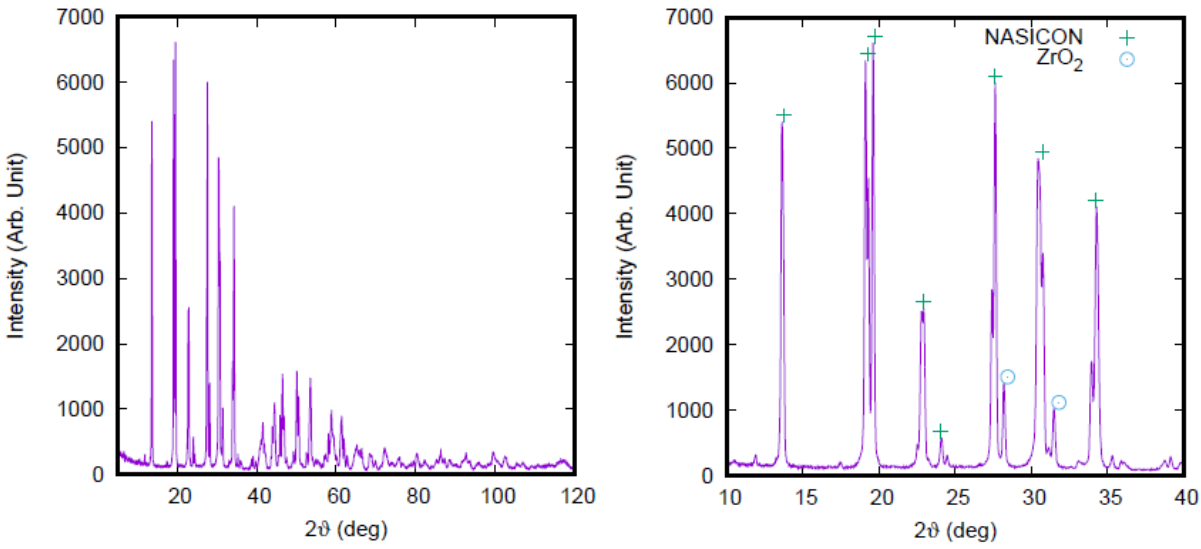

Figure 5.9. a) X-Ray diffractogram of the produced NASICON material. b) X-Ray diffractogram of the produced NASICON compared with the diffractogram of NASICON and zirconia found in literature.

In this procedure, the resulting zirconia does not significantly affect the performances of the NASICON phase.

Same results are confirmed by Scanning Electron Microscopy. Figure 5.10 are SEM images of a section of NASICON membranes with a thickness of 0.5 mm, obtained by fracture. It can be easily

observed how the material is mostly composed by large cubic crystals, with a dimension of nearly 50 µm. Between the crystals there are several spaces, on the scale of 20-30 µm. The structure is homogeneous across the thickness.

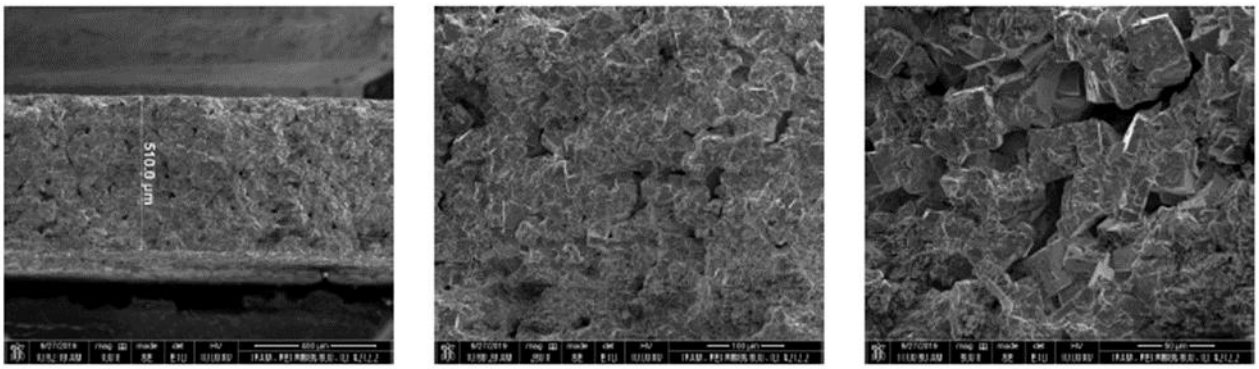

Figure 5.10. SEM images of a section of NASICON membrane, obtained by fracture.

The SEM images shown in Figure 5.11, are related to the ground side of the NASICON membranes; in fact, in order to reach the desired thickness of 0.5 mm, one side of the membrane is ground.
In this case, the crystals are less visible, due to the grinding process, while holes are easily detectable.

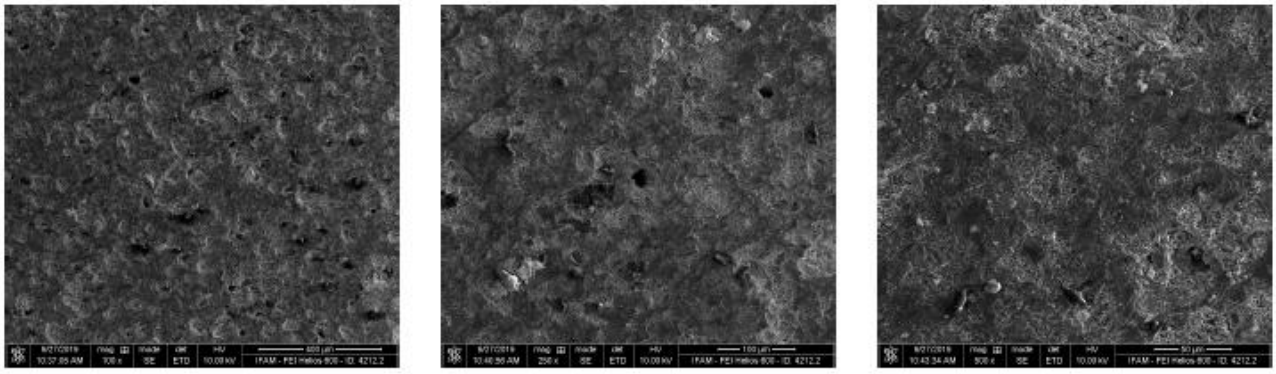

Figure 5.11. SEM images of a ground side of NASICON membrane.

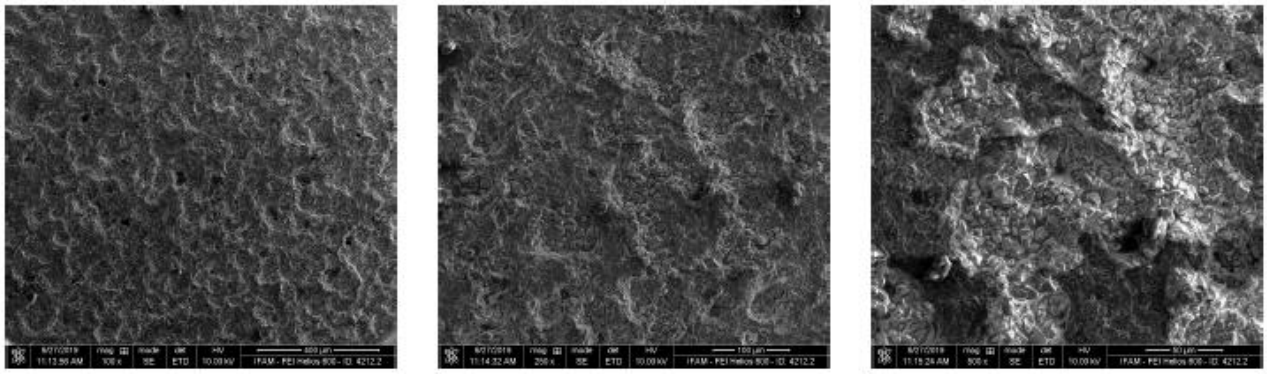

Figure 5.12. SEM images of the sintered surface of the NASICON membrane.

The result of the sintering procedure is studied by observation of the surface side of the NASICON membrane which has not be ground. These SEM images are reported in Figure 5.12. The surface appears compact. However, some regions are covered by different structure.
Besides the large cubic crystals, smaller platelets or needles can be detected. The acquisition of an image with the back-scattered electrons (BSE) technique, suggests that the composition of the smaller objects is different from the composition of the larger cubic crystals (Figure 5.13 b).

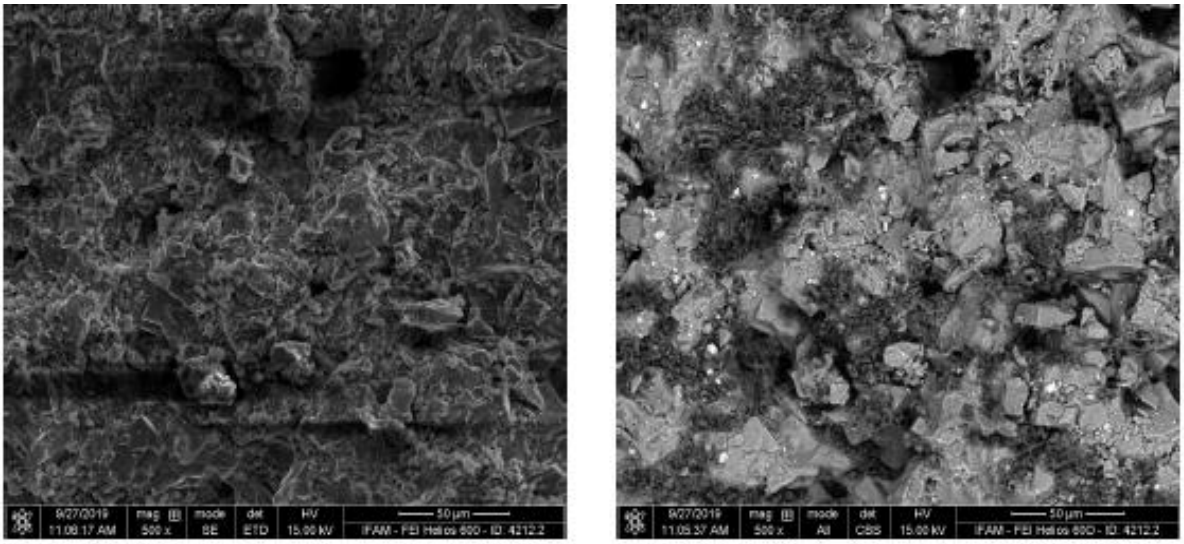

Figure 5.13. a) SEM image; b) BES image.

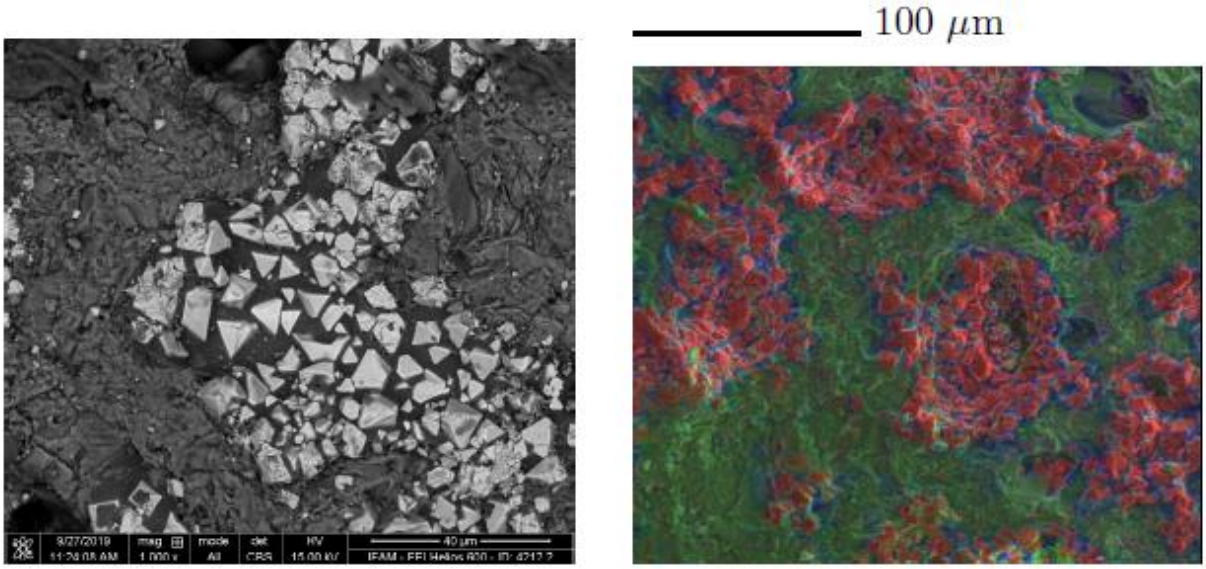

Figure 5.14. a) BES image of the surface of NASICON pellet where a second type of crystal structure is identified. b) combination of SEM image and EDX technique. The red zone is attributed to the zirconia phase, the blue areas are silica, and the green areas are NASICON phase.

A further investigation of the material found on the surface of the sintered NASICON is reported in Figure 5.14. The BSE image (Figure 5.14 a) shows a part of the surface covered by large morphologically bipyramidal crystals, embedded in a morphologically amorphous matrix. These bipyramidal crystals have dimensions around 10 μm. In the Figure 5.14 b, is reported an elaboration based on SEM and EDX (Energy Dispersive X ray Analysis) acquisition. The colors depend on the

measured composition, while the intensity depends on SEM. The red color is related to the presence of zirconium, blue is related to silicon, and green the presence of both silicon, zirconium in presence also of sodium. The presence of phosphorus is difficult to evaluate because of the superposition of peaks with the peaks of zirconium (Figure 5.15).

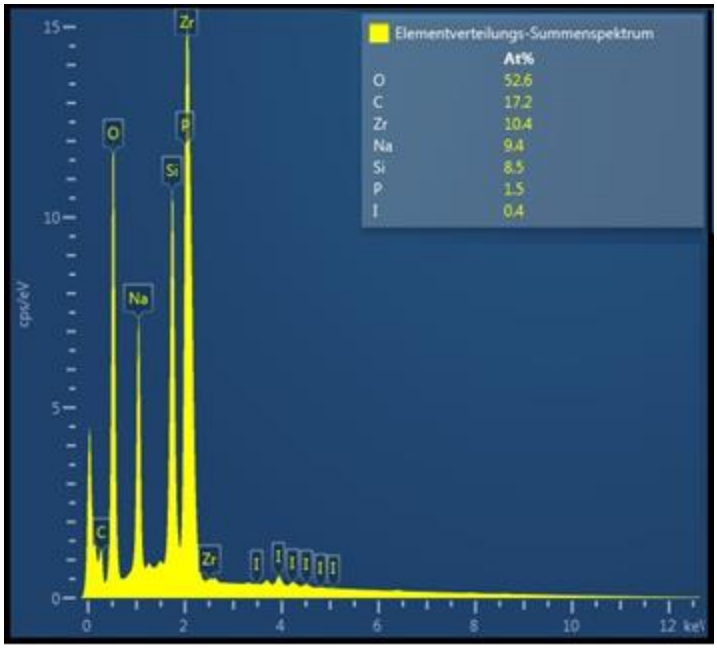

Figure 5.15. Peaks analysis of EDX measurements.

The red zone represents likely the area where zirconia is formed, the blue area is identified as silica, and, finally, the green area is NASICON. Therefore, the material described as morphologically bipyramidal crystals, is zirconia, which is embedded in a matrix of silica. In the end, the large surface of the membrane is rightly attributable to NASICON.

Silica has not visible crystal structure and, probable, the formation of the morphologically amorphous silica contributes to seal the porosity of the material on the surface.

5.3.2.2. NASICON Characterization: Conductivity

Impedance spectra of NASICON membranes are performed to evaluate its conductivity.

A four-electrodes cell is used to get rid of the contribution of the charge transfer and mass transfer at the surface of the electrodes. The Nyquist plots obtained by this analysis shows two arcs: the high frequency arc intercepts the real axe at a finite value. Resistance of the low frequency arc is almost negligible and vanishes as the temperature increases. The capacitance at low frequency arc is around 10^{-9} F, a typical value for grain boundary related processes in ceramic materials. Using the resistance associate to this second arc as the grain boundary resistance, and the high frequency intercept as an estimation of the bulk resistance, the respective conductivities are determined by a simple equation:

$$\sigma = \frac{h}{RS} \quad (5.18)$$

Where σ is the conductivity, *R* the resistance, *h* and *S* are the thickness and the surface of the sample, respectively.

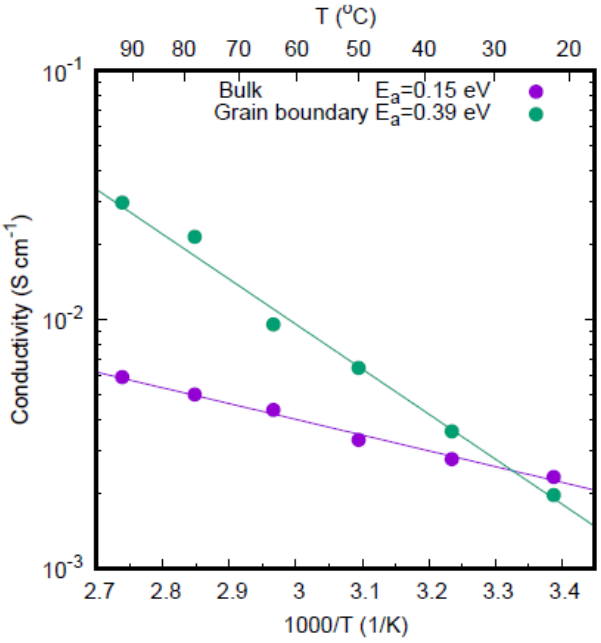

Figure 5.16. Values of bulk conductivity (purple) and grain boundary conductivity(green) as a function of temperature.

The conductivity of the grain boundary, σ_{GB}, and the conductivity of the bulk, σ_{bulk}, are reported in the Figure 5.16, as a function of the temperature.

The activation energy determined by fitting *lnT* vs *1/T* (both fits have $R^2 > 0.99$) are compatible with the values reported in literature: 0.15 eV for the bulk and 0.39 eV for the grain boundary. The high activation energy related to the grain boundary is presumably due to the low density of the membrane.

5.3.2.3. NASICON Characterization: Perm-selectivity[217]

The perm-selectivity of a membrane is evaluated by the ratio between the flux of specific component to the total mass flux through the membrane under a given driving force.

In an ion-exchange membrane, the perm-selectivity depends on the ion-exchange capacity of the membrane and the ion concentration in the solutions where the membrane is immersed.

The perm-selectivity can be calculated from the transport number of the counter- and co-ions in the membrane and in the solutions. In a cation-exchange membrane, the counter-ion are the cations while anions are the co-ions. Vice versa, the cations are the co-ions in an anion-exchange membrane and anions are the counter-ions.

The perm-selectivity is defined as

$$\Psi = \frac{T_{cou}^{m} - T_{cou}}{T_{co}} \quad (5.19)$$

Where *T* is the transport number of *co* co-ions, *cou* counter-ions in the solutions, and *m* in the membrane.

A method to determine the perm-selectivity of a membrane is based on the measurement of the potential gradient across a membrane which separates two electrolyte solutions of different concentrations. This static method, however, does not take the water transport through the membrane into account and it is referred to as "apparent" perm-selectivity.

The potential between two electrolyte solutions of different concentrations, the membrane potential, consists of the two Donnan potentials between the membrane and the adjacent solutions and the diffusion potential across the membrane:

$$\varphi_m = \varphi_D^1 + \varphi_D^2 + \varphi_{diff} \quad (5.20)$$

For a completely perm-selective membrane, the diffusion potential is zero and can be neglected.

For a strictly perm-selective membrane, there is no salt diffusion through the membrane, the transport number of ion (considering sodium ions) assumes value 1, that is why, according to Nernst law, the membrane potential is the cell voltage, and it is

$$OCV = \varphi_m = \frac{RT}{F} ln \frac{a^1}{a^2} \quad (5.21)$$

Where *a* is the activity of *1* concentrated solution and *2* diluted solution, respectively.

To evaluate this parameter, the membrane is placed in an electrochemical cell with two Ag/AgCl electrodes dipped in two sodium chloride solution at different concentrations, 1 M and 0.5 M (see page 73 and Figure 3.5).

The cell voltage of this cell would be 111 mV if the membrane is perfectly perm-selective. In the absence of perm-selectivity, the voltage decreases to one and half, 55 mV.

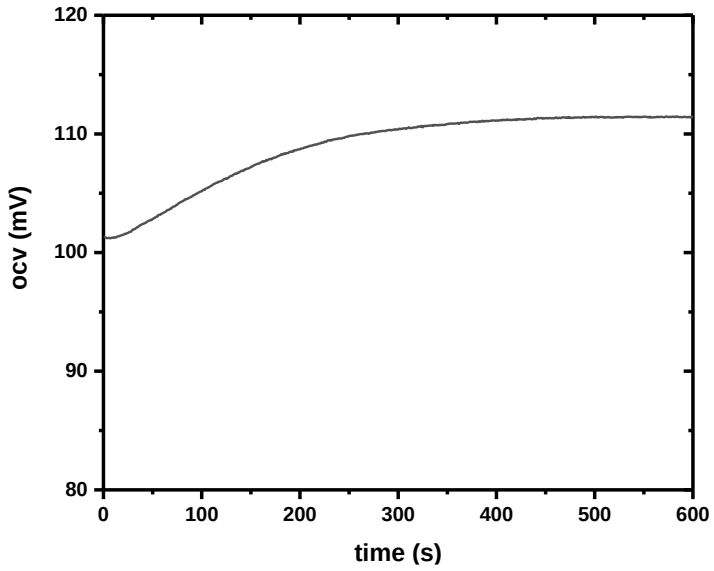

Figure 5.17. Open Circuit Voltage (OCV) of an electrochemical cell with NASICON membrane immersed in two water solutions of NaCl 0.5M and 1M, respectively.

The characterization of these membranes gives values between 100 and 110 mV, showing the excellent perm-selectivity of the produced membranes (Figure 5.17).

5.3.2.4. NASICON Characterization: Permeability

To evaluate the permeability of sintered NASICON membranes, a device, like the one schematizes in Figure 3.6, is used.

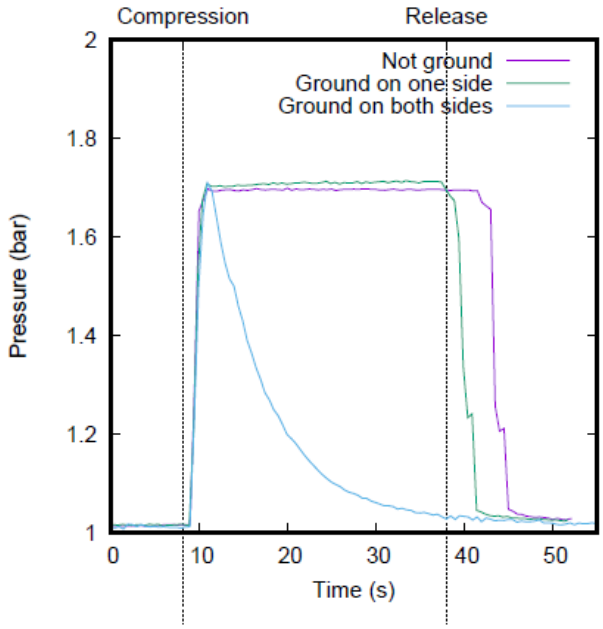

Figure 5.18. Pressure variation after the initial compression for NASICON membrane not ground (purple profile), NASICON ground on one side (green profile) and NASICON ground on both sides (blue profile).

In the Figure 5.18, the variation of the pressure is reported versus the time for three different NASICON membranes: NASICON membrane not ground (purple profile), NASICON membrane ground on one side (green profile), and NASICON membrane ground on both sides (blue profile).
In the NASICON membrane ground on one side or not ground, the pressure remains almost constant until the syringe is released. In the case of NASICON ground on both sides, the pressure decreases quite fast: this means that air permeates through the membrane.
This behavior is typical and reproducible: membranes that are not ground after sintering, or that are ground only on one side, appear impermeable to air and, therefore, to water. Instead, membranes ground on both sides are permeable. Their permeability is associated to the NASICON surface: in the case of not ground or ground only on one side NASICON membranes, the surface is a compact layer, likely the glassy material observed in the SEM images which seals the otherwise porous material.

5.3.2.5. Other syntheses

Several syntheses are tried to improve the morphological, structural, and electrochemical characteristics of NASICON pellets.
Different temperatures of calcination are tested on two different sets of reactants:

A) $SiO_2, Na_3PO_4 \cdot 12H_2O, ZrO_2$

B) $Na_2CO_3, ZrO_2, NH_4H_2PO_4, SiO_2$

In both the cases, the powders are finely ground and calcinated under different working conditions:

(1) 1100°C, 8h, 3°C/min;

(2) 1150°C, 8h, 3°C/min;

(3) 1150 °C, 15h, 3°C/min;

(4) 1150°C, 6h, 3°C/min,

(5) 1150°C, 6h, 5°C/min.

All the syntheses are then verified by means XRD diffraction in order to evaluate the NASICON formation and the development of other impurities.

For the A) set of reactants, all the combinations of temperatures and length of treatment do not allow to the synthesis of NASICON as main structure.

The best results are obtained using the set B) of reactants.

In particular, the thermal treatment (5) produces a high pure NASICON, as shown in Figure 5.19 a, where the diffractogram of the powder is reported.

From this powder, it is produced a pellet (20 mm diameter and 0.5 mm thick, Figure 5.19 c) which is sintered at 900°C for 2 hours. In Figure 5.19 b is reported the SEM image of the pellet where the typical NASICON cubes are identified.

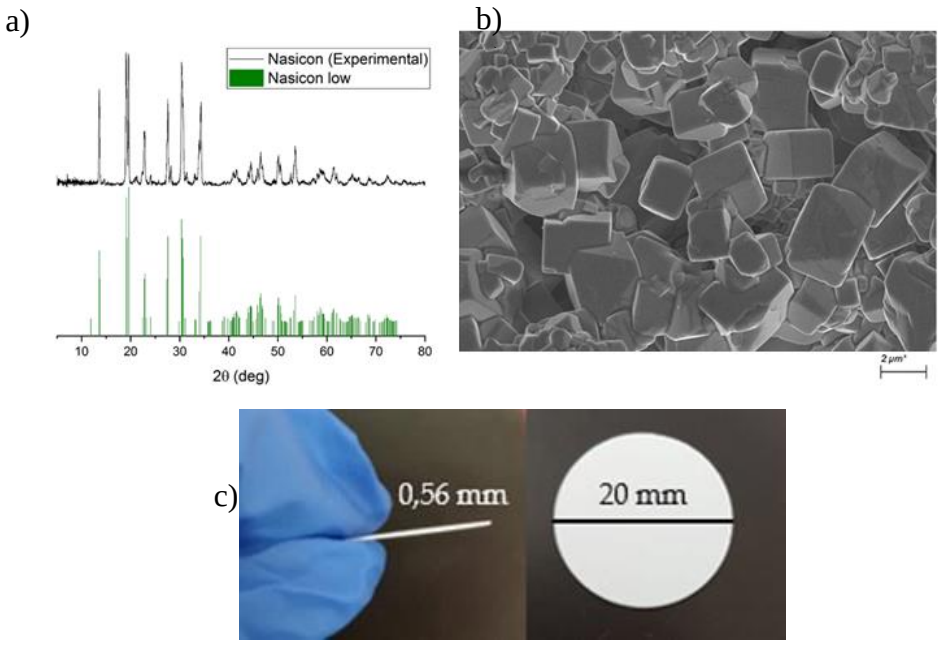

Figure 5.19. a) Diffractogram of NASICON powder obtained after a thermal treatment at 1150°C for 6hours, heating at 5°C/min starting from B) set of reactants. b) SEM image of the membrane obtained from the powder here described and sintered for 2 hours at 900°C; c) thickness and diameter of the resulting pellet.

From EDX (Figure 5.20 a) it is appreciable how all the elements are homogenously distributed on the membrane, demonstrating the NASICON formation. From the peak analysis of EDX (Figure 5.20 b) it is also present aluminum, which is an impurity that affects the power during the synthesis.

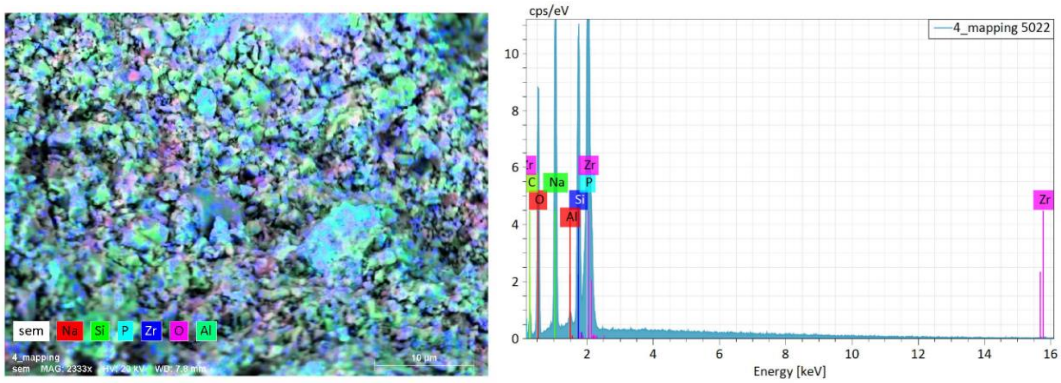

Figure 5.20 a) EDX of the NASICON pellet; b) peaks analysis of EDX measurement.

NASICON-Y and NASICON-La are also synthesized, in order to improve the conductivity of the pure NASICON. In fact, as reported in literature[211,218], the substitution of Zr^{4+} with La^{3+} or Y^{3+} doping, and the concomitant balance of charge with excess of Na^{+}, have resulted in well sintered ceramics having higher conductivities than the conductivity of pure NASICON. The general formula of doped-NASICON becomes $Na_{1+x+y}\,Zr_{2-y}\,Si_x\,D_y\,P_{3-x}\,O_{12}$, where D is the doping element.

NASICON-Y is synthesized starting from SiO_2, $Na_3PO_4 \cdot 12H_2O$, Na_2CO_3, $(ZrO_2)_{0,97}\,(Y_2O_3)_{0,003}$.

All the syntheses of NASICON-Y produce secondary phases in relevant amount as shown in Figure 5.21. In the SEM image (Figure 5.21 b) it can be noticed the typical cube-shape of NASICON structure but, at the same time, another secondary phase, zirconia, is present, affecting the overall structure.

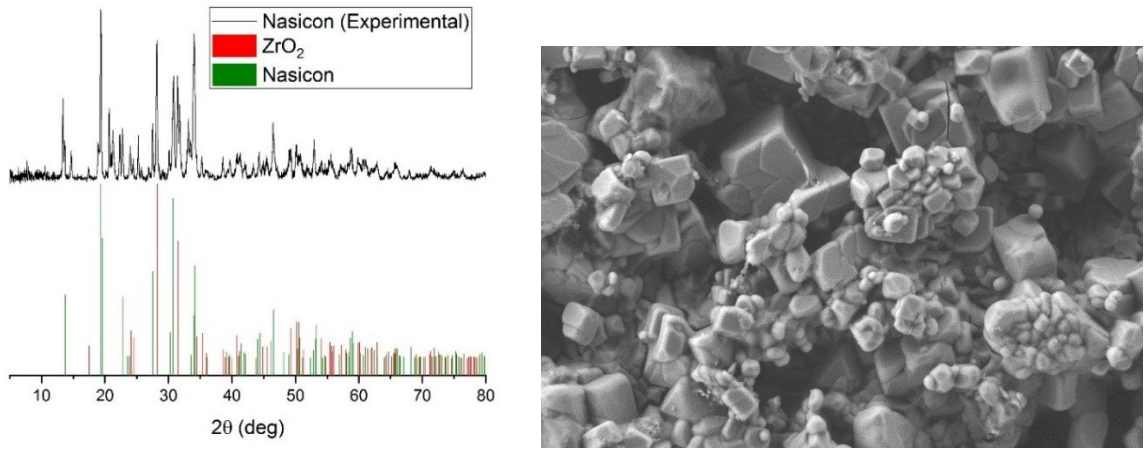

Figure 5.21. a) Diffractogram of NASICON-Y synthesized by a pre-treatment at 700°C for 2 hours, then a calcination treatment at 1150°C for 6 hours. b) SEM image of NASICON-Y pellet after sintering at 900°C for 2 hours.

NASICON-La is synthesized from a mixture of Na_2CO_3, ZrO_2, $NH_4H_2PO_4$, SiO_2 and La_2O_3.

As for NASICON-Y, the powder is pre-treated at 700°C for 2 hours, then it is calcinated for 6 hours at 1150°C heating at 5°C/min. Also in this case, a second phase of zirconia is formed in a relevant amount, affecting all the morphology, as shown in Figure 5.22 b and c.

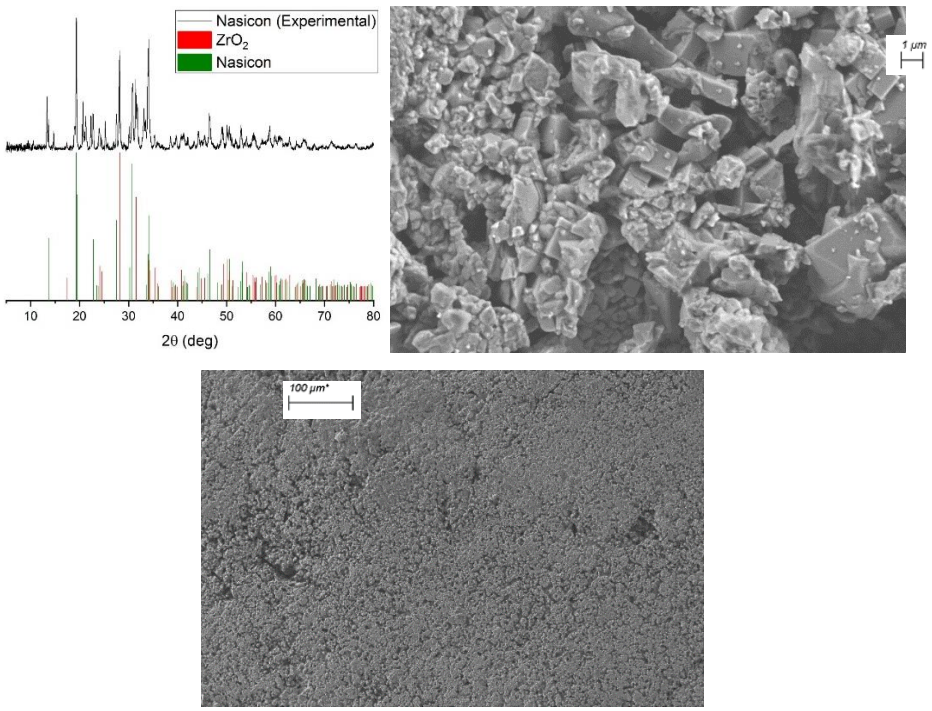

Figure 5.22. a) Diffractogram of NASICON-La and b) and c) SEM images of the pellet after sintering at 900°C for 2 hours.

The three pellets, NASICON, NASICON-Y and NASICON-La are evaluated in terms of density. Using the Archimedes method, the densities of the three pellets before and after the sintering are determined and compared with the literature value (Figure 5.23).

The results shown in Figure 5.23 agree with the XRD and SEM results: NASICON-Y has the higher density due to the presence of zirconia, which affects the overall structure. The reason why NASICON-La has a lower density, even if the structure is affected by a second phase of zirconia, is related to the high porosity of the pellet as shown in the SEM image (Figure 5.22 c).

NASICON and NASICON-Y are tested also to evaluate perm-selectivity and conductivity.

The results agree with the structural and morphological characterization: NASICON has the highest perm-selectivity, due to the compact morphology but it is not enough to find application in the device. NASICON-Y, which has nanometric pores on his surface, has a low perm-selectivity, nearly 60% (Figure 5.24) and even in this case could not be tested in the TRB. The two membranes show also the typical conductive behavior of an ionic conductor, linearly increasing its conductivity with the temperature (Figure 5.25 b). Arrhenius plot is calculated taking into account the resistance of the electrolyte, evaluated as the intercept of the semi-circle at lower frequencies on the x-axe (Figure 5.25 a).

From the Arrhenius plot, it is calculated the activation energy for both NASICON and NASICON-Y: for the first one, the result is in accordance with the literature[219], 31.5 kJ mol^{-1}, but for NASICON-Y, this value is too high, around 55 kJ mol^{-1}.

For all these reasons, these pellets are not tested in the TRB.

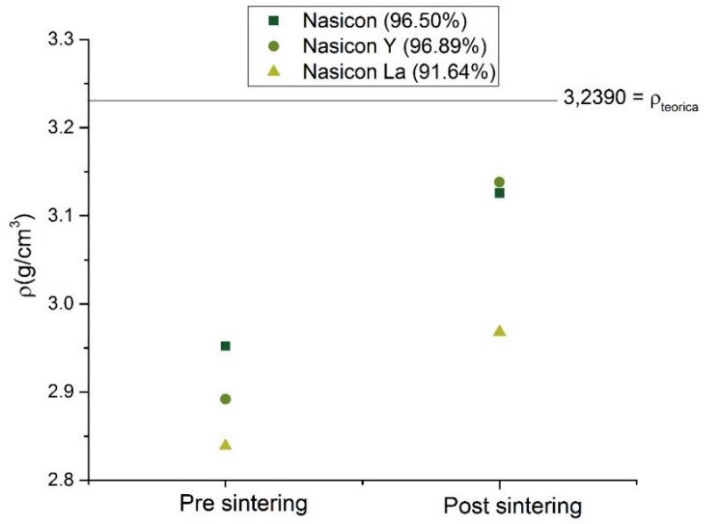

Figure 5.23. Density of the NASICON, NASICON-Y and NASICON-La pellets, pre and after sintering.

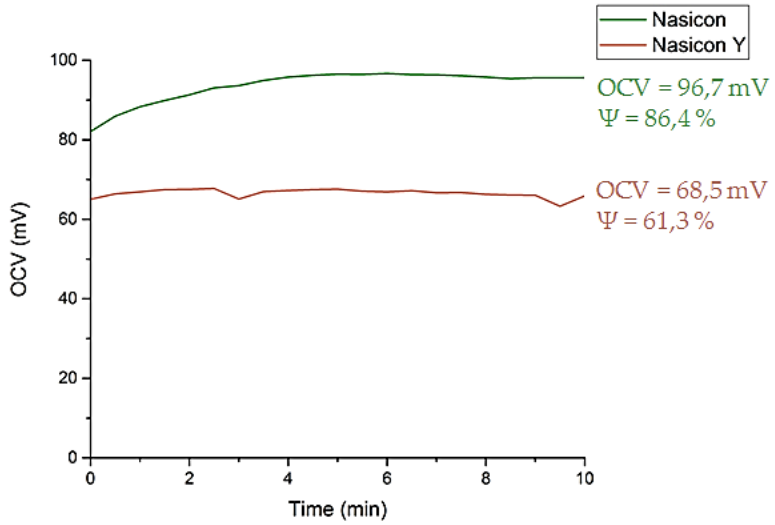

Figure 5.24. Perm-selectivity measurement for NASICON pellet (green line) and NASICON-Y membrane (red line).

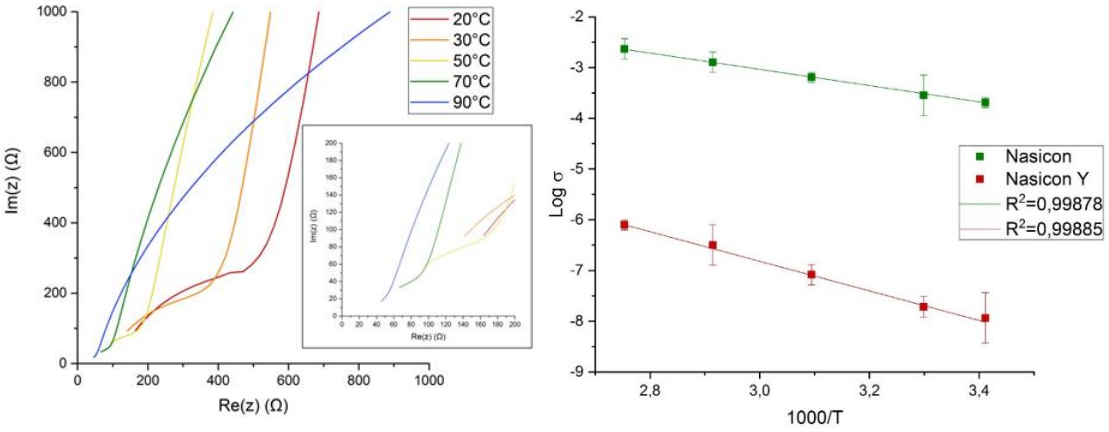

Figure 5.25. a) Nyquist diagram of NASICON pellet at different temperatures, b) Arrhenius plot of NASICON and NASICON-Y.

5.4. Electrochemical characterization

5.4.1. Through-Liquid Exchanger

Through-liquid exchanger is characterized in order to understand its function and all the parameters which affect its performances.

At the beginning, the electrochemical cell is tested without the implementation of TLE, to understand if its presence is necessaire or not.

In Figure 5.26 is reported the discharge of the cell with TLE connected in series to the electrochemical cell, under a constant current of 6.6 mA cm^{-2}. From t_A to t_B, the TLE is disconnected to demonstrate how the operation of the system is affected.

It is easy to note that TRB is able to be discharged for hours if the TLE is connected to the system (initial part) where the slow decrease in voltage is related to the consumption of the concentration gradient between the two compartments. Otherwise, TRB can be discharged only for 20 minutes without the implementation of the TLE due to the depletion of iodine in one half-cell; hence, the voltage drastically decreases to 0V. When the TLE is restored at time t_B, the voltage increases again because of the equilibration of the iodide activity, between the two solutions, by means TLE.

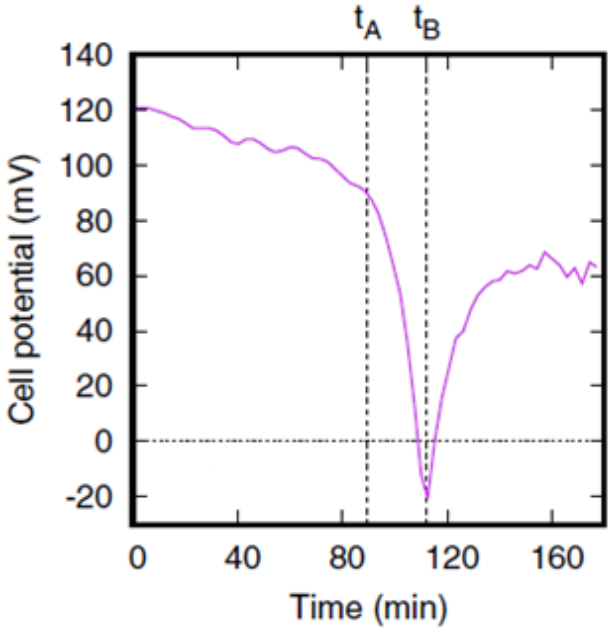

Figure 5.26. Discharge of TRB. From t_A to t_B, TLE is disconnected in order to show its importance for the correct behavior of the TRB.

To show the ability of TLE to exchange iodine and in order to evaluate the time constant of the equilibrium process, two different experiments are performed. The first one, a qualitative experiment, consists in the observation of the color change during the equilibration.

Two different NaI solutions are dropped in the TLE, 2 M solution in the left compartment and 1 M solution in the right side. TLE is then filled with the organic phase and few drops of concentrated solution of I_2 are injected in the left compartment. The water solution in the left side becomes brown-red due to the presence of iodine (Figure 5.27).

Figure 5.27. TLE during the injection of iodine solution in the left side. The bottom of TLE is filled with two water solution of NaI (1M on the left and 2M on the right). The device is then filled with toluene.

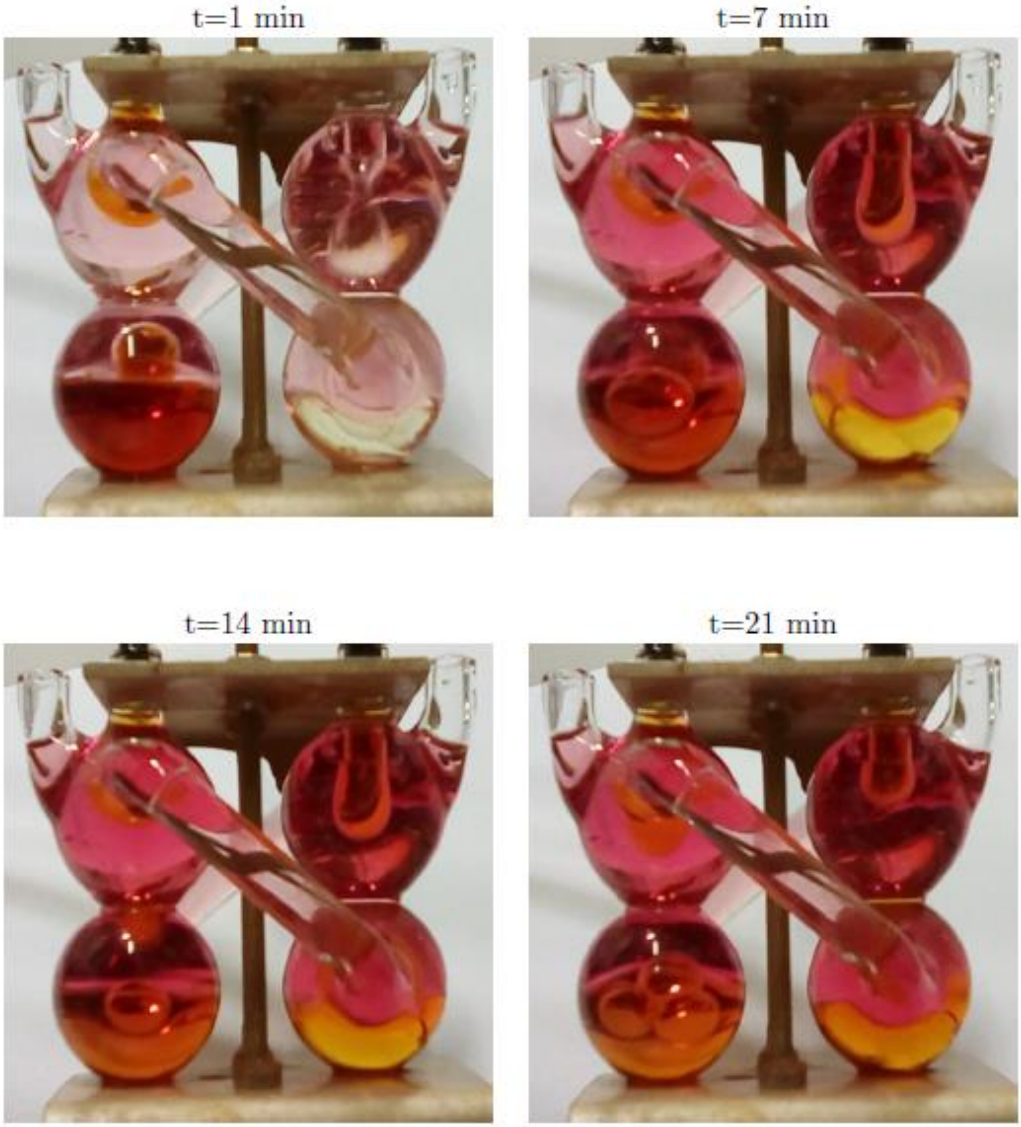

Figure 5.28. TLE at various times after the injection of iodine solution in the left compartment.

After the injection of iodine solution on the left side of TLE, a sequence of pictures is taken and showed in Figure 5.28.
Toluene, which is colorless, becomes pink and then red in the first minute, after the injection of iodine solution in the left compartment: this means that iodine dissolves in toluene.
In nearly 7 minutes, the NaI solution in the right sides becomes yellow, and, after 20 minutes, the two NaI solutions show the same brown-red color due to the iodine diffusion from the toluene to the NaI solution in the right compartment.

In addition, a quantitative experiment is performed, in order to the determine the time constant of the process.
Two solutions of NaI + I_2, 1.75% molar fraction, and 1.25 mM of I_2, respectively, are injected in the electrochemical cell connected to the TLE. Two measurements are conducted: the first one, without the organic phase in the TLE (TLE works only as a reservoir for the two solutions) and the second one with the TLE filled with a solution of I_2 1.25 mM in toluene.
A 0.7 mA cm^{-2} constant current is applied to the electrochemical cell for 7.5 minutes. This driving force induces to an iodine concentration difference between the two compartments of 0.8 mM.
Under these operational conditions, the NaI concentrations do not change significantly, since the initial values are so much larger that concentrations are not influenced by the small, transferred charge. Therefore, the final open circuit voltage, which is monitored during the experiment, depends only on the activity of iodine as follow:

$$OCV = \frac{RT}{2F} ln\left(\frac{a_{I_2}^1}{a_{I_2}^2}\right) \quad (5.22)$$

Where the superscripts *1* and *2* refer to the solution enriched and depleted in iodine, respectively. As it can be noticed in Figure 5.29, while the curve obtained without toluene stabilizes to a non-vanishing voltage, the curve obtained with toluene decays with time.
The reason why of these different behaviors is related to the TLE: in the first case, without the organic solvent, iodine is not equilibrated between the two solutions, therefore, a concentration difference of iodine involves a higher voltage compared to the second case, where iodine is equilibrated and thus, has the same activity in both the solution.
A theoretical curve is also reported in Figure 5.29 (dashed line), which is obtained assuming that the concentration difference decays exponentially.
Starting from the initial value of 1.25 mM, c_0, the concentration of I_2 in the two compartments changes after the application of the constant current as follow:

$$c_{I_2}^1 = c_0 + \frac{\Delta c_0}{2} \quad (5.23)$$

$$c_{I_2}^2 = c_0 - \frac{\Delta c_0}{2} \quad (5.24)$$

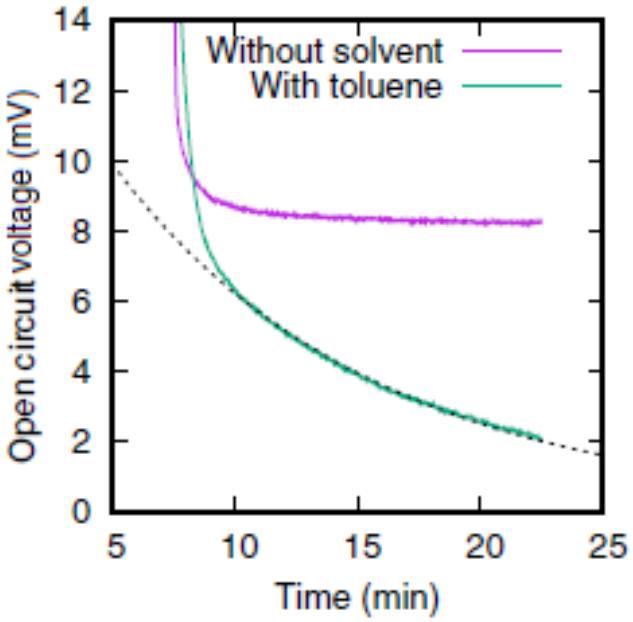

Figure 5.29. Measurement of the OCV during the time after the application of a constant current of 0.7mA cm^{-2} for 7 minutes, in a TRB filled with two NaI solution at 1.75% molar fraction and 1.25mM of I_2 using an empty TLE (purple) and a toluene filled TLE (green). The dashed line represents the fit of the theoretical curve.

TLE equilibrates the iodine concentrations between the two solutions exponentially:

$$c_{I_2}^1 = c_0 + \frac{\Delta c_0}{2} e^{-\frac{t}{\tau}} \quad (5.25)$$

$$c_{I_2}^2 = c_0 - \frac{\Delta c_0}{2} e^{-\frac{t}{\tau}} \quad (5.26)$$

Where τ is the constant time of the iodine equilibrium in the TLE and t is the time from the opening of the circuit. Equation 5.22 can be approximated as:

$$OCV = \frac{RT}{2F} ln\left(\frac{a_{I_2}^1}{a_{I_2}^2}\right) = \frac{RT}{2F} ln\left(\frac{c_{I_2}^1}{c_{I_2}^2}\right) \quad (5.27)$$

If equations 5.25 and 5.26 are substituted in equation 5.27, and the terms c_0 and $\frac{\Delta C_0}{2}$ are collecting in a unique parameter α which is equal to $\alpha = \frac{\Delta C_0}{2C_0}$, the result is:

$$OCV = \frac{RT}{2F} \ln\left[\frac{1 + \alpha e^{-\frac{t}{\tau}}}{1 - \alpha e^{-\frac{t}{\tau}}}\right] \quad (5.28)$$

The function 5.28 is fitted in the experimental results in order to determine the time constant of the iodine equilibrium mediated by TLE and it corresponds to 11 minutes.

The complete equilibration of the iodine chemical potential requires ideally infinite time. In real conditions, a chemical potential difference of iodine between the two compartments it will be present.

This is due to the operational limits of the TLE. Therefore, the potential is different from the one calculated in equation 5.15 and this difference is equal to

$$\delta E_{TLE} = \frac{(\mu_{I_2}^{H} - \mu_{I_2}^{L})}{2} \quad (5.29)$$

The voltage difference due to the chemical potential difference of iodine is similar to the mass transport overvoltage, despite the fact that this process does not take place at the electrode surface but in the TLE hence, outside the electrochemical cell. In the limit of low values of current, equation 5.29 can be linearized:

$$\delta E_{TLE} = IR_{TLE} \quad (5.30)$$

The resistance of TLE is estimated to be equal to 0.8 Ω which is a small value compared with the measured resistance of the entire electrochemical cell (see section 5.4.3.). This means that TLE does not significantly affect the performance of the TRB because it is not the limiting element of the system. Moreover, the iodine equilibration takes place fast enough for the operating conditions and therefore, TLE is an essential part of the successful operation of the TRB.

To determine the R_{TLE} value, it is necessary also to consider the iodine complexation, which takes place whenever iodine is dissolved in water in the presence of iodide ions:

$$I_2 + I^- \rightleftarrows I_3^-$$

At the equilibrium, if TLE perfectly works, the chemical potential of iodine in the *H* and *L* solutions would be the same:

$$\mu_{I2}^{H,0} = \mu_{I2}^{L,0} \quad (5.31)$$

The superscript "*0*" refers to the equilibrium quantities.

Considering the reaction of iodine complexation, the chemical potential of triiodide is equal to:

$$\mu_{NaI}^{H} + \mu_{I2}^{H} = \mu_{NaI3}^{H} \quad (5.32)$$

$$\mu_{NaI}^{L} + \mu_{I2}^{L} = \mu_{NaI3}^{L} \quad (5.33)$$

By subtracting equation 5.33 from equation 5.32 and considering the equilibrium conditions:

$$\mu_{NaI}^{H} + \mu_{I2}^{H} - \mu_{NaI}^{L} - \mu_{I2}^{L} = \mu_{NaI3}^{H} - \mu_{NaI3}^{L} \quad (5.34)$$

$$\mu_{NaI}^{H,0} - \mu_{NaI}^{L,0} = \mu_{NaI3}^{H,0} - \mu_{NaI3}^{L,0} \quad (5.35)$$

During the operation of the cell, a chemical potential difference of iodine is developed which represents the overvoltage of the TLE diffusion:

$$\mu_{I2}^{H} - \mu_{I2}^{L} = \mu_{NaI3}^{H} - \mu_{NaI3}^{L} - \mu_{NaI}^{H} + \mu_{NaI}^{L} = F\delta E_{TLE} \quad (5.36)$$

Since the amount of NaI exceeds the amount of iodine and triiodide in both the diluted and concentrated solutions, the chemical potential of sodium iodide can be considered the same as in equilibrium. Therefore, considering equation 5.36, the TLE diffusion overvoltage can be expressed as:

$$F\delta E_{TLE} = \mu_{NaI3}^{H} - \mu_{NaI3}^{L} - \mu_{NaI3}^{H,0} + \mu_{NaI3}^{L,0} \quad (5.37)$$

Using the approximation for the ideal solution:

$$\delta E_{TLE} = \frac{RT}{F} \ln\left(\frac{c_{NaI3}^{H}\, c_{NaI3}^{L,0}}{c_{NaI3}^{L}\, c_{NaI3}^{H,0}} \right) \quad (5.38)$$

In order to evaluate the resistance related to the TLE diffusion overvoltage, the limit for vanishing current has to be determined. In this condition, the amount of NaI_3 changes with respect to the equilibrium value of a small quantity, δc_{NaI3}, if the volumes of the diluted and concentrated solutions are assumed to be the same, *V*. In this way, the variation of concentration is the same in the two solutions when a given amount of solute is changed from one solution to the other one.

$$\delta E_{TLE} = \frac{RT}{F} \ln\left(\frac{c_{NaI3}^{H,0} + \delta c_{NaI3}}{c_{NaI3}^{L,0} - \delta c_{NaI3}} \right) \frac{c_{NaI3}^{L,0}}{c_{NaI3}^{H,0}} \quad (5.39)$$

By approximating at the first order in $\delta c/c^{0}$, equation 5.39 becomes:

$$\delta E_{TLE} = \frac{RT}{F} \left(\frac{1}{c_{NaI3}^{H,0}} + \frac{1}{c_{NaI3}^{L,0}} \right) \delta c_{NaI3} \quad (5.40)$$

The flux of iodine (Φ_{I2}) in TLE is proportional to the concentration difference of iodine and it is defined as:

$$\Phi_{I2} = VK(c_{I2}^{H} - c_{I2}^{L}) \quad (5.41)$$

Where *K* is a constant depending on the TLE performances. The concentration difference of iodine is linear with δc_{NaI3}:

$$\Phi_{I2} = VK'\delta c_{NaI3} \quad (5.42)$$

To understand the physical meaning of *K'* it is necessary to consider that iodine is present in solution as the complex NaI_3, therefore the iodine flux mostly alters the concentration of NaI_3:

$$-\Phi_{I2} = V\delta c_{NaI3} \quad (5.43)$$

Thus, taking in account equation 5.42 and 5.43 the result is a differential equation:

$$\delta c_{NaI3} = -K'\delta c_{NaI3} \quad (5.44)$$

K' is the reciprocal of the characteristic time constant of the iodine equilibration in the TLE: ($1/\tau_{TLE}$). As it has already discussed, τ_{TLE} is known from experimental measurements and it is around 11 minutes.

In stationary conditions, the current, which flows through the cell, is related to the iodine flux:

$$I = 2F\Phi_{I2} = \frac{2VF}{\tau_{TLE}}\,\delta c_{NaI3} \quad (5.45)$$

Combining the last equation with equation 5.40:

$$\delta E_{TLE} = \frac{RT}{F}\left(\frac{1}{c_{NaI3}^{H,0}} + \frac{1}{c_{NaI3}^{L,0}}\right)\frac{\tau_{TLE}}{2VF} I \quad (5.46)$$

Defining the resistance of the diffusion process in the TLE as:

$$R_{TLE} = \frac{RT}{F}\left(\frac{1}{c_{NaI3}^{H,0}} + \frac{1}{c_{NaI3}^{L,0}}\right)\frac{\tau_{TLE}}{2VF} \quad (5.47)$$

The TLE diffusion overvoltage becomes

$$\delta E_{TLE} = R_{TLE} I \quad (5.48)$$

Assuming that iodine is completely depleted in the diluted compartment, an equivalent of the diffusion limiting current can also be calculated.

Knowing that the iodine flux is

$$\Phi_{I2} = \frac{V}{\tau_{TLE}} c_{NaI3}^{H,0} \quad (5.49)$$

This flux is able to provide the amount of iodine necessary for a current flowing stationary:

$$I = 2F\Phi_{I2} = \frac{2VF}{\tau_{TLE}} c_{NaI3}^{H,0} \quad (5.50)$$

5.4.2. Maximum Current Density / Maximum Power Density

Experiments are conducted to test the electrochemical cell alone, without the TLE, to evaluate some general parameters like the open circuit voltage, the maximum power density and maximum current density that the system may achieve.

All the experiments in this section are performed for short time to avoid chemical consumption of the species. The electrochemical cell is filled with two solutions at molar fractions 17.5% and 1.75%, respectively, and heated at 90°C.

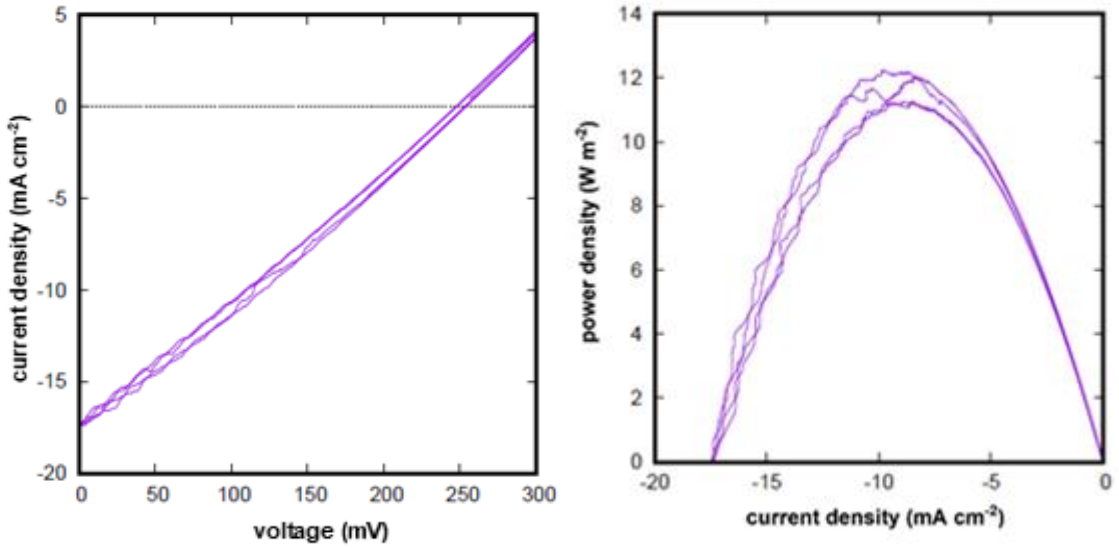

Figure 5.30. a) Cyclic voltammetry of the electrochemical cell; b) power density as a function of the current density.

Figure 5.30 a shows the result of the cyclic voltammetry.

The observed open circuit voltage is 245 mV, in accord with the theoretical value obtained by Nernst equation using the activity coefficients reported in literature[191].

The maximum current density reaches 17.5 mA cm^{-2}, while the maximum power density is approximately 1.2 mW cm^{-2} (12 W m^{-2}) and it is reached at a current density of around 8.5 mA cm^{-2} (Figure 5.30 b).

The profile of the cyclic voltammetry is linear: this means that the behavior of the cell is almost completely resistive. The resistance, evaluated by the fitting of the recorded cyclic voltammetry, is 14 Ω cm^{-2}. From the characterization of the NASICON membranes, its conductivity at 90°C results equal to 5 mS cm^{-1}. Thus, the membrane has a resistance of 10 Ω cm^{-2}, while further 1.3 Ω cm^{-2} are related to the electrical connections of the electrodes. Therefore, it can be concluded that the observed resistance is almost completely attributed to the Ohmic contribution of the NASICON membranes.

5.4.3. Discharge and Model

Several experiments are performed, carried on with different membrane samples and solutions in order to evaluate the electrical energy released during the discharge process.

Before any discharge process, the resistances of the electrochemical cell are evaluated by electrochemical impedance analysis (PEIS). The typical spectrum is reported in Figure 5.31.

The intercept at higher frequencies represents the resistance of the electrolyte, that means of NASICON diaphragms. This value, 6.4 Ω, is exactly the expected one considering three membranes connected in parallel. In this type of circuit, the equivalent resistance is the sum of the reciprocal resistances and any NASICON diaphragm has a resistance of nearly 20 Ω.

Two typical discharged profiles are reported in Figure 5.32, obtained at two different current densities: 5.3 mA cm^{-2} (orange profile) and 6.7 mA cm^{-2} (purple profile).

These currents have been chosen in order to work closer to the maximum power density but, at the same time, without sacrificing the electrochemical efficiencies.

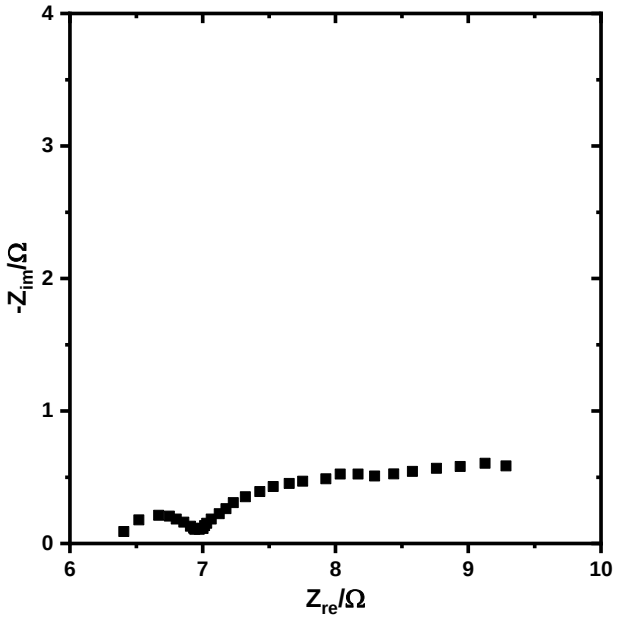

Figure 5.31. Electrochemical impedance spectrum of the electrochemical cell filled with H and L NaI solutions at 17.5% and 1.75% molar fractions, respectively.

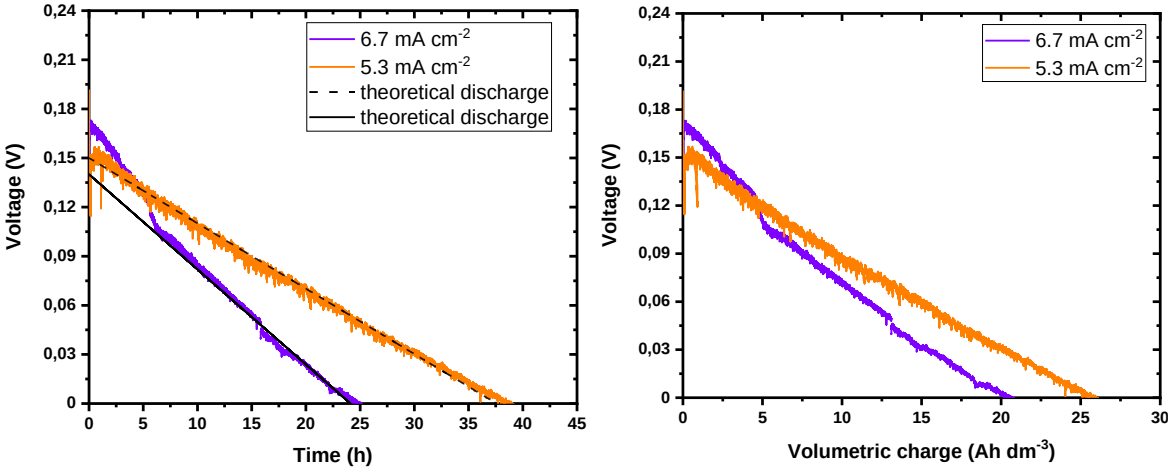

Figure 5.32. Complete discharge of the cell under an applied current of 6.7 mA cm^{-2} (violet curve) and 5.3 mA cm^{-2} (orange curve): a) voltage vs time and b) voltage vs volumetric capacity. In the graph a is also reported the theoretical discharge in black (solid line: under 6.7 mA cm^{-2} current; dashed line: under an applied current of 5.3 mA cm^{-2}).

The voltage decreases almost linearly with time: in fact, under the operating conditions, the chemical potentials of sodium iodide depend linearly on the concentration itself due to the non-ideality of the solutions.

The discharge process lasts until the cell voltage vanishes: the discharge under the higher current, 6.7 mA cm^{-2} requires 25 hours while the discharge under lower current, 5.3 mA cm^{-2}, lasts almost 39 hours. At this point, the open-circuit voltage is not yet zero because the solutions have not reached the same activities; however, the power production becomes negative due to the overvoltage.

Visible fluctuations of the voltage are noticed which are related to the formation of air bubble in the electrochemical cell. These bubbles are formed by the release of dissolved air occurring in the high-temperature part of the hydraulic circuit.

The system extracts nearly 21 Ah dm^{-3} in the experiment at higher current and 26 Ah dm^{-3} in the second experiment, even if it lasts fourteen hours more.

The solid and dashed black lines, reported in the Figure 5.32 a, are the theoretical discharges, obtained with the following approximated equation:

$$E(t) = \Delta E^0_{OCV}\left[1 - \frac{(I + I_L)t}{Q}\right] - RI \quad (5.51)$$

Where *t* is the time, ΔE^0_{OCV} is the initial value of the open circuit voltage, *I* is the current, *R* the resistance, *Q* is the electrical charge necessary to fully discharge the cell and I_L represents the leakage of charge due to parasitic processes. In fact, in this system, the unwanted passage of solution through the porosity of the NASICON membrane and the unwanted passage of water through the organic solvent may occur.

E(t) represents the discharge of the cell: it is assumed that the voltage decreases linearly with the time during the discharge since the chemical potentials of the salt are approximately linear in concentration in the used solutions. Finally, the term *RI* represents the ohmic drop.

The values of the parameters used in Equation 5.51 are reported in the next table.

I	*I*	ΔE^0_{OCV}	*Q*	I_L	*R*
5.3 mA cm^{-2}	*8 mA*	*250 mV*	*2480 C*	*3 mA*	*12.5 Ω*
6.7 mA cm^{-2}	*10 mA*	*250 mV*	*2480 C*	*6 mA*	*11 Ω*

Table 5.1. Values of the parameters used to calculate the theoretical discharge profiles of the TRBs.

The total duration of the discharge is the time t_f at which $E(t_f)$ = 0V.

By solving equation 5.49 for $E(t)$= 0V:

$$t_f = \left[1 - \frac{RI}{\Delta E^0_{OCV}}\right]\frac{Q}{(I + I_L)} \quad (5.52)$$

From the model, the total duration of the discharge under an applied current of 5.3 mA cm^{-2} is nearly 38 hours while the discharge under 6.7 mA cm^{-2} requires almost 24 hours.

The produced electrical energy *W* is:

$$W = \int_0^{t_f} E(t) I \, dt \quad (5.53)$$

Expressing *E(t)* as reported in equation 5.51 and solving the integral:

$$W = \left(\Delta E^0_{OCV} - RI\right) I t_f - \Delta E^0_{OCV} \frac{(I + I_L)}{2Q} I t_f^2 \quad (5.54)$$

Using equation 5.50 to express t_f :

$$W = \frac{1}{2}\left(\Delta E^0_{OCV} - RI\right)^2 \frac{Q}{\Delta E^0_{OCV}} \frac{I}{(I + I_L)} \quad (5.55)$$

The results are W = 81 J (6750 J L^{-1}) for the experiments under an applied current of I = 5.3mA cm^{-2} and W = 61 J (5083 J L^{-1}) for the second experiment where the applied current is I = 6.7 mA cm^{-2}. By using the free energy calculated from tabulated activity coefficients, 272 J (22666 J L^{-1}), the resulting electrochemical efficiencies are 30% and 22%, respectively, which are actually closed to the final points reported in Figure 5.33.

This means that the approximate model is accurate enough for this analysis.

In Figure 5.33 are reported the performances measured in the experiments. The abscissa represents the efficiency of the electrochemical cell (η_C) while the ordinate is the integral average power density (p).

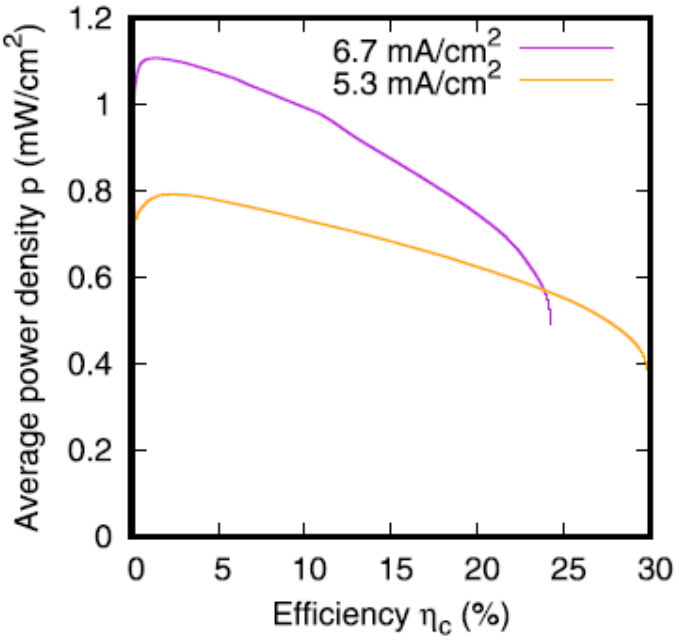

Figure 5.33. Average power density vs efficiency for the discharge process under an applied constant current of 6.7 mA cm^{-2} (violet curve) and 5.3 mA cm^{-2} (orange curve).

The efficiency is determined as:

$$\eta_{C=} \frac{\int_0^{t_f} P_C\,(t)dt}{\Delta G} \quad (5.56)$$

Where t_f is the duration time of the experiment, $P_c(t)$ is the instantaneous power at the time t, and ΔG is the mixing free energy of the two solutions that filled the cell. The average power density, reported on the vertical axe, is determined by the following equation:

$$p(t_f) = \frac{\int_0^{t_f} P_C(t)dt}{St_f} \quad (5.57)$$

The curves reported in Figure 5.33 are obtained parametrically in t_f: each point represents a different duration time of the experiment. Increasing the duration time increases the electrochemical efficiency but decreases the power density.

In the discharge at low current density, the electrochemical efficiency is up to 30%. Part of the energy is lost due to the ohmic resistance of the NASICON. The consumed energy by resistance, is around 55-60% of the available free energy. The remaining loss, of the order of 10-20%, is likely due to parasitic processes such as the dissolution of water in toluene in TLE or the passage of solution through the porosity of the NASICON membrane.

In an ideal quasi-equilibrium conditions, with I_L = 0V and $I \rightarrow 0$, the maximum energy that can be extracted, W_0 is:

$$W_0 = \frac{1}{2} Q \Delta E_{OCV}^0 \quad (5.58)$$

The efficiency is defined as:

$$\eta_C = \frac{W}{W_0} = \left(1 - \frac{RI}{\Delta E_{OCV}^0}\right)^2 \frac{I}{I + I_L} \quad (5.59)$$

The produced electrical energy is the difference between the maximum energy that can be extracted and the energy loss which is distinguished in two different contributions as reported in the following equation:

$$W = W_0 - W_R - W_L \quad (5.60)$$

Where W_R identifies the energy loss due to the ohmic drop:

$$W_R = QRI \left(1 - \frac{RI}{\Delta E_{OCV}^0}\right) \quad (5.61)$$

While W_L identifies the energy loss due to charge leakage and it is defined as:

$$W_L = (W_0 - W_R) \frac{I_L}{I + I_L} \quad (5.62)$$

In the next table are resumed the resulting values for the produced energy, the energy losses due to ohmic drop and charge leakage, in the two experiments performed at different currents.

In the table 5.2 are reported the percentage of produced energy and energy losses in the two experiments respect to the total energy.

EXPERIMENT	W (kJ L^{-1})	W_R (J L^{-1})	W_L (J L^{-1})
5.3 mA cm^{-2}	6.8	12.4	2.8
6.7 mA cm^{-2}	5.0	12.7	3.7

Table 5.2. Values of the produced energy and energy losses during the discharge processes.

What it can be easily noticed is that 20-30% of the energy is actually extracted in the two experiments, while 55-60% is dissipated due to the ohmic drop.

The rest 10-18% is lost due to leakage likely unwanted passage of solution through NASICON membrane or unwanted dissolution of water in toluene due to the higher solubility at higher temperature.

EXPERIMENT	W (%)	W_R (%)	W_L (%)
5.3 mA cm^{-2}	30.79	56.45	12.75
6.7 mA cm^{-2}	23.53	59.15	17.32

Table 5.3. Percentage of the produced energy and energy losses during the discharge processes.

5.5. Evaluation of Distillation and Efficiency

To regenerate the concentration difference of the solutions, the exhausted solution undergoes to a thermal separation. The thermal separation considered for this type of device is the vacuum distillation technology. The solution is in contact with a heat exchanger, which brings the heat from the heat source. The solution boils and concentrates while its vapor is condensed on a second heat exchanger.

In a vacuum distiller, the inside pressure is lowered, therefore the boiling occurs at lower temperature. After the initial evacuation, no mechanical work is required for keeping the vacuum. Connecting several stages in series, a multiple-effect distiller is obtained: in this device, the condensation heat from one effect is used as the heat input for boiling in the following.

The rate of production of mixing free energy of the solutions is defined as the power output of the distiller, P_D, while the efficiency of the distiller is defined as:

$$\eta_D = \frac{\Delta G}{Q} \quad (5.63)$$

Where Q is the heat provided by the heat sources and ΔG is the mixing free energy of the solutions.

Another important parameter to evaluate the distillation process is the size of the distiller, s, which is determined by the following equation:

$$s = \frac{S}{P_D} \quad (5.64)$$

Where S is the surface of the heat exchanger and P_D is the distiller power output, defined as the mixing free energy of the produced solutions per unit of time.

Vacuum distillation technique has been already explained at page 35 and a simplified model has been previously discussed in the thermodynamic section (2.3.2.) starting from models presented in literature[89,110,111]. The main parameters determining the efficiency of the thermal separation are the boiling point elevation, ΔT_{BP}, and the temperature difference across the heat exchanger, ΔT_{HE}, which is assumed to be constant during the distillation.

This thermodynamic model is used to evaluate the consumed heat, the number of effects and the surface of the heat exchangers for a vacuum distiller working with a solution of NaI 17.5% molar fraction, the solution experimentally studied in the TRB, and a solution of NaCl 8.6% molar fraction, a typical solution used in other distillation-SGP devices.

The parameters are calculated for a distiller power output of 1 kW in the form of mixing free energy of the solutions. Different ΔT_{HE} are considered during the parameter valuations (Figure 5.34).

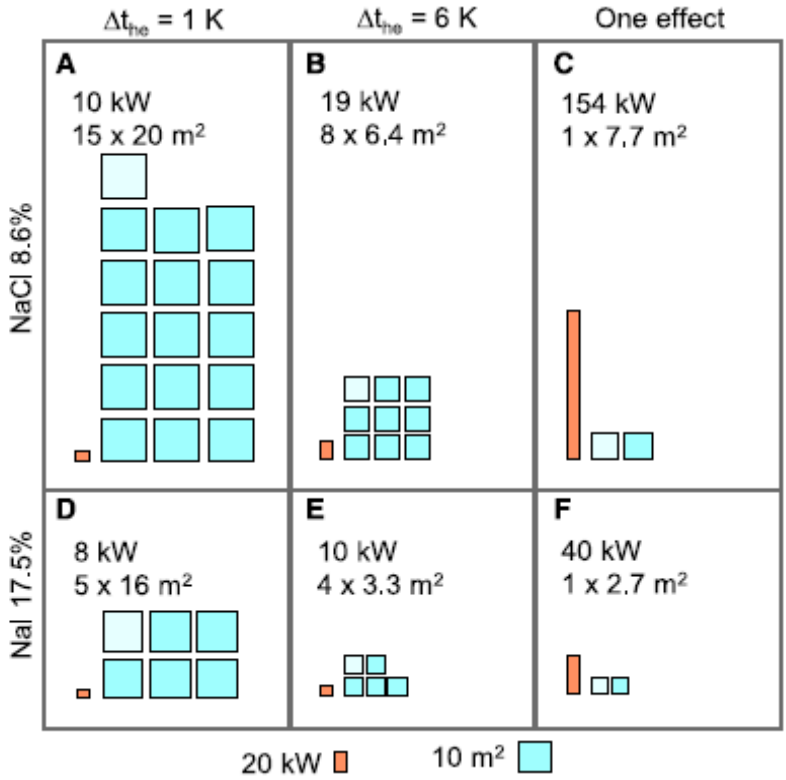

Figure 5.34. Parameter evaluation of a vacuum distiller to produce 1kW in the form of mixing free energy of solutions. The cyan square represents an effect, the pale cyan square represents the heat exchanger with the heat source. The surface of the squares is proportional to the surface of the heat exchanger of the effect. The orange bar represents the heat required by the distiller. The heat source is at 100°C (T_H) and the heat sink is at 25°C (T_L). The salt is NaCl (A-C) 8.6% molar fraction (ΔT_{BP} =5°K); NaI (D-F) 17.5% molar fraction (ΔT_{BP} = 17°K). Three different ΔT_{HE} are considered: ΔT_{HE} = 1°K in the cases A and D; ΔT_{HE} =6°K in the cases B and E; ΔT_{HE} =27°K in the case F; ΔT_{HE} =35°K in the case C. In the cases C and F, only one effect is used.

The first thing to notice is that values of ΔT_{HE} lower than 5°K are considered practically unfeasible: at the same time, increasing ΔT_{HE} also increases the heat consumption even if the dimension of the distiller decreases because the distiller requires a lower number of effects and a smaller surface for the heat exchangers.

Figure 5.34 also shows how the distillation of NaI solution gives always better performances compared to the NaCl solution distillation. This is easily noticed in the case B and E, when ΔT_{HE} = 6°K, a reasonable value for a real heat exchanger.

To evaluate the efficiency, the energy required for pumping the solutions through the electrochemical cell and the TLE are neglected, as reported in equation 5.3:

$$\eta = \eta_{el} \cdot \eta_{dis} \quad (5.3)$$

Considering a 4-effects distillation of a 17.5% molar fraction NaI solution, the distillation efficiency (η_{dis}) is equal to 10% with 16.5 m^2 of heat exchanger and a ΔT_{HE} = 6°K. The electrochemical efficiency (η_{el}) is equal to 30%, the result of the discharge process. Therefore, the overall heat conversion efficiency (η) is 3%.

The same heat conversion efficiency of 3% is obtained for a NaCl solution using 15 effects and a heat exchanger with a surface of 320 m^2 and an unfeasible ΔT_{HE} of 1°K.

5.6. Conclusion and future developments

A new kind of device is developed in order to convert LTH in electricity by means a redox-flow cell which is coupled with a vacuum distiller; this system is called Thermally Regenerable Battery.

The redox-flow battery releases electricity at the expense of two water solutions of NaI at different concentrations with a small concentration of iodine.

Iodine is always in equilibrium between the two NaI solutions thanks to the implementation of a new-technology called Through-Liquid Exchanger. This system is connected in series to the redox-flow cell and operates continuously with a mechanism typical of any liquid-liquid extraction.

The overall efficiency of the technology, combining both the electrochemical part and the thermal process, is 3%. This is one of the highest values obtained in this field considering realistic operational conditions.

To demonstrate the practical feasibility of the device proposed in this project, a preliminary study of a possible household plant is reported.

Considering a plant able to provide 1 kW of electrical power during the time of the availability of heat, and the operational conditions obtained during the discharge experiments (η_{el}=30%; P = 4 W m^{-2}; see Figure 5.30/ 5.32), if an overall surface membranes of 250 m^2 is implemented, which fits into a reactor of 200 L, the volume of the solutions can be, as an example, 40 L in the electrochemical cell (20 L for the *H* and *L* solutions, respectively), 40 L in the TLE (20 L for the *H* and *L* solutions, respectively) and 20 L in an external reservoir, from which the solutions are recirculated.

The amount of NaI is around 100 kg, with a cost of nearly 200-300 €. The heat input should be around 33 kW, which could be provided by a surface lower than 40 m^2 of state-of-the-art solar heat collectors with selective adsorbers and low concentration non-imaging optics.

It is clear that such figures refer to the preliminary results: significant improvements are foreseeing in the near future: using alternative more inexpensive salts will decrease the costs but, in some cases, will also increase the performance of the device.

CHAPTER 6

Thermally Regenerable Redox-Flow Battery based on LiBr

6.1. General Principles

Thermally-Regenerable Redox-Flow Battery is a system suitable to exploit the salinity gradient of aqueous solutions of lithium bromide. This halide shows higher boiling point elevation compared to iodide salts. The solubility of lithium bromide is also higher (1167g L^{-1}), which results in higher mixing free energy.

The overall idea consists, as for TRB based on NaI, in an electrochemical cell filled with two water solutions of LiBr/Br_2, at different concentrations. In the concentrated (*H*) compartment, the halide reacts to form the halogen, while, on the other compartment, the opposite reaction takes place.

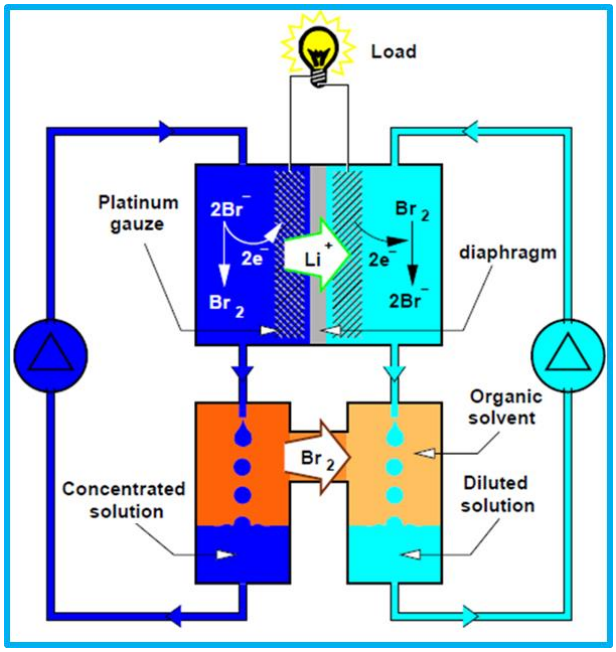

Figure 6.1. Scheme of the electrochemical cell and TLE based on LiBr solutions.

$$H: \quad Br^- + e^- \rightarrow \frac{1}{2} Br_2 \ (6.1)$$

$$L: \quad \frac{1}{2} Br_2 \rightarrow Br^- + e^- \ (6.2)$$

To maintain the electroneutrality, lithium ions move from the *H* compartment to the *L* one, through the electrolyte, a NASICON-like diaphragm (LICGC™). The cation-selective exchange membrane does not allow the passage of water, bromine, and bromide between the two solutions.

Here too, the so called “Through-Liquid Exchanger” is required to keep in equilibrium the bromine activity between the two solutions. In this way, the voltage does not depend on the activity of the halogen, which is complicated to determine.

At the same time, TLE allows that a redox couple is always present in both the compartments of the electrochemical cell. In fact, bromine is less soluble in water than lithium bromide: this means that bromine is the limiting agent of the redox process.

Thanks to the TLE, bromine is recirculated from the *H* compartment, where it is produced, into the *L* compartment, where it is consumed, maintaining the same activity value in the two sides.

6.2. Thermodynamic / Kinetic discussion

As already discussed for the TRB based on NaI, the total efficiency of the device depends on the efficiency of the electrochemical cell (η_{el}) and the efficiency of the distillation unit (η_{dis}):

$$\eta = \eta_{el} \cdot \eta_{dis} \quad (6.3)$$

The efficiency of the electrochemical unit is expressed as

$$\eta_{el} = \frac{W}{\Delta Gmix} \quad (6.4)$$

Where W is the extracted work from the cell and $\Delta Gmix$ is the mixing free energy of the two solutions and it is determined as a difference between the Gibbs free energy of the exhausted solution (G_f) and the sum of the Gibbs free energy of the H and L solutions, as reported in equation 6.5.
$\Delta Gmix$ represents the maximum energy that can be obtained if the electrochemical process is ideal and reversible:

$$\Delta G_{mix} = G_f - G_i = n_{tot}\mu_f - (n_H\mu_H + n_L\mu_L) \quad (6.5)$$

Therefore, to increase the mixing free energy that can be stored/extracted by the electrochemical cell it is necessary choose two solutions with a higher concentration difference.
The distillation efficiency is again defined as:

$$\eta_{dis} = \frac{\Delta Gmix}{Q_H} = \frac{n_W\lambda \cdot (1 - \frac{T_W}{T_s})}{n_W\lambda} \quad (6.6)$$

where Q_H is the absorbed heat from the heat sources, n_W are the moles of solvent that must evaporate; λ is the latent heat of evaporation; T_W is the boiling point of pure water; T_s is the boiling point of the LiBr solution.
To increase the efficiency of the heat conversion, thermodynamic analysis evidence the importance to increase the boiling point elevation of the implemented solutions compared to the pure solvent[89,110], as reported in equation 6.6. Moreover, equation 6.6 point out as a solvent with a large latent heat of evaporation leads to an increasing of the mixing free energy even if it also corresponds to an increase of the thermal energy consumption from the heat source.
Therefore, from a thermodynamic point of view, water solution of lithium bromide is the easiest choice because the high latent heat of evaporation of the water and the resulting high boiling point elevation of this salt (45°K) (Figure 4.2) which results in a distillation efficiency of η_{dis} = 13%, when the final concentration of the salt corresponds to the saturation point.
In order to choose the initial concentrations of the two solutions, it is important to keep in mind that higher is their difference in concentration, higher is the voltage and the relative electrical work that can be extracted (Figure 6.3).

6.2.1. Activity coefficients, Mixing Free Energy and Open Circuit Voltage

The Galvani representation of the TRB based on LiBr water solutions is:

α	ϵ	σ	ϵ'	α'
Pt	$LiBr_H\ (H_2O)$	LICGC™	$LiBr_L\ (H_2O)$	Pt

Where α and α' represent the phases related to the electronic conduction, the metal-based electrodes, ϵ and ϵ' are the phases composed by the redox couple LiBr/Br_2 in water solutions which react on the electrode surface and, in the end, σ is the ionic conductor phase, the electrolyte which, in the specific case, is a solid electrolyte based on a ceramic material NASICON-like.
On the interphase $\alpha|\epsilon$ and $\alpha'|\epsilon'$ the redox equilibrium which takes place is:

$$Br_2 + 2e^- \rightleftarrows 2Br^- \quad (6.7)$$

Therefore, the equilibrium equations are

$$\tilde{\mu}_{\epsilon}^{Br_2} + 2\tilde{\mu}_{\alpha}^{e^-} = 2\tilde{\mu}_{\epsilon}^{Br^-} \quad (6.8)$$

$$\tilde{\mu}_{\epsilon'}^{Br_2} + 2\tilde{\mu}_{\alpha'}^{e^-} = 2\tilde{\mu}_{\epsilon'}^{Br^-} \quad (6.9)$$

Two other equilibriums take place between the NASICON-like membrane and the solutions, related to the movement of Li^+ ions through the LICGC™ electrolyte:

$$\tilde{\mu}_{\epsilon}^{Li^+} = \tilde{\mu}_{\sigma}^{Li^+} = \tilde{\mu}_{\epsilon'}^{Li^+} \quad (6.10)$$

Combining the three equations 6.8, 6.9 and 6.10:

$$2\tilde{\mu}_{\alpha}^{e^-} - 2\tilde{\mu}_{\alpha'}^{e^-} = 2\tilde{\mu}_{\epsilon}^{Br^-} - 2\tilde{\mu}_{\epsilon'}^{Br^-} + \tilde{\mu}_{\epsilon'}^{Br_2} - \tilde{\mu}_{\epsilon}^{Br_2} + \tilde{\mu}_{\epsilon}^{Li^+} - \tilde{\mu}_{\epsilon'}^{Li^+} \quad (6.11)$$

$\tilde{\mu}^{Li^+} + \tilde{\mu}^{Br^-}$ is the electrochemical potential of the salt in the ϵ and ϵ' phases. Using the definition of the electrochemical potential, equation 6.11 can be rewritten explicating the open circuit voltage (OCV):

$$OCV = \frac{\tilde{\mu}_{\epsilon'}^{Br_2} - \tilde{\mu}_{\epsilon}^{Br_2}}{2F} + \frac{\tilde{\mu}_{\epsilon}^{LiBr} - \tilde{\mu}_{\epsilon'}^{LiBr}}{F} \quad (6.12)$$

Thanks to the TLE device connected to the electrochemical cell, the chemical potential of bromine is kept in equilibrium in both the two solutions H and L, respectively. For this reason, the first part of equation 6.12 can be deleted even in this case and the OCV can be calculated using a simplified Nernst equation:

$$OCV = \frac{RT}{F} ln\left[\frac{a_H^{Li^+} a_H^{Br^-}}{a_L^{Li^+} a_L^{Br^-}}\right] = \frac{RT}{F} ln\left[\frac{X_H^{LiBr^2} \gamma_H^{LiBr^2}}{X_L^{LiBr^2} \gamma_L^{LiBr^2}}\right] \quad (6.13)$$

To solve equation 6.13, the activity coefficients of LiBr solutions have to be determined.

As already discussed for NaI, even for LiBr there is not a thermodynamic model which is able to correlate and predict the activity coefficient of LiBr in water and its molality for high value of concentration.

The Debye-Hückel theory, considering also the extended one, is not enough accurate in the range of molality of interest in this research. Hence, a simple fitting of the literature values of activity coefficients[220] is applied to obtain the equation which can describe the relationship between molality and activity coefficients of LiBr in the more realistic way.

The best result is obtained with a polynomial fitting of the third order, as shown in Figure 6.2.

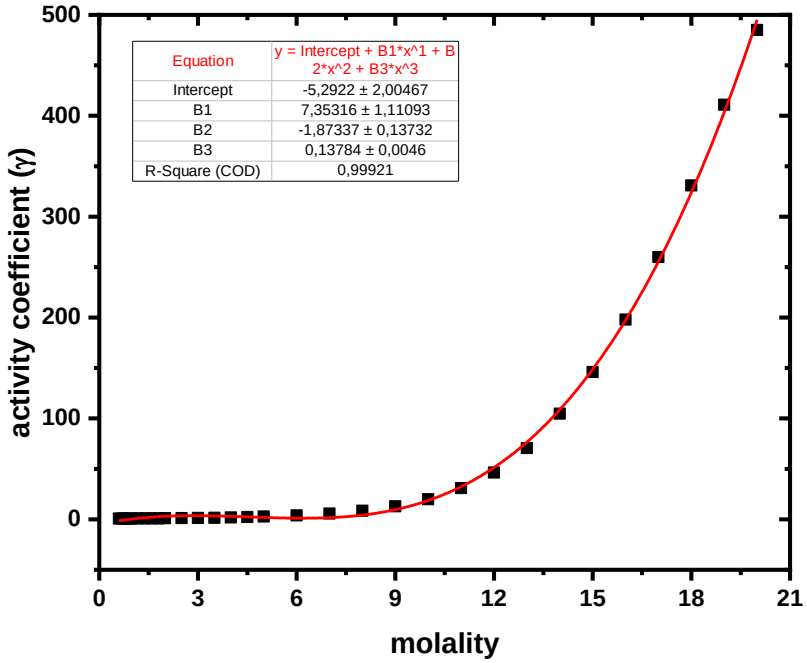

Figure 6.2. Fitting curve of the activity coefficient vs molality for LiBr. The activity coefficients are reported in literature. The fitting function is a polynomial curve.

The OCV profiles of a LiBr *H* solution at 26% molar fraction and 20% molar fraction is reported in Figure 6.3 at different concentrations of *L* solution.

In the graph are also reported experimental values obtained using *L* solution with a molar fraction of 1.7%: the experimental data agree with the thermodynamic results. This means that, even for the case of LiBr, the activity coefficients determined by fitting equation are enough accurate and, hence, they can be used for the calculation required in this research.

The open circuit voltage for $X_H = 20\%$ and $X_L = 1.7\%$ is 0.383V, at room temperature; while the OCV for $X_H = 26\%$ and $X_L = 1.7\%$ is 0.481V.

The resulting mixing free energy is:

$$1)\ \ X_H = 20\%;\ X_L = 1.7\% \rightarrow\ \Delta G_{mix} = 58.3\ kJ\ L^{-1} = 16\ WhL^{-1}\ \rightarrow\ \eta_{dis} = 12.56\%$$

$$2)\ \ X_H = 26\%;\ X_L = 1.7\% \rightarrow \Delta G_{mix} = 92.0\ kJL^{-1} = 25.5\ WhL^{-1}\ \rightarrow\ \eta_{dis} = 13\%$$

The case 2 represents the saturation point of LiBr in water solution, for the concentrated solution, which means the maximum boiling point elevation and, therefore, the maximum value of distillation efficiency.

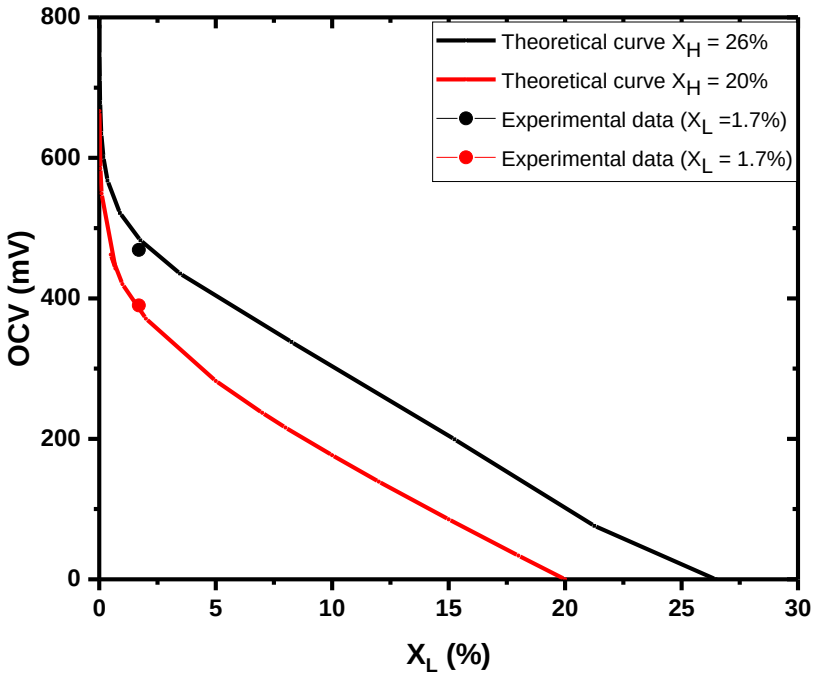

Figure 6.3. OCV of a TRB based on a concentrated solution with a molar fraction of 26% (black curve) or a molar fraction of 20% (red curve)vs increasing molar fraction of the diluted solution. Black and red points represent the experimental OCV using a diluted solution with a molar fraction of 1.7%.

6.2.2. Electrochemical reaction

Bromine, as iodine, can react with bromide ions in water solution to form the tribromide chemical specie, following the reaction:

$$Br_2 + Br^- \rightleftarrows Br_3^- \quad (6.14)$$

At high concentrations of bromide, also the pentabromide ions can be easily form:

$$2Br_2 + Br^- \rightleftarrows Br_5^- \quad (6.15)$$

Pentabromide ions are not significant in the determination of the standard potential of the bromine reaction and they do not affect the thermodynamic parameters, while the tribromide specie is more significant and affects the standard electrode potential because bromide ions are converted to tribromide, in aqueous bromine electrolytes, in large amount.

In the past century, different studies attempted to quantify the polybromide equilibrium constants at various temperatures[221,222]. One of the more recent studies by Ramette and Palmer[223] found the molal equilibrium constants to be K_3 = 16.73 for the tribromide formation.

Due to the presence of polybromides, the mechanism and kinetics of the bromide electrode reactions are complex.

Generally, the electrochemical reaction takes place with higher current density on platinum electrode than on carbon at the same temperature (exchange current density on platinum = 15 mA cm^{-2}; exchange current density on carbon = 0.2 mA cm^{-2}). However, bromine strongly reacts with platinum and can corroded and dissolved it into the electrolyte[224].

Therefore, a better electrode should be a carbon-based electrode, with high surface area, covered by platinum nanoparticles[224].

Bromine evolution reaction takes place via a Volmer-Heyrovsky mechanism:

$$Br^- \rightarrow Br_{ads} + e^- \ (Volmer)$$

$$Br^- + Br_{ads} \rightarrow Br_2 + e^- \ (Heyrovsky)$$

The rate-determining step is the second reaction, the Heyrovsky step, for the cathodic process while step one is the determining step for the anodic process[225,226].

From the study of Mastragostino and Gramellini[225], in presence of tribromide, the proposed mechanism consists in the preliminary reduction of tribromide via the formation of bromine, with which tribromide is in rapid equilibrium, whereupon bromine is reduced according to the mechanism reported before.

The problem of the mechanism of bromine-bromide reaction is still not solved but in these last years, the attention of the scientific community is focalized on it due to the diffusion of redox-flow battery based on this redox-couple[227–230].

6.3. Experimental Setup

6.3.1. Through-Liquid Exchanger

As widely discussed in the NaI TRB section, TLE is used to maintain the same activity of the halogen in all the system, recirculating it from the *H* compartment, where it is produced by oxidation of the halide, to the *L* compartment, where it is consumed by its reduction to halide.

TLE is based on the principle of the "liquid-liquid extraction": the two water solutions are directly in contact with an organic phase where bromine is soluble but not lithium ions, bromide ions nor water.

TLE is tailored glassware (shown schematically in Figure 6.4 a), whose particular shape allows the fasting mixing of the organic solvent, which is in contact with the two water solutions, but not the direct mixing of them.

The two water solutions, *H* and *L*, are dropped from the top of the TLE and drawn from the bottom and then recirculated into the electrochemical cell, which is connected in series. During the drop pathway and the contact time of the water solution with the organic one, bromine diffuses from one phase to the others until its activity is in equilibrium.

In the LiBr-based TRB, TLE is filled with octane, as organic solvent, instead of toluene: this choice is related to the lower operating temperature used to conduct all the experiments. Decreasing the temperature, the water solubility in the organic alkane also decreases, reducing the energy loses related to the mixing of the two water solutions.

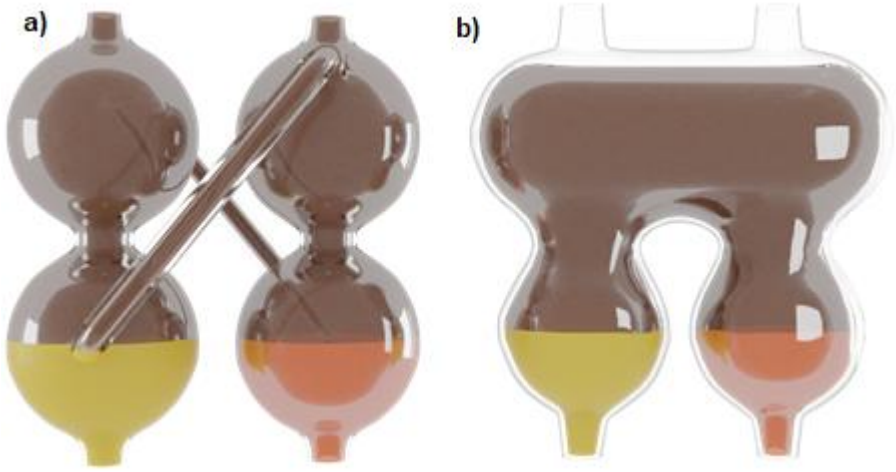

Figure 6.4. a) Scheme of the "original TLE"; b) Scheme of the new TLE, named TLE-2.

A second shape of TLE is also evaluated and compared to the original one, in order to achieve better performances in terms of equilibrium time, and to solve the problem related to the raise of the volume of the diluted solution during the discharge. In fact, during the discharge of the cell, the diluted solution becomes more concentrated in LiBr, which has a high molar volume, resulting in an increment of the volume of the solution. The schematic representation of the new TLE (named TLE-2) is reported in Figure 6.4 b.

This new shape is projected in order to increase the volume of the intimate contact between the two water solutions and the organic solvent. In this way, the equilibrium time is drastically decreased: the activity of bromine is equilibrated in a third of the time required with the "old" TLE.
Moreover, with TLE-2, part of the volume is empty and could be occupied by the raising volume of the diluted compartment during the discharge. In fact, during the concentration of the *L* solution, the molar volume of the solution increases: starting from 4 mL of solution, it is expected to reach a final *L* volume of 5 mL. The increasing volume in a setup which counts TLE instead of TLE-2, will be bring to the shutdown of the electrochemical cell before the complete discharge (when the two solutions reach the same concentration): in fact, if the volume of *L* solution arises, it will fill part of the tubes that connect and allow the passage of the bromine solution in octane from one compartment of the TLE in the other one. In this way, bromine could not be equilibrated anymore. With the new shape of TLE-2, this intimate contact is always possible due to the large contact volume at the top of the device.
Bromine can react with octane in the presence of light or high temperature; the function of ultraviolet light is to provide energy for the homolytic cleavage of halogen (Br-Br), forming the corresponding free radicals[231]. In the propagation step, bromine free-radicals can react with the alkane, removing a hydrogen atom to form hydrogen halide and alkyl free-radical. The alkyl free-radical then reacts with another halogen molecule to form haloalkane and regenerates the halogen free-radical.
To avoid this phenomenon, all the experiments are performed in a dark room.

6.3.2. NASICON-like membrane

As cation-exchange membrane is used a diaphragm made in Lithium Ion Conductive Glass Ceramic (LICGC^{TM}) a OHARA unique technology. It consists in a glass-ceramic which have isotropically dispersed Lithium-Ion Conductive Crystal particles and an amorphous glass phase. The result is a powder which is thermally stable (up to 600°C), nonflammable (Figure 6.5), with a conductivity in the order of 10^{-4} S cm^{-1} at room temperature (Figure 6.6) and without though hole: this means there is not water penetration.

Figure 6.5. LIGCG^{TM} diaphragms, OHARA technology.

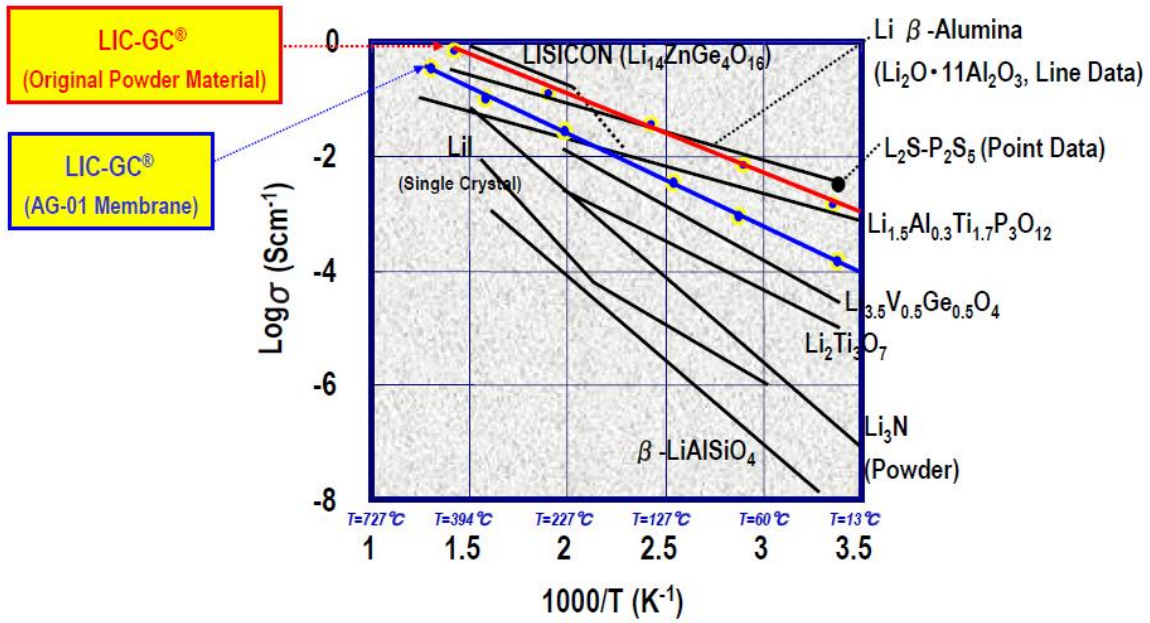

Figure 6.6. Arrhenius plot of LIC-GC powder and membrane compared to the Arrhenius plot of the main lithium-ion conductive inorganic materials. Symposium on Energy Storage Beyond Lithium Ion; Materials Perspective, October 7-8, 2010 Oak Ridge National Laboratory Kousuke Nakajima, OHARA INC.

The main composition of the powder is a NASICON-type crystal with formula $Li_{1+x}Al_xGe_yTi_{2-x-y}P_3O_{12}$.

A sub-crystal phase is also present: it is a NASICON-type crystal with formula $Li_{1+x+3z}Al_x(Ge,Ti)_{2-x}(Si_zPO_4)_3$.

It also possible to observe a small percentage of a third phase, $AlPO_4$, as shown in the XRD diffractogram and in the SEM images (Figure 6.7 and 6.8).

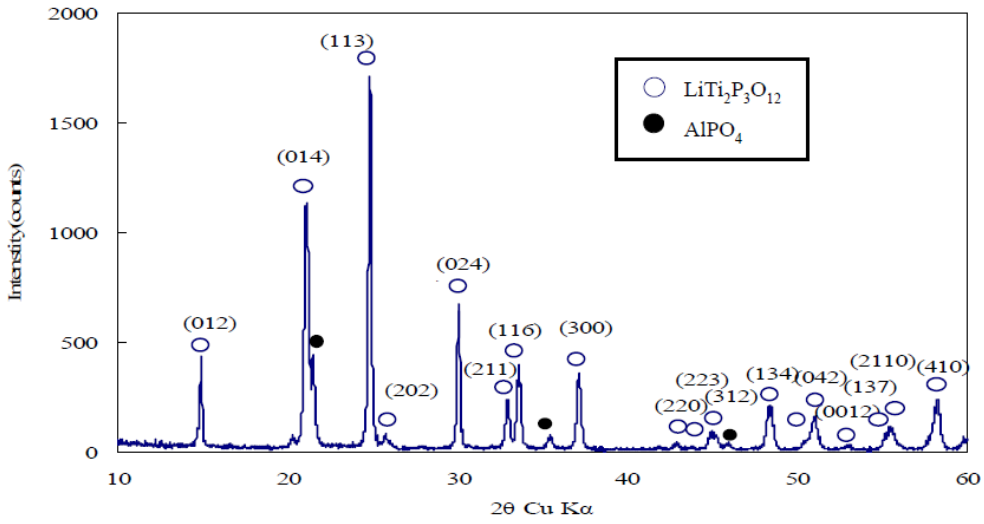

Figure 6.7. XRD diffractogram of LCGC powder. Symposium on Energy Storage Beyond Lithium Ion; Materials Perspective, October 7-8, 2010 Oak Ridge National Laboratory Kousuke Nakajima, OHARA INC.

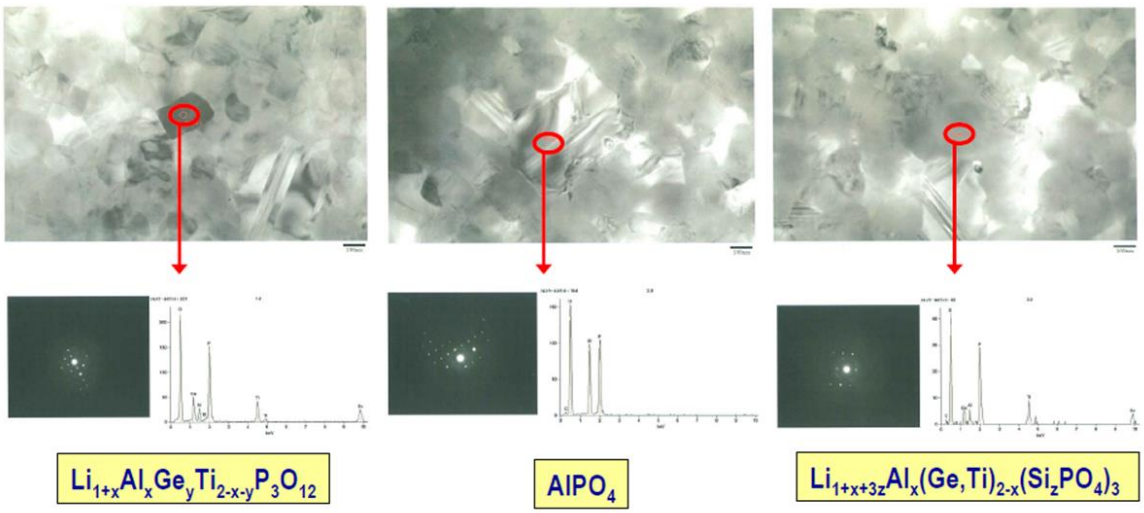

Figure 6.8. TEM and EDX pictures of LCGC powder. Symposium on Energy Storage Beyond Lithium Ion; Materials Perspective, October 7-8, 2010 Oak Ridge National Laboratory Kousuke Nakajima, OHARA INC.

6.4. Electrochemical Characterization

6.4.1. Through-Liquid Exchanger

The discharge of the cell, without the implementation of TLE, is reported in the Figure 6.9.

As it can be noticed, the discharge lasts only few minutes due the fast consumption of bromine in the diluted solution. Without TLE, there is not the possibility to recirculate the bromine produced in the *H* compartment (by the oxidation of bromide) towards the *L* compartment, where it is consumed. Therefore, the TRB gives energy until all the bromine dissolved in the *L* solution has completely reacted.

In any case, a smart way to proceed consists to recirculate bromine, keeping its activity in equilibrium in each side and avoiding the use of a big amount of bromine. In fact, the concentration of dissolved bromine in the solutions is the minimum required to elude the shutdown of the cell, during the energy extraction.

In the case of the TRB based on sodium iodide, several organic solvents have been studied in order to find the one that less solubilized water at 90°C. This study has not been performed for the LiBr-based TRB because the lower working temperature.

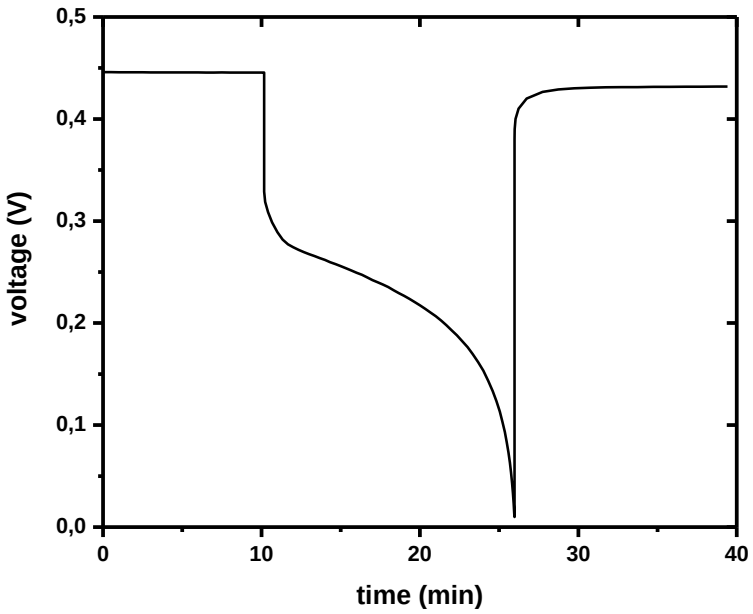

Figure 6.9. Discharge of the cell under constant current of 1.6 mA cm^{-2} without the implementation of the through-liquid exchanger. The open circuit voltage is measured for the first 10 minutes, after that, the current is switched on and the voltage decreased rapidly due to the ohmic drop. After only 16 minutes the cell reaches 0V due to the low concentration of bromine in the diluted compartment, where it is consumed undergoing a reduction reaction.

For the TRB based on LiBr, two different shapes of TLE are instead tested, in order to implement the one that gives the best performance in terms of equilibration time and to solve the problem related to the raise in the volume of the diluted solution.

To evaluate the performances of the two TLEs, several electrochemical titrations are performed.

Starting from two LiBr/Br_2 solutions at the same concentrations (X_{LiBr} = *10%; [Br_2] = 5mM*), the OCV is measured before and after an applied constant current for a fixed time without the implementation of TLE, with TLE, and with the TLE-2 (Figure 6.10 and 6.11).

The current imposition distances the system from the equilibrium: bromine is consumed in a compartment and produced in the other one. If TLE is not connected to the cell (Figure 6.10 a and 6.11 a), the final OCV depends on the concentration of bromine in the two solutions, which could not be easily determined.

However, when TLE or TLE-2 are connected in series to the cell, bromine is equilibrated in the two solutions keeping it always at the same activity via the use of the Through-Liquid Exchangers. Therefore, the final OCV, after the application of the current, it does not depend on the activities of bromine in the two compartments, but only on the activities of LiBr.

Knowing the applied current and the duration time, the new activities of the solutions can be easily calculated. Considering possible little errors in the calculation of the activity coefficients, which at this concentration values could change the OCV of few mV and taking into account that the bromine activity is the same in both the solutions when TLE or TLE-2 are connected, the OCV should be 2 mV in the case of the TLE-2 test (Figure 6.10), and 1.3 mV in the case of the old shape TLE test (Figure 6.11). In both the cases, the final measured OCV is 3 mV.

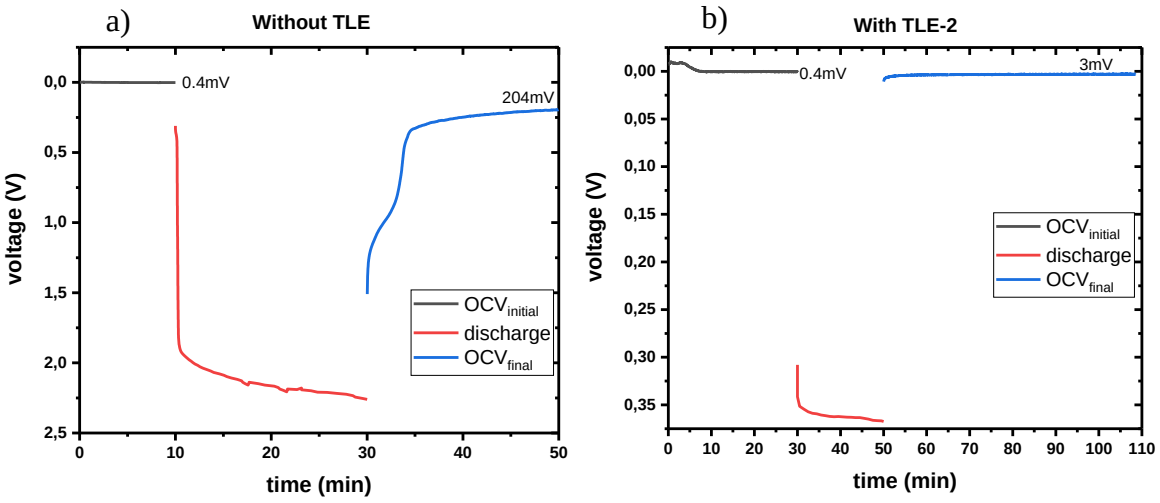

Figure 6.10. Voltage vs time profile without (a) and with (b) TLE-2 feeding the electrochemical cell with two LiBr/Br_2 solutions at the same concentrations: X_{LiBr} = 10%, [Br_2] = 5 mM. The black curve is the OCV of the electrochemical cell at the initial conditions; the red curve is the voltage profile during the discharge under a current of 10 mA for 20 minutes and the blue curve is the OCV after the discharge. If the bromine activity is the same in the two compartments, the final OCV should be 2 mV.

Considering a molecule flux proportional to the concentration difference, analogous to first-order chemical kinetics, the time constant of the TLEs may be determined by exponential fitting:

$$y = Ae^{-\left(\frac{x}{\tau}\right)} + y_0 \quad (6.16)$$

The time constant depends also on the temperature and the flux, which are kept constant during all the experiments.

The fitting, showed in Figure 6.12, results in a time constant of ≈15 minutes for the TLE and ≈5 minutes for TLE-2. This means that the halogen equilibrium is faster using the new shape of TLE-2.

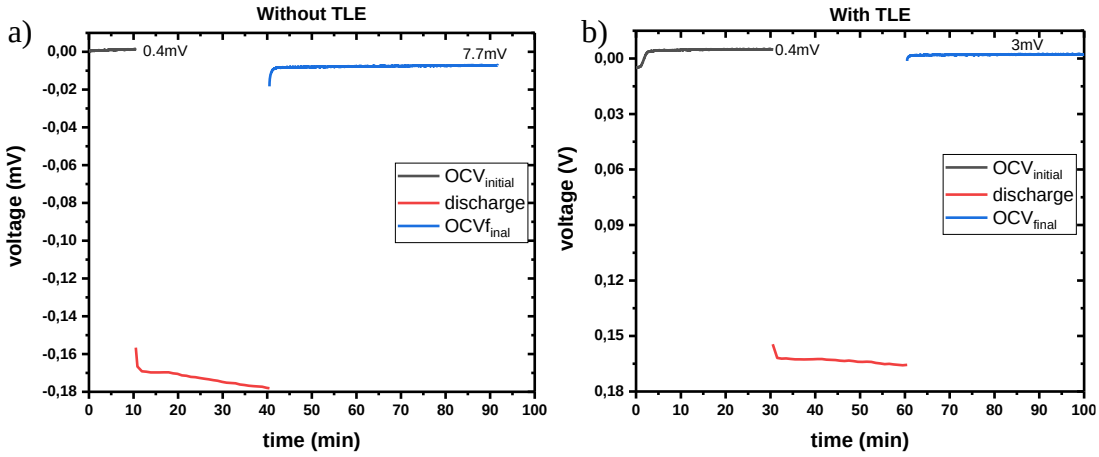

Figure 6.11. Voltage vs time profile without (a) and with (b) TLE feeding the electrochemical cell with two LiBr/Br₂ solutions at the same concentrations: X_{LiBr} = 10% [Br₂] = 5 mM. The black curve is the OCV of the electrochemical cell at the initial conditions; the red curve is the voltage profile during the discharge under a current of 5 mA for 30 minutes and the blue curve is the OCV after the discharge. If the bromine activity is the same in the two compartments, the final OCV should be 1.3 mV.

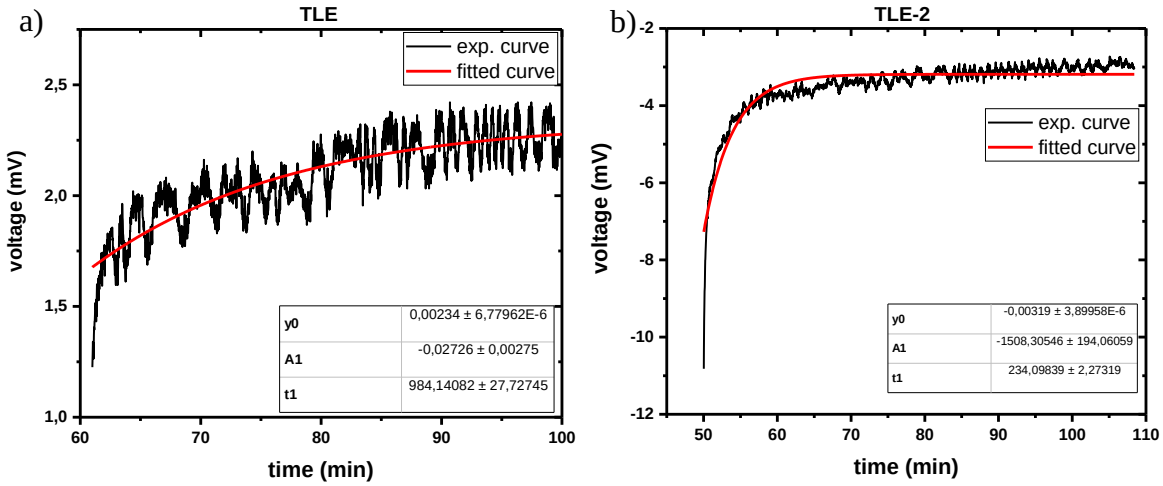

Figure 6.12. Experimental and fitted curve of final OCV vs time for a) TLE and b) TLE-2. From the fitted curve, the time constant τ was calculated. It results that TLE requires ≈15 minutes to equilibrate the bromine activity between the two compartments while TLE-2 requires only 5 minutes.

This result is also confirmed by a second test which consists in the measure of the open circuit voltage in continuous of an electrochemical cell filled with two LiBr solutions at different concentrations (X_H *= 20%;* X_L *= 2%* molar fraction) without dissolved bromine in the solution and without the utilization of TLE devices. When TLE, filled with a solution of bromine in octane, is connected to the electrochemical cell, the OCV reaches an equilibrium value in few minutes, which depends on the kind of TLE devices (Figure 6.13).

Fitting the OCV vs time profile after the connection of TLE, with the same exponential function used before, the time constant is determined for the TLE devices (Figure 6.14).

As in the other test, TLE-2 shows a lower time constant than TLE (≈ 2 minutes vs ≈ 12 minutes).

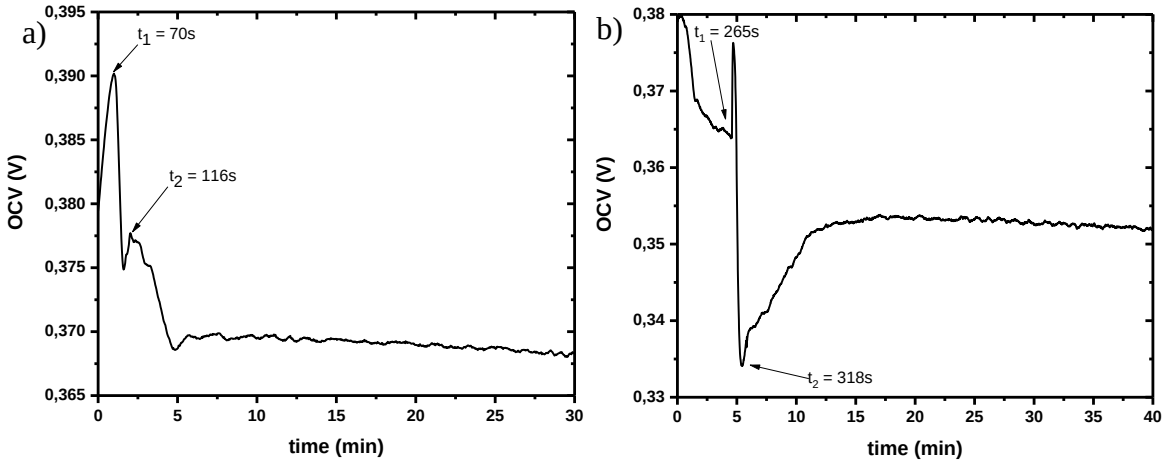

Figure 6.13. OCV vs time profile for an electrochemical cell filled with two different LiBr solutions (X_H = 20%; X_L = 2%) with no dissolved bromine. At the t_1 time, there is the first contact between the LiBr solutions and the bromine/octane solution in the a) TLE and b) TLE-2. At the t_2 time, TLEs are completely filled and the equilibration process starts.

In both the analysis, the results are the same: TLE requires 12/15 minutes to equilibrate the activity of bromine in both the *H* and *L* compartments while TLE-2 requires only 2/5 minutes. Consequently, all the other electrochemical characterizations of the TRB system based on lithium bromide, are performed connecting the new Through-Liquid Exchanger in series to the electrochemical cell, instead of the old shape TLE.

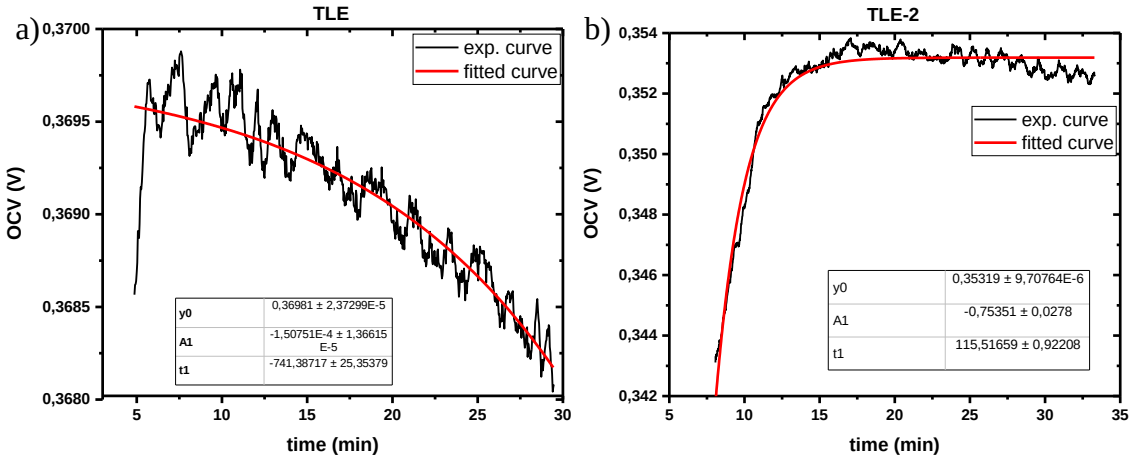

Figure 6.14. Experimental curve (black) and fitted curve (red) of OCV vs time for a) TLE and b) TLE-2. The time constant τ is calculated from the fitted curve. It results that TLE requires ≈12 minutes to equilibrate the bromine activity between the two compartments while TLE-2 requires only 2 minutes.

6.4.2. Diaphragm resistance

Two different diaphragms are tested in the electrochemical cell. Both are made by ceramic materials LICGC™, therefore conduct lithium ions but they avoid the transit of bromide, bromine, and water. The two diaphragms have a thickness of 150 µm and 50 µm, respectively and an exposed surface area of 3.14 cm^{-2}.

The thinner diaphragm decreases the ohmic drop because its lower resistance, which could be further decreases by operating at higher temperatures, as already reported in other works[183] on TRB systems. The Nyquist plots of the electrochemical cell fed with LiBr solutions (X_H = *20%*, X_L = *1.7%*) at 50°C and OCV are reported in Figure 6.15 for the low (red) and high (black) thickness membrane, respectively.

From the lower to the higher frequencies, the spectra show an arc shifted along the real axis.

The high-frequency intercept and the arc diameter are related to the electrolyte and the interfacial Pt-solution resistances, respectively. As expected, the surface resistance of the electrochemical process is similar for both cases (5.2 Ω and 5.4 Ω) since the cells are equipped with the same electrodes.

On the contrary, the spectrum of the cell with the thicker membrane is shifted to higher impedance value due to the larger electrolyte resistance.

The electrical resistances of the electrolytes (6.7 Ω and 13.5 Ω) are in good agreement with the theoretical ones (5 Ω and 16 Ω) obtained from manufacturer specifications, (LICGC™ has a conductivity of nearly 3 x 10^{-4} S cm^{-1} at 50°C).

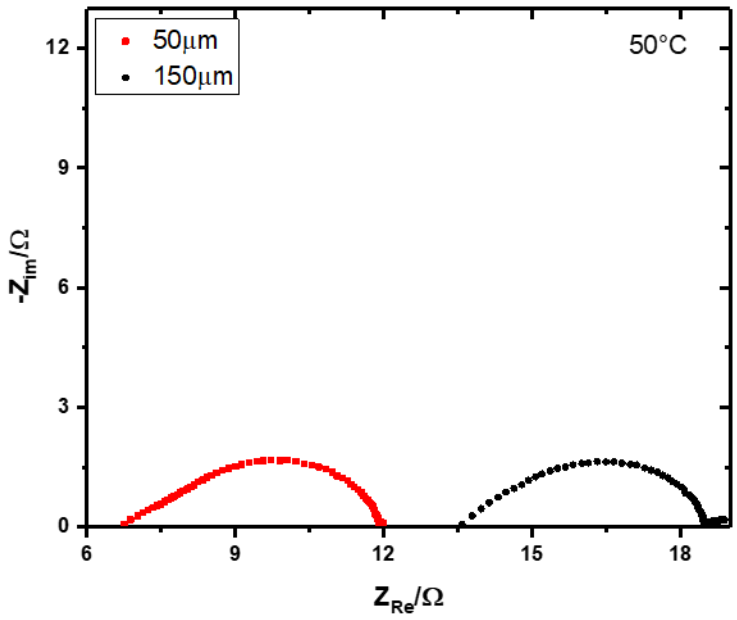

Figure 6.15. Electrochemical impedance spectra of the TRBs at 50°C, the operating temperature. The black squares represent the TRB which implements the thicker diaphragm (150 µm) while the red dots represent the electrochemical cell which implements the thinner diaphragm (50 µm).

The interfacial electrode solution, which affects the arc diameter of the impedance spectra, has been already optimized in the analysis showed in Figure 6.15. In fact, in the preliminary electrochemical tests, the cell was composed of platinum wires as electrodes instead of platinum meshes, resulting in higher impedances due to the lower actives surface (Figure 6.16).

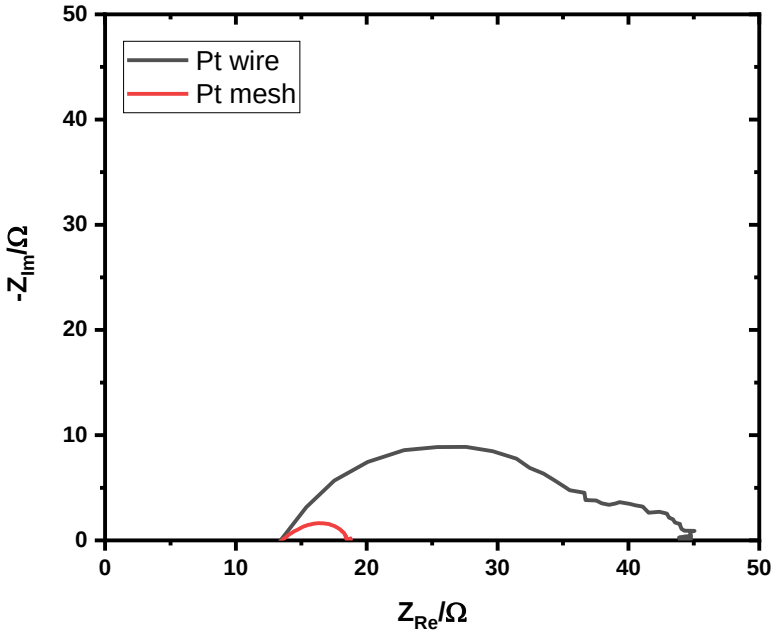

Figure. 6.16. Electrochemical impedance spectra of TRB based on 150µm membrane at 50°C using platinum mesh as electrodes (red line) and platinum wire as electrodes (black line). Increasing the active surface area of the electrodes, the total internal resistance decreases.

6.4.3. Maximum Current Density / Maximum Power Density

Experiments are conducted to test the electrochemical cell, without the TLE connected in series, to evaluate some general parameters like the open circuit voltage, the maximum power density, and the maximum current density that the system may achieve.

All the experiments in this section are performed for short time in order to avoid chemical consumption of the species.

A Linear Sweep Voltammetry (LSV) is performed for the two TRBs, one with the thicker diaphragm and one measurement for the TRB with the thinner diaphragm, in a voltage window between the open circuit voltage and 0 V at 1 mV s^{-1} (Figure 6.17).

The electrochemical cells are filled with two solutions at $X_H = 26\%$ and $X_L = 1.7\%$ molar fraction, respectively.

The observed OCVs of the TRBs are 479 mV for the TRB with 150 µm diaphragm and 430 mV for the TRB with the 50 µm diaphragm, while the expected OCV is 480 mV. The significant difference in the open circuit voltage for the TRB based on the thinner diaphragm is related to the lack of accuracy during the preparation of the solutions, which probably would not at the exact concentration required.

The profiles of the current density in the function of the voltage in the LSV graphs (Figure 6.17) are straight lines. From the slope of the lines is possible to determine the total resistances of the processes which are 22 Ω and 16 Ω for the high and low thickness, respectively, in good agreement with the OCV impedance values.

The maximum current density reached by the device is nearly 8 mA cm^{-2} and 6 mA cm^{-2} for the low and high thickness diaphragms.

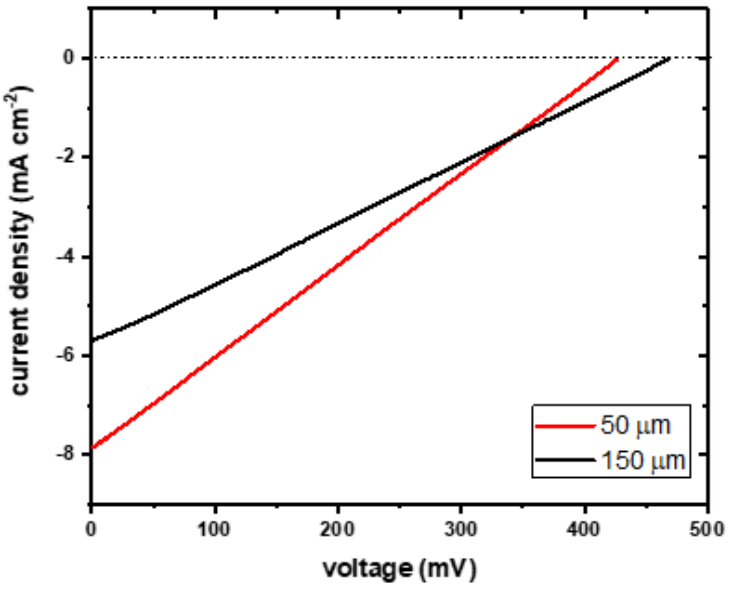

Figure. 6.17. LSV between OCV and 0V of TRB based on 150 µm thick (black line) and 50 µm thick (red line), respectively.

The linear behavior of the current-potential profiles determines the parabolic behaviors in the power-current graph reported in Figure 6.18.

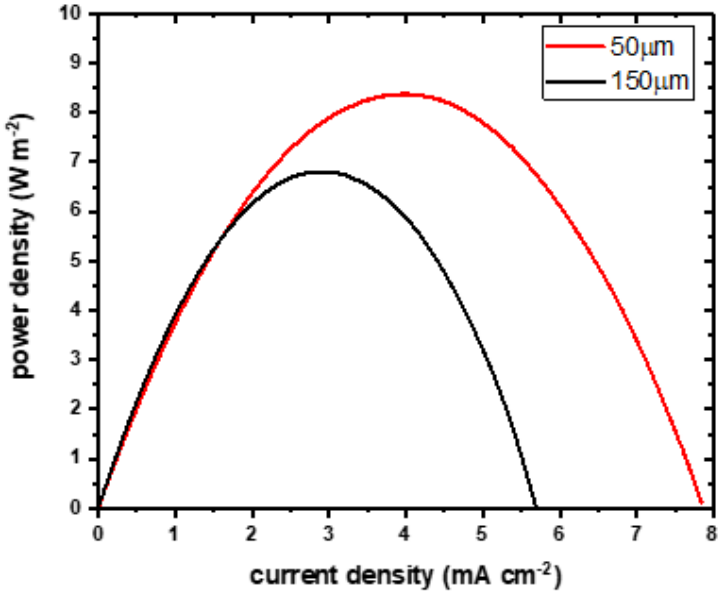

Figure. 6.18. Power density vs current density of TRB based on thinner diaphragm (red profile) and on thicker diaphragm (black profile).

The peak power for the TRB with the thicker diaphragm is nearly 7 mA cm^{-2}, reached at a current density of 3 mA cm^{-2}, while the maximum of power density in the case of TRB with the thinner membrane is approximately 8.5 W m^{-2}. This value is achieved at a current density of 4 mA cm^{-2}.

6.4.4. Discharge tests

All the discharge experiments are performed filling the electrochemical cell with two solutions of LiBr at the concentrations of X_H = *20%* molar fraction and X_L = *1.7%* molar fraction. The concentrated solution is prepared at lower concentration than the maximum possible in order to avoid issues related to the salt precipitations in the TLE or in the tubes during the cell preparation and handling. In fact, during these tests, it was not possible to control the room temperature which was always lower than 25°C.

Before showing you the discharge obtained with the final setup, it is going to be reported the discharge profile after the main improvements of the cell, in order to appreciate the contribution of any part of the cell on the final electrochemical performances.

6.4.4.1. Discharge of TRB in the old configurations

The first configuration of the TRB based on LiBr was composed by the old-shape TLE and platinum wires as electrodes.

This TRB suffered of high internal resistances which dramatically affect the cell, resulting in high ohmic drop (Figure 6.19).

The first discharge was performed under a constant load of 50 **Ω**, a value that was chosen because of the entire resistance of the device, which was based on the thicker diaphragm.

The experiment lasted nearly 17 hours, after this time, the membrane broke down.

In this condition, the extracted energy was so low that the resulting energy efficiency was only of 2%.

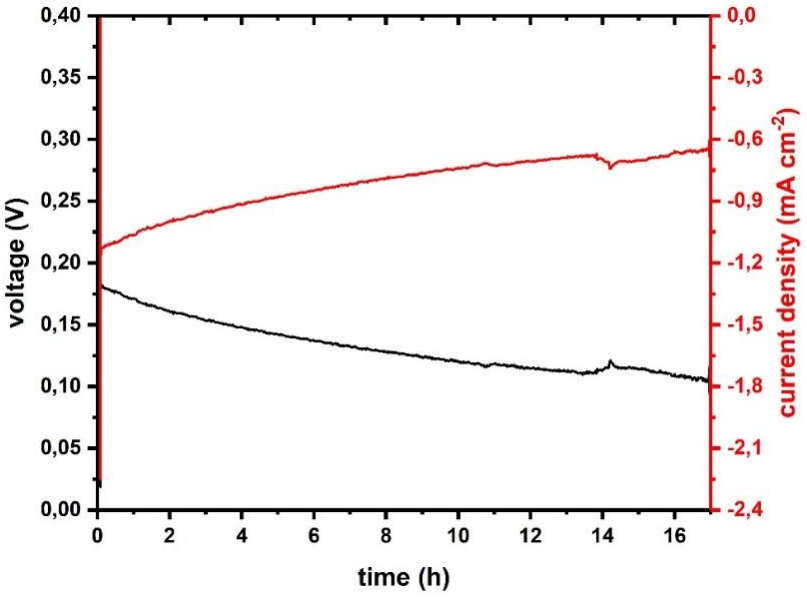

Figure 6.19. Discharge of a TRB based on 150µm membrane at constant load of 50Ω. Black curve represents the voltage profile vs the time while the red curve represents the current density.

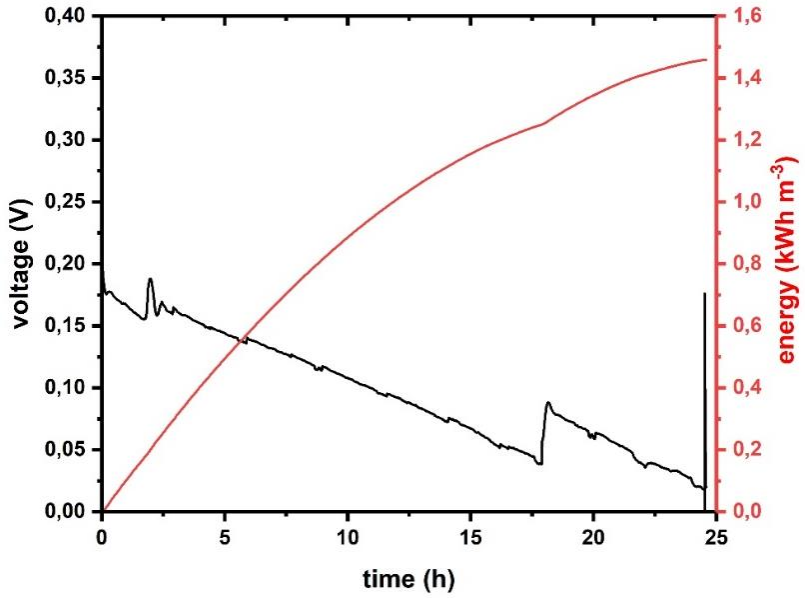

Figure 6.20. Discharge under constant current of 1.6mA cm^{-2}, for a TRB based on 50µm membrane and TLE. The black curve represents the behavior of the voltage vs the time while the red curve represents the extracted energy during the discharge.

Another discharge test is reported in Figure 6.20. In this case, the graph represents the discharge of a TRB with the thinner LICGC^{TM} membrane and the "old-shape" TLE.

For this experiment, platinum meshes were used as electrodes, reducing the resistances of the cell and therefore the energy loss due to the ohmic drop. The discharge was also performed under an applied constant current of 5 mA which means a current density of 1.6 mA cm^{-2}, referred to the diaphragm surface.

The voltage profile decreased almost linearly with the time due to the non-ideality of the solutions: in fact, in the operating conditions, the chemical potential of LiBr linearly depends on its concentration.

It was also observed small variations of the voltage which can be connected to the temperature fluctuations.

A tremendous voltage elevation was observed after ≈18 hours. This behavior was related to the reduction of the internal resistance of the cell, in particular, the part which is connected to the diffusion process: during the discharge, on the electrode surface, there are phenomena of adsorption of chemical species which affect the catalytic action of the electrode itself, decreasing its available active surface area and leading to an increment of the internal resistance. With the continuous fluxes of the solutions and the current which flows across the electrodes, these chemical species may be de-adsorbed, resulting in a reduction of the internal resistance which involves a raising voltage (Figure 6.21).

The total extracted energy, showed as red profile in Figure 6.20, is only 1.46 kWh m^{-3}, which corresponds to an electrochemical efficiency of 12.8%.

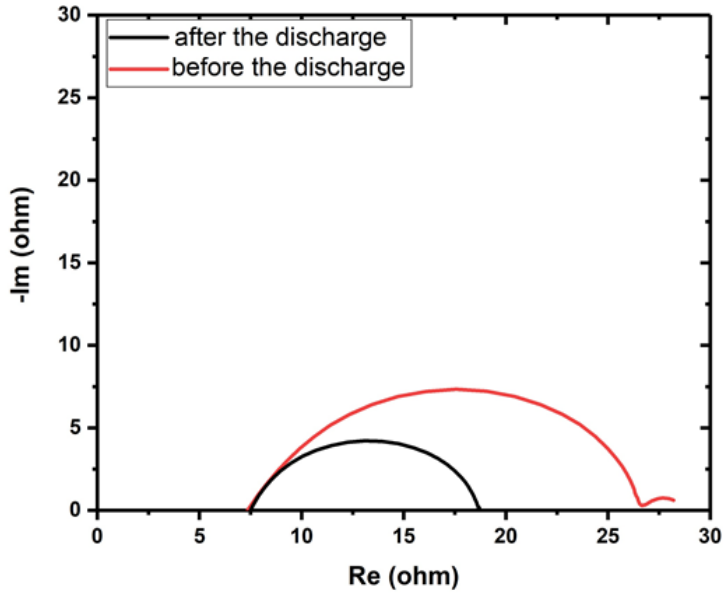

Figure 6.21. Electrochemical Impedance Spectra of TRB based on 50 µm diaphragm and "old-shape" TLE before (red profile) and after (black profile) discharge of the cell.

The maximum volumetric charge, the instantaneous value of charge, which changes during the discharge, reached by this system is 15.4 Ah dm^{-3} which represents only the 20% of the available capacity of the system.

Just before 25 hours of discharge, the electrochemical cell shut down. Once again, the membrane broke down.

In all the experiments performed, it was observed that, when almost 20% of the solutions reacted, the membrane ruptured. This was due to the raising in volume of the diluted solution; in fact, in the *L* compartment, bromine reacts to form bromide and sodium ions move from the *H* compartment to the *L* one in order to balance the released negative charges. In this way, the molar volume of the solution increases during the discharge process. The increased volume blocks the exchange of bromine in the "old-shape" TLE, filling one of the tubes that connect two opposite chambers of TLE and therefore, stopping the mixing of octane in the device. In this way two possible things may occur: the electrochemical cell turns off because the bromine activity is not equilibrated in the two solution by means TLE; or the increment of the internal pressure in the electrochemical cell results in the rupture of the diaphragm and the consequent mixing of the two solutions.

6.4.4.2. Discharge of TRB in the new configuration

The new setup, consisting in platinum meshes as electrodes and implementing the redesigned Through-Liquid Exchanger, TLE-2, is tested with 150 and 50 µm diaphragms.

The discharge profile of the two electrochemical cells, filled with concentrated solution $X_H = 20\%$ molar fraction, and diluted solution $X_L = 1.7\%$ molar fraction are reported in Figure 6.22.

The TRB which carries out the thicker diaphragm is completely discharged under a constant current of 1.6 mA cm^{-2} for ≈ 62 hours (Figure 6.22 a). Once the potential reaches almost 0 V, the current is

decreased to 0.3 mA cm^{-2} in order to reduce the ohmic losses and extract further energy (in Figure 6.22 a, on the right of the blue line). In fact, after the discharge at higher current, the LiBr concentration in the *H* and *L* solutions is not the same, but the voltage reached the value 0V due to the ohmic loss that reduces the available energy. Reducing the applied current, more energy could be extracted even if longer time is required to discharge the device.

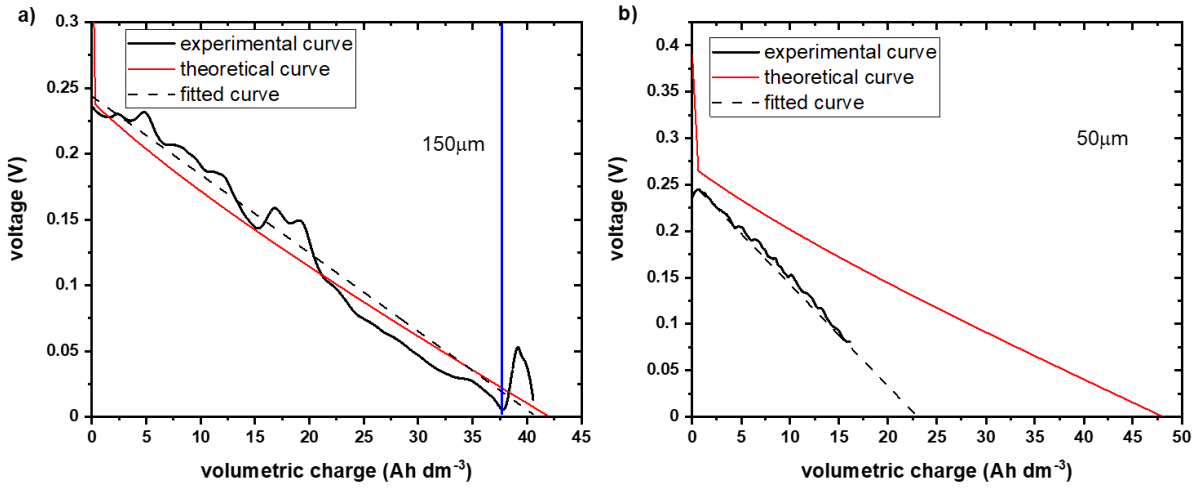

Figure 6.22. Discharge profiles of a) TRB with 150µm membrane, under a constant current of 1.6mA cm-2 (on the left of the blue line) and 0.3mA cm-2 (on the right of the blue line); b) TRB with 50µm membrane under a constant current of 3.2mA cm-2. The black-solid curves represent the experimental data, the dashed lines are the fitted curves while the red profiles are the theoretical discharges (the maximum one). The theoretical discharge process lasts a) 67 hours, extracting a volumetric charge of 42 Ah dm^{-3} and b) 38.5 hours, extracting a volumetric charge of 48 Ah dm^{-3}.

Here too, there are small variations of the voltage, which in generally decreases almost linearly with the time, that are associated to temperature fluctuations and the change in the internal resistances during the electrochemical process (Figure 6.23).

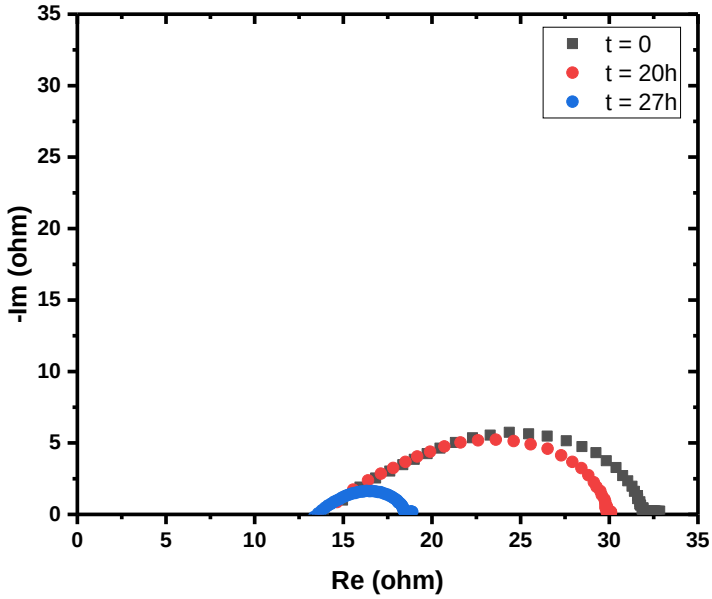

Figure 6.23. Electrochemical impedance spectra of the TRB, which implements the thicker diaphragm, before the discharge process (black curve), after 20h of discharge at 1.6mA cm-2 (red curve), and after 27h of discharge at 1.6mAcm-2 (blue curve).

These changes in resistance are related to the charge transfer process, that means related to the electrode-electrolyte interface, as already discussed. In general, the fluctuations are affecting the internal resistance for less than 10%.

The extracted volumetric charge corresponds to 42 Ah dm^{-3}: up to 37 Ah dm^{-3} is extracted under the higher current while less than 5 Ah dm^{-3} of charge is extracted under the lower current.

The fitting curve (dots line) has a behavior comparable to the theoretical discharge (red line) which is obtained modeling the discharge as a linear process where the slope is the ohmic drop and the intercept is the open circuit voltage minus the ohmic drop.

Instead, the discharge of the TRB with the thinner diaphragm is performed under 3.2 mA cm^{-2} current for less than 13 hours and it is incomplete: unfortunately, the brittleness of the thinner diaphragm, makes hardly possible its implementation in a laboratory scale (Figure 6.22 b). The experimental volumetric charge reached by the device is less than 20 Ah dm^{-3}.

Even the fitting curve of the experimental data (dots line) does not match with the theoretical one, resulting in a volumetric charge of only 22.6 Ah dm^{-3}, nearly a half of the expected volumetric charge.

The amount of extracted energy during the discharge can be easily determined by integration of the voltage vs extracted charge profile (Figure 6.22).

The extracted energy during the discharge with the thicker diaphragm, is up to 5 Wh dm^{-3} which means an electrochemical efficiency of 30.2%. The discharge at higher current (1.6 mA cm^{-2}) provides a considerable part of the energy, 4.75 Wh dm^{-3}, i.e. the 29.4% of the total energy. This value is in agreement with the maximum energy that can be extracted under these operational conditions: the maximum available energy that can be provided under a constant current of 1.6 mA cm^{-2}, considering an internal constant resistance of 32 Ω, is 4.8 Wh dm^{-3}, and this energy would be extracted in 67 hours (Figure 6.24). Therefore, the resulting theoretical electrochemical efficiency would be 29.6%.

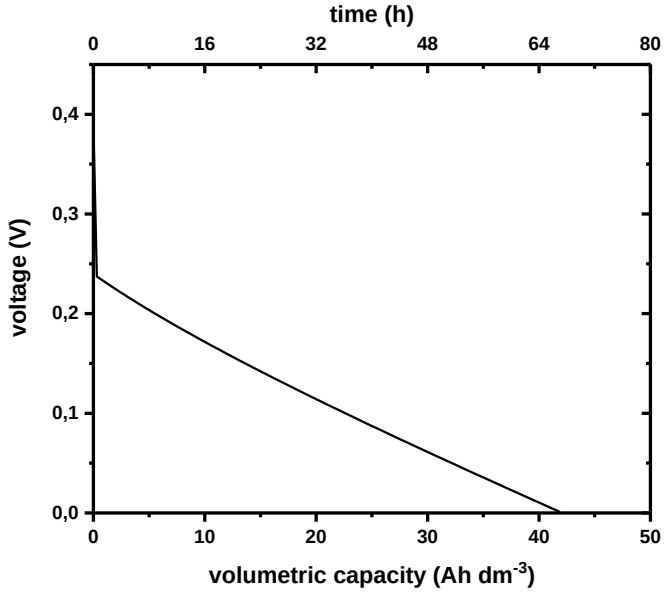

Figure 6.24. Theoretical discharge profile of a TRB based on thicker diaphragm under a constant current of 1.6 mA cm^{-2}. The discharge process lasts 67 hours, resulting in a volumetric capacity of 42 Ah dm^{-3}.

In the discharge experiment where TRB is composed by the thinner diaphragm, the total extracted energy is ≈ 2.7 Wh dm^{-3}. This is translated in a lower efficiency: only 17%. As already discussed before, this lower energy is due to the incomplete discharge of the system because of the ruptured diaphragm. If the discharge process was complete, it would be obtained 3.1 Wh dm^{-3} that means an efficiency of ≈ 19%.

The experimental amount of the extracted energy does not agree with the theoretical one: it was expected to reach an efficiency around 38% in less than 40 hours, considering an internal resistance of 12 Ω and the applied constant current of 3.2 mA cm^{-2} (Figure 6.25).

The reason why, experimentally, TRB based on the thinner membrane gives only half of the maximum available energy, is related to the membrane, which broke down after only 22 hours. The rupture process was not instantaneous but a progressive degradation which brought to a slow mixing of solution before the complete fragmentation. Considering an upscaling of the device, the handling problem related to the thinner membrane should be easily solved as already verified for RED systems, Redox-Flow Batteries and Fuel Cells[232–234].

Even in this experiment, if the membrane had not broken, the cell would have provided other energy: applying a lower current, the ohmic drop would be reduced and more energy would be available.

Considering that the complete discharge under 3.2 mA cm^{-2} proceeded with a profile like the fitted curve reported in Figure 6.22 b, the new open circuit voltage of the cell should be 223 mV.

Discharging the cell under a lower current such as 1.6 mA cm^{-2}, the ohmic drop should be 60 mV.

Therefore, it is possible to discharge the cell for, at least, other 35 hours reaching a global electrochemical efficiency of 30.7% (not considering further degradation of the membrane). Thus, the same electrochemical efficiency can be easily reached with the thinner diaphragm, in shorter time.

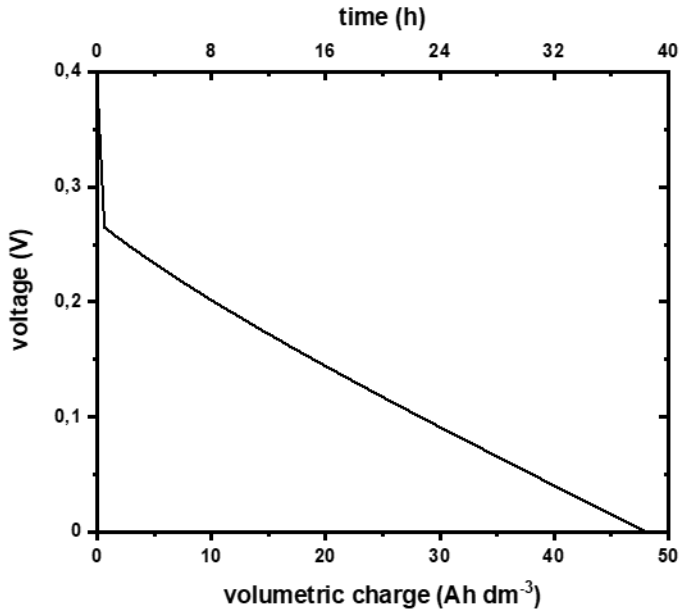

Figure 6.25. Theoretical discharge profile of a TRB based on thinner diaphragm (50µm) under a constant current of 3.12 mA cm^{-2}. The discharge process lasts 38.5 hours, resulting in a volumetric capacity of 48 Ah dm^{-3}.

This efficiency is obtained by theoretical construction of a discharge curve by comparison with other discharge profiles made in the same current/diaphragm conditions (Figure 6.26 a). Reporting the voltage trend against the volumetric charge and integrating this curve, the extracted energy can be easily determined (Figure 6.26 b). The sum of the extracted energy at the first and second discharge process, divide by the mixing free energy of the solutions, leads to an efficiency of 30.6%.

Thus, the same electrochemical efficiency obtained with the thicker diaphragm, can not only be easily reached with the thinner one, but also in shorter time (≈55h for 50µm thick diaphragm; ≈70h for 150µm thick diaphragm).

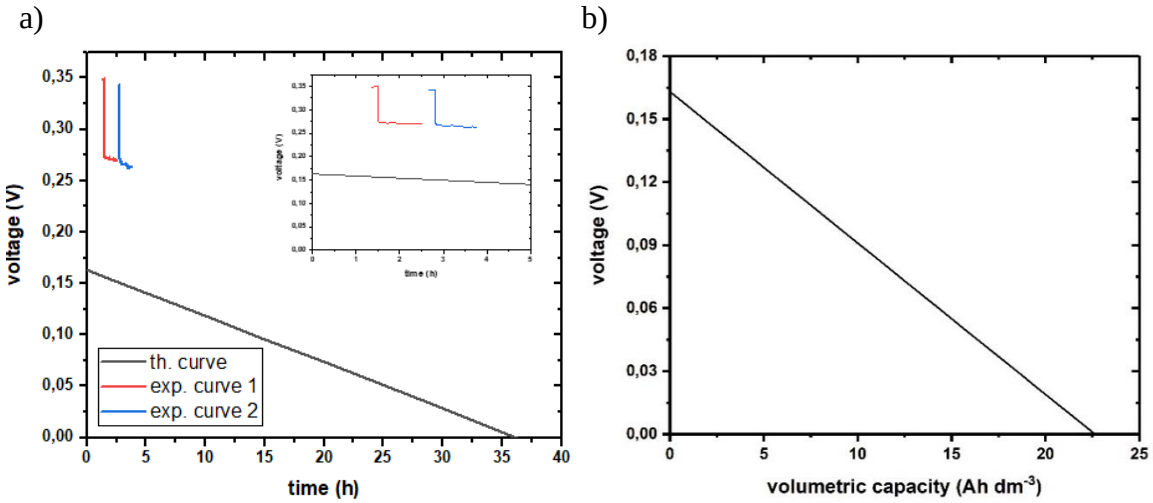

Figure 6.26. a) construction of a voltage vs time discharge profile (black curve) of the electrochemical cell with 50µm thick diaphragm, under a 1.6mA cm^{-2}constant current. The OCV is 223mV, resulted from the first discharge process. The blue and red curve represent experimental discharge profiles obtained at the same conditions in term of diaphragm and applied current. b) voltage vs extracted charge profile related to the theoretical curve of the graph on the left. The integration of this function results in 1.84Wh dm^{-3} extracted energy. The total efficiency is 30.6%.

6.5. Evaluation of the distillation and Efficiency

Vacuum distillation technology is proposed to restore the salinity gradient of the two solutions: its lower internal pressure allows boiling at low temperature, exploiting Low-Temperature Heat.

In the distiller, air is evacuated from the system, so that the pressure stabilizes to the vapor pressure of water at the temperature of the condenser, much lower than 1 atm. No external work is needed to keep the vacuum.

The exhausted solution is sent to the distiller where it boils and concentrates in contact with a heat exchanger, while its vapor is condensed in contact with a second heat exchanger. Each evaporation and condensation chamber is called "effect". At the end of the thermal process, the distilled water and the concentrated solution are sent to the electrochemical cell after the mixing of a small amount of concentrated solution with the distilled water to enhance the conductivity, regenerating the diluted solution. A pressure exchanger decouples the cell from the distiller, so that the cell can be operated at 1 atm without requiring external work.

The proposed scheme of the distiller for lithium bromide aqueous solutions is particularly simple, being composed by a "single" effect.

Starting from a simplified model of vacuum distiller and heat exchanger[89,110,111,235], the evaluation of the single-effect distiller efficiency is reported here in this section.

The efficiency of the single-effect distiller is defined as

$$\eta_{eff} = \frac{\Delta G_{eff}}{Q_{H,eff}} \quad (6.17)$$

Where $Q_{H,eff}$ is the absorbed heat from the heat sources and ΔG_{eff} is the mixing free energy of the two solutions. Distillation efficiency is limited by the Carnot law, as previously mentioned and discussed (section 2.3.2.) as follows

$$\eta_d \leq 1 - \frac{T_L}{T_H} (6.18)$$

Equation 6.18 can be rewrite for the single-effect distiller as:

$$\eta_{eff} \leq \frac{BPE}{BPE + T_{L,eff}} \quad (6.19)$$

Where $T_{L,eff}$ is the temperature of the condensing solvent while *BPE* is the boiling point elevation of the solution at the end of the evaporation process. In the working condition, the aqueous solution of lithium bromide shows a *BPE* of 45°K resulting in a distillation efficiency of 13%.

The distiller is kept at 85°C, which will be slightly less than the boiling temperature of the concentrated solution, with the exception of the condenser, kept at 40°C (85°C-40°C = 45K, i.e. the boiling point elevation). Moreover, the electrochemical cell is kept at 50°C: this is beneficial for the conductivity of the NASICON-like membrane. This scheme is particularly efficient: the heat

consumption is exactly equal to the latent heat needed for the evaporation of water plus the sensible heat needed to heat again the distilled water after condensation which is so small that it can be neglected. The electrochemical cell does not consume heat (the reaction is slightly exothermic).

Assuming a heat transfer coefficient U of the heat exchanger of 500 W m^{-2} K^{-1}, and considering an output power of 1 kW as target, the surface of heat exchanger and the dimension of the distiller is evaluated.

Any heat exchanger, one for the evaporation of the solution and one for the condensation of its vapor, requires a surface of 3.5 m^2 when the temperature difference across the heat exchanger is 15°K, a feasible value for realistic conditions (100°C-85°C=15K, 40°C-25°C=15K). This means the heat exchangers may be easily contained in sink of nearly 20 L of volume.

Finally, to produce 1 kw in the form of mixing free energy, 26.5 kW of heat are consumed.

6.6. Conclusion and future developments

Thermally Regenerable Battery developed to convert LTH in electricity is here improved.

The device exploits the mixing free energy of two water solutions of LiBr releasing electricity.

The electrochemical efficiency observed during the electrochemical tests is around 30% closer to the maximum power density ($P = 6\ W\ m^{-2}$; $P_{max} = 6.5\ W\ m^{-2}$), using a diaphragm 150 μm thick. If the electrochemical cell involves a thinner diaphragm (50 μm thick) could easily reach the same efficiencies in an upscale device showing higher power density ($P = 8\ W\ m^{-2}$; $P_{max} = 8.5\ W\ m^{-2}$). Unfortunately, in laboratory scale the brittleness of the membrane does not allow to perform a complete discharge of the cell, affecting the performances of the system.

Thanks to the high boiling point elevation of lithium bromide, the thermal process shows higher distillation efficiencies compared to the device based on the NaI water solutions: an efficiency of 13% is reached considering to use a single-effect distiller which works under vacuum, in order to exploit LTH.

Combining both the efficiencies, the technology shows an overall heat-to-electricity efficiency of 4% in the case of the thicker membrane, and 5% in the second setup.

These efficiency values are the highest values reached in experimental devices.

In a future upscale, both efficiency and power density could be easily improved, reducing dead volumes (considering a stack of cells as already made for RED systems) and enhancing the design of the hydraulic system.

In order to evidence the practical feasibility of the Thermally Regenerable Redox-Flow Battery based on lithium bromide water solutions, a preliminary study of a possible household plant is here discussed as done before for the device based on sodium iodide.

Taking in account a plant able to provide 1 kW of electrical power with an electrical efficiency of 30% and a power density of $8\ W\ m^{-2}$, if an overall surface membrane of $250\ m^{-2}$ is implemented in the reactor, which has a total volume of 200 L, the volume of the solution can be 40 L in both TLE and electrochemical cell (20L for the *H* and *L* solutions, respectively), and 20 L in the external sinks. The amount of LiBr is around 80 kg, with a cost of nearly 200 €. The heat input should be around 33 kW, which could be provided by a surface lower than $40\ m^2$ of state-of-the-art solar heat collectors with selective adsorbers and low concentration non-imaging optics.

It is clear that such figures refer to the preliminary results; significant improvements are foreseeing in the near future: using alternative more inexpensive electrodes, improving the performances of the ceramic material used as membrane and upscaling the system reducing the dead volumes.

6.6.1. New electrodes

Platinum is an expensive material which is also subjected to adsorption of chemical species during the discharge process, affecting the overall resistances, and thus the performances of the electrochemical cell (Figure 6.23).

A possible improvement consists in the exchange of the platinum electrode with a more catalytic, cheaper electrode that should resists to the adsorption of the species.

Carbon-based electrodes, as used in the TRB based on NaI solutions, are not electroactive towards Br_2/Br^- redox couple, therefore they cannot be directly used in the electrochemical cell.

A proposal is a MEA (Membrane Electrode Assembled)-like electrode, as used in the fuel cells.

A MEA electrode is composed by a polymer electrolyte membrane (proton exchange membrane, generally called PEM) which is a specially treated material permeable only to protons. On both sides of the membrane, a catalyst layer is added. Conventional catalyst layers include nanometer sized particles of platinum dispersed on a high-surface-area carbon support. The catalyst is mixed with an ion-conducting polymer and sandwiched between the membrane and a gas diffusion layer (GDL). This last layer is responsible of the transport of reactants into the catalyst layer.

For the Thermally Regenerable Battery, GDL layer is not required as well as the protonic membrane, which should be exchanged by the lithium ion-selective ceramic membrane. The support where nanoparticles of platinum are dispersed on it is another important part, and it would be the catalyst of the electrochemical reaction.

A preliminary test of only the electrocatalyst is performed using a carbon layer with nanoparticles of platinum dispersed on it, with a total platinum density of 1.95 mg cm^{-2}.

This electrode is tested and compared to the platinum mesh in terms of current density (mA cm^{-2} of electrode surface) and observed current normalized on the mass of platinum (A g^{-1}) as reported in Figure 6.27.

The results are really promising: pound for pound, platinum nanoparticles are more catalytic reaching a current which is higher of three orders of magnitude compared the whole platinum mesh.

Therefore, with these new electrodes is possible to improve the electrochemical performances of the cell (higher power density, higher current density, lower and constant resistances which means reduce the energy loses) and reduce the costs of the electrode materials, which actually are the predominant part of the overall costs.

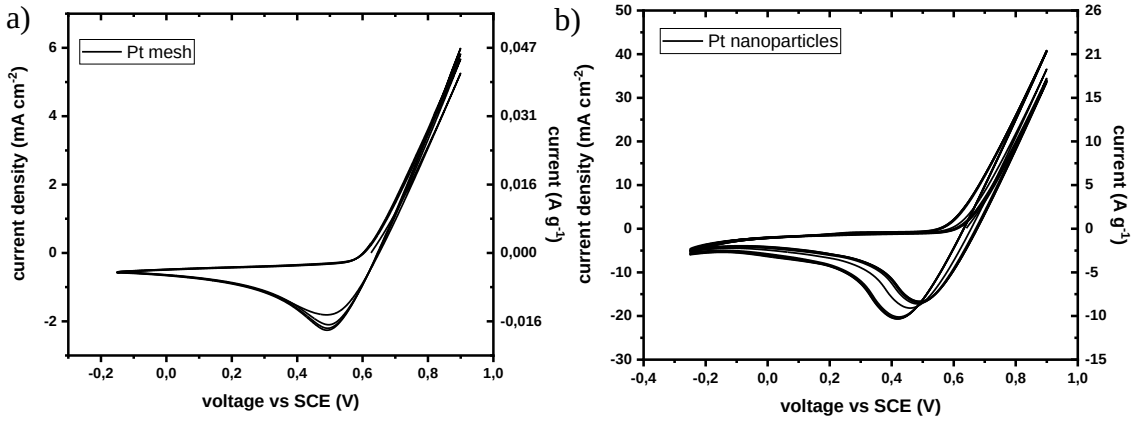

Figure 6.27. Cyclic voltammetry of LiBr/Br_2 water solution (X_{LiBr} = 26% molar fraction) in a 3-electrodes electrochemical cell where the Reference electrode is a calomel electrode; the Counter Electrode is a platinum wire and the Working Electrode is a) Platinum mesh and b) MEA-like electrode.

CHAPTER 7

Conclusion

The current global warming trend is the result of human activities which are changing the natural composition of our atmosphere, increasing the so-called “greenhouse effect”. In fact, over the last century, the consumption of fossil fuels, to produce energy, has increased the concentration of atmospheric carbon dioxide and other greenhouse gases.

The consequences of the modification of the natural atmospheric greenhouse are sum up in the term “climate change”: the Earth will become warmer, melting glaciers, increasing the sea level and leading to more evaporation and, therefore, more precipitations. Moreover, climate change can cause the emerging of new diseases affecting plants, animals, and humans.

The only way to avoid these terrible implications consists to reduce the production of carbon dioxide and reach the net zero production around 2050. Hence, energy production has to become more green and more efficient avoiding the use of fossil fuel.

One approach to reach this target is to exploit waste energy such has Low-Temperature Heat (LTH), which means heat below of 100°C. Actually, more than 60% of the global heat is lost in the environment as Low-Temperature Heat, without any other utilization.

LTH is not only a wasted form of energy deriving from human processes (industrial, transport, residential…) but it can also be found in nature as geothermal heat, solar heat, and heat produced by biomass.

The conversion of Low-Temperature Heat from various sources becomes therefore of utmost importance since it would allow decreasing the environmental footprint of energy production and can contribute to the overall reduction of fossil fuel consumption. However, the main problem related to its conversion is the low efficiency that can be reached due to thermodynamic limits, and, additionally, to technological limits.

This doctorate project has been focused on the development of a device able to store and convert in the most efficient way LTH sources, reducing the main drawbacks that affect the previous technologies proposed in literature: low power densities and high operational and material costs.

The device that is presented in this work has been designed, engineered, developed, and improved in order to maximize the power output and obtaining the highest conversion efficiency reached in this field.

The technology, called Thermally Regenerable Redox-Flow Battery (TRB) consists in a two stages device: a “power production” stage and a “thermal separation” stage. The “power production” takes place in an electrochemical cell which produces electricity at the expense of the mixing free energy of two water solutions of NaI or LiBr. In the two compartments of the cell, which are separated by a cationic-exchange membrane that allows the passage of only sodium or lithium ions, two redox reactions happen: the oxidation of the halide in to the halogen in the concentrated compartment and the opposite reaction in the diluted side. To maintain the process active, the halogen activity has to

be in equilibrium between the two solutions, therefore, an unconventional system has been connected in series to the cell, called it “Through Liquid Exchanger” (TLE).

Thanks to the particular shape of TLE, bromine or iodide are recirculated from the concentrated solution, where they are produced, into the diluted solution, where they are consumed, passing through an organic phase. After the completely discharge of the cell, the exhausted solution, composed by the concentrated and diluted solutions that have reached the same value of concentration, is sent to the second stage: the thermal separation. This second stage consists in the vacuum distillation of the exhausted solution to obtain the concentrated one and pure water, that can be easily stocked in reservoirs, exploiting LTH.

The heat-to-electricity conversion efficiency is determined as the product of the efficiency of the power production unit and thermal separation stage and is dramatically affected by this last one.

In fact, the efficiency of the thermal stage is limited by Carnot law, which is the thermodynamic limit that always affects these kinds of technologies.

From thermodynamic studies, it has been determined the better operational conditions in order to maximize the second stage efficiency improving the overall efficiency of the device. These conditions depend on the choice of the salt and solvent that will be used in the device: higher is the boiling point elevation, higher will be the resulting efficiency.

The power production stage is responsible to the power output. The right choice of electrodes, membranes, designed of the TLE, fluxes and concentrations of the solutions have led to obtain competitive results in terms of power density, current density and overall costs.

The preliminary results of this research are summarized in Figure 7.1.

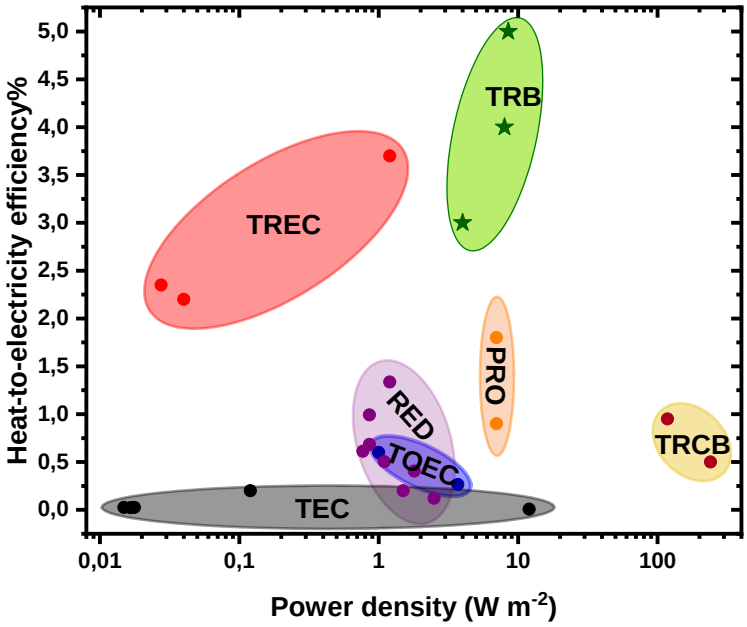

Figure 7.1. Energy efficiency vs power density of state-of-the-art technologies to harvest LTH reported in literature. Red points: Thermal Regenerative Electrochemical Cycle systems (TREC)[81,82,236]*; Black points: Thermal Electrochemical Cell devices (TEC)*[76,177,178]*; Blue points: Thermo-Osmotic Energy Conversion technologies (TOEC)*[57,97]*; Orange points: Pressure Retarded Osmosis systems (PRO)*[99,179,180]*; Purple points: Reverse Electrodialysis Devices (RED)*[115,116,181,182]*, Brown points: Thermally Regenerative Complex Batteries (TRCBs)*[139,183]*; Green stars: Thermally Regenerable Redox-Flow batteries (results of these research)*[237,238]*.*

Thermally Regenerable Redox-Flow batteries based on lithium bromide or sodium iodide water solutions show the highest conversion efficiency reached in the field of Low-Temperature Heat conversion. They also show high value of power density, making them feasible devices.

Several improvements can be done in order to maximize the power output performances, such as power density, applied current density, energy losses, and to reduce the costs. However, just from these preliminary results, what can be observed is that TRBs are the best compromise between all the proposed technologies to exploit Low-Temperature Heat sources.

Bibliography

1 M. R., Allen, O.P. Dube, W. Solecki, F. Aragón-Durand, W. Cramer, S. Humphreys, M. Kainuma, J. Kala, N. Mahowald, Y. Mulugetta, R. Perez, M. Wairiu, and K. Zickfeld, *Framing and Context. In: Global Warming of 1.5°C. An IPCC Special Report on the impacts of global warming of 1.5°C above pre-industrial levels and related global greenhouse gas emission pathways, in the context of strengthening the global response to the*, 2018.

2 C. to C.-N. by 2050: C. P. E. C. L. and C. on the E. C. P. 2020. A, European Climate Law, https://ec.europa.eu/clima/policies/eu-climate-action/law_en.

3 Z. Y. Xu, R. Z. Wang and C. Yang, *Energy*, 2019, **176**, 1037–1043.

4 M. Pehnt, J. Bödeker, M. Arens, E. Jochem and F. Idrissova, *ECEE 2011 Summer Study*, 2011, 691–700.

5 S. U. Khan, I. Khan, E. H. Khan, E. Qazi and W. Ali, 2013, **1**, 38–41.

6 N. D. Kaushika and K. S. Reddy, *Energy Convers. Manag.*, 2000, **41**, 713–726.

7 A. L. Biaou and M. A. Bernier, *Build. Environ.*, 2008, **43**, 651–660.

8 E. Wheatcroft, H. Wynn, K. Lygnerud, G. Bonvicini and D. Leonte, *Energies*, 2020, **13**, 1–19.

9 K. Ebrahimi, G. F. Jones and A. S. Fleischer, *Renew. Sustain. Energy Rev.*, 2014, **31**, 622–638.

10 B. N. Clarke, US-patent 4, 496, 314, 1985.

11 S. Jeong, B. H. Kang and S. W. Karng, *Appl. Therm. Eng.*, 1998, **18**, 1–12.

12 I. Horuz and B. Kurt, *Renew. Energy*, 2010, **35**, 2175–2181.

13 M. Fatouh and E. Elgendy, *Energy*, 2011, **36**, 2788–2795.

14 B. F. Tchanche, G. Lambrinos, A. Frangoudakis and G. Papadakis, *Renew. Sustain. Energy Rev.*, 2011, **15**, 3963–3979.

15 X. Zhang, M. He and Y. Zhang, *Renew. Sustain. Energy Rev.*, 2012, **16**, 5309–5318.

16 X. Niu, J. Yu and S. Wang, *J. Power Sources*, 2009, **188**, 621–626.

17 O. Badr, S. D. Probert and P. W. O'Callaghan, *Appl. Energy*, 1985, **21**, 1–42.

18 B. F. Tchanche, G. Papadakis, G. Lambrinos and A. Frangoudakis, *Appl. Therm. Eng.*, 2009, **29**, 2468–2476.

19 J. Bao and L. Zhao, *Renew. Sustain. Energy Rev.*, 2013, **24**, 325–342.

20 A. Desideri, S. Gusev, M. van den Broek, V. Lemort and S. Quoilin, *Energy*, 2016, **97**, 460–469.

21 D. Wang, X. Ling and H. Peng, *Appl. Therm. Eng.*, 2012, **48**, 63–71.

22 L. Sanne, *Energies*, 2016, **9**, 485.

23 S. A. M. Kiyarash Rahbar ,S. Mahmoud Raya, K. Al-Dadah, N. Moazami, *Energy Convers.*

Manag., 2017, **134**, 135–155.

24 F. Vélez, J. J. Segovia, M. C. Martín, G. Antolín, F. Chejne and A. Quijano, *Renew. Sustain. Energy Rev.*, 2012, **16**, 4175–4189.

25 B. Peris, J. Navarro-Esbrí, F. Molés, R. Collado and A. Mota-Babiloni, *Appl. Therm. Eng.*, 2015, **75**, 763–769.

26 H. Yu, T. Gundersen and X. Feng, *Energy*, 2018, **160**, 330–340.

27 H. D. M. Hettiarachchi, M. Golubovic, W. M. Worek and Y. Ikegami, *J. Energy Resour. Technol. Trans. ASME*, 2007, **129**, 243–247.

28 C. E. Campos Rodríguez, J. C. Escobar Palacio, O. J. Venturini, E. E. Silva Lora, V. M. Cobas, D. Marques Dos Santos, F. R. Lofrano Dotto and V. Gialluca, *Appl. Therm. Eng.*, 2013, **52**, 109–119.

29 W. Fu, J. Zhu, T. Li, W. Zhang and J. Li, *Appl. Therm. Eng.*, 2013, **58**, 224–233.

30 H. Jouhara, N. Khordehgah, S. Almahmoud, B. Delpech, A. Chauhan and S. A. Tassou, *Therm. Sci. Eng. Prog.*, 2018, **6**, 268–289.

31 A. Coskun, A. Bolatturk and M. Kanoglu, *Energy Convers. Manag.*, 2014, **78**, 39–49.

32 D. Beretta, N. Neophytou, J. M. Hodges, M. G. Kanatzidis, D. Narducci, M. Martin-Gonzalez, M. Beekman, B. Balke, G. Cerretti, W. Tremel, A. Zevalkink, A. I. Hofmann, C. Müller, B. Dörling, M. Campoy-Quiles and M. Caironi, *Mater. Sci. Eng. R Reports*, 2019, **138**, 210–255.

33 D. A. Casi, M. Araiz, M. Catalan, *Appl. Therm. Eng.*, 2020, 116275.

34 J. G. Haidar and J. I. Ghojel, *Int. Conf. Thermoelectr. ICT, Proc.*, 2001, 413–418.

35 A. Aranguren, P; Astrain, D; Rodriguez, A; Martinez, *Appl. Energy*, 2015, **152**, 121–130.

36 A. Y. Faraji, A. Date, R. Singh and A. Akbarzadeh, *Energy Procedia*, 2014, **57**, 2112–2120.

37 A. I. Hofmann, R. Kroon and C. Müller, *Handb. Org. Mater. Electron. Photonic Devices*, 2019, 429–449.

38 X. Gou, H. Xiao and S. Yang, *Appl. Energy*, 2010, **87**, 3131–3136.

39 F. J. Lesage and N. Pagé-Potvin, *Energy Convers. Manag.*, 2013, **66**, 98–105.

40 M. F. Remeli, L. Tan, A. Date, B. Singh and A. Akbarzadeh, *Energy Convers. Manag.*, 2015, **91**, 110–119.

41 A. Makki, S. Omer, Y. Su and H. Sabir, *Energy Convers. Manag.*, 2016, **112**, 274–287.

42 H. Fathabadi, *Renew. Energy*, 2020, **146**, 426–434.

43 M. Saufi Sulaiman, B. Singh and W. A. N. W. Mohamed, *Energy*, 2019, 628–646.

44 M. Araiz, A. Casi, L. Catalan, A. Martinez, P. Astrain, *Energy Convers. Manag.*, 2020, **205**, 112376.

45 W. A. Phillip, *Nat. Energy*, 2016, **1**, 10–11.

46 A. P. Straub, N. Y. Yip, S. Lin, J. Lee and M. Elimelech, *Nat. Energy*, , DOI:10.1038/nenergy.2016.90.

47 A. P. Straub and M. Elimelech, *Environ. Sci. Technol.*, 2017, **51**, 12925–12937.

48 M. Rahimi, A. P. Straub, F. Zhang, X. Zhu, M. Elimelech, C. A. Gorski and B. E. Logan, *Energy Environ. Sci.*, 2018, **11**, 276–285.

49 A. P. Straub, S. Lin and M. Elimelech, *Environ. Sci. Technol.*, 2014, **48**, 12435–12444.

50 K. Chen, L. Yao, F. Yan, S. Liu, R. Yang and B. Su, *J. Mater. Chem. A*, 2019, **7**, 25258–25261.

51 X. Chen, C. Boo and N. Y. Yip, *J. Memb. Sci.*, 2019, **588**, 117181.

52 Z. Ling, C. E. Ren, M. Q. Zhao, J. Yang, J. M. Giammarco, J. Qiu, M. W. Barsoum and Y. Gogotsi, *Proc. Natl. Acad. Sci. U. S. A.*, 2014, **111**, 16676–16681.

53 L. Fu, S. Merabia and L. Joly, *J. Phys. Chem. Lett.*, 2018, **9**, 2086–2092.

54 N. E. Holubowitch, J. Landon, C. A. Lippert, J. D. Craddock, M. C. Weisenberger and K. Liu, *ACS Appl. Mater. Interfaces*, 2016, **8**, 22159–22167.

55 H. Im, T. Kim, H. Song, J. Choi, J. S. Park, R. Ovalle-Robles, H. D. Yang, K. D. Kihm, R. H. Baughman, H. H. Lee, T. J. Kang and Y. H. Kim, *Nat. Commun.*, 2016, **7**, 1–9.

56 T. J. Abraham, D. R. MacFarlane and J. M. Pringle, *Chem. Commun.*, 2011, **47**, 6260–6262.

57 J. He, D. Al-Masri, D. R. MacFarlane and J. M. Pringle, *Faraday Discuss.*, 2016, **190**, 205–218.

58 T. Kim, J. S. Lee, G. Lee, H. Yoon, J. Yoon, T. J. Kang and Y. H. Kim, *Nano Energy*, 2017, **31**, 160–167.

59 T. Marquardt, G. Valadez Huerta and S. Kabelac, *Int. J. Hydrogen Energy*, 2018, **43**, 19841–19850.

60 W. B. Chang, C. M. Evans, B. C. Popere, B. M. Russ, J. Liu, J. Newman and R. A. Segalman, *ACS Macro Lett.*, 2016, **5**, 94–98.

61 M. S. Romano, J. M. Razal, D. Antiohos, G. Wallace and J. Chen, *J. Nanosci. Nanotechnol.*, 2015, **15**, 1–14.

62 M. F. Dupont, D. R. MacFarlane and J. M. Pringle, *Chem. Commun.*, 2017, **53**, 6288–6302.

63 Y. Mua and T. I. Quickenden, *J. Electrochem. Soc.*, 1996, **143**, 2558–2564.

64 R. Hu, B. A. Cola, N. Haram, J. N. Barisci, S. Lee, S. Stoughton, G. Wallace, C. Too, M. Thomas, A. Gestos, M. E. Dela Cruz, J. P. Ferraris, A. A. Zakhidov and R. H. Baughman, *Nano Lett.*, 2010, **10**, 838–846.

65 S. M. Jung, J. Kwon, J. Lee, K. Shim, D. Park, T. Kim, Y. H. Kim, S. J. Hwang and Y. T. Kim, *ACS Appl. Energy Mater.*, 2020, **3**, 6383–6390.

66 J. Duan, G. Feng, B. Yu, J. Li, M. Chen, P. Yang, J. Feng, K. Liu and J. Zhou, *Nat. Commun.*, 2018, **9**, 1–8.

67 L. Zhang, T. Kim, N. Li, T. J. Kang, J. Chen, J. M. Pringle, M. Zhang, A. H. Kazim, S. Fang,

C. Haines, D. Al-Masri, B. A. Cola, J. M. Razal, J. Di, S. Beirne, D. R. MacFarlane, A. Gonzalez-Martin, S. Mathew, Y. H. Kim, G. Wallace and R. H. Baughman, *Adv. Mater.*, 2017, **29**, 1–7.

68 L. Yang, H. Sun, S. Wang, L. Jiang and G. Sun, *Int. J. Hydrogen Energy*, 2017, **42**, 25877–25881.

69 R. Long, B. Li, Z. Liu and W. Liu, *Energy*, 2016, **107**, 388–395.

70 S. W. Lee, Y. Yang, H. W. Lee, H. Ghasemi, D. Kraemer, G. Chen and Y. Cui, *Nat. Commun.*, 2014, **5**, 1–6.

71 Y. Yang, J. Loomis, H. Ghasemi, S. W. Lee, Y. J. Wang, Y. Cui and G. Chen, *Nano Lett.*, 2014, **14**, 6578–6583.

72 R. Long, B. Li, Z. Liu and W. Liu, *Energy*, 2015, **93**, 1022–1029.

73 B. Shapira, I. Cohen, T. R. Penki, E. Avraham and D. Aurbach, *J. Power Sources*, 2018, **378**, 146–152.

74 Y. Yang, S. W. Lee, H. Ghasemi, J. Loomis, X. Li, D. Kraemer, G. Zheng, Y. Cui and G. Chen, *Proc. Natl. Acad. Sci. U. S. A.*, 2014, **111**, 17011–17016.

75 Y. Liu, C. Gao, S. Sim, M. Kim and S. W. Lee, *Chem. Mater.*, 2019, **31**, 4379–4384.

76 S. Lin, N. Y. Yip, T. Y. Cath, C. O. Osuji and M. Elimelech, *Environ. Sci. Technol.*, 2014, **48**, 5306–5313.

77 A. Carati, M. Marino and D. Brogioli, *Energy*, 2015, **93**, 984–993.

78 E. Shaulsky, C. Boo, S. Lin and M. Elimelech, *Environ. Sci. Technol.*, 2015, **49**, 5820–5827.

79 M. Marino, L. Misuri, A. Carati and D. Brogioli, *Energies*, 2014, **7**, 3664–3683.

80 P. Palenzuela, M. Micari, B. Ortega-Delgado, F. Giacalone, G. Zaragoza, D. C. Alarcón-Padilla, A. Cipollina, A. Tamburini and G. Micale, *Energies*, , DOI:10.3390/en11123385.

81 P. Luis, *Hybrid processes based on membrane technology*, Elsevier Inc., 2018.

82 F. Giacalone, F. Vassallo, F. Scargiali, A. Tamburini, A. Cipollina and G. Micale, *J. Memb. Sci.*, 2020, **595**, 117522.

83 M. Reali, *Energy*, 1980, **5**, 325–329.

84 K. L. Hickenbottom, J. Vanneste and T. Y. Cath, *J. Memb. Sci.*, 2016, **504**, 162–175.

85 Z. Zhang, S. Yang, P. Zhang, J. Zhang, G. Chen and X. Feng, *Nat. Commun.*, , DOI:10.1038/s41467-019-10885-8.

86 R. L. McGinnis and M. Elimelech, *Desalination*, 2007, **207**, 370–382.

87 R. L. McGinnis, J. R. McCutcheon and M. Elimelech, *J. Memb. Sci.*, 2007, **305**, 13–19.

88 Y. Zhong, X. Wang, X. Feng, S. Telalovic, Y. Gnanou, K. W. Huang, X. Hu and Z. Lai, *Environ. Sci. Technol.*, 2017, **51**, 9403–9409.

89 C. Boo, Y. F. Khalil and M. Elimelech, *J. Memb. Sci.*, 2015, **473**, 302–309.

90 H. Gong, D. D. Anastasio, K. Wang and J. R. McCutcheon, *Desalination*, 2017, **421**, 32–39.

91 N. N. Bui and J. R. McCutcheon, *Environ. Sci. Technol.*, 2014, **48**, 4129–4136.

92 X. Tong, X. Wang, S. Liu, H. Gao, R. Hao and Y. Chen, *ACS Omega*, 2018, **3**, 15501–15509.

93 Y. Mei and C. Y. Tang, *Desalination*, 2018, **425**, 156–174.

94 J. W. Post, H. V. M. Hamelers and C. J. N. Buisman, *Environ. Sci. Technol.*, 2008, **42**, 5785–5790.

95 E. Brauns, *Desalination*, 2009, **237**, 378–391.

96 D. A. Vermaas, M. Saakes and K. Nijmeijer, *Environ. Sci. Technol.*, 2011, **45**, 7089–7095.

97 X. Luo, X. Cao, Y. Mo, K. Xiao, X. Zhang, P. Liang and X. Huang, *Electrochem. commun.*, 2012, **19**, 25–28.

98 D. Brogioli, F. La Mantia and N. Y. Yip, *Desalination*, 2018, **428**, 29–39.

99 D. Brogioli, F. La Mantia and N. Y. Yip, *Renew. Energy*, 2019, **133**, 1034–1045.

100 K. Kwon, B. H. Park, D. H. Kim and D. Kim, *Energy Convers. Manag.*, 2015, **103**, 104–110.

101 D. H. Kim, B. H. Park, K. Kwon, L. Li and D. Kim, *Appl. Energy*, 2017, **189**, 201–210.

102 M. Bevacqua, A. Carubia, A. Cipollina, A. Tamburini, M. Tedesco and G. Micale, *Desalin. Water Treat.*, 2016, **57**, 23007–23018.

103 F. Giacalone, F. Vassallo, L. Griffin, M. C. Ferrari, G. Micale, F. Scargiali, A. Tamburini and A. Cipollina, *Energy Convers. Manag.*, 2019, **189**, 1–13.

104 A. Tamburini, M. Tedesco, A. Cipollina, G. Micale, M. Ciofalo, M. Papapetrou, W. Van Baak and A. Piacentino, *Appl. Energy*, 2017, **206**, 1334–1353.

105 D. Brogioli, *Phys. Rev. Lett.*, 2009, **103**, 31–34.

106 D. Brogioli, R. Zhao and P. M. Biesheuvel, *Energy Environ. Sci.*, 2011, **4**, 772–777.

107 M. L. Jiménez, M. M. Fernández, S. Ahualli, G. Iglesias and A. V. Delgado, *J. Colloid Interface Sci.*, 2013, **402**, 340–349.

108 F. Liu, O. Schaetzle, B. B. Sales, M. Saakes, C. J. N. Buisman and H. V. M. Hamelers, *Energy Environ. Sci.*, 2012, **5**, 8642–8650.

109 B. B. Sales, F. Liu, O. Schaetzle, C. J. N. Buisman and H. V. M. Hamelers, *Electrochim. Acta*, 2012, **86**, 298–304.

110 G. R. Iglesias, M. M. Fernández, S. Ahualli, M. L. Jiménez, O. P. Kozynchenko and A. V. Delgado, *J. Power Sources*, 2014, **261**, 371–377.

111 S. Ahualli, M. L. Jiménez, M. M. Fernández, G. Iglesias, D. Brogioli and V. Delgado, *Phys. Chem. Chem. Phys.*, 2014, **16**, 25241–25246.

112 M. Marino, L. Misuri, M. L. Jiménez, S. Ahualli, O. Kozynchenko, S. Tennison, M. Bryjak and D. Brogioli, *J. Colloid Interface Sci.*, 2014, **436**, 146–153.

113 C. Lian, C. Zhan, D. E. Jiang, H. Liu and J. Wu, *J. Phys. Chem. C*, 2017, **121**, 14010–14018.

114 D. Moreno and M. C. Hatzell, *ACS Sustain. Chem. Eng.*, 2019, **7**, 11334–11340.

115 B. B. Sales, O. S. Burheim, F. Liu, O. Schaetzle, C. J. N. Buisman and H. V. M. Hamelers, *Environ. Sci. Technol.*, 2012, **46**, 12203–12208.

116 O. S. Burheim, F. Liu, B. B. Sales, O. Schaetzle, C. J. N. Buisman and H. V. M. Hamelers, *J. Phys. Chem. C*, 2012, **116**, 19203–19210.

117 K. Smolinska-Kempisty, A. Siekierka and M. Bryjak, *Desalination*, 2020, **482**, 114384.

118 F. La Mantia, M. Pasta, H. D. Deshazer, B. E. Logan and Y. Cui, *Nano Lett.*, 2011, **11**, 1810–1813.

119 M. Ye, M. Pasta, X. Xie, Y. Cui and C. S. Criddle, *Energy Environ. Sci.*, 2014, **7**, 2295–2300.

120 M. Pasta, C. D. Wessells, N. Liu, J. Nelson, M. T. Mcdowell, R. A. Huggins, M. F. Toney and Y. Cui, *Nat. Commun.*, 2014, **5**, 1–9.

121 P. Peljo, D. Lloyd, N. Doan, M. Majaneva and K. Kontturi, *Phys. Chem. Chem. Phys.*, 2014, **16**, 2831–2835.

122 F. Zhang, N. LaBarge, W. Yang, J. Liu and B. E. Logan, *ChemSusChem*, 2015, **8**, 1043–1048.

123 C. Ponce de León, A. Frías-Ferrer, J. González-García, D. A. Szánto and F. C. Walsh, *J. Power Sources*, 2006, **160**, 716–732.

124 F. Zhang, J. Liu, W. Yang and B. E. Logan, *Energy Environ. Sci.*, 2015, **8**, 343–349.

125 X. Zhu, M. Rahimi, C. A. Gorski and B. Logan, *ChemSusChem*, 2016, **9**, 873–879.

126 M. Rahimi, T. Kim, C. A. Gorski and B. E. Logan, *J. Power Sources*, 2018, **373**, 95–102.

127 W. Wang, H. Tian, G. Shu, D. Huo, F. Zhang and X. Zhu, *J. Mater. Chem. A*, 2019, **7**, 5991–6000.

128 M. Rahimi, L. Zhu, K. L. Kowalski, X. Zhu, C. A. Gorski, M. A. Hickner and B. E. Logan, *J. Power Sources*, 2017, **342**, 956–963.

129 M. Rumayor, A. Dominguez-ramos, M. Fallanza and R. Ib, *Sustain. Energy Fuels*, , DOI:10.1039/d0se00372g.

130 N. A. A. Qasem, S. M. Zubair, B. A. Qureshi and M. M. Generous, *Energy Convers. Manag.*, 2020, **205**, 112448.

131 J. Kim, K. Park, D. R. Yang and S. Hong, *Appl. Energy*, 2019, **254**, 113652.

132 L. F. Greenlee, D. F. Lawler, B. D. Freeman, B. Marrot and P. Moulin, *Water Res.*, 2009, **43**, 2317–2348.

133 S. Al-Amshawee, M. Y. B. M. Yunus, A. A. M. Azoddein, D. G. Hassell, I. H. Dakhil and H. A. Hasan, *Chem. Eng. J.*, , DOI:10.1016/j.cej.2019.122231.

134 J.D.Green, *Encycl. Anal. Sci. (Second Ed.*, 2005, 281–285.

135 J. Tonner, *Barriers to Thermal Desalination in the United States*, 2008.

136 S. Kalogirou, *Energy*, 1997, **22**, 69–81.

137 A. Ghalavand, Y. Hatamipour, M. Rahimi, *Desalin. Water Treat.*, , DOI:10.1080/19443994.2014.892837.

138 M. Al-Shammiri and M. Safar, *Desalination*, 1999, **126**, 45–59.

139 S. A. Kalogirou, *Prog. Energy Combust. Sci.*, 2005, **31**, 242–281.

140 M. A. Sharaf, A. S. Nafey and L. García-Rodríguez, *Desalination*, 2011, **272**, 135–147.

141 M. A. Darwish and H. El-Dessouky, *Appl. Therm. Eng.*, 1996, **16**, 523–537.

142 M. L. Elsayed, O. Mesalhy, R. H. Mohammed and L. C. Chow, *Energy*, 2019, **166**, 552–568.

143 M. A. Sharaf, A. S. Nafey and L. García-Rodríguez, *Energy*, 2011, **36**, 2753–2764.

144 M. C. Garg, *Renewable Energy-Powered Membrane Technology : Cost Analysis and Energy Consumption*, Elsevier Inc., 2019.

145 N. B. and J. O. F.T. Najafi, M. Alsaffar, S.C. Schwerer, in *SEE Annual Conference & Exposition, New Orleans, Louisiana*, 2016, p. 26729.

146 M. Qtaishat, T. Matsuura, B. Kruczek and M. Khayet, *Desalination*, 2008, **219**, 272–292.

147 G. W. Meindersma, C. M. Guijt and A. B. de Haan, *Desalination*, 2006, **187**, 291–301.

148 M. A. E. R. Abu-Zeid, Y. Zhang, H. Dong, L. Zhang, H. L. Chen and L. Hou, *Desalination*, 2015, **356**, 1–14.

149 M. Khayet, P. Godino and J. I. Mengual, *J. Memb. Sci.*, 2000, **165**, 261–272.

150 E. K. Summers, H. A. Arafat and J. H. Lienhard V, *Desalination*, 2012, **290**, 54–66.

151 G. Zuo, R. Wang, R. Field and A. G. Fane, *Desalination*, 2011, **283**, 237–234.

152 Y. Zhang, Y. Peng, S. Ji, Z. Li and P. Chen, *DES*, 2015, **367**, 223–239.

153 G. H. Slattery, US-patent, 2, 764, 488, 1951.

154 A. J. P. Ingemar, US-patent, 2, 666, 304, 1951.

155 J. E. Miller, *Review of Water Resources and Desalination Technologies*, 2003.

156 A. Eghtesad, M. Salakhi, H. Afshin, S. K. Hannani, *Desalination*, , DOI:0.1016/j.desal.2020.114378.

157 K. C. Ng, K. Thu, Y. Kim, A. Chakraborty and G. Amy, *Desalination*, 2013, **308**, 161–179.

158 M. J. B. Jun W. Wu, Eric J. Hu, *Appl. Energy*, 2012, **90**, 316–322.

159 K. Thu, K. Choon, B. B. Saha, A. Chakraborty and S. Koyama, *Int. J. Heat Mass Transf.*, 2009, **52**, 1811–1816.

160 K. C. N. Xiaolin Wang, *Appl. Therm. Eng.*, 2005, **25**, 2780–2789.

161 red heat to power, *Very Low Temperature Regeneration Comparative performance analysis for the selection of main process options*, 2016.

162 L. Zhang, T. Kim, N. Li, T. J. Kang, J. Chen, J. M. Pringle, M. Zhang, A. H. Kazim, S. Fang,

C. Haines, D. Al-Masri, B. A. Cola, J. M. Razal, J. Di, S. Beirne, D. R. MacFarlane, A. Gonzalez-Martin, S. Mathew, Y. H. Kim, G. Wallace and R. H. Baughman, *Adv. Mater.*, 2017, **29**, 1–7.

163 K. Kim and H. Lee, *Phys. Chem. Chem. Phys.*, 2018, **20**, 23433–23440.

164 A. Altaee, P. Palenzuela, G. Zaragoza and A. A. AlAnezi, *Appl. Energy*, 2017, **191**, 328–345.

165 M. Rahimi, A. P. Straub, F. Zhang, X. Zhu, M. Elimelech, C. A. Gorski and B. E. Logan, *Energy Environ. Sci.*, 2018, **11**, 276–285.

166 F. Giacalone, C. Olkis, G. Santori, A. Cipollina, S. Brandani and G. Micale, *Energy*, 2019, **166**, 674–689.

167 R. Long, B. Li, Z. Liu and W. Liu, *J. Memb. Sci.*, 2017, **525**, 107–115.

168 F. Zhang, N. LaBarge, W. Yang, J. Liu and B. E. Logan, *ChemSusChem*, 2015, **8**, 1043–1048.

169 P. Atkins, *physical chemistry*, 1988.

170 Chemistry, Libre Texts, https://chem.libretexts.org/.

171 A. Bard, *Electrochemical methods: foundamental and applications*, 2000.

172 K. H. Mistry and J. H. Lienhard, *Entropy*, 2013, **15**, 2046–2080.

173 J. H. Lienhard, K. H. Mistry, M. H. Sharqawy and G. P. Thiel, *Thermodynamics, Exergy, and Energy Efficiency in Desalination Systems*, 2017.

174 K. H. Mistry, R. K. McGovern, G. P. Thiel, E. K. Summers, S. M. Zubair and J. H. Lienhard, *Entropy*, 2011, **13**, 1829–1864.

175 H. B. Kang and N. H. Cho, *J. Mater. Sci.*, 1999, **34**, 5005–5013.

176 William M. Haynes., *CRC Handbook of Chemistry and Physics*, 2015.

177 G. Jerkiewicz, G. Vatankhah, J. Lessard, M. P. Soriaga and Y. S. Park, *Electrochim. Acta*, 2004, **49**, 1451–1459.

178 D. A. Boryta, *J. Chem. Eng. Data*, 1970, **15**, 142–144.

179 B. M. L. Miller, 1956, **128**, 4–7.

180 A. I. Shahata, A. F. Elsafty and M. M. A. Elnasr, .

181 Y. Cerci, *Exergy, an Int. J.*, 2002, **2**, 15–23.

182 N. Y. Yip, D. Brogioli, H. V. M. Hamelers and K. Nijmeijer, *Environ. Sci. Technol.*, 2016, **50**, 12072–12094.

183 I. Y. Shilov and A. K. Lyashchenko, *J. Mol. Liq.*, 2017, **240**, 172–178.

184 W. J. Hamer and Y. Yung chi, *J. Phys. Chem. Ref. Data*, 1972, **1**, 1047–1100.

185 L. M. Dané, L. J. J. Janssen and J. G. Hoogland, *Electrochim. Acta*, 1968, **13**, 507–518.

186 A. Jameson, E. Gyenge, *Halogens as Positive Electrode Active Species for Flow Batteries and Regenerative Fuel Cells*, Springer Singapore, 2020, vol. 3.

187 R. W. Ramette and R. W. Sandford Jr., *J. Am. Chem. Soc.*, 1965, **87**, 5001–5005.

188 Vincent T. Calabrese and Arshad Khan, *J. Phys. Chem.*, 2000, **104**, 1287–1292.

189 Mansel Davies and Emrys Gwynne, *J. Am. Chem. Soc.*, 1952, **74**, 2748–2752.

190 Y. Zhang, C. Ma, X. Yang, Y. Song, X. Liang, X. Zhao, Y. Wang, Y. Gao, F. Liu, F. Liu, P. Sun and G. Lu, *Sensors Actuators, B Chem.*, 2019, **295**, 56–64.

191 L. Wang and R. V. Kumar, *Mater. Res. Bull.*, 2005, **40**, 1802–1815.

192 H. Y. Dang and X. M. Guo, *Solid State Ionics*, 2011, **201**, 68–72.

193 F. Mauvy, C. Gondran and E. Siebert, *Electrochim. Acta*, 1999, **44**, 2219–2226.

194 F. Mauvy and E. Siebert, *J. Eur. Ceram. Soc.*, 1999, **19**, 917–919.

195 X. Yu and A. Manthiram, *Matter*, 2019, **1**, 439–451.

196 Q. Zhang, F. Liang, T. Qu, Y. Yao, W. Ma, B. Yang, Y. Dai, *IOP Conf. Ser. Mater. Sci. Eng.*, , DOI:10.1088/1757-899X/423/1/012122.

197 O. Bohnke, S. Ronchetti and D. Mazza, *Solid State Ionics*, 1999, **122**, 127–136.

198 N. G. Bukun, *Ionics (Kiel).*, 1996, **2**, 63–68.

199 R. O. Fuentes, F. M. Figueiredo, F. M. B. Marques and J. I. Franco, *Solid State Ionics*, 2001, **140**, 173–179.

200 K. M. Bui, V. A. Dinh, S. Okada and T. Ohno, *Phys. Chem. Chem. Phys.*, 2016, **18**, 27226–27231.

201 R. S. Gordon, G. R. Miller, B. J. McEntire, E. D. Beck and J. R. Rasmussen, *Solid State Ionics*, 1981, **3**–**4**, 243–248.

202 L. Giorno, E. Drioli, *Encycl. Membr.*, 2015, 3–6.

203 N. Anantharamulu, K. Koteswara Rao, G. Rambabu, B. Vijaya Kumar, V. Radha and M. Vithal, *J. Mater. Sci.*, 2011, **46**, 2821–2837.

204 F. M. B. M. & J. I. F. R. O. Fuentes, F. Figueiredo, *Ionics (Kiel).*, 2002, **8**, 383–390.

205 R. A. Robinson and H. J. McCoach, *J. Am. Chem. Soc.*, 1947, **69**, 2244.

206 G.A.linhart, *J. Am. Chem. Soc.*, 1918, **40**, 158–163.

207 Gilbert N. Lewis and Merle Randall, *J. Am. Chem. Soc.*, 1916, **38**, 2348–2356.

208 R. W. Ramette and D. A. Palmer, *J. Solution Chem.*, 1986, **15**, 387–395.

209 A. M. Rajarathnam, Gobinath Pillai, Vassallo, *The Zinc Bromine Flow Battery: Materials Challenges and Practical Solutions for Technology Advancement.*, 2016.

210 M. Mastragostino and C. Gramellini, *Electrochim. Acta*, 1985, **30**, 373–380.

211 R. E. White and S. E. Lorimer, *J. Electrochem. Soc.*, 1983, **130**, 1096–1103.

212 R. Ronen, I. Atlas and M. E. Suss, *J. Electrochem. Soc.*, 2018, **165**, A3820–A3827.

213 L. Tong, Q. Chen, A. A. Wong, R. Gómez-Bombarelli, A. Aspuru-Guzik, R. G. Gordon and M. J. Aziz, *Phys. Chem. Chem. Phys.*, 2017, **19**, 31684–31691.

214 D. H. Han, S. Park, E. J. Kim and T. D. Chung, *Electrochim. Acta*, 2017, **252**, 164–170.

215 M. Kim, D. Yun and J. Jeon, *J. Power Sources*, 2019, **438**, 227020.

216 J. McMurry, *Organic chemistry*, 2015.

217 J. Moreno, S. Grasman, R. Van Engelen and K. Nijmeijer, *Environ. Sci. Technol.*, 2018, **52**, 10856–10863.

218 M. Schmuck, *Appl. Math. Res. eXpress*, 2017, **2017**, 402–430.

219 H. Leelasupakorn, A. Kaewchada, W. Traisantikul, W. Tiengtrakarnsuk, S. Limtrakul and T. Vatanatham, *Chiang Mai J. Sci.*, 2008, **35**, 89–94.

220 D. Brogioli and F. La Mantia, *AIChE J.*, 2019, **65**, 980–991.

221 Y. Yang, S. W. Lee, H. Ghasemi, J. Loomis, X. Li, D. Kraemer, G. Zheng, Y. Cui and G. Chen, *Proc. Natl. Acad. Sci. U. S. A.*, 2014, **111**, 17011–17016.

222 I. Facchinetti, R. Ruffo, F. La Mantia and D. Brogioli, *Cell Reports Phys. Sci.*, 100056, 2020.

223 I. Facchinetti, E. Cobani, D. Brogioli, F. La Mantia and R. Ruffo, *ChemSusChem*, 2020, **13**, 5460–5467.